UNIVERSITY OF
Southampton

Simulation Strategies for Complex Turbulent Flows

by

Markus Weinmann

A thesis submitted in partial fulfillment for the
degree of Doctor of Philosophy

in the
Faculty of Engineering and the Environment
Aerodynamics and Flight Mechanics Research Group

October 2011

UNIVERSITY OF SOUTHAMPTON

ABSTRACT

FACULTY OF ENGINEERING AND THE ENVIRONMENT
SCHOOL OF ENGINEERING SCIENCES

Doctor of Philosophy

SIMULATION STRATEGIES FOR COMPLEX TURBULENT FLOWS

by Markus Weinmann

Computational fluid dynamics in conjunction with the Reynolds-Averaged Navier-Stokes approach is nowadays routinely employed in a large variety of engineering and industrial applications despite some well-known reliability issues in more complex flows. In this study, the performance of a state-of-the-art Explicit-Algebraic-Stress Model (EASM) and a promising elliptic-blending approach is assessed on a range of test cases to predict complex turbulent flows. In an attempt to improve the quality of the predictions, near-wall-anisotropy modifications are introduced to the EASM, which provide better predictions for the Reynolds-stress and anisotropy tensor close to solid walls. In addition, a novel elliptic-blending RANS model is presented, which is based on the inverse turbulence time scale ω, and which is equipped with a non-linear constitutive stress-strain relationship. The coefficients of the non-linear stress-strain relationship are obtained from the explicit solution of a Second-Moment Closure in the limit of weak equilibrium, and by imposing an internal consistency constraint and near-wall-anisotropy modifications, such that the highly anisotropic state of turbulence and the limiting two-component state is correctly reproduced at solid boundaries. The performance of the modified EASM and the novel elliptic-blending model are illustrated and assessed for a range of complex turbulent flows.

It is expected that, due to ever increasing computational resources, unified or hybrid RANS/LES approaches will slowly penetrate into engineering applications where improved accuracy and reliability is needed. For this reason, a unified RANS/LES/DNS framework is presented, which is expected to provide the required amount of turbulence modelling for any mesh resolution and seamlessly operates between RANS and DNS mode. This is achieved by a revised Flow Simulation Methodology where the turbulence modelling contribution of a RANS model is rescaled using a damping function. The Flow Simulation Methodology is operating in conjunction with a newly developed damping function and a tailored convection discretisation scheme. In addition, a thorough calibration study is performed, which ensures proper turbulence resolving capabilities. It is conjectured that a sophisticated RANS model will also improve the overall quality of the predictions of any hybrid RANS/LES model. For this reason, the new elliptic-blending RANS model is incorporated, together with two successively simpler turbulence models, into the unified RANS/LES/DNS framework and the performance are assessed on a range of test cases, and compared to other widely used hybrid RANS/LES methods.

Contents

List of Figures

List of Tables

Declaration Of Authorship

I, Markus Weinmann, declare that the thesis entitled **Simulation Strategies for Complex Turbulent Flows** and the work presented in the thesis are both my own, and have been generated by me as the result of my own original research. I confirm that:

- this work was done wholly or mainly while in candidature for a research degree at this University;
- where any part of this thesis has previously been submitted for a degree or any other qualification at this University or any other institution, this has been clearly stated;
- where I have consulted the published work of others, this is always clearly attributed;
- where I have quoted from the work of others, the source is always given. With the exception of such quotations, this thesis is entirely my own work;
- I have acknowledged all main sources of help;
- where the thesis is based on work done by myself jointly with others, I have made clear exactly what was done by others and what I have contributed myself;
- parts of this work have been published as:

  - Weinmann, M. and Sandberg, R.D. (2009) Suitability of Explicit-Algebraic-Stress Models for Predicting Complex Three-Dimensional Flows. Proceedings of the 19th AIAA Computational Fluid Dynamics Conference, San Antonio, US, 22 - 25 Jun 2009.

- Weinmann, M., Sandberg, R.D. and Doolan, C. J. (2010) Flow and noise predictions for a tandem cylinder configuration using novel hybrid RANS/LES approaches. Proceedings of the 16th CEAS/AIAA Aeroacoustics Conference, Stockholm, Sweden, 07 - 09 Jun 2010.

- Weinmann, M., Sandberg R. D. and Doolan C. J. (2010) Assessment of advanced turbulence models for predicting the hydrodynamic and noise of a tandem cylinder configuration. Proceedings of the 1st Workshop on Benchmark Problems for Airframe Noise Computations (BANC-I) NASA/AIAA Stockholm, Sweden, 10 - 11 June 2010 .

Signed: .....

Date: .....

Acknowledgements

I would like to express my deepest gratitude to my supervisor Dr. Richard D. Sandberg for his continuous interest, support and guidance during this study. I would like to extend my appreciation to Dr. Kenji Takeda for his advice during my research.

The financial support provided by the School of Engineering Sciences is greatly acknowledged.

I am grateful to the following people for kindly providing reference data, computational grids and for the open exchange of ideas: Prof. Yukio Kaneda, Prof. Mikhael Strelets, Dr. Manuel Garcia-Villalba, Dr. Dominic von Terzi, Dipl.-Ing. Hayder Schneider. I am also very grateful to Prof. Gary Coleman for critically reviewing the manuscript, which has improved the quality of my thesis.

I want to thank the OpenFOAM® user community for their help and support on various issues related to OpenFOAM®.

I take this opportunity to thank all my colleagues at the Aerodynamics and Flight Mechanics Research Group for their companionship, assistance and many invigorating discussions over the years.

I am particularly indebted to my family and friends in Germany for their never-ending encouragement and for supporting me throughout all my endeavours.

Last, but by no means least, I thank all my friends in Southampton for making my stay here so enjoyable.

Nomenclature

Latin Letters

A	flatness parameter
a_{ij}	stress-anisotropy tensor
a,b,c	constants
A_0, A_1, A_2, A_3, A_4	closure constant
a_{ij}^{ex}	extra-anisotropy tensor
$CD_{k\omega}$	cross diffusion term
C_f	skin friction coefficient
c_s, C_1, C_1', C_1^0, C_1^*	closure constant
C_2, C_2^*, C_3, C_4, C_s^w, C_r^w	closure constant
C_L, C_η, C_T, , C_μ^ν	closure constant
C_S, C_{DES}, C_α, C_{SAS}	calibration constant
C_L,C_D	lift and drag coefficient
C_p	pressure coefficient
$C_\mu, C_{\epsilon_2}, C_{\epsilon_1}$	closure constants
C_k	constant
D/Dt	material derivative $\partial/\partial t + \overline{u}_k \partial/\partial x_k$
D	diameter
d, y	wall distance
D_ϵ	turbulence transport of turbulence kinetic energy dissipation rate
D_{ij}	total transport of Reynolds stress
D_{ij}^t	turbulence transport of Reynolds stress
D_{ij}^p	pressure transport of Reynolds stress
D_k	turbulence transport of turbulence kinetic energy
e_{ij}	dissipation-rate-anisotropy tensor
$F()$, $F_{ij}()$	tensor function

f_{22}	elliptic-relaxation variable
F, F_b, F_Δ, f_d, f_b, f_2	blending function
f_μ, f_1, f_2, $f_{\beta*}$, f_s, f_w,	wall damping functions
f_k, f_ϵ	ratio of un-resolved to total turbulence kinetic energy, dissipation rate
f_{ij}	redistribution tensor
f_Δ,f_η, f_z	functions of the damping function α
$G()$	filtering kernel
IV, V	fourth and fifth invariants
I_a	first invariant of the anisotropy tensor
II_a, II_S, II_Ω	second invariant of the anisotropy, strain, rotation-rate tensor
III_a, III_S	third invariant of the anisotropy, strain-rate tensor
k	turbulence kinetic energy
L	mean flow length scale, also correlation length scale
L_η	viscous or Kolmogorov length scale
L_I	integral length scale
L_{vK}	v. Karman length scale
l_{mix}	mixing length
L_T	turbulence length scale
M_{ijlm}	fourth-order tensor
n_i, $\boldsymbol{n}$	wall-normal vector
$N()$	Navier-Stokes operator
N, Q, P_1, P_2	variables of the EASM model
p	static pressure
$\overline{p}$	mean or filtered static pressure
Pe	Peclet number
P_ϵ^1, P_ϵ^3, P_ϵ^3, P_ϵ^4	production of turbulence kinetic energy dissipation rate
φ	normalised wall-normal fluctuating velocity scale
P_{ij}	production of Reynolds stress
P_k	production of turbulence kinetic energy
$p^{'}$	fluctuating or unresolved static pressure
$\boldsymbol{Q}$	orthogonal transformation matrix
Re	Reynolds number

Re_T	turbulence Reynolds number
Re_y	turbulence Reynolds number based on wall distance
S_{ij}	non-dimensionalised strain-rate tensor τS^*_{ij}
S_ϕ	source term
S^*_{ij}	strain-rate tensor
St	Strouhal number
$\boldsymbol{T}$,T_{ij}	second-order tensor
t	time
T_I	integral time scale
T_{ij}	resolved stresses
U	mean flow velocity scale
U_I	integral velocity scale
u_i	instantaneous velocity field
$\overline{u}_i$	mean or filtered velocity field
$u_i^{'}$	fluctuating or unresolved velocity field
u_τ	skin friction velocity
$\overline{u_i^{'}u_j^{'}}$	Reynolds stress tensor
$\overline{v}^2$	wall-normal fluctuating velocity scale
V_T	turbulence velocity scale
x_r	reattachment location
x_s	separation location
x,y,z	coordinate directions

Greek Letters

α	elliptic-blending variable also latency parameter
α_i	closure constants
β, β^*, γ	closure constants
β_i	coefficient of the EASM model
Δ	filter width
δ	boundary-layer thickness
δ_{ij}	Kronecker delta
$\Delta_x, \Delta_y, \Delta_z$	grid spacing
ρ	density

ϵ_ϵ	dissipation of turbulence kinetic energy dissipation rate
ϵ	turbulence kinetic energy dissipation rate
ϵ_{ij}	turbulence kinetic energy dissipation rate tensor
Γ	diffusion coefficient
γ_i	calibration constant
Γ_1,Γ_3,Γ_3	elements of the k-ω model
κ	wavenumber and v. Karman constant
λ_T	Taylor length scale
μ	dynamic viscosity
ν	kinematic viscosity
$\widetilde{\nu}$	modified kinematic viscosity
ν_T	turbulence kinematic viscosity
ω	specific turbulence kinetic energy dissipation rate
ϕ	generic variable
$\Phi_{ij}^{(s)}$	slow part of the pressure-strain correlation
$\Phi_{ij}^{(r)}$	rapid part of the pressure-strain correlation
Φ_{ij}	pressure-strain correlation
$\Phi_{ij}^{(w)}$	wall-reflection term of the pressure-strain correlation
Π_{ij}	velocity pressure-gradient correlation
$\Pi_{ij}^* = \Pi_{ij} - \epsilon_{ij}$	modified velocity pressure-gradient correlation
σ_k, σ_ϵ, σ_ω, σ_φ, σ_d	closure constants
σ_b	flux blending function
τ	turbulence time scale
τ_{ij}	Reynolds-stress tensor, Subgrid-scale-stress tensor
τ_w	wall shear-stress
Ω_{ij}	non-dimensionalised rotation-rate tensor $\tau\Omega_{ij}^*$
Ω_{ij}^*	rotation-rate tensor

Subscripts

0	free-stream value
1	first cell adjacent to walls
b	bulk quantity
f	face value
I	integral scale of the large scale motion
i, j, k, l, m	variable number
∞	free-stream value, equilibrium value
rms	root mean squared
sgs	subgrid-scale quantities
u, v, w	velocity component
w	wall value

Superscripts

$eq.$	equilibrium value
h, hom	homogeneous part
m,n, α	integer numbers
$+$	viscous sub-layer scaling
$'$	fluctuating quantity
$*$	non-dimensional wall distance
T	transpose
w	wall part

Glossary

ASM	Algebraic Stress Model
CDS	Central differencing scheme
CV	Control Volume
$DDES$	Delayed Detached Eddy Simulation
DES	Detached Eddy Simulation

$DHIT$	Decaying homogeneous isotropic turbulence
DNS	Direct Numerical Simulation
$DRSM$	Differential Reynolds Stress Model
$EASM$	Explicit Algebraic Stress Model
FSM	Flow Simulation Methodology
FVM	Finite Volume Method
$IDDES$	Improved Delayed Detached Eddy-Simulation
LES	Large Eddy Simulation
LLR	Launder, Reece, Rodi DRSM
LNS	Limited Numerical Scales
$PANS$	Partially Averaged Navier-Stokes
$PISO$	Pressure-Implicit with Splitting of Operators
$PITM$	Partially Integrated Transport Model
$PRNS$	Partially Resolved Navier-Stokes
PSD	Power Spectral Density
$RANS$	Reynolds-Averaged Navier-Stokes
RCP	Resolution Control Parameter
SAS	Scale-Adaptive Simulation
SGS	Subgrid Scale
$SIMPLE$	Semi-Implicit Method for Pressure-Linked Equations
SMC	Second Moment Closure
SSG	Speziale, Sarkar, Gatski DRSM
SST	Shear Stress Transport
$TPITM$	Temporally Partially Integrated Transport Model
$TRANS$	Turbulence-Resolving RANS
TVD	Total Variation Diminishing
UDS	Upwind differencing scheme
$UMIST$	University of Manchester Institute of Science and Technology
$URANS$	Unsteady Reynolds-Averaged Navier-Stokes
$VLES$	Very Large Eddy Simulation

Chapter 1

Introduction

1.1 Background

Computational Fluid Dynamics (CFD) is nowadays routinely applied to predicting turbulent flows in a large variety of engineering and industrial applications. CFD may deliver results at a fraction of the cost and time required for wind tunnel testing, and hence provides an ideal tool for product development and in design search and optimisation studies. The role of CFD in product development is expected to become even more important in the future due to ever increasing availability of computational resources, improvements in numerical algorithms and automated generation of computational grids for complex configurations.

Turbulent flows may be described as a multi-scale phenomenon where the non-linearity of the partial differential equations governing fluid flow, the Navier-Stokes equations, gives rise to a chaotic, irregular state of fluid motion, which contains a large spectrum of length and time scales. The spectrum of length and time scales present in a turbulent flow rapidly grows with increasing Reynolds number. Unfortunately, many flows of engineering and practical interest are characterised by a high Reynolds number with the consequence, that the spatial and temporal resolution required to perform Direct Numerical Simulation (DNS) of all turbulence length and time scales present in the flow is well beyond currently available computational resources.

The engineering approach to simulating turbulent flows at high Reynolds number is based on the Reynolds-Averaged Navier-Stokes (RANS) equations. In the RANS

approach, an ensemble-averaging procedure is applied to the Navier-Stokes equations such that all spatial and temporal scales of turbulence are removed and only mean flow quantities are computed from the governing equations. For many engineering applications the significantly reduced computational cost of RANS is very appealing and facilitates short turnaround times. In addition, predictions of the mean-flow field are sufficient to determine a range of relevant engineering parameters such as lift, drag or pressure loss. Nevertheless, there are other engineering applications where mean-flow quantities are not sufficient and where more detailed information about the unsteady nature of the flow field is required, for example, in aeroacoustic applications or fluid-structure interaction. The major drawback of the RANS approach is the requirement to model unknown terms appearing in the governing equations. The unknown term originates from the averaging procedure and accounts for the effects of the unresolved turbulence on the mean flow. It is unfortunately not possible to model the unknown term in a general and universal fashion, such that satisfactory predictions of the mean-flow field are obtained in every situation. The development of appropriate models of the unknown term is heavily based on empiricism and calibration for a limited number of rather simple flows (e.g. isotropic turbulence, homogeneous shear flow). As a consequence, the reliability of these so-called RANS models deteriorates when applied to more complex flows, which significantly differ from the inherent calibration assumptions. Typical examples of flows where the predictive performance of RANS models deteriorates are flows where large scale, anisotropic turbulence structures dominate the evolution of the mean-flow field.

Large-Eddy Simulation (LES) is another strategy for the simulation of turbulent flows. In LES, a spatial or temporal filter is applied to the Navier-Stokes equations, which effectively removes the smallest turbulence scales from the flow field. The large scales of turbulence remain unmodified by the filtering operation and are explicitly resolved by the simulation in space and time. Therefore, LES is more expensive than RANS but provides superior predictive accuracy, since the large-scale, anisotropic turbulence structures, which significantly contribute to the transport of mass, momentum and energy in the flow, and which strongly depend on boundary conditions, are explicitly resolved in the simulation. Despite the promise of LES, it is hardly used in industrial applications due to the fact that in high-Reynolds-number wall-bounded flows the all-important 'large' turbulence scales, which contain most of the turbulence kinetic energy and where production of turbulence kinetic energy occurs become very small close to the wall. As a consequence, the computational requirements of resolving the near-wall region in high-Reynolds-number flows becomes

prohibitive large and LES is not yet a feasible substitute for the RANS approach.

In order to make LES applicable at high-Reynolds-number wall-bounded flows, hybrid modelling approaches have been proposed, where RANS and LES are merged into a unified framework. In order to minimise computational costs, the RANS approach is used to model the flow close to the wall, whereas LES is used away from the wall. It is expected that unified or hybrid RANS/LES methods will slowly penetrate into engineering applications where improved accuracy and reliability is needed and where the computational cost of LES is not affordable.

1.2 Objectives

The RANS approach will continue to play a vital role for the simulation of turbulent flows within various industrial and engineering applications for many years to come. The majority of CFD engineers rely on one- and two-equation turbulence models, which are based on the concept of a turbulence or eddy-viscosity, and which employ a linear constitutive stress-strain relationship. Such models provide a simple, cheap and robust modelling framework, but have known deficiencies and reliability issues in more complex flows.

One defect of this modelling framework is associated with the assumption of a linear constitutive stress-strain relationship. This functional stress-strain relationship predicts results with fair accuracy for a range of simple and 'well-behaved' thin shear flows. In situations where the normal components of the Reynolds-stress tensor or stress anisotropy become important, such as in flow impingement, separation, recirculation or streamline curvature, to name a few, the linear stress-strain relationship fails to predict reliable results. The second defect is associated with the empirical treatment of wall-bounded flows. Traditional one- and two-equation turbulence models do not adequately account for the effect a wall exerts on the flow. Therefore, the effects of a solid wall need to be artificially introduced in order to recover the correct mean-velocity profile or the correct behaviour of the turbulence quantities. For this purpose, empirical viscosity-dependent damping functions have been introduced in various forms. These functions are calibrated for simple flows but, since the wall damping is primarily caused by a non-viscous kinematic blocking effect, there is not much justification that they are also appropriate in more complex flows. The progress in RANS modelling has been stagnant over the past years, even though many applications would benefit from improved RANS models, which include a more natural wall treatment and which are able to more reliably

predict the Reynolds-stress and anisotropy fields in complex flows, yet retain the robustness of traditional two-equation models. Therefore, the first objective of this work is the development of a RANS model with improved wall modelling capabilities and which provides more reliable predictions of the Reynolds-stress and anisotropy fields in complex flows.

Many hybrid RANS/LES methods rely on making the characteristic length scale of the model equations proportional to the grid resolution, and thus have the same resolution requirements as traditional LES models where most of the turbulence kinetic energy and all production mechanisms of turbulence kinetic energy need to be explicitly resolved. In engineering and industrial applications the mesh quality and resolution is sometimes sacrificed for short turnaround times. In such cases it would be advantageous if the hybrid RANS/LES method would allow Very Large-Eddy Simulation (VLES) to occur where most of the turbulence kinetic energy is statistically represented by the turbulence model, or if the method would even revert back to RANS mode if the flow is highly under-resolved. In order to allow for coarse grid LES or VLES, two issues require special attention. The first issue is associated with how the appropriate turbulence length scale is obtained in this situation. The second issue is related to the underlying RANS model. For a resolution cut-off located in the large scales of turbulence, the assumption of equilibrium and isotropy of the unresolved scales does not hold, and it seems beneficial to employ a turbulence model, which includes the ability to predict non-equilibrium and anisotropy effects. These features may not only become important in the LES region, they are also very desirable for an accurate representation of the flow in the RANS region close to the wall. Therefore, possible improvements in the RANS turbulence models are not limited to pure RANS applications. It is expected that improvements in the RANS model may also improve the quality of the predictions in the LES region. The second objective is to investigate the performance of advanced RANS closures within a hybrid modelling framework. The hybrid framework should ideally provide RANS/VLES/LES and DNS capabilities.

1.3 Contributions

The most important contributions of this work can be summarised as follows:

- Assessment and validation of Explicit-Algebraic-Stress-Models (EASM) and other state-of-the-art RANS turbulence models for predicting complex turbulent flows.
- Discussion and proposal of suitable near-wall anisotropy modifications for EASM models.
- Development of a novel RANS model, which combines the elliptic-blending approach for modelling near-wall flows with the advantages of a non-linear stress-strain relationship. A near-wall-consistency constraint and additional near-wall anisotropy modifications are introduced such that the highly anisotropic state of turbulence and the limiting two-component state is correctly reproduced as the wall is approached.
- Proposal and testing of a modified Flow Simulation Methodology, which provides a unified RANS/LES/DNS framework.
- Proposal of a tailored hybrid convection discretisation scheme for the modified Flow Simulation Methodology.
- Evaluation of Scale-Adaptive Simulation and Improved Delayed Detached-Eddy Simulation in comparison with the novel Flow Simulation Methodology.

1.4 Thesis outline

The thesis is organised as follows. In chapter 2, a brief introduction of the fundamentals of turbulent flows is given. This is followed by a discussion about the most popular and most promising strategies of statistical turbulence modelling (RANS) in chapter 3. The turbulence resolving approaches of Direct and Large-Eddy Simulation are introduced in chapter 4, in conjunction with available techniques to combine the framework of RANS modelling with turbulence-resolving LES. In chapter 5, the numerical framework used to solve the set of governing equations is briefly introduced. The constitutive relations of the baseline EASM, upon which the present work is based, are summarised in chapter 6. In addition, a range of different test and validation cases are presented in order to highlight the performance and deficiencies

of the baseline EASM closure. The test cases include the flow in a planar channel, the flow over the NASA hump configuration and the flow in a three-dimensional diffuser. In chapter 7, several strategies are presented, which aim at improving the predictions of the Reynolds-stress and anisotropy tensor of the baseline EASM close to the wall. The effectiveness of these modifications are illustrated and discussed. In chapter 8, a novel approach is presented, which aims at combining the advantages of the elliptic-blending approach for modelling near-wall flows with the advantages of a non-linear stress-strain relationship to provide more accurate predictions of the Reynolds-stress and anisotropy field in complex flows. The performance of the new turbulence model is again assessed for the flow in a planar channel, the flow over the NASA hump configuration and the flow in a three-dimensional diffuser. In chapter 9, a modified Flow Simulation Methodology is proposed, which provides a unified RANS/LES/DNS framework. In addition, a tailored hybrid convection discretisation scheme is proposed and a calibration procedure for the Flow Simulation Methodology is presented. The performance of the modified Flow Simulation Methodology is assessed in chapter 10 for complex internal and external flows and compared to reference data and Scale-Adaptive Simulation and Improved Delayed Detached-Eddy Simulation. The test cases include, amongst others, the flow in a three-dimensional diffuser and the flow around a tandem cylinder configuration. Finally, a summary of results and findings is given in chapter 11.

Chapter 2

Fundamentals of Turbulent Flows

This chapter is intended to give a brief introduction of the fundamental physics of turbulent flows, before a detailed discussion about modeling strategies will be presented in chapters 3 and 4. This short introduction will by no means be comprehensive and the interested reader is referred to the textbooks of Pope (2000), Hinze (1975) or Tennekes & Lumley (1972) for a more complete discussion.

Turbulence or turbulent flows can be described as an 'irregular condition of flow in which the various quantities show random variation with time and space coordinates', (Hinze, 1975). On the other hand, flows, which exhibit a smooth and organised variation in space and time are described as laminar flow. The turbulent state of fluid motion is the most frequently one encountered in flows of practical interest and, as stated by Tennekes & Lumley (1972), 'laminar flow is the exception, not the rule'. Turbulent flows exhibit some characteristic features, which are distinctly different from a laminar flow. The large-scale turbulent fluctuations increase mixing in the flow, which significantly enhances the momentum, heat and mass transfer. Turbulent flows also exhibit increased levels of energy dissipation, which may become noticeable as an increase in friction or drag on an object placed in the flow.

Laminar flows can only exist where inertial effects are small compared to viscous effects. The ratio of inertial forces to viscous forces can be expressed in terms of the non-dimensional Reynolds number $Re = UL/\nu$, where U is a characteristic velocity scale, L a characteristic length scale and ν the kinematic viscosity. For example, the flow in a pipe remains laminar for a Reynolds number $Re_D < 2000$, where Re_D is based on the pipe diameter D. Laminar flow at low Reynolds number tends to remain stable in the presence of ambient perturbations (surface vibration, surface

roughness) due to the dissipative action of viscosity, which damps or suppresses the growth of disturbances. With increasing Reynolds number, inertial forces exceed the influence of viscous forces and when a critical Reynolds number is reached, perturbations may grow and the laminar flow becomes unstable for sufficiently large disturbances. The laminar flow then undergoes a series of instability mechanisms before it eventually becomes a fully irregular, three-dimensional turbulent flow.

Turbulence can only be generated or sustained in the presence of a mean rate of strain, which distorts the large-scale motion and transfers kinetic energy from the mean flow to turbulent fluctuations. The largest scales of turbulent motion are generally anisotropic and depend on the flow under consideration as well as boundary conditions. The largest turbulence scales also contain most of the kinetic energy, and their size is either limited by geometrical constraints or it is of the same order as the shear-layer thickness. The large-scale turbulence motion has characteristic velocity and length scales U_I and L_I, which are approximately of the same order as the mean-flow scales U and L. This implies that for high-Reynolds-numbers flows, the Reynolds number of the large-scale turbulent motion $Re_I = U_I L_I/\nu$ is of the same order of magnitude as the mean-flow Reynolds number, with the consequence, that the direct effect of viscosity onto the largest turbulence scales is negligible.

The large-scale turbulent motions pass parts of their kinetic energy on to eddies of successively smaller size by an inviscid vortex-stretching mechanism. The vortex stretching is an intrinsically three-dimensional mechanism, which results in a net stretching of a vortex tube (reduction of the vortex tube diameter) and in an increase of vorticity due to conservation of angular momentum. This process transfers kinetic energy to successively smaller scales until the eddies reduces to a size where the characteristic turbulence Reynolds number becomes small and the viscosity starts to directly act upon the scales of motion. The action of viscosity at the small scales dissipates the turbulence kinetic energy by conversion into internal thermal energy.

It can be estimated that the largest scales of turbulence possess a kinetic energy of order U_I^2 and a characteristic time scale $T_I = L_I/U_I$. Therefore, the rate at which the large scales transfer energy to smaller scales can be approximated as $U_I^2/T_I = U_I^3/L_I$. Thus, in equilibrium conditions, where production of turbulence kinetic energy and transfer-rate from the large scales to smaller scales equals the rate at which energy is dissipated at the smallest scales, it can be estimated, that the dissipation rate scales as $\epsilon = U_I^3/L_I$. This also suggests that the dissipation rate is essentially set by the dynamics of the large scales.

In high-Reynolds-number flows, where the energy containing and dissipative scales are sufficiently separated, an intermediate range exists where the turbulence scales are smaller than the large scales, but still larger than the dissipative scales. Turbulent eddies in this regime merely transfer the kinetic energy produced at the largest scales to successively smaller scales and are not directly affected by viscosity. Kolmogorov (1941) suggested that eddies in this range only dependent on the dissipation rate ϵ and that, on dimensional grounds, the energy is distributed according to $E(\kappa) = C_\kappa \epsilon^{2/3} \kappa^{-5/3}$, with the constant C_κ and the wavenumber $\kappa = 2\pi/l$, where l corresponds to the spatial scale of the eddies. The range of scales where the $-5/3$ law is valid is referred to as the inertial subrange or universal equilibrium range, since the time scale of these eddies is much smaller than that of the large scales, so that they adapt quickly to changes in the large scales. Kolmogorov also suggested that the large anisotropic scales loose their directional preference, or anisotropy, in the cascade process. This has the consequence that, providing the Reynolds number is high enough, the small scales approach a more isotropic and universal state. Kolmogorov further argued that the smallest scales solely depend on the viscosity ν and the rate at which they are dissipated. Based on dimensional arguments, a characteristic length scale of the smallest turbulence scales can be obtained as $L_\eta = (\nu^3/\epsilon)^{1/4}$. With this information, the ratio of smallest to largest length scales present in a turbulent flow is given by $L_\eta/L_I = (\nu^3/U_I^3 L_I^3)^{1/4} = Re_I^{-3/4}$. Therefore, the separation of scales in a turbulent flow increases as the Reynolds number increases. The presence of a wide spectrum of spatial and temporal scales is another characteristic feature of turbulent flows, and is the main reason why direct numerical simulation is currently limited to low or moderate Reynolds numbers.

Chapter 3

Reynolds-Averaged Navier-Stokes Modelling

In this chapter the approach of statistical turbulence modelling will be discussed in detail. Statistical turbulence modelling is almost exclusively used for the simulation of high-Reynolds-number turbulent flows of practical interest and is based on the RANS equations, where the mean flow is computed directly and the effects of turbulence are incorporated by models. The existence of an overwhelming number of possible RANS models makes it virtually impossible to present a complete review. For this reason, the present review is limited to the most popular and most promising strategies of statistical turbulence modelling. For a more comprehensive review the reader is referred to the textbooks of Launder & Sandham (2002), Durbin & Petterson-Reif (2001), Wilcox (1998), Hanifi *et al.* (1999) or Gatski *et al.* (1996).

3.1 The RANS Equations

In order to derive governing equations, which describe the evolution of the mean flow only, all variables are decomposed into a mean and fluctuating part. This procedure is commonly referred to as Reynolds decomposition. For example, the decomposition for the velocity vector can be written as

$$u_i = \overline{u}_i + u_i^{'}, \tag{3.1}$$

where u_i is the instantaneous velocity vector, $\overline{u}_i$ the mean velocity and $u_i^{'}$ the fluctuating velocity vector.

The Reynolds-averaged quantities are most generally defined as an ensemble average over N different realisations

$$\overline{u}_i\left(\underline{\mathbf{x}},t\right)=\lim_{N\to\infty}\frac{1}{N}\sum_{n=1}^{N}u_i^{(n)}(\underline{\mathbf{x}},t). \tag{3.2}$$

For statistically steady turbulence the ensemble average is equal to the time average

$$\overline{u}_i\left(\underline{\mathbf{x}}\right)=\lim_{T\to\infty}\frac{1}{T}\int_0^T u_i(\underline{\mathbf{x}},t)\mathrm{d}t, \tag{3.3}$$

or equal to a volume average in case of homogeneous turbulence

$$\overline{u}_i\left(\underline{t}\right)=\lim_{V\to\infty}\frac{1}{V}\int_V u_i(\underline{\mathbf{x}},t)\mathrm{d}V. \tag{3.4}$$

Substituting the decomposed quantities into the continuity and momentum equation for incompressible flow

$$\frac{\partial u_i}{\partial x_j}=0, \tag{3.5}$$

$$\frac{\partial u_i}{\partial t}+u_j\frac{\partial u_i}{\partial x_j}=-\frac{1}{\rho}\frac{\partial p}{\partial x_i}+\nu\nabla^2 u_i, \tag{3.6}$$

and averaging the same yields the RANS equations, which govern the evolution of the mean flow. Taking into account the Reynolds averaging rules

$$\begin{aligned}\overline{\overline{u_i}} &= \overline{u}_i, \quad \overline{u_i'}=0, \quad \overline{\overline{u_i}u_j'}=\overline{\overline{u_j}u_i'}=0,\\ \overline{\partial u_i/\partial x_j} &= \partial\overline{u_i}/\partial x_j, \quad \overline{\partial u_i/\partial t}=\partial\overline{u_i}/\partial t, \quad \overline{u_iu_j}=\overline{u}_i\overline{u}_j+\overline{u_i'u_j'},\end{aligned} \tag{3.7}$$

the RANS equations can be written as

$$\frac{\partial\overline{u}_i}{\partial x_j}=0, \tag{3.8}$$

$$\frac{\partial\overline{u}_i}{\partial t}+\overline{u}_j\frac{\partial\overline{u}_i}{\partial x_j}=-\frac{1}{\rho}\frac{\partial\overline{p}}{\partial x_i}+\nu\nabla^2\overline{u}_i-\frac{\partial\overline{u_i'u_j'}}{\partial x_j}. \tag{3.9}$$

The Reynolds-averaging procedure applied to the nonlinear convection term in the momentum equation has introduced the additional term $\partial/\partial x_j\left(\overline{u_i'u_j'}\right)$ on the right-hand side of the RANS momentum equation (3.9). The divergence of the correlation tensor $\overline{u_i'u_j'}$ can be considered as an additional source of momentum due to turbulent fluctuations, that appears in the momentum equation in the form of an additional effective stress tensor. The correlation $\overline{u_i'u_j'}$ is therefore also referred to

as the Reynolds-stress tensor. The appearance of the Reynolds-stress tensor has the consequence that the RANS momentum equations are no longer closed. In order to obtain a solvable system of equations, a turbulence model needs to be employed, which relates the Reynolds-stress tensor to the velocity gradient tensor $\partial\overline{u}_i/\partial x_j$ or other variables in the equations set.

The Boussinesq Approximation

In the early days of turbulence modelling, Boussinesq (1877) proposed to close the RANS equations using an analogy between the viscous stress in a Newtonian fluid and the turbulent Reynolds-stress, where the kinematic viscosity ν is replaced by a scalar turbulence viscosity ν_T. The Boussinesq approximation is still widely in use today and reduces the closure problem to determining the turbulence or eddy-viscosity ν_T. In contrast to the kinematic viscosity of the fluid, the turbulence viscosity is a property of the turbulent flow under consideration. The Boussineq hypothesis can be written as

$$\overline{u_i' u_j'} = \frac{2}{3} k \delta_{ij} - 2\nu_T S_{ij}^*, \tag{3.10}$$

where $k = \overline{u_i' u_i'}/2$ is the turbulence kinetic energy and $S_{ij}^* = (1/2)\left(\partial\overline{u}_i/\partial x_j + \partial\overline{u}_j/\partial x_i\right)$ the strain-rate tensor.

The assumption of a viscous Newtonian-like, linear relation between the stress and rate of strain is a drastic oversimplification. In reality, the behaviour of a turbulent flow bears more similarity with a non-Newtonian fluid, where the viscosity may depend on the strain-rate or strain-rate history, and where the stress-strain relationship may be of a non-linear form.

An algebraic stress-strain relationship, where the transport of Reynolds stress is not accounted for, has some justification for simple, 'well behaved' flows where the flow is not subject to rapid changes, and where the Reynolds stress is mainly determined by local processes such as production or dissipation. In more complex flows, where the flow experiences rapid spatial changes and where the flow is not in equilibrium (where the production to dissipation ratio of turbulence kinetic energy P_k/ϵ is not close to unity) or where stress transport dominates the evolution of the Reynolds-stress tensor, an algebraic stress-strain relationship cannot be justified. This is partly, because turbulent flows require a finite time to adapt to sudden changes in strain-rate. This is opposed to the viscous stress, where the molecular timescale is small enough to almost instantly adjust to sudden changes in strain-rate, which justifies the algebraic stress-strain relationship.

The Boussinesq approximation may provide reasonable predictions for thin parallel shear flows where the shear stress is the only active component of the Reynolds-stress tensor. In situations where the normal components of the Reynolds-stress tensor or stress anisotropy become important, the linear stress-strain relationship fails to produce reliable results. Example of such cases include turbulence-driven secondary motion, flow impingement, separation, recirculation and where extra-strain rates such as curvature of the mean flow, rotation or skewing alter the structure of turbulence

To summarise, a linear constitutive stress-strain relationship in conjunction with a scalar eddy viscosity may provide accurate predictions for simple, well-behaved thin shear flows. For more complex three-dimensional flows, the Boussinesq approximation suffers from fundamental limitations and predictive accuracy may deteriorate. In the following section, several approaches are introduced, which alleviate some of the limitations of the Boussinesq approximation.

3.2 Evolution Equations

3.2.1 Reynolds-Stress Tensor

A differential transport equation for the unknown correlation $\overline{u_i' u_j'}$ can directly be derived from the Navier-Stokes equation. First, the instantaneous momentum equations are expressed as $N(u_i) = 0$, where the operator $N(u_i)$ is defined as

$$N(u_i) = \frac{\partial u_i}{\partial t} + u_k \frac{\partial u_i}{\partial x_k} + \frac{1}{\rho}\frac{\partial p}{\partial x_i} - \nu \nabla^2 u_i. \tag{3.11}$$

A transport equation for the second moments can now be constructed by taking the following average

$$\overline{u_i' N(u_j) + u_j' N(u_i)} = \overline{u_i' N\left(\overline{u}_j + u_j'\right) + u_j' N\left(\overline{u}_i + u_i'\right)} = 0. \tag{3.12}$$

Assuming incompressible flow and neglecting additional body forces, the evolution equation for the Reynolds-stress tensor is obtained as

$$\begin{aligned}\frac{D\overline{u_i'u_j'}}{Dt} &= \underbrace{\overline{u_i'u_k'}\frac{\partial\overline{u}_j}{\partial x_k} - \overline{u_j'u_k'}\frac{\partial\overline{u}_i}{\partial x_k}}_{P_{ij}} - \underbrace{\overline{\left(u_i'\frac{\partial p'}{\partial x_j} + u_j'\frac{\partial p'}{\partial x_i}\right)}}_{\Pi_{ij}} \\ &\quad \underbrace{- 2\nu\overline{\left(\frac{\partial u_i'}{\partial x_k}\frac{\partial u_j'}{\partial x_k}\right)}}_{\epsilon_{ij}} + \underbrace{\frac{\partial}{\partial x_k}\left(-\overline{u_i'u_j'u_k'}+\right)}_{D_{ij}^t} + \nu\nabla^2\overline{u_i'u_j'}. \end{aligned} \tag{3.13}$$

The operator on the left-hand side of (3.13) is the material derivative defined as $D\overline{u_i'u_j'}/Dt = \partial\overline{u_i'u_j'}/\partial t + \overline{u}_k\partial\overline{u_i'u_j'}/\partial x_k$. The terms on the right-hand side of (3.13) are referred to as stress production P_{ij}, velocity-pressure gradient correlation Π_{ij}, dissipation rate ϵ_{ij}, turbulent transport D_{ij}^t and viscous diffusion $\nu\nabla^2\overline{u_i'u_j'}$.

The velocity-pressure gradient correlation Π_{ij} is sometimes further decomposed as

$$-\overline{\left(u_i'\frac{\partial p'}{\partial x_j} + u_j'\frac{\partial p'}{\partial x_i}\right)} = \underbrace{\overline{\frac{p'}{\rho}\left(\frac{\partial u_i'}{\partial x_j} + \frac{\partial u_j'}{\partial x_i}\right)}}_{\Phi_{ij}} - \underbrace{\frac{\partial}{\partial x_k}\left(\frac{\overline{p'u_i'}}{\rho}\delta_{jk} + \frac{\overline{p'u_j'}}{\rho}\delta_{ik}\right)}_{D_{ij}^p}, \tag{3.14}$$

where Φ_{ij} is the pressure-strain correlation and D_{ij}^p the pressure transport term. Based on this decomposition the short form of the evolution equations for the Reynolds-stress tensor can be written as

$$\frac{D\overline{u_i'u_j'}}{Dt} = P_{ij} + \Phi_{ij} - \epsilon_{ij} + D_{ij} \tag{3.15}$$

where the flux-gradient terms are lumped together into $D_{ij} = D_{ij}^t + D_{ij}^p + \nu\nabla^2\overline{u_i'u_j'}$.

The nonlinearity of the momentum equations has again introduced unknown higher-order correlations in the evolution equations of the Reynolds-stress tensor. Hence, the closure problem is now shifted to providing a closure for the unknown higher moments rather than providing closure for the second moments directly. In the transport equation for the Reynolds-stress tensor, the terms, which can directly be computed from known quantities are stress production, convection and viscous diffusion. All other terms involve unknown correlations and require additional modelling in order to express them in terms of available quantities and to obtain a system of transport equations that can be solved numerically.

3.2.2 Turbulence Kinetic Energy

Another useful quantity, particularly in the framework of two-equation modelling, which will be discussed in more detail in section 3.8, is the evolution equation for the turbulence kinetic energy. The turbulence kinetic energy is defined as one-half of the trace of the Reynolds-stress tensor, $k = (1/2)\overline{u_i' u_i'}$. The evolution equation for the turbulence kinetic energy in exact form follows directly from (3.13) as

$$\frac{Dk}{Dt} = \underbrace{-\overline{u_i' u_k'}\frac{\partial \overline{u}_i}{\partial x_k}}_{P_k} - \underbrace{\nu\overline{\frac{\partial u_i'}{\partial x_k}\frac{\partial u_i'}{\partial x_k}}}_{\epsilon} - \underbrace{\frac{\partial}{\partial x_k}\left(\frac{1}{2}\overline{u_i' u_i' u_k'} - \overline{\frac{p'}{\rho}u_k'}\right)}_{D_k} + \nu\nabla^2 k, \tag{3.16}$$

where P_k is the production of turbulence kinetic energy, ϵ the dissipation rate of turbulence kinetic energy, D_k the sum of turbulence and pressure transport and $\nu\nabla^2 k$ corresponds to the viscous-diffusion term. The pressure-strain correlation tensor appearing in (3.2) has zero trace $\Phi_{ii} = 0$ and hence, no counterpart in the governing equation for the turbulence kinetic energy. The dissipation rate, turbulence and pressure transport terms involve unknown correlations and must be approximated by suitable models in order to close the transport equation.

3.2.3 Turbulence Kinetic Energy Dissipation Rate

A transport equation for the turbulence kinetic energy dissipation rate ϵ can be derived in exact form from the Navier-Stokes equation using

$$\overline{2\nu\frac{\partial u_i'}{\partial x_j}\frac{\partial}{\partial x_j}N\left(u_i\right)} = 0. \tag{3.17}$$

The resulting evolution equation of the turbulence kinetic energy dissipation rate takes the form

$$\begin{aligned}\frac{D\epsilon}{Dt} &= \underbrace{-2\nu\left[\overline{\frac{\partial u_i'}{\partial x_k}\frac{\partial u_j'}{\partial x_k}}+\overline{\frac{\partial u_k'}{\partial x_i}\frac{\partial u_k'}{\partial x_j}}\right]\frac{\partial \overline{u}_i}{\partial x_j}}_{P_\epsilon^1+P_\epsilon^2} \underbrace{-2\nu\overline{\frac{\partial u_i'}{\partial x_k}\frac{\partial u_i'}{\partial x_m}\frac{\partial u_k'}{\partial x_m}}}_{P_\epsilon^3} \\ &\quad \underbrace{-2\nu\overline{u_k'\frac{\partial u_i'}{\partial x_j}\frac{\partial^2 \overline{u}_i}{\partial x_k\partial x_j}}}_{P_\epsilon^4} \underbrace{-2\nu^2\overline{\frac{\partial^2 u_i'}{\partial x_k\partial x_m}\frac{\partial^2 u_i'}{\partial x_k\partial x_m}}}_{\epsilon_\epsilon} \\ &\quad \underbrace{+\frac{\partial}{\partial x_j}\left[-2\nu\overline{\frac{\partial p'}{\partial x_m}\frac{\partial u_j'}{\partial x_m}}-\nu\overline{u_j'\frac{\partial u_i'}{\partial x_m}\frac{\partial u_i'}{\partial x_m}}\right]}_{D_\epsilon}+\nu\nabla^2\epsilon, \end{aligned} \tag{3.18}$$

where P_ϵ^1, P_ϵ^2, P_ϵ^3 and P_ϵ^4 are four contributions to the production of turbulence kinetic energy dissipation rate, ϵ_ϵ the dissipation of turbulence kinetic energy dissipation rate, D_ϵ the pressure and turbulence transport of turbulence kinetic energy dissipation rate and $\nu\nabla^2\epsilon$ corresponds to the viscous-diffusion term. The evolution equation for the dissipation rate is obviously much more complex and contains a significant number of unknown correlations, which need modelling. In fact, only the viscous-diffusion term can be computed directly. All other terms require modelling.

3.3 Preliminary Remarks

The main task in closing the exact evolution equations is to express the unknown terms, for example, the velocity-pressure gradient correlation in the Reynolds-stress transport equation, in terms of available quantities, for example, $\partial\overline{u}_i/\partial x_j, \overline{u_i'u_j'}, k, \epsilon$. Suitable models should ideally relate the available quantities to the exact processes in a physically consistent fashion. This, however, is often not possible and further simplifying assumptions are required, such as homogeneity of turbulence, in order to reduce the level of complexity. Even though it may sometimes be very difficult to adequately represent the real physical processes with the limited number of available quantities, which are at ones disposal, the resulting model should satisfy some fundamental properties and constraints such as dimensional consistency, coordinate-frame invariance or realisability.

Isotropic Tensor Functions

Within the framework of Reynolds-stress modelling, the unknown terms in the transport equation need to be modelled as tensor-valued functions. These tensor functions need to be formulated properly as isotropic tensor functions, which guarantees that the model takes the same functional form for any chosen coordinate system and thus preserves coordinate-frame invariance. A tensor function $F\left(\boldsymbol{T}_1, \boldsymbol{T}_2, ...\right)$ is isotropic if it satisfies

$$F\left(\boldsymbol{T}_1, \boldsymbol{T}_2, ...\right) = F\left(\boldsymbol{Q}\boldsymbol{T}_1\boldsymbol{Q}^T, \boldsymbol{Q}\boldsymbol{T}_2\boldsymbol{Q}^T, ..\right), \tag{3.19}$$

with the second-order tensors $\boldsymbol{T}_i$ and an orthogonal transformation matrix $\boldsymbol{Q}$.

It frequently occurs in turbulence modelling that an unknown second-order tensor ϕ_{ij} is assumed to be a function of a range of other second-order tensors and scalar variables. In the simplest case, ϕ_{ij} is a function of only one second-order tensor, $\phi_{ij} = F(a_{ij})$. The most general expression for ϕ_{ij} is given by a polynomial expansion in powers of α of the form

$$\phi_{ij} = \sum_{\alpha=0}^{\infty} \beta_\alpha a_{ij}^\alpha, \tag{3.20}$$

where the coefficients β_α may depend on all possible scalar invariants of a_{ij}. Making use of the Cayley-Hamilton theorem (see, for example, Poole, 2006), which states that the matrix a_{ij} satisfies its own characteristic equation, all terms in a polynomial expansion with powers 3 or larger can be reduced to a combination of lower powers and are therefore redundant. The Cayley-Hamilton theorem can be written as

$$a_{ik}a_{kl}a_{lj} = I_a a_{ik}a_{kj} + \frac{1}{2}(II_a - I_a^2)a_{ij} + \frac{1}{6}(2III_a - 3I_a II_a + I_a^3)\delta_{ij} \tag{3.21}$$

with the invariants $I_a = a_{kk}$, $II_a = a_{kl}a_{lk}$ and $III_a = a_{kl}a_{lm}a_{mk}$. Therefore, the isotropic tensor function and most general expression for ϕ_{ij} is given by

$$\phi_{ij} = \beta_1\delta_{ij} + \beta_2 a_{ij} + \beta_3 a_{ik}a_{kj}. \tag{3.22}$$

A similar procedure can be applied if ϕ_{ij} depends on more than one second-order tensor, e.g. $\phi_{ij} = F(S_{ij}, \Omega_{ij})$. This is discussed in more detail in section 3.6 and in Durbin & Petterson-Reif (2001).

Realisability

Another fundamental constraint, which a closure model should ideally fulfill is that it does not predict physically unrealisable solutions such as negative energy components. Even though violation of the realisability constraints may not always have catastrophic consequences, it may improve robustness and predictive capabilities of the closure model (see Batten *et al.*, 2009). In fact, a range of two-equation models may yield unrealisable results for large strain-rates. A turbulence model is said to be realisable if it satisfies the two following constraints (see Schumann, 1977),

$$\overline{u'_\alpha u'_\alpha} \geqslant 0, \quad \left(\overline{u'_\alpha u'_\beta}\right)^2 \leqslant \overline{u'^2_\alpha} \cdot \overline{u'^2_\beta} \quad \text{'no summation on } \alpha, \beta\text{'}. \tag{3.23}$$

The former constraint ensures positiveness of the components of turbulence kinetic energy and the latter constraint is the Schwarz inequality for the shear-stress components.

It is sometimes more convenient to express the Reynolds-stress tensor in terms of the stress-anisotropy tensor $a_{ij} = \overline{u'_i u'_j}/k - (2/3)\delta_{ij}$ and the turbulence kinetic energy k. The anisotropy tensor is symmetric and traceless ($a_{ii} = 0$), i.e. it merely provides a measure for the departure from an isotropic state of turbulence and it does not provide any information about the magnitude of turbulence kinetic energy. The advantage of the anisotropy tensor is that its diagonal components are limited to the finite interval $-2/3 \leqslant a_{\alpha\alpha} \leqslant 4/3$ for all realisable states of turbulence. For example, the value $a_{\alpha\alpha} = -2/3$ indicates that the energy contributed by $\overline{u'_\alpha u'_\alpha}$ is vanishing and a value of $a_{\alpha\alpha} = 4/3$ would indicate that all energy is contained in $\overline{u'_\alpha u'_\alpha}$ (see Hanifi *et al.*, 1999). In addition, all realisable values of the off-diagonal elements are also bounded within $|a_{\alpha\beta}| \leqslant 1$.

As a consequence of the boundedness of all possible realisable states of the anisotropy tensor, the first and second invariant of the anisotropy tensor $II_a = a_{ik}a_{ki}$ and $III_a = a_{ik}a_{kj}a_{ji}$ are also limited to finite intervals. Lumley & Newman (1977) derived a II_a,III_a anisotropy-invariant map where all realisable anisotropy states are confined within a finite region. The anisotropy-invariant map is depicted in figure 3.1. The boundaries of the invariant map are given by the line $II_a^{1/2} = 6^{1/6}\,|III_a|^{1/2}$ and $II_a = (8/9)III_a$, where the former represents the limit of axisymmetric turbulence and the latter the two-component limit of turbulence. The two anisotropy invariants are very useful to describe important features of a turbulent flow and therefore often used in turbulence modelling, particularly in modelling of near-wall flows.

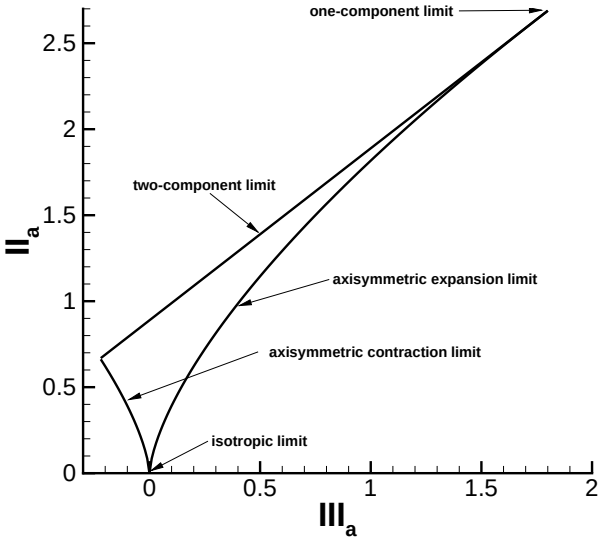

FIGURE 3.1: Anisotropy Invariant Map

3.4 Differential-Reynolds-Stress Model

The highest level of turbulence closure, which is currently feasible for the simulation of turbulent flows of practical interest are Differential-Reynolds-Stress Models (DRSM) or Second-Moment Closures (SMC). DRSM completely abandon the assumption of an algebraic stress-strain relationships together with the concept of an eddy viscosity and with that the shortcomings inherent in these assumptions. Instead, a transport equation for each component of the unknown second-moments $\overline{u_i' u_j'}$ is solved. This results in a minimum of six transport equations, which are usually solved in conjunction with a transport equation for a length-scale providing variable, for example, the dissipation rate of turbulence kinetic energy ϵ.

The obvious advantage of DRSM is that a range of physical processes are naturally included in the evolution equation of the Reynolds-stress tensor. This not only includes convection and diffusion of the Reynolds-stress components but also terms, which describe the exact production mechanisms of turbulence as well as redistribution terms, which transfer turbulence kinetic energy among its components. These terms are a particularly important ingredient for predicting the correct representation of the stress and anisotropy field in a complex turbulent flow. Nevertheless, a number of important terms appearing in the evolution equation of the second-moments are not closed and are frequently modelled by employing rather strong simplifications such as quasi-homogeneity of turbulence.

In the following, all terms appearing in the evolution equation for the Reynolds stress are discussed separately and suitable modelling approaches are presented.

3.4.1 Production Term

The production term P_{ij} represents the generation of Reynolds stress by the interaction with the mean flow. The production tensor can be computed in exact form, since all required quantities are available. This term is an important ingredient when simulating complex turbulent flows, since it is sensitive to both strain and rotation/curvature effects. This sensitivity becomes more obvious when the velocity gradient tensor $\partial\overline{u}_i/\partial x_j$ is decomposed into a symmetric and antisymmetric part $\partial\overline{u}_i/\partial x_j = S^*_{ij} + \Omega^*_{ij}$ with

$$S^*_{ij} = \frac{1}{2}\left(\frac{\partial\overline{u}_i}{\partial x_j} + \frac{\partial\overline{u}_j}{\partial x_i}\right), \quad \Omega^*_{ij} = \frac{1}{2}\left(\frac{\partial\overline{u}_i}{\partial x_j} - \frac{\partial\overline{u}_j}{\partial x_i}\right). \tag{3.24}$$

The symmetric part S^*_{ij} is the strain-rate tensor and the antisymmetric part Ω^*_{ij} is the vorticity or rotation-rate tensor. The production term can be re-written in terms of the symmetric and antisymmetric part of the velocity gradient tensor and the stress-anisotropy tensor $a_{ij} = \overline{u_i'u_j'}/k - (2/3)\delta_{ij}$. The normalised form is as follows

$$\frac{P_{ij}}{\epsilon} = -\frac{4}{3}S_{ij} - (a_{ik}S_{kj} + S_{ik}a_{kj}) + (a_{ik}\Omega_{kj} - \Omega_{ik}a_{kj}), \tag{3.25}$$

where the strain- and rotation-rate tensors have been normalised by the turbulence timescale $\tau = k/\epsilon$ such that

$$S_{ij} = \frac{\tau}{2}\left(\frac{\partial\overline{u}_i}{\partial x_j} + \frac{\partial\overline{u}_j}{\partial x_i}\right), \qquad \Omega_{ij} = \frac{\tau}{2}\left(\frac{\partial\overline{u}_i}{\partial x_j} - \frac{\partial\overline{u}_j}{\partial x_i}\right). \tag{3.26}$$

It is now obvious that the production tensor is sensitive to both strain-rate and rotational components of the velocity gradient tensor. The production term in the evolution equation for the turbulence kinetic energy reduces to $P_k = -\overline{u_i'u_j'}\partial\overline{u}_i/\partial x_j$ or to $P_k = \nu_T S^2$ with $S = \sqrt{2S^*_{ij}S^*_{ij}}$ by assuming a linear stress-strain relationship. Therefore, the sensitivity of the production term to rotation or curvature is completely lost in the equation for the turbulence kinetic energy, unless empirical modifications are introduced to account for these effects. Also, the strain-rate magnitude S cannot distinguish positive from negative strain-rates and produces the same results for accelerated/decelerated flows in, for example, a nozzle/diffuser.

3.4.2 Transport Terms

The transport term D_{ij} spatially redistributes $\overline{u_i' u_j'}$ without creating or destroying it. Here, it is composed of three parts, diffusion due to the action of viscosity $\nu\nabla^2\overline{u_i' u_j'}$, transport by turbulent fluctuations D_{ij}^t and transport due to fluctuating pressure D_{ij}^p .

The viscous-diffusion term does not involve any new unknowns and thus requires no modelling. The turbulence and pressure transport terms are not closed and need to be modelled. It is common practice to model the turbulence transport by a generalised gradient-diffusion model, following the proposal of Daley & Harlow (1970)

$$D_{ij}^t = c_s \frac{\partial}{\partial x_k}\left[\frac{k}{\epsilon}\overline{u_k' u_l'}\frac{\partial \overline{u_i' u_j'}}{\partial x_l}\right]. \tag{3.27}$$

More complex, coordinate-frame invariant models for the turbulence transport term have been proposed in Hanjalic & Launder (1972) and are reviewed in Hanjalic (1994). Even though the pressure transport term D_{ij}^p is of different nature, it is often lumped together with the turbulent transport term. Therefore, the combined effect of turbulence and pressure transport can be accounted for by calibrating the constant c_s such that it absorbs both effects. In high-Reynolds-number formulations, D_{ij}^p is sometimes neglected, since its contribution is much smaller than D_{ij}^t (see Lai & So, 1991). The generalised gradient-diffusion model may result in numerical instabilities. As an alternative, it is possible to resort to a simple scalar gradient-diffusion model, which can be written as

$$D_{ij}^t = \frac{\partial}{\partial x_k}\left(\frac{\nu_T}{\sigma_s}\frac{\partial \overline{u_i' u_j'}}{\partial x_k}\right), \tag{3.28}$$

where ν_T is the turbulence viscosity and σ_s a calibration constant. The drawback of the scalar diffusion model is that it loses the character of a vector-valued flux gradient.

3.4.3 Pressure-Strain Correlation

The pressure-strain term Φ_{ij} plays a pivotal role in Reynolds-stress closures, since it has a significant contribution to the balance of the Reynolds stresses. A lot of research has focused on the modelling of this term. Its effect is to redistribute $\overline{u_i' u_j'}$ among its components without creating or destroying it. The pressure-strain term

is traceless in incompressible conditions ($\Phi_{ii} = 0$) and therefore does not appear in the governing equation for the turbulence kinetic energy.

More insight into the role of the fluctuating pressure $p^{'}$, which is the source of the redistribution process, can be gained by deriving the exact Poisson equation for the fluctuating pressure. This equation can be obtained by subtracting the Poisson equation ($\partial/\partial x_i \cdot N(\overline{u}_i)$) for the mean pressure $\overline{p}$ from the Poisson equation ($\partial/\partial x_i \cdot N(u_i)$) for the instantaneous pressure p . The result is

$$\frac{1}{\rho}\nabla^2 p^{'} = -2\frac{\partial \overline{u}_i}{\partial x_j}\frac{\partial u_j^{'}}{\partial x_i} - \frac{\partial^2}{\partial x_i \partial x_j}\left(u_i^{'}u_j^{'} - \overline{u_i^{'}u_j^{'}}\right). \tag{3.29}$$

The solution for $p^{'}$ consists of a superposition of the solution to the homogeneous part $\nabla^2 p^{'} = 0$, with the inhomogeneous boundary condition $\partial p^{'}/x_2 = \mu \partial^2 u_2^{'}/\partial x_2^2$, which is obtained from the wall-normal momentum equation for the fluctuating velocity, and the particular solution associated with the source terms on the right-hand side of (3.29), with the homogeneous boundary condition $\partial p^{'}/\partial x_2 = 0$, where x_2 denotes the wall-normal direction (see, for example, Hanifi *et al.*, 1999).

According to (3.29), pressure fluctuations have two different sources. The particular solution to the first term on the right-hand side contains the mean-velocity gradient, whereas the solution to the second term contains a non-linear product of fluctuating velocities. The first term is usually referred to as the rapid contribution, since it responds immediately to changes in the mean velocity and becomes zero in the absence of any mean-velocity gradient. The second, non-linear, term is sometime referred to as the slow part, since it is independent of the mean-velocity gradient. Both contributions to the fluctuation pressure will be reflected in the pressure-strain correlation.

The Poisson equation for the fluctuating pressure can be integrated using the Green's function technique to give

$$\frac{p^{'}}{\rho} = \frac{1}{4\pi}\int_V \left[2\frac{\partial \overline{u}_l(\boldsymbol{x}^{'})}{\partial x_m^{'}}\frac{\partial u_m^{'}(\boldsymbol{x}^{'})}{\partial x_l^{'}} + \frac{\partial^2}{\partial x_l^{'}\partial x_m^{'}}\left(u_l^{'}(\boldsymbol{x}^{'})u_m^{'}(\boldsymbol{x}^{'}) - \overline{u_l^{'}(\boldsymbol{x}^{'})u_m^{'}(\boldsymbol{x}^{'})}\right)\right]\frac{\mathrm{d}V(\boldsymbol{x}^{'})}{|\boldsymbol{r}|}, \tag{3.30}$$

where $\boldsymbol{r} = \boldsymbol{x}^{'} - \boldsymbol{x}$ and $\mathrm{d}V(\boldsymbol{x}^{'}) = \mathrm{d}^3\boldsymbol{x}^{'}$.

Multiplying (3.30) with $\left(\partial u_i^{'}/\partial x_j + \partial u_j^{'}/\partial x_i\right)$ and taking the average yields the following relation for the pressure-strain correlation:

$$\begin{aligned}\Phi_{ij} \;=\; & \underbrace{\frac{1}{4\pi}\int_V \overline{\left(\frac{\partial u_i^{'}(\boldsymbol{x})}{\partial x_j}+\frac{\partial u_j^{'}(\boldsymbol{x})}{\partial x_i}\right)\frac{\partial^2 u_l^{'}(\boldsymbol{x}^{'})u_m^{'}(\boldsymbol{x}^{'})}{\partial x_l^{'}\partial x_m^{'}}}\frac{\mathrm{d}V(\boldsymbol{x}^{'})}{|\boldsymbol{x}-\boldsymbol{x}^{'}|}}_{\Phi_{ij}^{(s)}} \\ & + \underbrace{\frac{1}{2\pi}\int_V \overline{\frac{\partial \overline{u}_l(\boldsymbol{x}^{'})}{\partial x_m^{'}}\frac{\partial u_m^{'}(\boldsymbol{x}^{'})}{\partial x_l^{'}}\left(\frac{\partial u_i^{'}(\boldsymbol{x})}{\partial x_j}+\frac{\partial u_j^{'}(\boldsymbol{x})}{\partial x_i}\right)}\frac{\mathrm{d}V(\boldsymbol{x}^{'})}{|\boldsymbol{x}-\boldsymbol{x}^{'}|}}_{\Phi_{ij}^{(r)}} \\ & + \underbrace{\frac{1}{4\pi}\int_A \left[\frac{1}{r}\frac{\partial}{\partial n^{'}}\overline{p^{'}\left(\frac{\partial u_i(\boldsymbol{x})}{\partial x_j}+\frac{\partial u_j(\boldsymbol{x})}{\partial x_i}\right)}-\overline{p^{'}\left(\frac{\partial u_i(\boldsymbol{x})}{\partial x_j}+\frac{\partial u_j(\boldsymbol{x})}{\partial x_i}\right)}\frac{\partial}{\partial n^{'}}\frac{1}{r}\right]\mathrm{d}A}_{\Phi_{ij}^{(w)}}.\end{aligned} \tag{3.31}$$

In addition to the volume integrals, a surface integral over the bounding surfaces $\mathrm{d}A$ occurs, which accounts for the refection or 'echo' of pressure fluctuations from the wall. Even though the pressure-strain correlation is a single-point correlation there are two-point correlations appearing on the right-hand side of (3.31). The two-point correlations reflect the non-local nature of the pressure fluctuations and its influence at a distance. The best that can be done in the present single-point framework is to try to model the non-local effect with local quantities only.

A common starting point for the derivation of suitable models for Φ_{ij} is to invoke a local homogeneity assumption. For homogeneous turbulence away from solid boundaries the surface integral vanishes and the velocity gradient $\partial\overline{u}_l/\partial x_m$ can be taken outside the integral. The pressure-strain term can then be written in shorter from

$$\Phi_{ij} = \Phi_{ij}^{(s)} + \Phi_{ij}^{(r)} = \Phi_{ij}^{(s)} + M_{ijlm}\frac{\partial \overline{u}_l}{\partial x_m}, \tag{3.32}$$

where M_{ijlm} is a fourth-order tensor.

Slow Pressure-Strain Term $\Phi_{ij}^{(s)}$

The slow pressure-strain term only contains velocity fluctuations and its effect is to redistribute the energy components of anisotropic turbulence towards a more isotropic state in the absence of a mean strain-rate. The slow term is thus sometimes also referred to as the return-to-isotropy term. It is common practice to assume that the rate at which anisotropic turbulence returns to a more isotropic state only depends on the degree of anisotropy. In other words, the slow term is an isotropic tensor function, which depends on the anisotropy tensor a_{ij} and possibly other

scalars, thus

$$\Phi_{ij}^{s} = \epsilon F_{ij}^{(s)}\left(a_{ij}\right). \tag{3.33}$$

Multiplication by the turbulence kinetic energy dissipation rate ϵ is required for dimensional consistency. Based on the previous discussion about isotropic tensor functions, the slow pressure-strain term can be written in its most general form as

$$\frac{\Phi_{ij}^{1}}{\epsilon} = -C_1\left[a_{ij} + C_1^{'}\left(a_{ik}a_{kj} - \frac{1}{3}II_a\delta_{ij}\right)\right], \tag{3.34}$$

where $II_a = \mathrm{tr}\left\{a_{ik}a_{kj}\right\}$. When the constant $C_1^{'} = 0$, the general non-linear model reduces to the linear model of Rotta (1951), which assumes that the return to isotropy is proportional to the degree of anisotropy. The constant C_1 is referred to as the Rotta constant. Later proposals redefine the Rotta constant to be a function of the turbulence Reynolds number Re_T or the second and third invariant of the stress-anisotropy II_a, III_a, respectively (see Launder, 1989). The model of Speziale *et al.* (1991) additionally sensitises the Rotta constant to the ratio of production to dissipation with $C_1 = 0.5\left(C_1^0 + C_1^* P_k/\epsilon\right)$, which improves the predictions for non-equilibrium flows.

Rapid Pressure-Strain Term $\Phi_{ij}^{(r)}$

The second term in equation (3.34), or the 'rapid' part of the pressure-strain correlation, promotes an 'isotropisation' of stress production or, in other words, counteracts the effect of production to increase the stress-anisotropy. Consider, for example, a parallel shear flow where the mean shear feeds energy into $P_{11} = -2\overline{u'v'}\partial\overline{u}/\partial y$. The other components do not receive energy from the mean shear, since $P_{22} = P_{33} = 0$. The effect of the rapid pressure fluctuations is to redistribute energy to the other components and hence make the turbulence more isotropic.

According to (3.31) the rapid part also depends on the velocity gradient tensor, which introduces another dependence in the tensor function for the rapid pressure-strain model, thus

$$\Phi_{ij}^{(r)} = \epsilon F_{ij}^{(r)}\left(a_{ij}, S_{ij}, \Omega_{ij}\right). \tag{3.35}$$

As mentioned before, the assumption of local homogeneity allows the velocity gradient to be taken outside the integral, and the rapid term can be written as

$$\Phi_{ij}^{(r)} = M_{ijlm}\frac{\partial\overline{u}_l}{\partial x_m}, \tag{3.36}$$

where the fourth-order tensor M_{ijkl} now only includes a functional dependency on a_{ij}. An expression for the tensor M_{ijkl} can be derived by expansion in powers of the anisotropy tensor a_{ij}. The resulting tensor function must also satisfy the symmetry properties in i, j ($M_{ijkl} = M_{jikl}$), vanishing trace upon contraction of $i = j$ ($M_{iikl} = 0$) and the normalisation constraint $M_{ijjl} = 2\overline{u_i' u_l'}$ (see Durbin & Petterson-Reif (2001) or Hanifi *et al.* (1999) for more details). The most general form of the fourth-order tensor contains 15 tensor groups up to the fourth powers of a_{ij} (see Johansen & Hallback, 1994). Speziale *et al.* (1991) used an expansion for M_{ijkl}, which is quadratically non-linear in a_{ij}. For the present work, only expansions, which are linear in a_{ij} are considered. Using a linear expansion of M_{ijkl} and substituting into (3.36) yields the General Quasi-Linear Model (GQLM) for the rapid pressure-strain correlation. All of the widely used linear and quasi-linear pressure-strain models (for example, Launder *et al.* (1975), Gibson & Launder (1978) or the linearised model of Speziale *et al.* (1991)) can be expressed in the following general form:

$$\begin{aligned} \frac{\Phi_{ij}}{\epsilon} &= -\frac{1}{2}\left(C_1^0 + C_1^* \frac{P_k}{\epsilon}\right) a_{ij} + \left(C_2 - \frac{C_2^*}{2}\sqrt{II_a}\right) S_{ij} \\ &\quad + \frac{C_3}{2}\left(a_{ik}S_{kj} + S_{ik}a_{kj} - \frac{2}{3}\mathrm{tr}\left\{a_{ik}S_{kj}\right\}\delta_{ij}\right) - \frac{C_4}{2}\left(a_{ik}\Omega_{kj} - \Omega_{ik}a_{kj}\right). \end{aligned} \tag{3.37}$$

Alternatively, it is possible to directly model the velocity-pressure gradient correlation $\Pi_{ij} = \Phi_{ij} + D_{ij}^p$, which includes the effects of D_{ij}^p and has the additional advantage that it vanishes at the wall whereas Φ_{ij} does not (see Lai & So, 1991).

3.4.4 Dissipation Rate

The dissipation rate ϵ_{ij} is a tensor-valued quantity for which an anisotropy measure can be defined as $e_{ij} = \epsilon_{ij}/\epsilon - (2/3)\delta_{ij}$, analogous to the stress-anisotropy tensor a_{ij}. For high-Reynolds-number flows, the Kolmogorov hypothesis of local isotropy of the smallest scales is invoked. Since the dissipation occurs at the smallest scales, the dissipation in high-Reynolds-number flows is usually assumed to be isotropic, i.e. $e_{ij} = 0$ or $\epsilon_{ij} = (2/3)\epsilon\delta_{ij}$. Therefore, knowing the dissipation rate of turbulence kinetic energy ϵ, the tensor-valued dissipation rate ϵ_{ij} can be computed.

The assumption of isotropy of the dissipation rate is tantamount to an equal drain of energy from each of the diagonal components of ϵ_{ij}. It is known that this is a questionable assumption for highly anisotropic flows, such as those close to solid

boundaries (see, for example, Mansour *et al.*, 1988). Therefore, better approximations for the dissipation rate tensor have been devised, that assume the dissipation rate anisotropy e_{ij} is proportional to the stress anisotropy, i.e.

$$e_{ij} = f_s a_{ij}, \tag{3.38}$$

where f_s is a blending function, which approaches zero away from the wall and thereby recovers the isotropic dissipation rate $e_{ij} = 0$ (see Hanjalic (1994) or Launder (1989)). The blending function f_s may depend on quantities like turbulence Reynolds number $Re_T = k^2/\epsilon\nu$ or second and third invariants of the stress and dissipation rate anisotropy tensor. Models based on (3.38) are also not fully satisfactory, since the anisotropy state of the energy containing, large scales does not correlate well with the state of the more isotropic dissipative scales. This has the consequence that some of the components of ϵ_{ij} do not obey the correct asymptotic near-wall limit. Modifications to (3.38) have been introduced using information from the wall-normal vector to recover the correct near-wall limits of ϵ_{ij}. A more detailed discussion can be found in Jakirlic & Hanjalic (2002).

A different means of accounting for the anisotropy of the dissipation rate follows the proposal of Shima (1988), where the deviatoric part of the dissipation rate tensor is absorbed into the modelling of the slow pressure-strain correlation, such that

$$\Phi_{ij} - \epsilon_{ij} = \Phi_{ij}^{(s^*)} + \Phi_{ij}^{(r)} - \frac{2}{3}\epsilon\delta_{ij}, \tag{3.39}$$

with the modified slow pressure-strain correlation $\Phi_{ij}^{(s^*)} = \Phi_{ij}^{(s)} - \epsilon_{ij} + (2/3)\epsilon\delta_{ij}$. This approach requires modification of the Rotta constant C_1 in the model for the slow pressure-strain term in (3.34).

3.4.5 Extension to Near-Wall Flows

The pressure-strain models presented above were derived by assuming local homogeneity and the influence of solid boundaries was neglected. Local homogeneity may be a fair approximation for flows, which evolve relatively slowly in space. However, this assumption breaks down in more complex flows of practical interest, and is not appropriate in the presence of solid boundaries.

The solid boundary introduces a no-slip and impermeability constraint on the flow. The no-slip condition results in high shear rates and strongly inhomogeneous flow.

The local Reynold number close to the wall decreases and the direct effect of viscosity onto the velocity fluctuations becomes important. The action of viscosity damps the velocity fluctuations equally, independent of their direction. Therefore, the first modification is the inclusion of viscous or low-Reynolds-number effects into the model formulations. This is mostly limited to the modelling of viscous dissipation ϵ_{ij}, which exhibits a considerable amount of anisotropy close to the wall, and to the transport equation for the dissipation rate of turbulence kinetic energy ϵ.

In addition to viscous effects there are two non-local, kinematic, effects which are non-viscous in nature, and which influence the flow away from and in the vicinity of a wall. The impermeability constraint imposes a kinematic wall-blocking effect onto the wall-normal velocity fluctuations. The kinematic wall-blocking effect strongly suppresses the wall-normal fluctuations, which results in highly anisotropic turbulence close to the wall. In fact, the wall-normal fluctuations $\overline{v'v'}$ approach zero as $O(y^4)$, where y is the distance from the wall, whereas the other normal-stress components behave as $O(y^2)$. Therefore, at the edge of the viscous sublayer the wall-normal fluctuations have almost vanished and the turbulence has reached a two-component state.

Another effect of a solid boundary is the reflection or 'echo' of the pressure fluctuations. Manceau *et al.* (2001) have shown that the reflected pressure fluctuations may enhance the total magnitude of pressure fluctuations, and with that the redistribution process. Consequently, the reflected pressure disturbances are promoting a reduction of the anisotropic state of turbulence and therefore, counteract the wall-blocking effect. The wall-echo, or pressure reflections, originate from the wall boundary conditions, which are imposed on the Poisson equation for the fluctuating pressure. It can be included by taking the surface integral in (3.31) into account. Alternatively, the wall-boundary condition $\partial p'/\partial x_2 = 0$ for equation (3.30) allows the use of the method of images for the solution of the Poisson equation for the fluctuating pressure. With this approach, the surface integral disappears and the Green's function takes the following form for a plane wall

$$G(\boldsymbol{x}, \boldsymbol{x}') = \frac{1}{4\pi \left|\boldsymbol{x} - \boldsymbol{x}'\right|} + \frac{1}{4\pi \left|\boldsymbol{x} - \boldsymbol{x}^*\right|}, \tag{3.40}$$

where $\boldsymbol{x}^*$ is the mirror image point of $\boldsymbol{x}'$ (see, for example, Launder *et al.*, 1975). This form of Green's function suggests that the pressure-strain correlation, which would be valid for wall bounded flows could be written as an extension to the

quasi-homogeneous pressure strain model (3.32) in the following form

$$\Phi_{ij} = \Phi_{ij}^{(s,hom)} + \Phi_{ij}^{(r,hom)} + \Phi_{ij}^{(s,w)} + \Phi_{ij}^{(r,w)}, \tag{3.41}$$

where the effect of the wall (wall-echo) is contained in $\Phi_{ij}^{(s,w)}$ and $\Phi_{ij}^{(r,w)}$, respectively.

Typical formulations for the wall-echo correction rely on information about the wall-normal vector n_i and wall distance to identify the orientation of the wall and to suppress the intensity of the wall-normal fluctuation $\overline{v'v'}$ and to enhance the streamwise component $\overline{u'u'}$, respectively. Gibson & Launder (1978), for example, use the modifications

$$\Phi_{ij}^{s,w} = C_s^w \frac{\epsilon}{k} \left(\overline{u_k' u_m'} n_k n_m \delta_{ij} - \frac{3}{2} \overline{u_k' u_i'} n_k n_j - \frac{3}{2} \overline{u_k' u_j'} n_k n_i \right) f_w, \tag{3.42}$$

$$\Phi_{ij}^{r,w} = C_r^w \frac{\epsilon}{k} \left(\Phi_{km}^{r,hom} n_k n_m \delta_{ij} - \frac{3}{2} \Phi_{ik}^{r,hom} n_k n_j - \frac{3}{2} \Phi_{jk}^{r,hom} n_k n_i \right) f_w. \tag{3.43}$$

The damping function f_w ensures that the modifications are only active close to the wall and that the quasi-homogeneous model is recovered away from the wall. The constants need to be tailored to reproduce the correct behaviour in conjunction with a specific quasi-homogeneous model. Wall-echo corrections of this form may improve the predictions in simple shear flows. However, they are not very successful for flows in complex geometries where the wall-normal vector cannot be rigorously defined in the presence of sharp corners and multiple walls. Another major defect exists for the prediction of impinging flows where the wall-normal fluctuation $\overline{v'v'}$ are erroneously amplified (see, for example, Durbin & Petterson-Reif, 2001).

Another approach that has been used to take into account the strong inhomogeneity close to the wall is to use a higher-order expansion for M_{ijkl}. Using a non-linear expansion provides more degrees of freedom to place additional constraints onto the free coefficients. Craft & Launder (1995) use a non-linear expansion, which additionally satisfies the two-component limit and gives improved predictions close to the wall.

3.4.6 Elliptic-Relaxation/Blending Approaches

The elliptic-relaxation/blending approach is yet another technique that accounts for the non-local, wall-echo and blocking effects of solid walls. This approach is distinctly different from what has been presented above. Instead of modelling the

pressure-strain correlation with local quantities, the elliptic-relaxation approach attempts to model the two-point correlation appearing in (3.31).

In modelling wall-bounded flows, it is usually more convenient to model the velocity-pressure gradient correlation as a whole rather than using the decomposition into redistributive and transport part. This is motivated by the fact that the transport part plays a role in the near-wall balance for the Reynolds-stress component $\overline{v'v'}$ and cannot be neglected. In order to illustrate the elliptic-relaxation concept, consider the velocity-pressure gradient correlation

$$\overline{u_i' \frac{\partial p'(\boldsymbol{x})}{\partial x_j}} = \int_V \overline{u_i'(\boldsymbol{x}) \frac{\partial S(\boldsymbol{x}')}{\partial x_j}} \frac{\mathrm{d}V(\boldsymbol{x}')}{4\pi |\boldsymbol{x} - \boldsymbol{x}'|}, \tag{3.44}$$

where $S(\boldsymbol{x}')$ corresponds to the source terms on the right-hand side of (3.30). The two-point correlation $\overline{u_i'(\boldsymbol{x})\, \partial S(\boldsymbol{x}')/\partial x_j}$ has been modelled by Durbin (1991, 1993) as

$$\overline{u_i'(\boldsymbol{x}) \frac{\partial S(\boldsymbol{x}')}{\partial x_j}} = \overline{u_i'(\boldsymbol{x}') \frac{\partial S(\boldsymbol{x}')}{\partial x_j}} \cdot \exp\left(\frac{-|\boldsymbol{x} - \boldsymbol{x}'|}{L} \right), \tag{3.45}$$

where L is a correlation length scale. As a result of this modelling, the integration kernel has changed and now corresponds to a Green's function for the modified Helmholtz equation. Thus, the velocity-pressure gradient correlation can be written as the solution to the elliptic-relaxation (modified Helmholtz) equation of the form

$$\Pi_{ij} - L^2 \nabla^2 \Pi_{ij} = \Phi_{ij}^{(hom)}. \tag{3.46}$$

Note that the second term on the left-hand side vanishes for homogeneous turbulence and the elliptic-relaxation equation reduces to $\Pi_{ij} = \Phi_{ij}^{(hom)}$. It is now possible to include the correct asymptotic near-wall behaviour close to the wall by specifying appropriate boundary conditions to the elliptic-relaxation equation.

The elliptic-relaxation formulation proposed by Durbin (1993) is based on a modified redistribution tensor of the form

$$\Pi_{ij}^* = \Pi_{ij} - \epsilon_{ij} + \frac{\overline{u_i' u_j'}}{k} \epsilon = k f_{ij}, \tag{3.47}$$

which describes the net effect of $\Pi_{ij} - \epsilon_{ij}$ and where $(\epsilon/k)\overline{u_i' u_j'}$ is added to ensure that Π_{ij}^* vanishes at solid boundaries. Durbin introduced the intermediate variable f_{ij}, which is multiplied by k to ensure that the right-hand side approaches zero at

the wall. The tensor f_{ij} is obtained from

$$f_{ij} - L^2 \nabla^2 f_{ij} = \frac{1}{k} \left(\Phi_{ij}^{(hom)} - \frac{2}{3} \epsilon \delta_{ij} + \frac{\overline{u_i' u_j'}}{k} \epsilon \right), \tag{3.48}$$

where the correlation length scale is given by

$$L = C_L \max \left[\frac{k^{3/2}}{\epsilon}, C_\eta \left(\frac{\nu^3}{\epsilon} \right)^{1/4} \right]. \tag{3.49}$$

The lower bound to L is given by the Kolmogorov length-scale. It should be noted that $\Phi_{ij}^{(hom)}$ can be chosen as any quasi-homogeneous redistribution model without the need to recalibrate other parts of the elliptic-relaxation concept. Although the elliptic-relaxation concept provides convincing results for wall-bounded flows, it requires six additional differential equations to be solved numerically. In addition, the boundary condition for f_{ij} involve terms, which behave as $1/y^4$, which inevitably increases numerical stiffness.

An elliptic-blending model has been proposed by Manceau & Hanjalic (2002), which is somewhat simpler and preserves the idea of the elliptic-relaxation concept, i.e. the correct prediction of $\Pi_{ij} - \epsilon_{ij}$. In the elliptic-blending model the redistribution tensor is computed from

$$\Pi_{ij} = (1 - k\alpha)\, \Phi_{ij}^{(w)} + k\alpha \Phi_{ij}^{(hom)}. \tag{3.50}$$

The dissipation is computed as

$$\epsilon_{ij} = (1 - Ak\alpha)\, \frac{\overline{u_i' u_j'}}{k} \epsilon + Ak\alpha \frac{2}{3} \epsilon \delta_{ij}, \tag{3.51}$$

with Lumley's flatness parameter $A = 6^{1/6} \left| III_a \right|^{1/3} / II_a^{1/2}$. The elliptic-blending parameter α reduces to a scalar differential equation determined by

$$\alpha - L^2 \nabla^2 \alpha = \frac{1}{k}, \tag{3.52}$$

with the wall-boundary condition $\alpha_w = 0$. The components of the wall redistribution tensor $\Phi_{ij}^{(w)}$ need to be chosen such that $\Pi_{ij} - \epsilon_{ij}$ has the same behaviour as in the elliptic-relaxation model. A model, which satisfies this requirement is

$$\Phi_{ij}^{(w)} = -5 \frac{\epsilon}{k} \left(\overline{u_i' u_k'} n_j n_k + \overline{u_j' u_k'} n_i n_k - \frac{1}{2} \overline{u_k' u_l'} n_k n_l \cdot (n_i n_j - \delta_{ij}) \right). \tag{3.53}$$

The wall-normal vector is computed from $\boldsymbol{n} = \nabla\alpha / |\nabla\alpha|$.

3.5 Algebraic-Stress Models

The increased computational effort required by DRSMs coupled with the numerical difficulties for complex three-dimensional flows have led to the emergence of alternative approaches, where the robustness of traditional turbulence models that are based on the Boussinesq approximation is combined with the improved predictive capabilities of a second-moment closure. The first such attempts goes back to the pioneering work of Rodi (1972, 1976), where an equilibrium hypothesis was introduced, which reduces the transport equations of a DRSM to an algebraic expression, yielding an implicit algebraic relation between the Reynolds-stress components and the velocity gradients. Rodi proposed that in a weak-equilibrium condition, where $\overline{u_i' u_j'}/k$ is approximately constant, convection minus diffusion of $\overline{u_i' u_j'}$ can be approximated to be proportional to convection minus diffusion of the turbulence kinetic energy k, thus

$$\frac{D\overline{u_i' u_j'}}{Dt} - D_{ij} \approx \frac{\overline{u_i' u_j'}}{k}\left(\frac{Dk}{Dt} - D_k\right) = \frac{\overline{u_i' u_j'}}{k}\left(P_k - \epsilon\right). \tag{3.54}$$

Substituting the weak-equilibrium approximation into the differential RSM (equation 3.13) yields a set of implicit algebraic relations for the Reynolds-stress tensor

$$\frac{\overline{u_i' u_j'}}{k}\left(P - \epsilon\right) = P_{ij} + \Phi_{ij} - \epsilon_{ij}. \tag{3.55}$$

Another way to illustrate Rodi's weak-equilibrium assumption is to transform the evolution equation for the Reynolds-stress tensor (3.13) into a transport equation for the stress-anisotropy tensor a_{ij}

$$k\frac{Da_{ij}}{Dt} - kD_{ij}^{(a)} = -\frac{\overline{u_i' u_j'}}{k}\left(P_k - \epsilon\right) + P_{ij} - \epsilon_{ij} + \Phi_{ij}, \tag{3.56}$$

where $D_{ij}^{(a)}$ contains the diffusion/transport terms of a_{ij}. Adopting the most general form of a quasi-linear model for the pressure strain correlation (3.37), the transport

equation for the stress-anisotropy can be written as

$$\frac{\tau}{A_0}\left(\frac{Da_{ij}}{Dt} - D_{ij}^{(a)}\right) = \left(A_3 + A_4\frac{P_k}{\epsilon}\right)a_{ij} + A_1 S_{ij} - (a_{ik}\Omega_{kj} - \Omega_{ik}a_{kj}) + A_2\left(a_{ik}S_{kj} + S_{ik}a_{kj} - \frac{2}{3}\mathrm{tr}\left\{a_{ik}S_{kj}\right\}\right), \quad (3.57)$$

see Grundestam *et al.* (2005) for more details. The weak-equilibrium assumption now amounts to neglecting convection and all diffusion/transport terms in the evolution equation for a_{ij}, i.e. $Da_{ij}/Dt - D_{ij}^{(a)} = 0$. The resulting quasi-linear Algebraic-Stress Model (ASM) takes the form

$$Na_{ij} = -A_1 S_{ij} - A_2\left(a_{ik}S_{kj} + S_{ik}a_{kj} - \frac{2}{3}\mathrm{tr}\left\{a_{ik}S_{kj}\right\}\right) + (a_{ik}\Omega_{kj} - \Omega_{ik}a_{kj}), \quad (3.58)$$

where

$$N = A_3 + A_4\frac{P_k}{\epsilon}. \quad (3.59)$$

The constants A_i are directly related to the constants C_i of the model for the pressure-strain correlation and are summarised in table 3.1 for the model of Launder *et al.* (1975) (LRR), Speziale *et al.* (1991) (SSG) and Wallin & Johansen (2000) (WJ).

	A_1	A_2	A_3	A_4
LRR	1.54	0.37	1.45	2.89
SSG	1.22	0.47	0.88	2.37
WJ	1.20	0	1.8	2.25

TABLE 3.1: Constants A_i for the pressure-strain models of Launder *et al.* (1975) (LRR), Speziale *et al.* (1991) (SSG) and Wallin & Johansen (2000) (WJ).

The set of implicit equations can be solved for the Reynolds-stress or anisotropy tensor using an iterative procedure. The ASM needs to be supported by an equation for the turbulence kinetic energy as well as a length-scale-providing equation to compute the dissipation rate ϵ. Even though all transport terms in the evolution equation for the anisotropy have been neglected, some history effects are still present in the ASM through the evolution equation for the turbulence kinetic energy and its dissipation rate.

In the limit of equilibrium, the algebraic stress relationship can be considered an exact approximation to the Differential-Reynolds-Stress Model. It is also a fair approximation for flows, which evolve slowly and which are close to an equilibrium

condition. For strong non-equilibrium flows or where convection and transport dominate the evolution of the Reynolds-stress tensor, the weak-equilibrium assumption is not valid and hence the performance of the ASM deteriorates. In addition to the limitations imposed by the weak-equilibrium assumption, the ASM also inherits all deficiencies of the 'parent' DRSM.

The Extended Weak-Equilibrium Assumption

Flows, which involve significant streamline curvature can be most accurately modelled by DRSM closures, since curvature/rotation effects are naturally included in the transport equation for the Reynolds-stress tensor. However, ASM were found to be inferior to a full DRSM closure in predicting the effects of streamline curvature. Even though the exact production term P_{ij}, and with that the sensitivity to rotational effects, is retained in the ASM approximation, it has been shown by Rumsey *et al.* (1999, 2000) that the weak-equilibrium assumption is incorrect in strongly curved flows, and that Da_{ij}/Dt should not be neglected.

Rodi & Scheuerer (1983) and Girimaji (1997) both argued that weak-equilibrium should preferably be invoked in a suitable curvilinear coordinate system, which in some way is aligned with the flow direction (for example, in a coordinate system, which is aligned with streamlines). In such a curvilinear coordinate system the weak-equilibrium assumption is more likely to hold.

The extended weak-equilibrium constraint is obtained by considering the anisotropy tensor transformed into a curvilinear coordinate system $\boldsymbol{a}^c = \boldsymbol{T}\boldsymbol{a}\boldsymbol{T}^T$, where $\boldsymbol{T}$ is the coordinate transformation matrix. The anisotropy $\boldsymbol{a}^c$ can be transformed back into a Cartesian system and expanded to give the relation

$$\boldsymbol{T}^T \frac{D\boldsymbol{a}^c}{Dt}\boldsymbol{T} = \frac{D\boldsymbol{a}}{Dt} + \boldsymbol{a}\frac{D\boldsymbol{T}^T}{Dt}\boldsymbol{T} + \boldsymbol{T}^T\frac{D\boldsymbol{T}}{Dt}\boldsymbol{a}, \tag{3.60}$$

see Gatski & Jongen (2000) or Wallin & Johansen (2002). It follows that

$$\frac{D\boldsymbol{a}}{Dt} = \boldsymbol{T}^T\frac{D\boldsymbol{a}^c}{Dt}\boldsymbol{T} - \left(\boldsymbol{a}\boldsymbol{\Omega}^r - \boldsymbol{\Omega}^r\boldsymbol{a}\right), \tag{3.61}$$

with $(D\boldsymbol{T}^T/Dt)\boldsymbol{T} = -\boldsymbol{T}^T D\boldsymbol{T}/Dt = \boldsymbol{\Omega}^r$. The extended weak-equilibrium approximation can now be understood as neglecting the term $\boldsymbol{T}^T(D\boldsymbol{a}^c/Dt)\boldsymbol{T}$ in the curvilinear coordinate system, which gives

$$\frac{D\boldsymbol{a}}{Dt} \approx \left(\boldsymbol{a}\boldsymbol{\Omega}^r - \boldsymbol{\Omega}^r\boldsymbol{a}\right). \tag{3.62}$$

It is straightforward to account for these additional terms in the ASM formulation by using a modified rotation-rate tensor of the form

$$\boldsymbol{\Omega}^c = \boldsymbol{\Omega} - (\tau/A_0)\boldsymbol{\Omega}^r. \tag{3.63}$$

It is, however, much more difficult to determine a suitable transformation matrix $\boldsymbol{T}$ or $\boldsymbol{\Omega}^r$ in such a way, that $\boldsymbol{T}^T(D\boldsymbol{a}^c/Dt)\boldsymbol{T}$ becomes negligible, and the error introduced by ignoring this term is not significant. Different approaches have been used to estimate $\boldsymbol{\Omega}^r$ (see Hellsten, 2002, for a short discussion). The first approach relates $\boldsymbol{\Omega}^r$ to the rate of change of the principle axes of the strain-rate tensor. A detailed description of this method is beyond the scope of this review. More details about this method can be found in Gatski & Jongen (2000) or Wallin & Johansen (2002). The second method employs the acceleration vector $D\overline{u}_i/Dt$ and its rate of change to approximate $\boldsymbol{\Omega}^r$ (see Girimaji (1997) or Wallin & Johansen (2002) for more details).

3.6 Explicit-Algebraic-Stress Model

The implicit algebraic stress relations, as introduced above, can be solved using an iterative procedure. However, it has been found that the iterative solution may be very expensive in complex flows and may lead to multiple roots and convergence to non-physical solutions (see, for example, Speziale, 1997). Therefore, the benefit of using an ASM model compared to a full DRSM is partly lost.

A more practical alternative is to derive an explicit solution to the algebraic stress-relations (3.58). This results in considerably improved robustness of the resulting Explicit-Algebraic-Stress Model (EASM), and hence constitutes a practical and robust alternative to traditional linear two-equation models by providing improved predictive capabilities at slightly increased numerical expense.

The solution to the algebraic stress relations (3.58) obviously has to be of the functional form $a_{ij} = F_{ij}\left(S_{ij}, \Omega_{ij}, P_k/\epsilon\right)$, where F_{ij} is an isotropic second-order tensor-valued function. Ignoring P_k/ϵ for the moment, the solution for a_{ij} can be expanded into an infinite tensor polynomial, which contains all second-order tensors that are symmetric and traceless, that can be formed from S_{ij} and Ω_{ij}. The coefficients depend on all possible invariants of S_{ij} and Ω_{ij}. The Caley-Hamilton theorem limits the most general form of the tensor polynomial to ten terms and five invariants. It has been shown by Spencer & Rivlin (1959) that the most general

tensor polynomial, also referred to as integrity base, is of the form

$$a_{ij} = F_{ij}\left(S_{ij}, \Omega_{ij}\right) = \sum_{\alpha=1}^{10} \beta_\alpha T_{ij}^{(\alpha)}, \tag{3.64}$$

with

$$\begin{aligned}
T_{ij}^{(1)} &= S_{ij}, \quad T_{ij}^{(2)} = S_{ik}S_{kj} - \frac{1}{3} II_S \delta_{ij}, \quad T_{ij}^{(3)} = \Omega_{ik}\Omega_{kj} - \frac{1}{3} II_\Omega \delta_{ij}, \\
T_{ij}^{(4)} &= S_{ik}\Omega_{kj} - \Omega_{ik}S_{kj}, \quad T_{ij}^{(5)} = S_{ik}S_{kl}\Omega_{lj} - \Omega_{ik}S_{kl}S_{lj}, \\
T_{ij}^{(6)} &= S_{ik}\Omega_{kl}\Omega_{lj} + \Omega_{ik}\Omega_{kl}S_{lj} - \frac{2}{3} IV \delta_{ij}, \\
T_{ij}^{(7)} &= S_{ik}S_{kl}\Omega_{lm}\Omega_{mj} + \Omega_{ik}\Omega_{kl}S_{lm}S_{mj} - \frac{2}{3} V \delta_{ij}, \\
T_{ij}^{(8)} &= S_{ik}\Omega_{kl}S_{lm}S_{mj} - S_{ik}S_{kl}\Omega_{lm}S_{mj}, \\
T_{ij}^{(9)} &= \Omega_{ik}S_{kl}\Omega_{lm}\Omega_{mj} - \Omega_{ik}\Omega_{kl}S_{lm}\Omega_{mj}, \\
T_{ij}^{(10)} &= \Omega_{ik}S_{kl}S_{lm}\Omega_{mn}\Omega_{nj} - \Omega_{ik}\Omega_{kl}S_{lm}S_{mn}\Omega_{nj},
\end{aligned} \tag{3.65}$$

and where the β_i-coefficients are functions of the invariants

$$II_S = \mathrm{tr}\left\{S_{ik}S_{kj}\right\}, \quad II_\Omega = \mathrm{tr}\left\{\Omega_{ik}\Omega_{kj}\right\}, \quad III_S = \mathrm{tr}\left\{S_{ik}S_{kl}S_{lj}\right\},$$

$$IV = \mathrm{tr}\left\{S_{ik}\Omega_{kl}\Omega_{lj}\right\}, \quad V = \mathrm{tr}\left\{S_{ik}S_{kl}\Omega_{lm}\Omega_{mj}\right\}. \tag{3.66}$$

The ten tensor groups are required to guarantee that tensorial expansion provides non-singular solutions even in cases where some of the tensor groups vanish. In two-dimensional mean flow the tensor polynomial reduces to only three terms

$$T_{ij}^{(1)} = S_{ij}, \quad T_{ij}^{(2)} = S_{ik}S_{kj} - \frac{1}{3} II_S \delta_{ij}, \quad T_{ij}^{(3)} = S_{ik}\Omega_{kj} - \Omega_{ik}S_{kj}, \tag{3.67}$$

and two invariants

$$II_S = \mathrm{tr}\left\{S_{ik}S_{kj}\right\}, \quad II_\Omega = \mathrm{tr}\left\{\Omega_{ik}\Omega_{kj}\right\}. \tag{3.68}$$

Pope (1975) was the first to derive an explicit solution for the ASM proposed by Rodi (1972, 1976). His derivation was limited to two-dimensional mean flow for which the tensor polynomial takes a more manageable form. Substituting the tensor polynomial into the ASM equation (3.58), and applying the Caley-Hamilton theorem to reduce higher-order terms, leads to a linear system of equations, which can be inverted to obtain the coefficients β_i (see Pope (1975) or Gatski & Speziale (1993) for more details on the solution procedure). Gatski & Speziale (1993) later

extended Pope's approach to three-dimensional mean flows for the general class of ASM models that are tensorially linear in the Reynolds-stress anisotropy. Taulbee (1994) and Wallin & Johansen (2000) both derive EASM for three-dimensional flow using a modified pressure-strain model of LRR. The modification is chosen such that some of the terms naturally vanish, which effectively reduces the tensor polynomial to five independent tensor groups. Even though the resulting model is more compact, it is achieved at the expense of the predictive performance, i.e. it always predicts $a_{33} = 0$ in situations where no anisotropy is induced by the mean strain rate S_{33}.

A major difficulty in solving the linear system of equations is related to the appearance of the production to dissipation ratio P_k/ϵ in the ASM model, which introduces a non-linear behaviour through the relationship $P_k/\epsilon = -\mathrm{tr}\{a_{ik}S_{kj}\}$. Gatski & Speziale (1993) and Taulbee (1992) apply a linearisation of the algebraic stress-equations by retaining the ratio of production to dissipation implicit during the derivation, i.e. specifying a constant equilibrium value for the production to dissipation ratio.

The assumption of a constant ratio of production to dissipation results in an inconsistent behaviour of the model for flows, which are far from equilibrium. This inconsistency may lead to singular behaviour for large localised strain rates, which in turn results in numerical difficulties. Gatski & Speziale (1993) therefore had to apply a regularisation procedure to remove the resulting model singularities. The more versatile approach is to solve the algebraic equations in their full non-linear form. Consistency for the production to dissipation ratio is achieved by writing P_k/ϵ using the solution for a_{ij}, which yields a scalar polynomial equation that needs to be solved additionally. For two-dimensional mean flow, solutions to the scalar polynomial equation have been obtained by Girimaji (1996), Ying & Canuto (1996) or Wallin & Johansen (2000). Hence, the resulting model becomes a fully explicit and fully consistent approximation to the 'parent' DRSM, which is free of singularities. In the case of general three-dimensional mean flow the non-linear equation is of sixth order (see Wallin & Johansen, 2000), and no explicit solution can be found in this case. Wallin & Johansen (2000) instead suggest to provide an initial guess using the solution of the non-linear equation for two-dimensional flow and to obtain a more accurate solution by using a perturbation solution for the three-dimensional equation. As a consequence, the fully explicit character of the EASM in three-dimensional mean flow can only be retained by sacrificing the internal consistency of the EASM approximation.

In the limit of two-dimensional mean flow, the EASM formulations reduce to much more compact forms and provide fully explicit and fully consistent solutions. Therefore, it seems very appealing to apply these two-dimensional formulations even for genuinely three-dimensional mean flows. On the other hand, the additional terms appearing in three-dimensional EASM formulations constitute additional higher-order nonlinear coupling terms, which may significantly improve the performance of the EASM in general three-dimensional flows. Weinmann & Sandberg (2009) investigated the differences between two and three-dimensional EASM formulations for predicting complex three-dimensional flows. Their results indicate that the overall difference in the predictions is very small and that the use of the simplified 2D-EASM formulation provides improved predictions in complex three-dimensional flows over turbulence models based on a linear stress-strain relationship. Naji *et al.* (2004) performed a priori testing of the 2D-EASM described in Gatski & Rumsey (2002) and the 3D-EASM of Wallin & Johansen (2000) for a square duct flow, and came to the conclusion, that the 2D-EASM is a good approximation for the three-dimensional flow in a square duct.

3.7 Non-linear Eddy-Viscosity Models

The tensor polynomial or integrity base in equation (3.65) constitutes a general non-linear stress-strain relationship of the form $\overline{u_i' u_j'} = (2/3)k\delta_{ij} + ka_{ij}$. Therefore, Explicit-Algebraic-Stress Models formally belong to the class of Non-Linear Eddy-Viscosity Models (NLEVM), i.e. models, which use a non-linear constitutive stress-strain relationship. In the case of EASM modelling, the coefficients β_i are directly determined from the parent 'DRSM' without requiring additional calibration of closure constants. In addition, the EASM constitutive relations are not strictly based on the concept of an eddy viscosity. However, comparing equation (3.65) with the Boussinesq assumption (3.10) reveals that an equivalent turbulence viscosity of the EASM model is given as $\nu_T = -0.5\beta_1 k\tau$. NLEVM are derived by taking a different route and are therefore discussed separately from EASMs. The route taken with NLEVM is to determine the β_i coefficients by empirical calibration for a range of flows. As a consequence of the calibration procedure, the coefficients may take different values dependent on which flow is used to calibrate them. For example, Craft *et al.* (1995) calibrated a cubic non-linear eddy-viscosity model using simple shear and more complex flows. Shih *et al.* (1995) proposed a NLEVM, which is calibrated using constraints from rapid-distortion theory (RDT), realisability and calibration of homogeneous shear and channel flows. Many other NLEVM's exists,

some of which are discussed in section 7.2. The success of NLEVM largely depends on the experience of the developer to include as much physics as possible in the modelling of the β_i coefficients.

Applications

NLEVM and EASM turbulence models have been applied to a broad range of academic and engineering validation cases, where the superior performance compared to linear models has been demonstrated. Abid *et al.* (1997) applied a k-ϵ EASM to airfoil flow, with and without incipient separation, and compared the results to a linear model. None of the models were able to predict the incipient separation, but the EASM model predicted realistic normal-stress components. Another important conclusion was that the improvements are limited by the ϵ equation, which does not respond accurately to adverse pressure gradients flows. This is also confirmed by Rumsey & Gatski (2001), where k-ϵ and k-ω EASM models were applied to a multi element airfoil. In Rumsey *et al.* (1999, 2000), an EASM model was successfully applied to the flow in a U-duct, where the flow exhibits significant streamline curvature. Jang *et al.* (2001, 2002) tested various NLEVM, EASM and DRSM models for the flow over a periodic hill configuration. They confirmed the poor performance of models based on the ϵ equation, whereas models based on the ω equation gave much better results. The nonlinear models were found to over-predict the separation region due to insufficient shear-stress in the separated shear layer. Luebke *et al.* (2001) assessed the performance of linear eddy-viscosity models and EASM models for bluff body flows. The results obtained with the EASM model are clearly superior to linear models. Moreover, the EASM model shows many features of LES but, naturally, is less accurate than LES. Deng *et al.* (2005) compare a quadratic EASM with ASM and DRSM models for the prediction of ship flows. In their case, the EASM and ASM gave similar predictions, and the DRSM was found to be better for regions with convex curvature. The better performance of the DRSM was linked to the weak-equilibrium assumption inherent in the EASM and ASM model. Franke *et al.* (2005) and Jouvray & Tucker (2007) evaluated the performance of NLEVM and EASM models. Both came to the conclusion that the predictions were improved compared to traditional turbulence models.

3.8 Linear Eddy-Viscosity Turbulence Models

The common feature of all linear eddy-viscosity models is that they are based on the concept of a scalar eddy viscosity ν_T and use the Boussinesq approximation

as the constitutive stress-strain relationship. The Boussinesq approximation can be considered a first-order (linear) approximation to the more general, non-linear, tensor polynomial of equation (3.65), and even though it suffers from various deficiencies (see discussion in section 3.1), it is still widely in use today. In fact, linear eddy-viscosity models are by far the most popular of all turbulence models, mainly because they are computationally reasonably cheap and robust and may deliver results of sufficient accuracy for not too complex flows.

On dimensional grounds, an expression for the turbulence viscosity has to be of the following form

$$\nu_T = C_\mu V_T L_T, \tag{3.69}$$

where V_T is a characteristic turbulence velocity scale and L_T is a characteristic turbulence length scale of the energy containing eddies.

In the pioneering work of Prandtl in 1925, the velocity and length scale was approximated as $V_T = l_{mix} \left| \mathrm{d}\overline{u}/\mathrm{d}y \right|$ and $L_T = l_{mix}$, where l_{mix} corresponds to a characteristic length scale of the flow under consideration. The major difficulty is now associated with specifying the appropriate length scale. Even though l_{mix} can be tuned for specific cases (for example, jets, mixing layers or boundary layers), there is not much hope that it can be chosen with sufficient accuracy in more complex flows. Another weakness is the purely local nature of such algebraic formulations, since it cannot account for history effects, which the flow has experienced at some station upstream.

The lowest level of turbulence closure, which is nowadays accepted for the simulation of turbulent flows in engineering applications are models, which include some history effects. This is achieved by introducing one or more evolution equation to determine the characteristic velocity and length scale. The characteristic velocity scale is usually determined from a transport equation for the turbulence kinetic energy $k = (1/2)\overline{u_i' u_i'}$, such that $V_T = k^{1/2}$. The exact equation for the turbulence kinetic energy has already been derived in section 3.2.2 and is not repeated here. The exact equation contains unclosed terms, which require modelling. It is common practice to lump the turbulence transport and pressure transport together and to model their net effect using a gradient-diffusion approximation of the following form

$$\frac{\partial}{\partial x_j}\left(\frac{1}{2}\overline{u_i' u_i' u_j'} - \overline{\frac{p'}{\rho} u_j'}\right) = -\frac{\partial}{\partial x_j}\left(\frac{\nu_T}{\sigma_k}\frac{\partial k}{\partial x_j}\right). \tag{3.70}$$

The constant σ_k is a closure coefficient, which needs to be calibrated. The resulting equation for the modelled turbulence kinetic energy k then takes the form

$$\frac{Dk}{Dt} = -\overline{u_i' u_j'} \frac{\partial \overline{u}_i}{\partial x_j} - \epsilon + \frac{\partial}{\partial x_j} \left[\left(\nu + \frac{\nu_T}{\sigma_k} \right) \frac{\partial k}{\partial x_j} \right]. \tag{3.71}$$

A simple one-equation turbulence model could now be derived by using the relation $\epsilon \propto k^{3/2}/L_T$ for the turbulence kinetic energy dissipation rate. The turbulence length scale can be determined based on an algebraic relation, similar to the mixing length concept as introduced above (see, for example, Wolfshtein, 1969).

In order to avoid the specification of an algebraic turbulence length-scale relation, Spalart & Allmaras (1992) proposed to use a transport equation for the product of the turbulence velocity and length scale, or in other words, for the turbulence viscosity itself. Instead of considering the turbulence viscosity directly, Spalart & Allmaras considered a modified turbulence viscosity $\tilde{\nu}$ as the transported quantity, from which the turbulence viscosity is obtained as $\nu_T = \tilde{\nu} f_{\nu 1}$, where $f_{\nu 1}$ is a damping function. The Spalart & Allmaras (1992) model has proven to be successful in many applications and is therefore widely in use today.

Another approach to avoid the specification of an algebraic turbulence length-scale relation is to solve another evolution equation from which the turbulence length scale L_T can be computed. Assuming that the turbulence kinetic energy is known, the length-scale-providing variable can be any combination of the form $\phi = k^m L_T^n$. The question, which then arises is what the optimum length-scale-providing variable would be. Hellsten (2004) has proposed a set of fundamental requirements, which the length-scale determining equation should fulfill. These are

- Wall boundary condition $\phi_w = 0$
- Growth rate at the wall not steeper than $\phi = O(y^2)$
- The free stream value ϕ_∞ should be non-growing
- Non-singular source terms.

Unfortunately, it is not possible to devise a length-scale-providing evolution equation, which satisfies all constraints above. Two of the most popular choices for the variable ϕ are considered next.

3.8.1 The k-ϵ Model

The most widely used quantity to compute the turbulence length scale is the dissipation rate of turbulence kinetic energy ϵ, from which the length scale can be determined as $L_T = k^{3/2}/\epsilon$ ($m = 3/2$, $n = -1$). It then follows that the turbulence viscosity is given by $\nu_T = C_\mu k^2/\epsilon$. The first route to derive an evolution equation for the dissipation rate would be to model all unclosed terms in the exact evolution equation for the dissipation rate (3.2.3). Unfortunately, the exact transport equation for the dissipation rate involves various unknown higher-order correlations of fluctuating quantities, which makes it much more difficult to model than the exact transport equation for the turbulence kinetic energy k. As a consequence, the uncertainties introduced by ad hoc modelling of the ϵ equation is significantly higher than for the turbulence kinetic energy equation and is often considered one of the main weaknesses of this type of two-equation modelling.

The second and more practical route to derive a transport equation for the turbulence length scale is based on a generic modelling approach where the length-scale variable is assumed to be governed by certain physical processes. Typical processes, which are included in a generic transport equation are, for example, convection by the mean flow, production by the mean flow, viscous dissipation and transport of the length-scale variable. Such a transport equation can be written in the general form for the arbitrary quantity ϕ

$$\frac{D\phi}{Dt} = C_{\phi_1}\frac{\phi}{k}P_\phi - C_{\phi_2}\frac{\phi}{k}\epsilon + \frac{\partial}{\partial x_i}\left[\frac{\nu_T}{\sigma_\phi}\frac{\partial\phi}{\partial x_i}\right]. \tag{3.72}$$

For high-Reynolds-number flows, the ϵ equation is commonly modelled following the proposal of Jones & Launder (1972)

$$\frac{D\epsilon}{Dt} = C_{\epsilon 1}\frac{\epsilon}{k}P_k - C_{\epsilon 2}\frac{\epsilon^2}{k} + \frac{\partial}{\partial x_j}\left[\left(\nu + \frac{\nu_T}{\sigma_\epsilon}\right)\frac{\partial\epsilon}{\partial x_j}\right], \tag{3.73}$$

where $C_{\epsilon 1}, C_{\epsilon 2}$ and σ_ϵ are closure coefficients, which need to be calibrated. Equation (3.73) is not applicable to low-Reynolds-number or near-wall flows. Suitable low-Reynolds-number modifications will be discussed in section 3.8.1.2.

3.8.1.1 Calibration Strategy

There are a total of five closure constants, which need to be determined. In order to derive suitable values for the closure constants a range of simple idealised flows

are considered, for which the modelled equations can be reduced to an analytical solution. This allows isolation of the closure constants and determination of suitable values by reference to data from experiment or direct numerical simulation.

Decaying Homogeneous Isotropic Turbulence (DHIT)

The constant C_{ϵ_2} can be determined by considering Decaying Homogeneous Isotropic Turbulence (DHIT) where all gradients of the mean flow and turbulence statistics vanish. For DHIT the transport equation reduces to the much simpler form

$$\frac{\mathrm{d}k}{\mathrm{d}t} = -\epsilon, \qquad \frac{\mathrm{d}\epsilon}{\mathrm{d}t} = -C_{\epsilon_2}\frac{\epsilon^2}{k}, \tag{3.74}$$

which can be solved analytically. Experimental data suggest that the decay of turbulence kinetic energy of grid-generated turbulence approximately follows a power-law $k(t) = k_0(1 + t/t_0)^{-n}$, where the subscript 0 denotes initial values and n is the decay exponent. Integrating $\mathrm{d}k/\mathrm{d}t = -\epsilon$ gives the solution for the dissipation rate ϵ. Substituting the solution into the dissipation rate equation gives the constraint for $C_{\epsilon_2} = (n + 1)/n$. It is now straightforward to match C_{ϵ_2} to a reference decay rate of DHIT.

Homogeneous Shear Flow

Next, homogeneous shear flow will be considered, from which the coefficient C_{ϵ_1} can be determined. In homogeneous shear flows, both k and ϵ grow exponentially and the turbulence time scale $\tau = k/\epsilon$, and the anisotropy $a_{12} = \overline{u'v'}/k$ reach approximately constant values. This also implies that the production to dissipation ratio $P_k/\epsilon = -a_{12}(k/\epsilon)\mathrm{d}\overline{u}/\mathrm{d}y$ is approximately constant. The simplified equation for the k and ϵ equations take the form

$$\frac{\mathrm{d}k}{\mathrm{d}t} = P_k - \epsilon, \qquad \frac{\mathrm{d}\epsilon}{\mathrm{d}t} = C_{\epsilon_1}\frac{k}{\epsilon}P_k - C_{\epsilon_2}\frac{\epsilon^2}{k}. \tag{3.75}$$

Combining the equations for k and ϵ yields

$$\frac{\mathrm{d}}{\mathrm{d}t}\left(\frac{k}{\epsilon}\right) = \frac{\mathrm{d}\tau}{\mathrm{d}t} = (1 - C_{\epsilon_1})\frac{P_k}{\epsilon} - (1 - C_{\epsilon_2}). \tag{3.76}$$

Assuming that the turbulence has reached an asymptotic state, i.e. $\mathrm{d}\tau/\mathrm{d}t \approx 0$, and using experimental data for the production to dissipation ratio in homogeneously sheared turbulence, for example, $(P_k/\epsilon)_\infty \approx 1.8$, the constant C_{ϵ_1} can be determined.

The Log-Law region

The last closure coefficients, which can be determined are σ_ϵ and C_μ. The flow regime under consideration is the logarithmic region of a zero pressure-gradient boundary layer, where the logarithmic velocity profile is give by $\mathrm{d}\overline{u}/\mathrm{d}y = u_\tau/\kappa y$ and the shear-stress $-\overline{u'v'}$ is constant and equal to $-\overline{u'v'} = u_\tau^2 = \tau_w/\rho$ with the wall shear stress τ_w. It directly follows that the eddy viscosity is given by $\nu_T = -\overline{u'v'}/(\mathrm{d}\overline{u}/\mathrm{d}y) = u_\tau \kappa y$. Further, it can be assumed that the flow is locally in equilibrium, i.e.

$$P_k = -\overline{u'v'}\frac{\mathrm{d}\overline{u}}{\mathrm{d}y} = \frac{u_\tau^3}{\kappa y} = \epsilon, \tag{3.77}$$

from which follows that $k = \sqrt{\nu_T \epsilon/C_\mu} = u_\tau^2/\sqrt{C_\mu}$. Substituting all variables into the modelled equation for the dissipation rate and rearranging for σ_ϵ yields the relation

$$\sigma_\epsilon = \kappa^2/\sqrt{C_\mu}\,(C_{\epsilon 2} - C_{\epsilon 1})\,. \tag{3.78}$$

What remains is the calibration of the constant C_μ appearing in the turbulence viscosity relation (3.69) and in the definition of σ_ϵ. Within the framework of EASM modelling the constant is given by $C_\mu = -0.5\beta_1$ and is determined as part of the constitutive relation of the EASM model. In the present context a specific value for C_μ needs to be specified. For the log-law region of a zero pressure gradient boundary layer, it follows from the discussion above that $C_\mu = \left(-\overline{u'v'}/k\right)^2 = a_{12}^2$. It can be found from experimental data or DNS, that the stress-intensity ratio or a_{12} anisotropy is approximately constant in the log-region and takes a value of $a_{12} \approx -0.3$. It follows that $C_\mu \approx 0.09$.

The closure coefficients proposed by Launder & Sharma (1974) (LS) were obtained based on a slightly different procedure than introduced above. Nevertheless, their set of closure coefficients is still widely in use due to the LS models reasonable predictive capabilities for a range of flows. The LS model is nowadays referred to as the 'standard' k-ϵ model, with the closure coefficients given by

$$C_\mu = 0.09, C_{\epsilon 1} = 1.44, C_{\epsilon 2} = 1.92, \sigma_k = 1.0, \sigma_\epsilon = 1.3. \tag{3.79}$$

More information about the calibration of the closure coefficients can be found in Hanifi *et al.* (1999), Durbin & Petterson-Reif (2001) and Hellsten (2004).

3.8.1.2 Near-Wall Modifications

The k-ϵ model, presented above, is only applicable to high-Reynolds-number flows and has to be used in conjunction with wall functions or log-law boundary conditions in the presence of solid walls. Suitable log-law boundary conditions follow from the discussion in section 3.8.1.1. It is important to note that these boundary conditions are only applicable if they are applied at a location outside the viscous sublayer, in the log-region where the non-dimensional wall distance $y^+ = u_\tau \nu / y$ is in the range $30 - 100$. Wall functions are computationally attractive, since the viscous sublayer does not need to be resolved with a fine numerical discretisation. Even though wall functions may give reasonable results for 'well-behaved' high-Reynolds-number flows, they are usually not applicable for flows with low Reynolds numbers, strong non-equilibrium or strong pressure gradients, separated flows, wall-bounded flows with strong curvature or general complex three-dimensional flows.

For more accurate predictions in such cases modifications can be introduced to the high-Reynolds-number formulation, which allows direct integration across the viscous sublayer to the solid wall. A large number of such low-Reynolds-number formulations have been proposed. A detailed review and evaluation of some models can be found in Patel *et al.* (1985), Rodi & Mansour (1993) or Sarkar & So (1997). The modifications commonly introduced to the modelled equations for the turbulence kinetic energy and its dissipation rate can be summarised as follows:

$$\frac{Dk}{Dt} = P_k - \tilde{\epsilon} + \frac{\partial}{\partial x_j}\left[\left(\nu + \frac{\nu_T}{\sigma_k}\right)\frac{\partial k}{\partial x_j}\right], \tag{3.80}$$

$$\frac{D\tilde{\epsilon}}{Dt} = f_1 C_{\epsilon 1}\frac{\tilde{\epsilon}}{k}P_k - f_2 C_{\epsilon 2}\frac{\tilde{\epsilon}^2}{k} + \frac{\partial}{\partial x_j}\left[\left(\nu + \frac{\nu_T}{\sigma_\epsilon}\right)\frac{\partial \tilde{\epsilon}}{\partial x_j}\right] + E, \tag{3.81}$$

with

$$\nu_T = f_\mu C_\mu \frac{k^2}{\tilde{\epsilon}} \tag{3.82}$$

and

$$\tilde{\epsilon} = \epsilon - D. \tag{3.83}$$

The first modification to note is that the transported quantity is now $\tilde{\epsilon}$, which has the advantage of a simplified wall boundary condition $\tilde{\epsilon}_w = 0$, rather than $\epsilon_w = D = \nu \partial^2 k / \partial y^2$ for the unmodified ϵ equation. The function f_1 and the extra term E are both used to enhance the magnitude of the dissipation rate close to the wall, which reduces the peak values of turbulence kinetic energy. The damping function f_2 is introduced in order to eliminate the singularity of the destruction

term at the wall where $k \to 0$. It is sometimes also used to adjust the decay-rate of isotropic turbulence at low Reynolds number. The last and most important modification is the damping function f_μ, which is applied to the constant C_μ. It accounts for the suppression of turbulence close to the wall. The near-wall damping primarily originates from the suppression or blocking of wall-normal fluctuations $\overline{v'^2}$ and viscous damping only plays a minor role close to the wall. Nevertheless, viscosity-dependent damping functions, which are sensitive to parameters like $y^+ = u_\tau y/\nu$, $Re_y = k^{1/2}y/\nu$ or $Re_T = k^2/\nu\epsilon$ are mainly used. It seems that such functions are not suited to achieve good correlation with the non-viscous, non-local effect of suppression of turbulence close to the wall.

A typical and widely used low-Reynolds-number formulation is the model of Launder & Sharma (1974) given by

$$f_\mu = \exp\left(\frac{-3.4}{(1+Re_T/50)^2}\right), \quad f_1 = 0, \quad f_2 = 1 - 0.3\exp\left(-Re_T^2\right), \tag{3.84}$$

$$E = 2\nu\nu_T\left(\frac{\partial\overline{u}_i}{\partial y}\right)^2, \quad D = 2\nu\left(\frac{\partial k^{1/2}}{\partial y}\right)^2. \tag{3.85}$$

3.8.2 The k-ω Model

A different scale-determining variable, which is frequently used is the specific dissipation rate of turbulence kinetic energy ω, from which the length scale is determined as $L_T = k^{1/2}/\omega$ and $\nu_T = k/\omega$ ($m = 1/2$, $n = -1$). Since the scale-determining variable is not the dissipation rate ϵ itself, the destruction term in the equation for the turbulence kinetic energy is usually modelled as $\epsilon = C_\mu k\omega$. The pioneering work on ω-based turbulence models can be attributed to the work of Kolmogorov (1942) and extensive contributions of Wilcox (see Wilcox, 1998, where his work is summarised).

The 'standard' k-ω (1988) model can be represented by the generic transport equation (3.72) as introduced earlier. The turbulence kinetic energy k and the specific dissipation rate ω are obtained from

$$\frac{Dk}{Dt} = P_k - \beta^* k\omega + \frac{\partial}{\partial x_j}\left[\left(\nu + \sigma_k\nu_T\right)\frac{\partial k}{\partial x_j}\right], \tag{3.86}$$

$$\frac{D\omega}{Dt} = \gamma\frac{\omega}{k}P_k - \beta\omega^2 + \frac{\partial}{\partial x_j}\left[\left(\nu + \sigma_\omega\nu_T\right)\frac{\partial \omega}{\partial x_j}\right], \tag{3.87}$$

where the turbulence viscosity is $\nu_T = k/\omega$ and the closure coefficients are given by

$$\gamma = 5/9, \quad \beta = 3/40, \quad \beta^* = 0.09, \quad \sigma_\omega = 0.5, \quad \sigma_k = 0.5. \tag{3.88}$$

The k-ω model has proven to be superior to the k-ϵ models in predicting boundary-layer flows. For boundary layers under an adverse pressure gradient the ϵ equation significantly over-predicts the level of turbulence, which may delay or even prevent separation (see, for example, Wilcox, 1988). Similar shortcomings are observed for the recovery of reattaching flows (see Jang *et al.*, 2001). Even though the k-ω model could be used in conjunction with wall functions, a distinct advantage of the ω-equation is that it can be integrated through the viscous sublayer, directly to the wall without the need of ad hoc modifications or empirical damping functions to reproduce the correct velocity profile of a turbulent boundary layer.

Despite these advantages, the standard k-ω model is also not entirely trouble free. First, the specific dissipation rate ω exhibits singular behaviour $\omega \to 1/y^2$ close to the wall. The near-wall behaviour of the ω equation is given by the balance of destruction and viscous-diffusion terms, which both behave as $1/y^4$ and involve computation of second derivatives of the singular quantity ω. Several approaches exist that alleviate the numerical difficulties close to the wall. The first approach is to compute ω from the asymptotic near-wall behaviour $\omega = 6\nu/\beta y^2$ in the near-wall region, say below $y^+ < 2.5$, rather than solving the ω equation in this region. The second, and most frequently employed, approach is to use rough-wall boundary conditions with a small roughness height. This has the advantage that ω remains finite at the wall. Alternatively, it has been proposed by Gullman-Strand *et al.* (2004) to use the decomposition $\omega = \tilde{\omega} + \omega_w$, where $\tilde{\omega}$ is the new transported quantity with the wall boundary condition $\tilde{\omega}_w = 0$, and where the correct near-wall behaviour is contained in $\omega_w = 6\nu/\beta y^2$. This approach seems particularly interesting and deserves some attention. However, more testing and validation is required before it can be generally recommended.

The second weakness of the standard k-ω model is the spurious sensitivity to free-stream values of ω_∞. This sensitivity is undesirable, since it allows a free shear-layer to attain almost any spreading rate by simply adjusting ω_∞. It is instructive to compare the transport equation model for ω with the exact transport equation obtained by transforming the exact ϵ equation (3.18) into a form based on ω. The resulting equation is as follows:

$$\frac{D\omega}{Dt} = \frac{P_\epsilon}{k} - \frac{\epsilon_\epsilon}{k} - \frac{D_\epsilon}{k} - \frac{\omega P_k}{k} + \omega^2 + \frac{\omega D_k}{k} + \frac{2\nu}{k}\frac{\partial\omega}{\partial x_i}\frac{\partial k}{\partial x_i} + \nu\nabla^2\omega. \tag{3.89}$$

The transformation reveals that the closure coefficients of the standard k-ω model should be chosen as $\gamma = (C_{\epsilon 1} - 1) = 0.44$ and $\beta = C_\mu (C_{\epsilon 2} - 1) = 0.0828$ in order to be consistent with the standard k-ϵ model. Since the coefficients of the standard k-ω model are quite different, it might be asked whether the better performance in adverse pressure gradient flows is due to the different set of closure coefficients.

A closer comparison between the exact ω equation with the generic form also reveals that the modelled ω equation lacks additional cross-diffusion terms (terms which involve $(\partial k/\partial x_i)(\partial \omega/\partial x_i)$). Menter (1992) proposed a two-layer k-ω model where the standard k-ω model is used close to the wall and the k-ϵ model of Jones & Launder (1972), which is transformed into a formulation based on ω, is used away from solid boundaries. The motivation for the two-layer concept is twofold. First, the favourable behaviour of the ω equation close to the wall and in flows with strong adverse pressure gradients is retained. Second, the transformed k-ϵ model includes a turbulent cross-diffusion term, which is activated in the outer region of a turbulent boundary layer, which effectively eliminates the free-stream sensitivity. Another possible approach to eliminate the free-stream sensitivity of the standard k-ω model is to add the cross-diffusion to the transport equation only if it has a positive contribution. This requires retuning of the diffusion coefficients such that the correct diffusive behaviour of ω is ensured at a turbulent/non-turbulent interface. Such a modified version of Wilcox's k-ω model has been proposed by Kok (1999) and is referred to as the k-ω TNT model. Note that the cross-diffusion term is also present in the latest release of the Wilcox (2008) k-ω model.

Another major and very successful upgrade was the introduction of a shear-stress-transport (SST) limiter by Menter (1992). The SST limiter corrects the tendency to predict too high levels of turbulence in flows with strong adverse pressure gradient, or non-equilibrium flows where the production of turbulence kinetic energy exceeds the dissipation rate $P_k > \epsilon$. Inside a boundary layer the shear-stress may be determined as $-\overline{u'v'} = \nu_T \partial \overline{u}/\partial y$. Using Bradshaw's assumption, that $-\overline{u'v'}/k = -a_{12} = 0.3$ is a good approximation in a range of turbulent wall bounded flows, the turbulence viscosity can be expressed as $\nu_T = -a_{12} k/S$, where $S = \sqrt{2 S^*_{ij} S^*_{ij}}$. For boundary-layer flows, the SST limiter is now simply obtained by imposing an upper limit to the turbulence viscosity $\nu_T = \min(k/\omega, -a_{12} k/S)$. Wilcox (2008) also recognised the importance of limiting the shear-stress in strong non-equilibrium flows and introduced a limiter, which multiplies ν_T with a factor that is sensitive to the production to dissipation ratio P_k/ϵ.

Menter's k-ω-SST model is obtained by using the shear-stress-transport limiter in conjunction with the two-layer formulation, as discussed above. Since the SST model is sometimes used in this work as a reference, the complete formulation will be given here (see also Menter, 2009). The transport equations for the turbulence kinetic energy and the specific dissipation rate take the form

$$\frac{Dk}{Dt} = \tilde{P}_k - \beta^* k\omega + \frac{\partial}{\partial x_j}\left[\left(\nu + \sigma_k \nu_T\right)\frac{\partial k}{\partial x_j}\right], \tag{3.90}$$

$$\frac{D\omega}{Dt} = \gamma\frac{1}{\nu_T}\tilde{P}_k - \beta\omega^2 + \frac{\partial}{\partial x_j}\left[\left(\nu + \sigma_\omega \nu_T\right)\frac{\partial \omega}{\partial x_j}\right] + 2(1-F_1)\sigma_{\omega 2}\frac{1}{\omega}\frac{\partial k}{\partial x_i}\frac{\partial \omega}{\partial x_i}, \tag{3.91}$$

where the turbulence viscosity is given by

$$\nu_T = \frac{a_1 k}{\max\left(a_1\omega, SF_2\right)}. \tag{3.92}$$

The production term is limited to ten times the dissipation rate, thus $\tilde{P}_k = \max(P_k, 10\beta^* k\omega)$ to avoid an unphysical build-up of turbulence kinetic energy in stagnation regions. The blending functions F_1 and F_2 are unity close to the wall and approach zero away from solid walls, and are given by

$$F_1 = \tanh\left\{\left\{\min\left[\max\left(\frac{\sqrt{k}}{\beta^*\omega y}, \frac{500\nu}{y^2\omega}\right), \frac{4\sigma_{\omega 2}k}{y^2 CD_{k\omega}}\right]\right\}^4\right\}, \tag{3.93}$$

$$F_2 = \tanh\left\{\left[\max\left(\frac{2\sqrt{k}}{\beta^* k\omega}, \frac{500\nu}{y^2\omega}\right)\right]^2\right\}, \tag{3.94}$$

where $CD_{k\omega} = \max(2\sigma_{\omega 2}(1/\omega)(\partial k/\partial x_i)(\partial\omega/\partial x_i), 10^{-10})$ and $\beta^* = 0.09$. The closure constants are obtained by a blending of the form $\phi = \phi_1 F_1 + (1-F_1)\phi_2$, where ϕ_1 and ϕ_2 correspond to set 1 and 2, respectively.

Set 1: $\gamma_1 = 5/9, \quad \beta_1 = 3/40, \quad \sigma_{K_1} = 0.85, \quad \sigma_{\omega_1} = 0.5.$
Set 2: $\gamma_2 = 0.44, \quad \beta_2 = 0.0828, \quad \sigma_{K_2} = 1, \quad \sigma_{\omega_2} = 0.856.$

3.8.3 Elliptic-Relaxation/Blending Approaches

The traditional way to include wall effects within the framework of two-equation models is to introduce empirical damping functions, which involve viscosity-dependent parameters (for example, $y^+ = u_\tau z/\nu$, $Re_T = k^2/\nu\epsilon$ or $Re_y = \sqrt{k}y/\nu$). For the low-Reynolds-number formulation of a k-ϵ model, up to three empirical functions are

required: f_1, f_2 and f_μ. It is also important to mention in this context that even though the high-Reynolds-number k-ω model can be integrated to solid boundaries without requiring ad-hoc modifications, if accurate predictions of the turbulence quantities close to the wall are desired, damping functions are also required for the k-ω model.

The damping function f_μ applied to C_μ is of critical importance and accounts for the suppression of turbulence close to the wall. It has already been mentioned that the near-wall damping primarily originates from the suppression or blocking of wall-normal fluctuations $\overline{v'^2}$ and viscous damping only plays a minor role close to the wall. The kinematic wall blocking is a non-viscous effect, and strictly speaking should not be modelled using viscosity-dependent parameters. Figure 3.2 shows the behaviour of $f_\mu C_\mu = C_\mu^{eff}$ close to the wall, computed directly from DNS data of Coleman *et al.* (2003) for a turbulent channel flow at $Re_\tau = 390$, and for the same configuration with an imposed uniform straining, which mimics the effect of an idealized adverse pressure gradient on the flow. In addition, C_μ^{eff} computed from the relation $C_\mu^{eff} = C_\mu^\nu \overline{v'^2}/k$, where $C_\mu^v = 0.22$, is plotted as well.

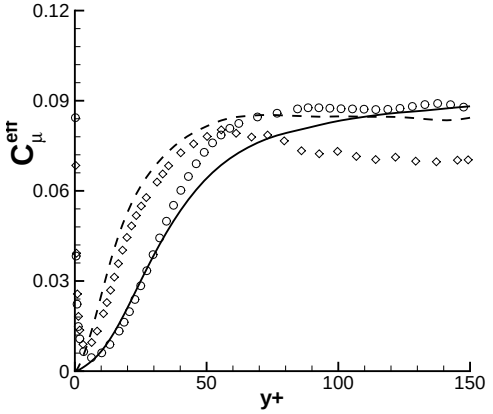

FIGURE 3.2: Near-wall behaviour of C_μ^{eff}. Symbols correspond to DNS of Coleman *et al.* (2003); (○) and (—) channel flow, (◊) and (- - -) channel flow with imposed APG. The lines are computed from $C_\mu^{eff} = C_\mu^\nu \overline{v'^2}/k$.

This clearly illustrates that the damping of C_μ close to the wall is very well correlated with the suppression of the wall-normal fluctuations and has not much to do with viscous damping effects. Therefore, any attempt to model the near-wall behaviour correctly should ideally be based on a damping function of the form $f_\mu = (C_\mu^\nu/C_\mu)\overline{v'^2}/k$. Such a damping function is of course only useful if $\overline{v'^2}$ can be determined with sufficient accuracy close to the wall. Durbin (1991) derived a scalar

transport equation for the wall-normal fluctuations $\overline{v^2}$ from the elliptic-relaxation technique presented in section 3.4.6. Even though the wall-normal velocity scale $\overline{v^2}$ is not exactly equal to the component $\overline{v'^2}$ of the Reynolds-stress tensor, close to the wall their behaviour is very similar. Based on the elliptic-relaxation approach of Durbin (1991), an eddy-viscosity turbulence model can be derived, which does not rely on empirical viscosity-dependent damping functions.

The scalar transport equation for the wall-normal velocity scale $\overline{v^2}$ can be written as

$$\frac{D\overline{v^2}}{Dt} = \Pi_{22}^* - \epsilon\frac{\overline{v^2}}{k} + \frac{\partial}{\partial x_k}\left[\left(\nu + \sigma_\varphi \nu_T\right)\frac{\partial \overline{v^2}}{\partial x_k}\right], \tag{3.95}$$

with the scalar redistribution term

$$\Pi_{22}^* = \Pi_{22} - \epsilon_{22} + \frac{\overline{v^2}}{k}\epsilon = k f_{22}, \tag{3.96}$$

and the elliptic equation for the intermediate variable f_{22}

$$f_{22} - L^2\nabla^2 f_{22} = \frac{1}{k}\left(\Phi_{22}^{(hom)} - \frac{2}{3}\epsilon + \epsilon\frac{\overline{v^2}}{k}\right). \tag{3.97}$$

The turbulence viscosity is now obtained from the relation $\nu_T = C_\mu^v \overline{v^2}\tau$. In order to take viscous effects into account, the turbulence length and time scales are limited by the viscous or Kolmogorov length and time scales, respectively:

$$L = C_L \max\left[\frac{k^{3/2}}{\epsilon}, C_\eta\left(\frac{\nu^3}{\epsilon}\right)^{1/4}\right], \quad \tau = \max\left[\frac{k}{\epsilon}, C_T\sqrt{\frac{\nu}{\epsilon}}\right]. \tag{3.98}$$

The elliptic-relaxation concept is usually used in conjunction with a k-ϵ model to compute the turbulence length and time scales. The transport equation for the turbulence kinetic energy and dissipation rate are given by

$$\frac{Dk}{Dt} = P_k - \epsilon + \frac{\partial}{\partial x_j}\left[\left(\nu + \sigma_k \nu_T\right)\frac{\partial k}{\partial x_j}\right], \tag{3.99}$$

$$\frac{D\epsilon}{Dt} = \frac{C'_{\epsilon 1}P_k - C_{\epsilon 2}\epsilon}{\tau} + \frac{\partial}{\partial x_j}\left[\left(\nu + \sigma_\epsilon \nu_T\right)\frac{\partial \epsilon}{\partial x_j}\right]. \tag{3.100}$$

Note that the near-wall singularity of the destruction term in the transport equation for the dissipation rate is no longer a problem, since the time scale τ remains finite at the wall. The closure constant $C'_{\epsilon 1} = f_1 C_{\epsilon 1}$ includes the empirical function $f_1 = 1 + 0.0045\sqrt{k/\overline{v^2}}$, which is designed to enhance the dissipation rate close the

wall (see, for example, Parneix *et al.*, 1998).

The wall boundary condition for the elliptic equation is given by $f_{22,w} = -5(\overline{v^2}/k^2)\epsilon = -20\nu^2\overline{v^2}/\epsilon y^4$. This boundary condition introduces a strong coupling between the $\overline{v^2}$ and f_{22} equation and the highly non-linear behaviour of $\overline{v^2} = O(y^4)$ and y^4 in the denominator introduces considerable numerical stiffness close to the wall. The strong coupling of $\overline{v^2}$ and f_{22} via the boundary conditions results in considerable numerical difficulties when solved with a segregated solver, and may lead to oscillations or divergence particularly for too small values of $y^+ < 1$ (see, for example, Laurence *et al.* (2004) or Hanjalic *et al.* (2004)). Therefore, various modifications to Durbin's original elliptic-relaxation approach were introduced in the literature in an attempt to make it applicable for segregated solvers.

Lien & Durbin (1996) and Lien & Kalitzin (2001) redefined the elliptic-relaxation variable as $\tilde{f}_{22} = f_{22} - f_{22,w} = f_{22} + 5(\overline{v^2}/k^2)\epsilon$ with the benefit that homogeneous boundary conditions can be prescribed for the new dependent variable $\tilde{f}_{22,w} = 0$. This reduces the coupling between the $\overline{v^2}$ and $\tilde{f}_{22}$ equation. In the equation for the new elliptic variable $\tilde{f}_{22}$ the term $5L^2\nabla^2(\epsilon\overline{v^2}/k^2)$ resulting from the transformation has been neglected. Laurence *et al.* (2004) argued that this term needs to be retained, since in the log-region it has similar magnitude to the other terms in the $\tilde{f}_{22}$ equation.

Hanjalic *et al.* (2004) and Laurence *et al.* (2004) both proposed modelling the variable $\varphi = \overline{v^2}/k$ rather than $\overline{v^2}$ directly. This has the advantage that the non-linearity at the wall is reduced to $\varphi = O(y^2)$ as the wall is approached, and the boundary condition for f_{22} reduces to $f_{22,w} = -10\nu\varphi/y^2$. Laurence *et al.* (2004) additionally transform the elliptic variable into a more convenient definition, $\tilde{f}_{22} = f_{22} + 2\nu(\nabla\phi\nabla k)/k + \nu\nabla^2\phi$, for which homogeneous boundary conditions can be prescribed at the wall, $\tilde{f}_{22,w} = 0$. In the final form of the $\tilde{f}_{22}$ equation, the term $\nu L^2\nabla^2(2(\nabla\varphi\nabla k)/k + \nabla^2\varphi)$ originating from the transformation has been neglected based on the argument that its effect is limited to the viscous sublayer and the magnitude is significantly smaller as compared to the term neglected by Lien & Durbin (1996).

Keshmiri *et al.* (2008) used the new variable $\varphi = \overline{v^2}/k$ in conjunction with the elliptic-blending concept of Manceau & Hanjalic (2002), where the elliptic-blending parameter α already has the homogeneous boundary condition $\alpha_w = 0$ and hence does not require a transformation to another variable where certain terms have to be neglected in the derivation. The φ-α model is considered a good compromise between predictive accuracy and numerical robustness of the formulation. The

constitutive equations for φ and α take the form

$$\frac{D\varphi}{Dt} = (1-\alpha^p)\, f^{wall} + \alpha^p f^{hom} - \frac{\varphi}{k} P_k + \frac{2}{k}\left(\sigma_k \nu_T\right) \frac{\partial k}{\partial x_j}\frac{\partial \varphi}{\partial x_j} + \frac{\partial}{\partial x_j}\left[\left(\nu + \sigma_\varphi \nu_T\right)\frac{\partial \varphi}{\partial x_j}\right], \tag{3.101}$$

$$L^2 \Delta\alpha - \alpha = -1. \tag{3.102}$$

The redistribution term f^{hom} in the φ-α model is based on the quasi-homogeneous redistribution model of Speziale *et al.* (1991), thus

$$f^{hom} = -(1/\tau)\left(C_1 - 1 + C_2 P_k/\epsilon\right)\left(\varphi - 2/3\right), \quad f^{wall} = -\varphi\epsilon/k. \tag{3.103}$$

The turbulence viscosity is given as

$$\nu_T = C_\mu^\nu \varphi k \tau. \tag{3.104}$$

The closure constants can be summarised as $C_\mu^\nu = 0.22$, $C_L = 0.161$, $C_T = 6$, $C_\eta = 90$, $\sigma_k = \sigma_\varphi = 1$, $p = 3$, $C_1 = 1.7$, $C_2 = 1.2$.

Chapter 4

Turbulence-Resolving Approaches

In this chapter the turbulence-resolving approaches of Direct and Large-Eddy Simulation will be briefly introduced. This is followed by a detailed review of available techniques to combine the framework of statistical turbulence modelling (RANS) with a turbulence-resolving approach, such as Large-Eddy Simulation (LES). The unified framework of RANS/LES modelling aims at providing improved predictions for complex flows at high Reynolds number where traditional RANS closures fail to predict reliable results and where conventional LES is prohibitively expensive in terms of computational cost.

4.1 Direct and Large-Eddy Simulation

The most accurate approach for the simulation of turbulent flows is Direct Numerical Simulation (DNS) where the Navier-Stokes equations are solved in exact form. The aim of DNS is to explicitly resolve all inherent mechanisms of turbulence in the simulation, such as, for example, production and dissipation of turbulence. Hence, DNS does not require any modelling apart from the numerical discretisation. Direct simulation of turbulent flows is only possible if unsteady simulations are performed with adequate resolution in space and time to capture both the smallest and largest turbulence scales in the flow. It has already been discussed in chapter 2, that the range of time and length scales or, in other words, the ratio of largest to smallest scales present in a turbulent flow, increases with Reynolds number. Unfortunately, many flows of engineering and more practical interest are characterised by high Reynolds number, with the consequence that the spatial and temporal resolution required to perform DNS is well beyond currently available computational resources.

Even though there is no need for physical modelling of turbulence in DNS, there are other issues, which require careful attention. The numerical scheme has to be very accurate in order not to contaminate the smallest turbulence scales by excessive levels of numerical dissipation and dispersion. Furthermore, the inflow or initial conditions often need to contain realistic turbulence with a full spectrum of turbulence scales as well as temporal and spatial correlations, if possible.

The resolution requirements for DNS can be relaxed by applying a spatial or temporal filter to the Navier-Stokes equations, which effectively removes the smallest scales from the flow field. As opposed to the RANS approach, where all turbulence scales are removed from the governing equations, filtering only removes the contribution of the smallest turbulence scales, which otherwise, would require a very fine spatial and temporal resolution. The large scales of turbulence remain unmodified by the filtering operation and are explicitly resolved in the simulation in space and time, similar to DNS. This approach is referred to as Large-Eddy Simulation (LES). The filtering operation introduces additional unknown terms in the momentum equations, which need to be modelled and which account for the effect of the unresolved small scales on the resolved flow. LES is naturally more reliable and accurate than traditional RANS modelling for the following two reasons. First, the large scales of turbulence, which most significantly influence the transport of mass, momentum and energy, and which are highly anisotropic and strongly depend on boundary conditions, are explicitly resolved in the simulation. Second, the unresolved small scales tend to be more universal than the large ones (at high Reynolds numbers) and are mainly responsible for dissipating turbulence kinetic energy introduced at the large scales. This makes the unresolved small scales easier to model, compared to having to model the entire range of scales, including the anisotropic large scales, in the RANS approach.

In order to remove the smallest scales from the flow a low-pass filter can be applied to the velocity vector u_i. The filtered velocity vector $\overline{u}_i$ can be defined by

$$\bar{u}_i(\mathbf{x},t) = \int_{-\infty}^{\infty} G(\Delta, \mathbf{x}-\mathbf{x}^{'}) u_i(\mathbf{x}^{'},t) \mathrm{d}^3\mathbf{x}^{'}, \tag{4.1}$$

where $G(\Delta, \mathbf{x}-\mathbf{x}^{'})$ represents a general filter kernel and Δ the filter cut-off length scale. For a box or top-hat filter, for example, the filter function is unity in case $\left|\mathbf{x}-\mathbf{x}^{'}\right| > O(\Delta)$, and zero for the range $\left|\mathbf{x}-\mathbf{x}^{'}\right| < O(\Delta)$. Thus the filtering operation removes all turbulence scales, which are smaller than $O(\Delta)$ and leaves the scales larger than $O(\Delta)$ unmodified. The filter width Δ usually corresponds to a measure of the spatial resolution of the computational grid. It follows that the

unresolved component of the velocity vector is given by $u_i^{'} = u_i - \overline{u}_i$. Thus the velocity field can be decomposed, similarly as in the RANS case, as $u_i = \overline{u}_i + u_i^{'}$. However, $\overline{u}_i$ denotes the filtered velocity vector, which does not correspond to the mean value. Contrary to Reynolds-averaging, double-filtering does not necessarily reproduce the original filtered field, $\overline{\overline{u_i}} \neq \overline{u}_i$. In addition, filtering the unresolved velocity component does not necessarily result in zero, i.e. $\overline{u_i^{'}} \neq 0$.

Substituting the decomposed quantities into the continuity and momentum equation for incompressible flow and filtering the same yields the governing equation for the filtered velocity field

$$\frac{\partial \overline{u}_i}{\partial x_j} = 0, \tag{4.2}$$

$$\frac{\partial \overline{u}_i}{\partial t} + \frac{\partial \overline{u}_i \overline{u}_j}{\partial x_j} = -\frac{1}{\rho}\frac{\partial \overline{p}}{\partial x_i} + \nu \nabla^2 \overline{u}_i - \frac{\partial}{\partial x_j}\left(\tau_{ij}^{LES}\right). \tag{4.3}$$

Note that the filtered non-linear convection term $\overline{u_i u_j}$ can be written as

$$\begin{aligned} \overline{u_i u_j} &= \overline{(\overline{u}_i + u_i^{'}) \cdot (\overline{u}_j + u_j^{'})} \\ &= \overline{u}_i \overline{u}_j + (\overline{\overline{u}_i \overline{u}_j} - \overline{u}_i \overline{u}_j) + (\overline{\overline{u}_i u_j^{'}} + \overline{u_i^{'} \overline{u}_j}) + \overline{u_i^{'} u_j^{'}}, \end{aligned} \tag{4.4}$$

which gives the following expression for the residual subgrid-stress tensor

$$\tau_{ij}^{LES} = (\overline{\overline{u}_i \overline{u}_j} - \overline{u}_i \overline{u}_j) + (\overline{\overline{u}_i u_j^{'}} + \overline{u_i^{'} \overline{u}_j}) + \overline{u_i^{'} u_j^{'}}. \tag{4.5}$$

The residual stress tensor is obviously more complex than in the RANS case (recall that $\tau_{ij}^{RANS} = \overline{u_i^{'} u_j^{'}}$). The additional terms account for the interaction of the resolved flow field with both, the unresolved and resolved flow field.

Comparing the filtered equations with the RANS equations reveals that both approaches result in an un-closed momentum equation due to the appearance of τ_{ij}^{LES} or τ_{ij}^{RANS}. The filtered and mean momentum equations are both derived without specifying or knowing the exact form of the filtering kernel or averaging operation. Therefore, the only difference between both approaches is the magnitude of the unresolved turbulence velocity and length scales. Hence the magnitude of the extra stress-tensor τ_{ij}^{LES} or τ_{ij}^{RANS} determines whether the RANS or filtered momentum equations are recovered.

4.1.1 Subgrid-Scale Modeling

The consequence of the additional term τ_{ij}^{LES} on the right-hand side of (4.3) is that the system of equations is no longer closed. In order to close the system of equations, this term needs to be modelled. It is common practice to model τ_{ij}^{LES} as a whole rather than on a term by term basis. The model needs to account for the effect of the turbulence scales, which are smaller than the grid size Δ onto the resolved flow field. The turbulence models in LES are therefore referred to as Subgrid-Scale (SGS) Model . The smallest scales of turbulence mainly dissipate turbulence kinetic energy by conversion into thermal energy. Therefore, assuming the turbulence structures corresponding to the inertial subrange are well resolved, the SGS model merely has to provide an adequate amount of dissipation such that the energy cascade is correctly reproduced and no energy accumulates at the smallest resolved scales. For this reason, SGS models are usually purely dissipative and do not aim at modelling large amounts of unresolved stress. Within the finite-volume framework used here to solve the governing equations, the truncation error of the numerical discretisation introduces numerical dissipation, which provides an implicit filtering operation and hence additionally drains energy from the resolved flow field. Therefore, in order to ensure a physically consistent energy cascade the overall dissipative effect of the SGS model and numerical framework needs to be optimised.

The SGS stress tensor τ_{ij}^{LES} is frequently modelled using the Boussinesq (1877) approximation, which relates the subgrid-stress tensor to the filtered velocity field using a Newtonian stress-strain relationship and a scalar turbulence viscosity ν_T,

$$\tau_{ij}^{LES} - \frac{1}{3}\mathrm{tr}\left\{\tau_{ij}^{LES}\right\}\delta_{ij} = -2\nu_T \overline{S}_{ij}^{*}. \tag{4.6}$$

The most prominent subgrid-scale model has been proposed by Smagorinsky (1963) and is still used today due to its simplicity. The Smagorinsky model shows close resemblance to Prandtl's mixing length model where the turbulence viscosity is given by

$$\nu_T \propto V_T L_T. \tag{4.7}$$

In the context of LES, the characteristic length scale is assumed to be proportional to the spatial resolution provided by the computational grid, with $L_T = C_S\Delta$, where Δ is frequently determined as the cube root of the cell volume $\Delta = \mathrm{d}V^{1/3}$ or as $\Delta = (\Delta_x\Delta_y\Delta_z)^{1/3}$ for rectangular grids. Note that many other options are possible to determine Δ. The characteristic velocity scale is given by $V_T = L_T\left|\overline{S_{ij}^{*}}\right|$, where $\left|\overline{S_{ij}^{*}}\right| = \sqrt{2\overline{S^{*}}_{ij}\overline{S^{*}}_{ij}}$ is the magnitude of the filtered strain-rate. Hence, the

Smagorinsky model is given by

$$\nu_T = (C_S \Delta)^2 \left| \overline{S_{ij}^*} \right| . \tag{4.8}$$

The constant C_S is usually optimised to provide an inertial subrange energy spectrum for isotropic turbulence. The major shortcoming of the Smagorinsky model is that the constant C_S is, in reality, not universal and strongly depends on the flow under consideration. Moreover, the model is not able to operate in DNS mode, since the SGS model contribution only vanishes for infinitesimally fine grids where $\Delta \to 0$. Consequently, it is not suitable for transitional flows, since the model always returns $\nu_T \geqslant 0$, even in laminar flows. In addition, the Smagorinsky model is purely dissipative and thus does not account for local or instantaneous backscatter of energy from the unresolved to the resolved turbulence fluctuations. Beside the traditional Smagorinsky model many other models exist. Some of them alleviate the difficulties discussed above. The reader is referred to Sagaut (2001) for a comprehensive overview of existing SGS models.

4.1.2 Wall Models

The region very close to the wall in a turbulent boundary layer is populated with longitudinal streamwise structures, which are responsible for the transfer of energy close to the wall. In order to resolve the driving mechanisms of the near-wall turbulence, these streaky structures need to be resolved explicitly in LES and typically require a grid resolution of at least $\Delta_x^+ \approx 100$, $\Delta_z^+ \approx 20$ and $\Delta_y^+ < 2$, where Δ_x^+, Δ_y^+ and Δ_z^+ are respectively the streamwise, wall-normal and spanwise non-dimensionalised grid spacing in wall units (see, for example, Piomelli & Balaras, 2002). On the other hand, in the outer part of the boundary layer the dominant structures scale with the boundary-layer thickness. Piomelli & Balaras (2002) estimated the number of grid points required to adequately resolve the near-wall region to be proportional to $Re^{1.8}$. The resolution requirements for the outer region of the boundary layer was estimated to be proportional to $Re^{0.4}$. Assuming a time-accurate simulation is performed the total computational cost scales as $Re^{0.5}$ for the outer layer and as $Re^{2.4}$ for the inner layer of the boundary layer. The need to resolve the turbulent near-wall structures in LES is considered the major bottleneck of LES in high-Reynolds-number flows. In fact, for wall-bounded flows the required computational resources are not very different from DNS, which currently prohibits the application of LES at high Reynolds number.

In order to make LES applicable for high-Reynolds-number wall-bounded flows the near-wall dynamics cannot be computed explicitly in the simulation and therefore need to be modelled. Performing LES on too coarse a grid in the near-wall region is not an option, since it considerably deteriorates the results. Larsson *et al.* (2007) investigated the performance of LES on coarse grids to predict the fully developed flow in a planar channel. It was shown that the skin-friction coefficient was in error by up to 40%. This is, because subgrid-scale models are generally not designed to model a significant amount of the unresolved stress, which is required on too coarse grids. The only way to reduce the cost of LES in high-Reynolds-number wall-bounded flows is to employ suitable approximations to model the near-wall region altogether. One approach to wall-modelled LES (WMLES) is to use wall functions, which bridge the near-wall region of a turbulent boundary layer. Thereby, the first grid point can be placed in the log-layer ($y^+ > 30$) and the mean or instantaneous velocity can be related to the wall shear-stress based on log-law relations. This idea is analogous to wall functions in RANS modelling. The wall function approach works fairly well for attached boundary layers and flows in equilibrium. For complex flows with strong wall curvature and pressure gradient, and for separated flows, the log-law assumptions do not hold.

More sophisticated wall models, which do not rely on log-law assumptions, are so called Two-Layer Models (see, for example, Balaras & Benocci, 1994). Thin Boundary Layer Models (TBLM) belong to this class of wall models and are based on a set of simplified boundary-layer equations, which are solved on a separate grid embedded between the first LES grid point and the wall and which employ an algebraic wall-damped eddy-viscosity RANS model. Particularly for flows departing from the log-law assumptions, this approach may help to provide improved predictions. The results of TBLM models could obviously be further improved if the thin-boundary-layer equations and the mixing length model were replaced by a RANS layer near the wall, combined with a state-of-the-art RANS model. Such hybrid RANS/LES approaches will be discussed in more detail in the subsequent chapter. The interested reader is referred to Piomelli & Balaras (2002), Cabot & Moin (1999) and Sagaut (2001) for a more comprehensive review of existing wall-models in LES.

4.2 Statistically Unsteady Turbulence Modelling

The group of Statistically Unsteady Turbulence Modelling (Sagaut *et al.*, 2006) or second-generation Unsteady-RANS approaches (Froehlich & von Terzi, 2008) are

formally based on the RANS paradigm. These approaches are distinctly different compared to other LES and hybrid RANS/LES approaches, since they do not incorporate a grid-dependent filter width Δ in the model equations. Nevertheless, some of these approaches are able to fully resolve turbulence structures up to the grid limit.

4.2.1 Unsteady RANS

In the RANS approach, as discussed in chapter 3, all variables are decomposed into a mean and fluctuating part and Reynolds averaging is performed in order to derive governing equations, which describe the evolution of the mean-flow field. In statistically stationary flows, with no time variation of the mean flow, the Reynolds averaging corresponds to a time-average operator, where the averaging time has to be significantly larger than the characteristic turbulence time scale.

It is possible to solve the RANS equation in a time-accurate fashion. The application of time-accurate or unsteady RANS (URANS) is particularly justified in situations where unsteady boundary conditions, such as time dependent inflow conditions or body motion, impose a low-frequency unsteadiness on the mean-flow field. The time variation of the mean-flow field has to be significantly slower than the characteristic turbulence time scale, or in other words, there needs to be a clear separation (or spectral gap) between the mean and turbulence time scale. Under such conditions, the Reynolds averaging and equilibrium calibration of the RANS models for statistically steady-state flows remain valid, and URANS is justified. There are other situations, for example, in bluff body flows with massive separation, where URANS will resolve some unsteadiness, which is triggered by strong, internal instability mechanisms of the flow. The resolved large-scale flow structures, directly interact and influence the mean flow and are not distinguishable from real turbulence, i.e. there is no spectral gap between the resolved large-scale structures and turbulence fluctuations. As a consequence, the RANS equations are formally not applicable in this situation. In addition, the calibration procedure of the closure constants in the RANS model, which aim at reproducing mean-flow quantities of a statistically steady-state flow, becomes questionable. Nevertheless, it has been shown in Shur *et al.* (2005) and Travin *et al.* (2004*a*), that when URANS is applied in a three-dimensional computational domain, as it is used in LES, improved predictions can be obtained over steady RANS or even 2D-URANS. The improvements are related to the capability of URANS to explicitly resolve the dominant three-dimensional flow structures, which directly interact and influence the mean flow.

For unsteady flows which contain an organised, periodic motion, the Reynolds decomposition can be extended to a triple decomposition. Following the proposal of Hussain & Reynolds (1970), the decomposition for the velocity vector can be written as

$$u_i = \overline{u}_i + \widetilde{u}_i + u_i^{'}, \tag{4.9}$$

where $\overline{u}_i$ is the time-mean value, $\widetilde{u}_i$ is the contribution of the organised motion, and $u_i^{'}$ is the random, fluctuating part of turbulence. The organised part is equivalent to $\widetilde{u}_i = \langle u_i \rangle - \overline{u}_i$, where the brackets $\langle . \rangle$ correspond to a phase-average procedure or a conditional ensemble average at the same phase, that occurs at the time intervals $t_n = nT$, where T is the time-cycle of the periodic motion. Based on the triple decomposition of variables Reynolds & Hussain (1972) derived the conservation equations for the mean velocity $\overline{u}_i$ and for the organised motion $\widetilde{u}_i$. It is shown, that the resulting mean-momentum equations contain the Reynolds stress $-\overline{u_i^{'} u_j^{'}}$, which accounts for the interaction of the turbulence with the mean flow, and additionally, the Reynolds stress $-\overline{\widetilde{u}_i^{'} \widetilde{u}_j^{'}}$ of the organised motion, which accounts for the interaction of the organised motion with the mean flow.

An alternative to the triple decomposition is the decomposition into coherent and incoherent part according to $u_i = u_i^c + u_i^{ic}$. The coherent part correspond to the organised motion and the incoherent part to the small scale turbulence fluctuations. The coherent part, $u_i^c = \overline{u}_i + \widetilde{u}_i$, is directly computed from the phase-averaged Navier-Stokes equations and the incoherent part, $u_i^{ic} = u_i^{'}$, is modelled using a RANS closure. Note that the phase-averaged conservation equations are identical to the URANS equations. Nevertheless, the modelled contribution is different between both approaches, since the length and time scales are not the same (see Sagaut *et al.*, 2006). The decomposition into a coherent and incoherent part is also referred to as the Semi-Deterministic Method or Organized-Eddy Simulation.

The RANS closure aims at modelling the effects of the entire spectrum of turbulence on the mean flow and hence, all turbulence kinetic energy is statistically represented by the RANS model. In a resolved flow field, with small scale turbulence, the length-scale-providing equation of traditional RANS closures does not produce the correct length-scale or dissipation rate. The reason being, that the length-scale-providing equation does not contain any information about the grid spacing, nor is sensitive to the resolved turbulence length scales present in the flow. Thus, in situations with explicitly resolved turbulence fluctuations and resolved turbulence kinetic energy, the contribution of the turbulence model has to be reduced and only a fraction of the turbulence kinetic energy needs to be statistically represented

by the turbulence model. This is not the case for traditional RANS models and the reason why URANS models are overly diffusive and damp most of the flow unsteadiness associated with resolved turbulence fluctuations. Again, the main problem of traditional URANS is, that the length-scale-providing equation does not produce the correct length-scale or turbulence dissipation rate when the resolution of the computational grid is fine enough to allow for an explicitly resolved flow field. This is an artefact of the calibration procedure, which aims at reproducing mean-flow quantities of the flow. For example, homogeneous shear flow is used to calibrate the length-scale-providing equation. For homogeneous shear flow the transport equations for the turbulence kinetic energy and turbulence dissipation rate reduce to

$$\frac{\mathrm{d}k}{\mathrm{d}t} = P_k - \epsilon, \quad \frac{\mathrm{d}\epsilon}{\mathrm{d}t} = C_{\epsilon_1}\frac{\epsilon}{k}P_k - C_{\epsilon_2}\frac{\epsilon^2}{k}. \tag{4.10}$$

In the limit of an asymptotic equilibrium state, the time scale k/ϵ and turbulence production to dissipation ratio P_k/ϵ, amongst others, reach constant values. The equations above can be combined to yield

$$\frac{\mathrm{d}}{\mathrm{d}t}\left(\frac{k}{\epsilon}\right)_\infty = \left(1 - C_{\epsilon_1}\right)\frac{P_k}{\epsilon} - \left(1 - C_{\epsilon_2}\right) = 0. \tag{4.11}$$

This may be rewritten in the following form

$$\left(\frac{P_k}{\epsilon}\right)_\infty = \frac{C_{\epsilon_2} - 1}{C_{\epsilon_1} - 1}. \tag{4.12}$$

The closure coefficients of the 'standard' k-ϵ model (Jones & Launder, 1972) yields a turbulence production to dissipation ratio $(P_k/\epsilon)_\infty = 2.1$. It is shown in Girimaji *et al.* (2006) that the ratio of unresolved to total turbulence kinetic energy k_{sgs}/k approaches almost unity, independent of the initial conditions, as a long-time behaviour. This has the consequence that any initially well-resolved flow field with small-scale turbulence, where the modelled turbulence kinetic energy k_{sgs} is small, will eventually approach a state where all fine scale turbulence in the flow field is eliminated and most of the turbulence kinetic energy is contained in the modelled contribution k_{sgs}. This long-time behaviour of the URANS equations is linked to a too high value of the turbulence kinetic energy production to dissipation ratio of $(P_k/\epsilon)_\infty = 2.1$. In case of resolved turbulence content in the flow field, most of the production P_k directly increases the velocity fluctuations and hence the resolved turbulence kinetic energy and only a small part increases the unresolved (modelled) turbulence kinetic energy, i.e. $P_{k_{sgs}} < P_k$. Since $\epsilon_{sgs} = \epsilon$ in situations where the

dissipative scales are not explicitly resolved, it follows that the turbulence production to dissipation ratio of the modelled scales $P_{k_{sgs}}/\epsilon_{sgs}$ has to be smaller than the URANS value, i.e. $P_{k_{sgs}}/\epsilon_{sgs} < P_k/\epsilon$. Relation (4.12) is particularly useful, since it reveals possible routes to modify the URANS equation in order to resolve or sustain turbulence. The key issue here is that the production to dissipation ratio needs to be reduced by suitable modifications. One possibility is to increase the dissipation rate by employing an inertial range scaling of the form $\epsilon \propto k^{3/2}/\Delta$. This is, for example, the idea of Detached Eddy Simulation based on a two-equation model, which will be discussed in section 4.3. Alternatively, the turbulence production P_k can be reduced by applying a damping function to the Reynolds-stress tensor or the turbulence viscosity. This is, for example, the idea of the Flow Simulation Methodology (see discussion in section 4.3). A third possibility is based on modifying the closure constant C_{ϵ_2}. For example, for $C_{\epsilon_2} = C_{\epsilon_1}$ the URANS equation will operate in DNS mode where any turbulence model contribution will vanish. This forms the basis of the Partially-Averaged Navier-Stockes approach of Girimaji (2006) and the Partially-Integrated Transport Model of Schiestel & Dejoan (2005).

4.2.2 Scale-Adaptive Simulation

The Scale-Adaptive Simulation (SAS) methodology is formulated based on the k-kL_I model of Rotta (1968) where, L_I is the turbulence integral length scale and k the turbulence kinetic energy. In the original attempt of Rotta (1968) to model the exact kL_I equation a sink term was introduced, which contained the third derivate of the velocity field. Menter *et al.* (2003) (see also Menter & Egorov, 2010) have proposed a new model for this term, which includes the second derivative of the velocity field. The sensitivity of the length-scale providing equation to the second derivative of the velocity field introduces some remarkable features to the k-kL_I model. For flows with sufficiently strong instabilities the model contribution is automatically reduced and fine-scale turbulence structures are allowed to develop up to the grid limit, without any explicit grid dependency, as in LES. On the other hand, for flows with only weak instabilities the model operates in RANS mode. The capability to automatically adapt the model contribution to the turbulence length scales present in the flow is highly desirable, since it will eventually revert back to RANS mode when the spatial or temporal resolution is insufficient to support the explicit resolution of turbulence structures. None of the present LES methodologies or other hybrid RANS/LES formulations provides such capabilities and instead

require that the spatial and temporal resolution is sufficient to support the resolution of turbulence scales well within the inertial subrange. If this is not case, the predictive accuracy of LES will deteriorate.

The SAS concept is not limited to the kL_I scale providing equation. It can also be used with, for example, the specific turbulence dissipation rate ω. Menter & Egorov (2005) have transformed the k-kL_I formulation to a formulation based on the k-ω-SST model. The consequence of this transformation is the appearance of a new source term P_{SAS} in the equation for the specific turbulence dissipation rate, thus the k and ω equations are given by

$$\frac{Dk}{Dt} = P_k - \beta^* k\omega + \frac{\partial}{\partial x_j}\left[(\nu + \sigma_k \nu_T)\frac{\partial k}{\partial x_j}\right], \tag{4.13}$$

$$\frac{D\omega}{Dt} = \gamma\frac{\omega}{k}P_k + P_{SAS} - \beta\omega^2 + \frac{\partial}{\partial x_j}\left[(\nu + \sigma_\omega \nu_T)\frac{\partial \omega}{\partial x_j}\right] + 2(1-F_1)\sigma_{\omega 2}\frac{1}{\omega}\frac{\partial k}{\partial x_i}\frac{\partial \omega}{\partial x_i}. \tag{4.14}$$

The additional source term has been modified since the very first proposal. Here, the formulation given in Egorov & Menter (2007) is used. The source term takes the from

$$P_{SAS} = \max\left[\zeta_2 \kappa S^2 \left(\frac{L_T}{L_{vK}}\right)^2 - C\frac{2k}{\sigma_\Phi}\max\left[\frac{1}{\omega^2}\frac{\partial \omega}{\partial x_j}\frac{\partial \omega}{\partial x_j}, \frac{1}{k^2}\frac{\partial k}{\partial x_j}\frac{\partial k}{\partial x_j}\right], 0\right], \tag{4.15}$$

where $S = \sqrt{2S_{ij}S_{ij}}$ and $L_T = k^{1/2}/\left(C_\mu^{1/4}\omega\right)$. The SAS formulation was tested on decaying homogeneous isotropic turbulence and it was found that the model is not dissipative enough and results in an artificial accumulation of energy at the smallest resolved scales. As a consequence, the v. Karman length scale L_{vK}, which contains the second derivative of the velocity field, had to be limited to be no smaller than the minimum resolvable scales, which are of the order of the grid spacing $\Delta = \mathrm{d}V^{1/3}$. Thus the limited v. Karman length scale is given by

$$L_{vK} = \max\left[\frac{\kappa S}{|\nabla^2 U|}, C_{SAS}\sqrt{\frac{\kappa\zeta_2}{\frac{\beta}{\beta^*} - \gamma}}\Delta\right], \tag{4.16}$$

where C_{SAS} is a calibration constant, which depends on the discretisation scheme. For the commercial Ansys CFX solver the constant is given as $C_{SAS} = 0.11$. The other extra closure coefficients of SAS are given by $\zeta_2 = 3.51$, $\sigma_\Phi = 2/3$ and $C = 2$.

Davidson (2006) has evaluated the performance of SAS based on the k-ω-SST model compared to steady and unsteady RANS predictions for the flow in planar channel,

asymmetric plane diffuser and around a three-dimensional axisymmetric hill. For the flow in the diffuser the SAS model was found to perform worse than the URANS model. It was argued that in this specific case the SAS model operates in a grey area, where the model is neither in RANS nor in LES mode. The axisymmetric hill was poorly predicted by all models. In both cases the turbulence viscosity was over predicted compared to other hybrid RANS/LES methods. Egorov *et al.* (2010) conducted a similar study and compared SAS to steady and unsteady RANS predictions for a range of applications of practical interest. It was found that SAS may provide improved prediction over steady and unsteady RANS predictions for the range of test cases considered.

4.2.3 Turbulence-Resolving RANS

A Turbulence-Resolving RANS (TRRANS) formulation has been presented in Travin *et al.* (2004*a*). TRRANS is a simple modification to Wilcox's k-ω RANS turbulence model, which effectively lowers the predicted turbulence viscosity and hence allows for turbulence fluctuations to develop. In the equation for the turbulence kinetic energy the turbulence dissipation rate is modelled as

$$\epsilon^{TRRANS} = (\beta^* \omega k) \cdot \max\left[1, \left(\frac{\left|S^*_{ij}\right|}{C_T \left|\Omega^*_{ij}\right|}\right)^2\right], \tag{4.17}$$

with the strain-rate and vorticity magnitude $\left|S^*_{ij}\right|$ and $\left|\Omega^*_{ij}\right|$, respectively. Depending on the ratio of strain-rate to vorticity magnitude, the dissipation of turbulence kinetic energy k is increased. This has the consequence that the magnitude of k and the resulting turbulence viscosity is reduced. The ratio of strain-rate to vorticity magnitude controls whether the turbulence dissipation is increased above the RANS level. For example, in thin shear flows where $\left|S^*_{ij}\right| \approx \left|\Omega^*_{ij}\right|$ or in general, where $\left|S^*_{ij}\right| \ll \left|\Omega^*_{ij}\right|$ the TRRANS formulation operates in RANS mode. In strain dominated flows where $\left|S^*_{ij}\right| \gg \left|\Omega^*_{ij}\right|$ the turbulence dissipation is increased and TRRANS operates in a LES-type mode. The constant C_T is calibrated to provide the correct amount of dissipation in decaying homogeneous isotropic turbulence and is given as $C_T = 1.25$.

Travin *et al.* (2004*a*) applied the TRRANS formulation to a range of test cases, such as boundary layers, an airfoil at 45° angle of attack, a cylinder with laminar separation and a backward facing step. The results of TRRANS, when applied to a boundary layer, is consistent with a steady RANS solution. The flow around the

airfoil and cylinder are qualitatively similar to the results of other hybrid RANS-LES methods. However, for the backward facing step TRRANS was not able to sustain any turbulence fluctuations and converged to a steady 2D solution. This is a somewhat disappointing result, because other hybrid methods perform well for this test case.

4.2.4 Partially-Averaged Navier-Stokes

The Partially-Averaged Navier-Stokes (PANS) model was proposed by Girimaji (2006) and Girimaji *et al.* (2006) and employs two resolution control parameters, namely the ratio of unresolved to total turbulence kinetic energy $f_k = k_{sgs}/k$ and the ratio of unresolved to total turbulence dissipation rate $f_\epsilon = \epsilon_{sgs}/\epsilon$ to control the damping or extent of partial averaging employed in the RANS model. For $f_k = 1$, PANS is consistent with full statistical modelling (RANS) and for $f_k = 0$, the contribution from the RANS model vanishes and PANS is operating in the DNS limit. The result of the partial averaging are transport equations, which govern the evolution of the unresolved turbulence kinetic energy k_{sgs} and turbulence dissipation rate ϵ_{sgs}. The effect of partial averaging, which is determined by the resolution control parameters, is limited to the closure coefficients of the transport equations and does not change the constitutive relations of the RANS model. For a k-ϵ model the closure coefficient $C_{\epsilon 2}$ is replace by $C_{\epsilon 2}^{PANS} = C_{\epsilon 1} + f_k\,(C_{\epsilon 2} - C_{\epsilon 1})$. In the original PANS formulation, appropriate values for the parameters f_k and f_ϵ had to be specified prior to the simulation and were assumed constant in the entire domain. For a resolution with a cut-off wavenumber within the inertial subrange, the parameter f_ϵ is set to unity and f_k is the only relevant parameter. This makes the implementation of PANS into an existing RANS solver straightforward and only requires to change the value of $C_{\epsilon 2}$. Later extensions to PANS redefine the resolution control parameter f_k to be a function of the grid spacing Δ (see, for example, Abdol-Hamid & Girimaji (2004), Elmiligui *et al.* (2004) and Song & Park (2009)). PANS has also been extended to the k-ω model framework (see Lakshmipathy & Girimaji, 2006). For k-ω models the closure constant β has to be replaced by $\beta^{PANS} = \gamma\beta^* - f_k(\gamma\beta^* + \beta)$. The PANS approach seems very appealing, since the subgrid-scale turbulence dissipation rate ϵ_{sgs} is obtained from a transport equation and not from an algebraic relation of the form $\epsilon_{sgs} \propto k^{3/2}/\Delta$, as used in many subgrid-scale models. The transport equation is believed to be superior over the algebraic relations, since it naturally includes effects such as production, dissipation and transport of the subgrid-scale turbulence dissipation rate ϵ_{sgs}. It is difficult to assess

the performance of the PANS approach, since the number of test and validation cases are very limited or do not allow for a rigorous comparison with reference data.

4.3 Overview of Hybrid RANS/LES Methods

In this section a review of some existing hybrid RANS/LES methodologies will be presented. All of these methodologies aim at reducing the cost of LES in the near-wall region and hence make LES applicable for high-Reynolds-number wall-bounded flows. Since large parts of the flow are explicitly resolved, hybrid RANS/LES methods are expected to be naturally more accurate in predicting complex flows compared to traditional RANS closures.

All hybrid RANS/LES methods can be grouped into two different categories. In this work the terminology of Froehlich & von Terzi (2008) is adopted where hybrid RANS/LES methods are classified as 'unified' and 'segregated' approaches. Another possibility is to group hybrid RANS/LES methods into 'global' and 'zonal' hybrid RANS/LES approaches (see, for example, Sagaut *et al.*, 2006). Unfortunately, the word 'zonal' is not used consistently in the literature and the classification of Froehlich & von Terzi (2008) is therefore preferred.

Segregated hybrid RANS/LES approaches

In segregated modelling the computational domain is divided into different sub-zones in which the different modelling concepts, RANS or LES, are applied. In addition to switching the underlying turbulence modelling concept it is also possible to switch the numerical discretisation or solver strategy. In this way, the sub-zones can be tailored to the flow problem under consideration such that RANS is applied in regions where it is expected to provide reliable predictions and that LES is applied in regions with complex flow or where the RANS model is expected to provide an insufficient representation of the flow. In addition, higher-order low-dissipation schemes can be used in the LES region and a more robust scheme with increased levels of numerical dissipation in the RANS zones. For complex three-dimensional computational domains with multiple bodies, decomposing the domain into suitable sub-zones is not a trivial task at all and may explain why segregated modelling, despite some theoretical advantages over unified modelling, is currently not supported by any commercial CFD code.

In contrast to unified modelling, segregated modelling is based on an entirely discontinuous treatment of flow variables, for example, the velocity field across the

interface. Even though the zones are formally treated segregated of each other, information needs to be exchanged across the interface in both directions. Therefore, the exchange of information across the interface and specifying appropriate boundary conditions to each zone are the key issues in segregated hybrid RANS/LES approaches.

The main problem of specifying inflow boundary conditions for an LES zone downstream of a RANS zone is that the RANS zone only provides mean flow quantities. The LES approach, in turn, relies on the existence of resolved turbulence fluctuations. Consequently the LES inflow conditions are prescribed by using mean flow quantities from the RANS zone and superimposing turbulent fluctuations to yield time-dependent boundary conditions. The influence of inflow conditions was, amongst others, studied by Aider & Danet (2006), where the importance of boundary conditions with realistic turbulence structures was demonstrated. The influence of unphysical boundary conditions can persist for a long downstream distance and may deteriorate the results. Therefore, considerable effort has been put into the development of techniques to create physically realistic turbulent fluctuations at LES inflow boundaries. For an overview of existing techniques the reader is referred to Sagaut (2001) and Sagaut *et al.* (2006). Appropriate inflow boundary conditions for a RANS zone downstream of an LES zone are usually obtained by calculating averaged/mean quantities in the LES zone. These quantities are then used as inflow boundary conditions for the RANS zone. A complete specification of boundary conditions to the RANS zone also requires boundary conditions for the transported quantities used in the turbulence model. The evaluation of the turbulence dissipation rate ϵ based on LES quantities is not straightforward. A robust alternative would be to solve the turbulence model equations in the LES zone using mean flow quantities (see Quemere & Sagaut, 2002). This method, however, is not able to conserve the total (modelled plus resolved) turbulence kinetic energy of the LES zone across the interface.

Appropriate outflow conditions for the LES zone are also important. It is shown in Schluter & Pitsch (2001) that the LES outflow boundary condition may have an impact on the entire flow field in the LES zone. The outflow boundary conditions of the LES zone needs to be designed such that it allows information from a downstream RANS zone to propagate upstream into the LES zone. Schluter & Pitsch proposed a method to match the mean-flow quantities of the LES zone to a RANS solution in an overlap region using an additional body force in the momentum equations. It is also important that the LES outflow boundary conditions do allow fluctuations to leave the domain without giving rise to spurious reflections.

The issue of specifying outflow conditions for the RANS zone is very similar to that of an LES outflow boundary. The outflow boundary condition needs to allow information about the mean-flow from the downstream LES zone to travel upstream. Celic (2004) suggested a RANS outflow condition similar to the outflow condition for LES, where a body force is applied in a forcing region to match RANS quantities with averaged/mean LES quantities.

Unified hybrid RANS/LES approaches

The characteristic feature of all unified hybrid RANS/LES approaches is that the flow quantities are continuous across the RANS/LES interface. The switch from RANS to LES can be achieved by modifying the underlying RANS model to a subgrid-scale model or by altering terms in the turbulence model formulation. The switching may be controlled by blending functions or by comparing characteristic quantities such as the turbulence length scale and grid spacing or the magnitude of different turbulence viscosity norms. The switching location may even be pre-determined, similar to the segregated approaches. The difference of unified approaches compared to segregated modelling is that no boundary conditions are specified at the interface location between RANS and LES zones and vice versa. Instead, the resolved flow propagates by convection and diffusion across the interface.

This has the consequence that, for example, an LES zone downstream of RANS zone is not supplied with resolved turbulence fluctuations. Therefore, the spectrum of turbulence scales has to be generated in the LES zone by natural instability mechanisms of the flow. This leads to the existence of a 'grey area' where the hybrid approach reduces the model contribution to an LES level but resolved turbulence (resolved stress) does not yet exist to compensate the reduction of modelled stress. Obviously, the weaker the instability mechanisms in the flow the longer it takes to generate resolved turbulence fluctuations. The segregated approach alleviates the existence of grey areas, since appropriate boundary conditions are specified at the LES inflow boundary, which contain turbulence fluctuations superimposed onto the mean flow.

4.4 Comments on Unified RANS/LES Methods

In hybrid RANS/LES modelling different possibilities exist how the cost of LES in the near-wall region can be alleviated. The first and most rigorous one is to treat the entire attached boundary layer in RANS mode and to switch to LES mode

outside the boundary layer. The second option is to initiate the switch from RANS to LES close to the wall such that only the near-wall region is treated as RANS and the outer layer of the boundary layer is treated in LES mode, thus functioning as WMLES. This seams reasonable due to a week Reynolds number scaling ($Re^{0.5}$) of the computational cost in the outer layer of the boundary layer.

A common flaw shared by all unified hybrid RANS/LES methods is the existence of a 'grey area' where the model switches form RANS to LES modelling. Grey areas are mainly an issue if the entire attached boundary layer is treated in RANS mode and not so much for WMLES where turbulence is resolved in the outer region of the boundary layer. If the entire boundary layer is modelled in RANS mode no resolved turbulence fluctuations exist and all turbulence kinetic energy is statistically represented by the RANS model. As the hybrid model switches to LES mode the model contribution reduces and turbulence is allowed to develop. Since the RANS layer does not contain any turbulence fluctuations, natural instability mechanisms transfer energy into resolved turbulence fluctuations, which will eventually result in fully developed turbulence. Therefore, modelling the entire boundary layer in RANS mode is particularly justified in the presence of strong instability mechanisms, which quickly generate resolved turbulence and hence limits the extent of the grey area. Examples of such flows include cavities, wakes, massive separation and so on. In cases where only weak stability mechanisms exist, the transition from a RANS to LES flow field will be comparably slower and the flow may take a long time to generate turbulence fluctuations, which compensate the reduction of modelled stress. For such scenarios WMLES seem better justified.

Using a unified hybrid RANS/LES method to provide WMLES capabilities is also not trouble free. Since the near-wall region is treated in RANS mode the energy-producing events close to the wall, which generate and transfer turbulence kinetic energy into resolved turbulence fluctuations, is suppressed by the RANS model. Consequently, the LES region away from the wall is not fed with these resolved, energy-carrying turbulent structures. Again, switching the model from RANS to LES mode and the associated reduction of modelled stress does not imply an instantaneous change of resolved turbulence fluctuation at the switching location. The reduction of modelled Reynolds-stress is not instantly compensated for by resolved turbulence fluctuation (resolved stress). The result is a drop of total (modelled+resolved) stress. It was shown in Nikitin *et al.* (2000) that the switch from RANS to LES mode inside the boundary layer causes an under-prediction of the skin friction coefficient by about 15%. In addition the mean-velocity profile exhibited a modelled log layer (from the RANS model) and a resolved log layer predicted by the

LES model. Unfortunately, the modelled and resolved log-layer show a mismatch of several u^+ units compared to DNS data. Similarly, Baggett (1998) investigated the fully developed channel flow at $Re_\tau = 1000$ using a WMLES hybrid RANS/LES approach. Unrealistically high velocity fluctuations close to the wall combined with unphysically large streamwise vortices and streaks were observed near the wall. Consequently, it was claimed that merging RANS and LES in the near-wall region is unlikely to be successful where an accurate mean flow and accurate turbulence statistics are required. Piomelli *et al.* (2003) investigated the sensitivity of the resolved log layer depending on the interface location between RANS and LES. It was found that when the interface was moved closer to the wall, the resolved log layer was also shifted closer to the wall. The unphysical near-wall turbulence structure could not be removed completely. Subsequent attempts to eliminate the log-layer mismatch are based on superimposing turbulence fluctuations at the interface with the purpose of providing improved physical boundary conditions to the LES region and disrupting the development of unphysical large structures close to the wall. A large range of subsequent studies have examined the effect of adding turbulence fluctuations at the interface location when RANS is used to bridge the near-wall region. This approach has been effective in reducing the log-layer mismatch. The interested reader is referred to Cabot & Moin (1999), Dahlstrom & Davidson (2003), Batten *et al.* (2003, 2004), Piomelli *et al.* (2003), Davidson & Billson (2006), Benarafa *et al.* (2006), Hamba (2003, 2006), Keating & Piomelli (2006) or Larsson *et al.* (2006) for further details.

4.5 Unified Hybrid RANS/LES Methods

4.5.1 Blending Approaches

Blending approaches in hybrid RANS/LES have been published in various forms. The most general form of the blending approach is a linear combination of RANS and LES quantities according to $\phi^{hybrid} = F\phi^{RANS} + (1 - F)\phi^{LES}$, where F is a blending function. The arbitrary quantity ϕ may stand for the modelled stress tensor τ_{ij}, the turbulence viscosity ν_T or the transport equation for the turbulence kinetic energy k and its dissipation rate ϵ.

Baurle *et al.* (2003) used the blending technique of Menter to construct a linear combination of a one-equation subgrid-scale model and RANS turbulence model. In addition to blending the equations for the turbulence kinetic energy, the turbulence

viscosity is blended as well. Using the blending function F_1 or F_2 proposed by Menter enforces a transition from RANS to LES away from the wall even though the grid is too coarse to support LES. To avoid a switch in areas where the grid cannot support LES the blending function is modified, inspired from Limited-Numerical-Scales by Batten *et al.* (2002) (see discussion following later in this chapter). This modification ensures that the RANS equations are retained if the SGS viscosity is greater than the RANS viscosity. The blending function is given by

$$F = \max\left[\tanh(\eta^4), F_{LNS}\right], \tag{4.18}$$

where $\eta = \max\left[L_T/d, 500\nu C_d L_T/\left(d^2 k^{1/2}\right)\right]$ and $F_{LNS} = \min\left[\nu^{SGS}/\nu^{RANS}, 1\right]$. Baurle *et al.* applied this blending approach to incompressible Poiseulle flow, supersonic base flow and supersonic flow over a cavity and observed improved accuracy in the prediction over traditional RANS models.

Xiao *et al.* (2004) used a blending function to combine a one-equation subgrid-scale model with a k-ζ (enstrophy) model. In addition to blending the transport equations, the turbulence viscosity is blended as well. Three different blending functions were proposed. The first blending function is designed to be explicitly independent of the grid and the geometry and takes the form $F_{vK} = \tanh(l_{vK}/\alpha_1\lambda)^2$, where L_{vK} is the von Karman length-scale and $\alpha_1\lambda$ is proportional to the Taylor microscale. The second blending function explicitly depends on the distance to the nearest wall, $F_d = \tanh(d/\alpha_1\lambda)^2$. The third blending function explicitly depends on the grid resolution, $F_\Delta = \tanh(L_T/\alpha_2\Delta)^2$. The constants α_1 and α_2 where chosen such that the blending functions reach a value of 0.5 in the log-law region. The blending approach was tested for the compressible flow over a compression ramp and a compression-expansion corner and partly improved the predictions compared to the unmodified k-ζ turbulence model.

The blending function approach has also been used by Abe (2005) and Inuzuka & Abe (2007) to combine an anisotropy-resolving eddy-viscosity turbulence model with a SGS model. Both use a blending of the Reynolds-stress tensor and the subgrid-stress tensor. The following blending function is used:
$F = 1 - \exp\left[-\left(y/\left(C_{hb}\Delta\right)\right)^6\right]$, where $C_{hb} = 4.0$ and $\Delta = \sqrt{\max\left(\Delta_x\Delta_y, \Delta_y\Delta_z, \Delta_z\Delta_x\right)}$.
Both applied the hybrid method to fully developed plane channel flow. It was shown that anisotropy-resolving turbulence models are effective in improving the prediction of the near-wall anisotropy and the accuracy of the total Reynolds-stress tensor (resolved plus modelled.)

Baggett (1998) has examined the feasibility of supplementing a SGS model with a RANS model in the near-wall region using a blending approach. Two different formulations were suggested

$$\tau_{ij} - \frac{1}{3}\tau_{kk}\delta_{ij} = -\left[(1-F)\,\nu_T^{SGS} + F\nu_T^{RANS}\right]\overline{S}_{ij}^{*}, \tag{4.19}$$

and

$$\tau_{ij} - \frac{1}{3}\tau_{kk}\delta_{ij} = -\nu_T^{SGS}\left[\overline{S}_{ij}^{*} - (1-F)\left\langle\overline{S}_{ij}^{*}\right\rangle\right] - F\nu_T^{RANS}\left\langle\overline{S}_{ij}^{*}\right\rangle, \tag{4.20}$$

where ν_T^{SGS} is determined from the dynamic Smagorinsky model and ν_T^{RANS} is determined from the $\overline{v}^2$-f model of Durbin (1995a). The angle brackets $\langle\rangle$ denotes a time-averaged quantity. Baggett tested the proposed models using channel flow at $Re_\tau = 1000$. No specific form of the blending function F has been proposed, instead Baggett estimated the blending function using a mean momentum balance prior to the simulation. The blending function ensures that for $F = 0$, LES is recovered and for $F = 1$, RANS is recovered. The results of Baggett show improved mean-flow results. However, the turbulence velocity fluctuations close to the wall were found to be far too high and are combined with an artificial near-wall structure with streamwise streaks too large in spanwise direction.

A similar approach was proposed by Uribe *et al.* (2010) where a blending of the following form is used

$$\tau_{ij} - \frac{1}{3}\tau_{kk}\delta_{ij} = -2\nu_T^{SGS}F\left[\overline{S}_{ij}^{*} - \left\langle\overline{S}_{ij}^{*}\right\rangle\right] - 2(1-F)\nu_T^{RANS}\left\langle\overline{S}_{ij}^{*}\right\rangle. \tag{4.21}$$

The turbulence viscosity ν_T^{SGS} is computed from the Smagorinsky model using the fluctuating strain-rate tensor $(\overline{S}_{ij}^{*} - \left\langle\overline{S}_{ij}^{*}\right\rangle)$ and ν_T^{RANS} is obtained from an elliptic-relaxation RANS model. The first term on the right-hand side contains the fluctuating strain-rate tensor, which in the mean does not contribute to the Reynolds-stress tensor. The second term on the right-hand side is evaluated using the mean strain-rate tensor and hence determines the mean shear stress and velocity profile. The blending function needs to be designed such that it approaches unity where the resolution of the computational grid is sufficient to resolve most of the turbulence fluctuations (away from the walls) and is zero in regions where the flow is under-resolved, such as close to the wall. The blending function used in Uribe *et al.* (2010) is given by $F = \tanh\left(C_l L_T/\Delta\right)$. Encouraging results have been obtained for the separated flow over a trailing edge and for planar channel flow up to $Re_\tau = 4000$. The channel flow results did not show the commonly observed log-layer mismatch.

4.5.2 Layering RANS and LES

The concept of layering RANS and LES is inspired by the two-layer wall model for LES, as discussed in section 4.1.2, where the thin-boundary-layer equations are replaced by a RANS layer and a state-of-the-art RANS turbulence model. In the hybrid RANS/LES approach the grid is split up into two different regions. This is either done by specifying a separating grid line prior to the simulation or by using an adaptive interface location, which adjusts itself in the course of the simulation.

Davidson & Peng (2003) use a one-equation SGS model and a k-ω RANS model. A pre-selected grid line determines the switching location. The grid line is chosen such that the switch occurs in the log-region of the attached boundary layer. At the switching location y^* an additional constraint is placed on ω, namely $\partial\omega/\partial y|_{y^*} = 0$. The results for a fully developed planar channel flow show the typical unphysical kink in the mean-velocity profile at the interface location. Results were also obtained for the flow over periodic 2D hills in a channel, which predicted the correct velocity field with moderate success.

Hamba (2003) has observed that the turbulence viscosity drops sharply at the interface location from a high RANS level to the much lower LES level. In order to avoid this problem Temmerman *et al.* (2005) and Tessicini *et al.* (2006) placed the constraint $\nu_T^{LES,mod} + \nu_T^{LES,res} = \nu_T^{RANS,mod} + \nu_T^{RANS,res}$ on the turbulence viscosity at the interface. Therefore, the following relation must hold at the interface: $C_{\mu,int} = \nu_T^{LES,mod}/(f_\mu k^2/\epsilon)$ or in the mean, $\langle C_{\mu,int}\rangle = \left\langle \nu_T^{LES,mod} \right\rangle / \langle f_\mu k^2/\epsilon\rangle$. In order to satisfy a smooth transition between the RANS and LES region, the constant C_μ of the RANS model is modified to satisfy this constraint. It is proposed in Temmerman *et al.* (2005) to use the following modified relation for C_μ in the RANS model:

$$C_\mu = \begin{cases} \frac{15}{40-y^+}\left(0.09 + (C_{\mu,int} - 0.09)\frac{1-\exp(-y/\Delta)}{1-\exp(-y_{int}/\Delta_{int})}\right), & \text{if} \quad y^+ < 25 \\ 0.09 + (C_{\mu,int} - 0.09)\frac{1-\exp(-y/\Delta)}{1-\exp(-y_{int}/\Delta_{int})}, & \text{if} \quad y^+ > 25 \end{cases}$$

and where the subscipt 'int' denotes quantities evaluated at the interface location. This relation effectively damps the excessive level of turbulence viscosity close to the interface produced by the RANS model. The hybrid method has been applied to a fully developed planar channel flow where the switching location was fixed at a pre-defined wall distance y^+ and the flow over periodic 2D hills in a channel where the switching location was fixed using a grid line. The channel flow showed an

unphysical kink in the mean-velocity profile and the recirculation zone behind the hill was found to be too long but only weakly dependent on the interface location.

Switching the turbulence model formulation at a pre-determined grid line is not practical for three-dimensional geometries. Similarly, switching at a certain wall distance y^+ is also problematic due to the inherent scaling with the wall shear stress. Breuer *et al.* (2007*a*,*b*) have employed a dynamic switching criterion, which is somewhat more robust and more generally applicable. The switching location is determined based on the non-dimensional wall distance $y^* = k^{1/2}y/\nu$, which offers the advantage of being applicable in regions where the wall shear-stress vanishes, such as close to the separation point. In regions where $y^* < C_{y^*}$, the RANS model is active and for $y^* > C_{y^*}$ the hybrid model operates in LES mode. The switching location was chosen as $C_{y^*} = 60$.

4.5.3 Detached Eddy Simulation

The most prominent hybrid RANS/LES method is called Detached Eddy Simulation (DES). A lot of effort has focused on testing, validating and improving the formulation of DES. The initial version of DES was proposed by Spalart *et al.* (1997) and is based upon the one-equation turbulence model of Spalart & Allmaras (1992). In DES the switch from a RANS to LES mode is achieved by modifying a term in the transport equation of the RANS turbulence model. The destruction term in the transport equation for the modified turbulence viscosity $\tilde{\nu}$ of the Spalart & Allmaras model is proportional to $(\tilde{\nu}/d)^2$, where d is the wall distance. In the DES formulation, the RANS length scale d is replaced with a hybrid length scale defined as $\tilde{d} = \min(d, C_{DES}\Delta)$, which away from the wall, reduces the magnitude of the turbulence viscosity ν_T. In regions where $d < C_{DES}\Delta$, the model operates in RANS mode and for $d > C_{DES}\Delta$, the model operates as a SGS model. The model constant C_{DES} is analogous to the Smagorinsky constant C_S and determined from decaying homogeneous isotropic turbulence as $C_{DES} = 0.65$. It should be noted that the idea of DES to replace the RANS length scale with a hybrid DES length scale is not limited to the Spalart & Allmaras model. Travin *et al.* (2004*b*), for example, transformed the k-ω-SST model into a DES formulation by rewriting the dissipation term in the turbulence kinetic energy equation as $\epsilon = k^{3/2}/L_{DES}$ with $L_{DES} = \min\left[L_T, C_{DES}\Delta\right]$ and $L_T = k^{1/2}/\beta^*\omega$. Therefore, in LES mode the turbulence dissipation rate is determined from the algebraic relation $\epsilon = k^{3/2}/C_{DES}\Delta$. DES has also been used in conjunction with non-linear eddy-viscosity turbulence models (see Bunge *et al.* (2007) or Mockett (2009)).

The natural use of DES is to treat the entire boundary layer in RANS mode and to switch to LES outside the boundary layer. For this reason the length scale Δ has been defined as $\Delta = \max(\Delta_x, \Delta_y, \Delta_z)$, which helps to maintain a RANS mode in boundary layers where highly anisotropic cells are usually used. Nevertheless, the location where DES switches from a RANS to LES mode depends on the grid design. It is the user's responsibility to supply a grid properly designed for DES, such that the switch occurs at the correct location, i.e. outside the boundary layer. In order to handle the entire boundary layer in RANS mode the grid needs to be designed such that the boundary layer thickness $\delta < C_{DES}\Delta$. The intricate griding issue inherent in DES has led to publications giving explicit guidelines on how to design suitable grids for DES (see Spalart, 2001). Unfortunately, there are many possible scenarios where it cannot be guaranteed that the entire boundary layer is handled in RANS mode, e.g. in cases where thick boundary layers are involved such as close to the separation point, in grid convergence studies, in regions with high geometric curvature and when using unstructured meshes. In such cases it is very likely that the switch from RANS to LES occurs inside the boundary layer. This poses a possible danger, particularly if the computational grid in the LES region is too coarse, since the turbulence viscosity is reduced but the coarse resolution does not allow resolved fluctuations to compensate the reduction of modelled Reynolds-stress through resolved stress. This leads to a drop of total Reynolds-stress components at the switching location. This effect is referred to as Modelled Stress Depletion (MSD) and may result in a severe under-prediction of the skin friction coefficient and may cause premature separation. Since the switch from RANS to LES mode is triggered by the grid design, this phenomenon is also called Grid Induced Separation (GIS) (see Menter *et al.*, 2003).

Since the original proposal of DES, different modifications have been proposed, which aim at avoiding the difficulty of generating DES grids in complex configurations and which eliminate the effects of MSD and GIS. Deck (2005) used a zonal DES approach to simulate a high-lift airfoil configuration with deployed slat and flap. The zones for RANS and LES were explicitly defined prior to the simulation. The zonal approach ensured that the thick boundary layers present on the airfoil configuration were covered in RANS mode and that the other areas of interest were covered in LES mode whatever the grid resolution was. In Spalart *et al.* (2006) a more robust formulation of the hybrid DES length scale in terms of grid dependency was proposed. The new length scale is obtained using additional elements from the Spalart & Allmaras (1992) model to prevent or 'delay' the switch inside

the boundary layer. The new hybrid length scale is given by

$$\tilde{d} = d - f_d \max\left(0, d - C_{DES}\Delta\right), \tag{4.22}$$

where $f_d = 1 - \tanh\left[(8r_d)^3\right]$ and $r_d = (\nu_T + \nu)/(\kappa^2 d^2 \sqrt{\overline{u}_{i,j}\overline{u}_{i,j}})$. The function f_d shields the DES length scale from being activated inside the boundary layer. Therefore, for $f_d = 0$, a RANS mode is enforced where the RANS length scale is given by $\tilde{d} = d$. For $f_d = 1$, the switch to LES is allowed and the length scale is obtained as $\tilde{d} = C_{DES}\Delta$. Spalart *et al.* called this modified version Delayed Detached Eddy Simulation (DDES).

The latest major modification to the original DES formulation is introduced in Shur *et al.* (2008) and is referred to as Improved-DDES (IDDES). In IDDES, the capabilities of DDES are combined with the capability of the original DES to provide wall modelling capabilities (WMLES). The new IDDES formulation is able to operate in the DDES and WMLES mode depending on turbulence initial and inflow conditions. This is achieved by the following hybrid length-scale definition

$$\tilde{d} = f_d(1 + f_e)d + (1 - f_d)\Psi C_{DES}\Delta. \tag{4.23}$$

The function f_d is a blending function, which blends between the DDES and WMLES mode and Ψ is a function, which compensates for the erroneous activation of near-wall/low-Reynolds-number modifications of the baseline RANS model. The definition of the filter length scale is also modified and includes a dependency on the wall distance, $\Delta = f(\Delta_x, \Delta_y, \Delta_z, d)$. Another important ingredient is the function f_e, which increases the Reynolds-stress of the underlying RANS model above the natural RANS level. This is an effective measure to reduce the extend of the log-layer mismatch in WMLES mode.

The original DES and DDES formulation have been applied to a wide range of flows of engineering and industrial interest. For further information and discussions about applications of DES, the reader is referred to Spalart (2009), Squires *et al.* (2002) and Squires (2004).

4.5.4 Flow Simulation Methodology

At roughly the same time when DES was proposed Speziale (1998*a*,*b*) proposed a combined LES and time-dependent RANS approach, which was intended to close the gap between RANS and DNS. Speziale argued that a hybrid RANS/LES method

should possess at least the following three properties: 1) The subgrid-scale model should be able to resolve anisotropy of the flow and allow for a direct integration to the wall without using empirical damping functions, 2) In the limit of a very coarse mesh or infinite Reynolds number the hybrid method needs to revert to a state-of-the-art RANS turbulence model, 3) Absence of any test filters or double-filtered fields. The points 1) and 2) seem particularly important, since most subgrid-scale models are derived based on the assumption that the unresolved subgrid-scales are isotropic. This assumption is not justified, for example, for anisotropic computational grids or close to the wall where subgrid scales are likely to exhibit anisotropy. In addition, subgrid-scale models are not able to model a significant amount of Reynolds-stress; if the resolution becomes too coarse to explicitly resolve, say, 80% of the turbulence kinetic, subgrid-scale models are not adequate and results will deteriorate.

In order to satisfy these properties, Speziale suggested that the unresolved stress components can be computed by damping the Reynolds-stress tensor predicted from a state-of-the-art RANS turbulence model. Hence, the unresolved stress components are given by the following relation

$$\tau_{ij} = F \cdot \tau_{ij}^{RANS}. \tag{4.24}$$

The damping function F, in its initial proposal, is sensitised to the ratio of grid spacing Δ to Kolmogorov length scale $L_\eta = \nu^{3/4}/\epsilon^{1/4}$. In principle, the damping function allows for a continuous blending between RANS and DNS, depending on the local and instantaneous grid resolution. In general, the blending function needs to be designed such that the DNS limit $F \to 0$ is recovered if the grid resolution is sufficient to resolve all scales of turbulence. In the coarse grid or infinite-Reynolds-number limit, F needs to approach unity such that a RANS closure is recovered. For values $0 \leqslant F \leqslant 1$ the model is able to operate in LES or Very Large-Eddy Simulation (VLES) mode. VLES may be defined as an LES-like simulation where most of the turbulence kinetic energy is modelled and not explicitly resolved.

For this purpose Speziale proposed to use the following damping function

$$F\left(\Delta/L_K\right) = \left[1 - \exp\left(\frac{-\beta\Delta}{L_\eta}\right)\right]^n, \tag{4.25}$$

where the constants are given by $\beta = 0.001$ and $n = 1$. In general, any RANS model can be used to model τ_{ij}^{RANS}. Speziale used an Explicit-Algebraic-Stress Model, which is able to account for flow anisotropy and non-equilibrium effects through

strain-dependent coefficients. Since this hybrid approach is distinctly different from existing RANS and LES methods, Zhang *et al.* (2000) and Fasel *et al.* (2002) later referred to this approach as Flow Simulation Methodology (FSM).

The damping function is the key to success of the FSM approach. A properly designed damping function would be able to provide the required amount of turbulence modelling at any grid resolution. The choice of the damping function and the constants β and n in the initial proposal were never completely justified. However, Hussaini *et al.* (2006) used Renormalization Group Theory (RNG) to modify an existing RANS model for subgrid-scale applications while maintaining the correct RANS and DNS limits. They derived a set of possible damping functions and arrived, amongst others, at the following form $F(\Delta) = 1 - \exp(-\beta\Delta^2)$, which is somewhat similar to Sepziale's proposal. Sandberg & Fasel (2006) investigated transitional and turbulent supersonic base flows using FSM. It was found that the best results were obtained for $0.001 \leqslant \beta \leqslant 0.004$ and a grid resolution such that the damping function is smaller than 10%. Fasel *et al.* (2006) applied FSM to a backward facing step, subsonic plane wake and a supersonic axisymmetric wake. The optimum value of β was again found to be approximately $\beta = 0.001$ for $n = 1$. These investigations confirm the suitability of the proposed values for β. The effect of the parameter n has so far not been investigated.

Zhang *et al.* (2000) proposed a modified version of the damping function, which takes the following form: $F(\Delta/L_\eta) = [1 - \exp(-5\max(0, \Delta - 2L_\eta)/NL_\eta)]^n$. It was shown that this damping function recovers a RANS mode across almost the entire thickness of a flat plate boundary layer for $N = 10$. Using a value of $N = 2500$ would recover the original damping function.

Germano (1998) suggested a modified damping function of the form $F = 1 - \tau_{ij}^{RANS}\tau_{ij}^{res}/\tau_{ij}^{RANS}\tau_{ij}^{RANS}$, where τ_{ij}^{res} is the resolved stress. If no turbulence is resolved, the resolved stress $\tau_{ij}^{res} \rightarrow 0$ and the RANS limit is recovered. For $\tau_{ij}^{res} \rightarrow \tau_{ij}^{RANS}$ the DNS limit is recovered.

It can be anticipated that the damping function based on Δ/L_η is able to provide the correct DNS limit, since L_η is a relevant length scale in DNS. However, the viscous, or Kolmogorov, length scale L_η is not a relevant length scale when performing LES. It seems very difficult, using this length scale, to achieve the correct amount of damping in LES mode. In addition, the damping function does not incorporate a characteristic length scale of the largest scales in the flow and it appears even more difficult to approach the correct RANS limit in case of too coarse a grid. Motivated by this issue, Israel (2005) introduced an integral length scale into the damping

function. The modified damping function is as follows:

$$F\left(\Delta, L_\eta, L_I\right) = \frac{\left(\beta\Delta\right)^{2/3} - L_\eta^{2/3}}{L_I^{2/3} - L_\eta^{2/3}}, \tag{4.26}$$

where $L_I = k^{3/2}/\epsilon$ is used as an estimate for the integral length scale.

Another issue, which was not been addressed by Speziale is how the Reynolds-stress tensor τ_{ij}^{RANS} is computed in case of resolved turbulence, where $\tau_{ij} \ll \tau_{ij}^{RANS}$. Assuming the hybrid method operates in a pure RANS mode, i.e. $\tau_{ij} = \tau_{ij}^{RANS}$, the computed quantities of the flow field correspond to Reynolds-averaged quantities, which are consistent with the derivation and the applicability of the RANS equations. In case a considerable amount of turbulence is resolved in the simulation, the computed quantities in the flow field are filtered quantities and not equivalent to a Reynolds-averaged quantity. Strictly speaking, Reynold averaged quantities are required for the RANS equations in order to be consistent in the computation of the Reynolds-stress tensor. This raises the fundamental question of which quantities should be used to compute the Reynolds-stress tensor in case of resolved turbulence. As pointed out by Batten *et al.* (2000), there are two different possibilities. First, the Reynolds-stress tensor can be computed in a time-accurate fashion from the filtered flow field as the simulation progresses. Alternatively, a RANS computation can be performed prior to the simulation or time-averaged quantities can be obtained as the simulation progresses.

4.5.5 Limited Numerical Scales

Based on Sepziale's combined RANS/LES method, Batten *et al.* (2000, 2002) proposed a modified form of the damping function, which does not incorporate any parameter that needs to be defined by the user. This modified approach of Speziale has been termed Limited Numerical Scales (LNS). Batten *et al.* expressed the damping function as a ratio of effective viscosity norms and called this term latency parameter α. In the latest publication of Batten *et al.* (2004) the latency factor is defined as

$$\alpha = \min\left[\frac{\nu_T^{LES}}{\nu_T^{RANS}}, 1\right], \tag{4.27}$$

where ν_T^{LES} is obtained from the Smagorinsky model and the ν_T^{RANS} from a non-linear k-ϵ model. The filter width has been defined as $\Delta = 2\max\left[\Delta_x, \Delta_y, \Delta_z, \sqrt{\overline{u_i}^2}\Delta t\right]$. The last term ensures that RANS is recovered as the time step Δt becomes large,

whatever the spatial resolution of the grid is. The property of the latency parameter is that it automatically selects the model, ν_T^{LES} or ν_T^{RANS}, which provides the smallest shear stress. Regarding the ambiguity of which quantities should be used to calculate the Reynolds-stress tensor, Batten *et al.* employs the scaled Reynolds-stress tensor τ_{ij} (or damped turbulence viscosity $\alpha\nu_T^{RANS}$) in the transport equations for the turbulence kinetic energy and dissipation rate, k and ϵ respectively. This effectively reduces the production term as well as transport/diffusion terms in the transport equations and the RANS model turns into a model for the subgrid scales k_{sgs} and ϵ_{sgs}. LNS has been applied to the flow around a square cylinder and a periodic 2D hills in a channel. The results are generally improved compared to traditional RANS and URANS approaches.

4.5.6 Partially-Integrated and Partially-Resolved Transport Modeling

The Partially Integrated Transport Model (PITM) has been proposed by Schiestel & Dejoan (2005) for the framework of k-ϵ turbulence modelling and was extended by Chaouat & Schiestel (2005) to a DRSM closure. PITM is derived by splitting the energy spectrum into a resolved and unresolved part and performing partial integration of the energy spectrum function $E(\kappa, t)$ in spectral space. The result is a transport equation for the sub-grid turbulence kinetic energy k_{sgs} and turbulence dissipation rate ϵ_{sgs}, which depend on the parameter $f_k = k_{sgs}/k$. An expression for f_k is analytically derived using a model energy spectrum and does not take a constant value as in the PANS approach. The latest proposal for f_k in Chaouat & Schiestel (2009) is derived from an energy spectrum function, which is valid from small to large wavenumbers. The free coefficients in the expression are determined by reference to decaying homogeneous isotropic turbulence. It is interesting to note that the PITM approach results in the same constitutive relations as for the PANS approach if $f_\epsilon = 1$.

It is sometimes argued that traditional seamless RANS/LES approaches are conceptually inconsistent, since the Reynolds-averaging operator provides time-averaged quantities whereas LES provides spatially filtered quantities. In homogeneous turbulence the spatial filtering operation in the limit $\Delta \to \infty$ is indeed consistent with the Reynolds-averaging operator. This is not true for inhomogeneous flows where spatial filtering operation in the limit $\Delta \to \infty$ is not consistent with the Reynolds-averaging operator. Based on this argument Fadai-Ghotbi *et al.* (2009) derived a Temporally Partially Integrated Transport Model (TPITM) by splitting the energy

spectrum into a resolved and unresolved part and performing partial integration of the energy spectrum function $E(\omega, t)$ in the spectral frequency space. TPITM provides temporally filtered quantities, which are consistent with Reynolds averaging if the temporal filter width goes to infinity (for statistically steady flows).

The Partially Resolved Navier-Stokes (PRNS) method has been proposed by Liu & Shih (2006). The main difference to TPITM is the choice of the resolution control parameter. In PRNS the resolution control parameter is a function of the temporal filter width $RCP = \Delta_T/T$, where T is the integral time scale. The value of RCP is specified prior to the simulation and the resulting turbulence viscosity is defined as $\nu_T = RCP \cdot C_\mu k^2/\epsilon$. Here, RANS model equations are used to determine the values for k and ϵ.

Chapter 5

Numerical Methodology

In this chapter the numerical framework used to solve the set of governing equations will be introduced. Most of the numerical framework is extensively discussed in various textbooks and other publications, e.g. Patankar (1981) or Ferziger & Peric (2002). For this reason only a brief overview will be given here with emphasis placed on the elements, which are particularly important for this work.

The flow solver used in this work is the open-source CFD code OpenFOAM, which has been used and validated in a wide range of previous studies such as, for example, Weller *et al.* (1998), Jasak (1996) and de Villiers (2006). The finite volume method is used to solve the set of governing equations on arbitrarily unstructured meshes with a cell-centered (co-located) variable arrangement. A segregated approach is used to solve the governing equations in incompressible form. The discretisation procedure is second-order accurate in space and time and employs a fully implicit time advancement scheme.

5.1 Governing Equations

The governing equations for momentum or any other transported quantity takes the form of an unsteady, convection diffusion equation, which can be written in the following form for the arbitrary quantity ϕ,

$$\frac{\partial \phi}{\partial t} + \nabla \cdot (\phi \overline{\boldsymbol{u}}) - \nabla \cdot (\Gamma \nabla \phi) = S_\phi. \tag{5.1}$$

The terms on the left-hand side respectively represent the local rate of change, convection by mean velocity and diffusion of ϕ, with the diffusion coefficient Γ. The right-hand side term represents the sum of all sources and sinks of ϕ.

In the finite-volume method (FVM) the governing equations are integrated in time and over a control volume (CV) to yield the integral form of (5.1)

$$\int_t^{t+\Delta t} \frac{\partial}{\partial t}\left(\int_{CV} \phi \mathrm{d}V\right) \mathrm{d}t + \int_t^{t+\Delta t} \int_{CV} \nabla \cdot (\phi \overline{\boldsymbol{u}})\, \mathrm{d}V \mathrm{d}t - \int_t^{t+\Delta t} \int_{CV} \nabla \cdot (\Gamma \nabla \phi)\, \mathrm{d}V \mathrm{d}t = \int_t^{t+\Delta t} \int_{CV} S_\phi \mathrm{d}V \mathrm{d}t. \tag{5.2}$$

In the first step (pre-processing) the flow domain must be subdivided into a finite number of small control volumes (CV) or cells where the centre of each control volume corresponds to the point where the solution to the governing equations is calculated. In general, there are no restrictions regarding the shape of the control volumes as long as each CV is completely surrounded by an arbitrary number of faces and each face only connects to one adjacent CV. In the second step, the integral-conservation equations are applied to each CV and the volume integrals are approximated and converted into integrals over the bounding surfaces of each CV. The flow variables at the CV surfaces are obtained by interpolation between the cell-centered values, which introduces a dependency of the variables in the CV centre to the neighbouring control volumes. This procedure results in a system of algebraic equations, which can then be solved using an iterative procedure.

5.2 Spatial Discretisation

5.2.1 Convection Term

Using Gauss Divergence Theorem the volume integrals appearing in (5.2) can be converted into integrals over the bounding surface elements ∂A of the control volume, i.e.

$$\int_{CV} \nabla \cdot \phi \mathrm{d}V = \oint_{\partial A} \mathrm{d}\boldsymbol{A} \cdot \phi, \tag{5.3}$$

where $\mathrm{d}\boldsymbol{A}$ is the outward-pointing vector normal to the surface element ∂A. Assuming a linear variation of the variable ϕ the surface integral can be further approximated with second-order accuracy as

$$\int_{\partial A} \mathrm{d}\boldsymbol{A} \cdot \phi = \sum_f \left(\int_f \mathrm{d}\boldsymbol{A}\phi \right) = \sum_f \boldsymbol{A}\phi_f. \tag{5.4}$$

that is, as the sum of the product of the outward pointing surface area vector $\boldsymbol{A}$ times the face-centered value of the quantity ϕ_f. This procedure applied to the convection term yields

$$\int_{CV} \nabla \cdot (\overline{\boldsymbol{u}}\phi)\, \mathrm{d}V = \sum_f \boldsymbol{A} \left(\overline{\boldsymbol{u}}\phi\right)_f = \sum_f \left(\boldsymbol{A}\overline{\boldsymbol{u}}_f\right) \phi_f = \sum_f F\phi_f, \tag{5.5}$$

where $F = \boldsymbol{A}\overline{\boldsymbol{u}}_f$ corresponds to the mass flux through the bounding face f. The face values of ϕ_f or $\overline{\boldsymbol{u}}_f$ can be obtained by interpolation between the cell-centered values ϕ_P and ϕ_U of the two cells connecting to the face f. This situation is depicted in figure 5.1.

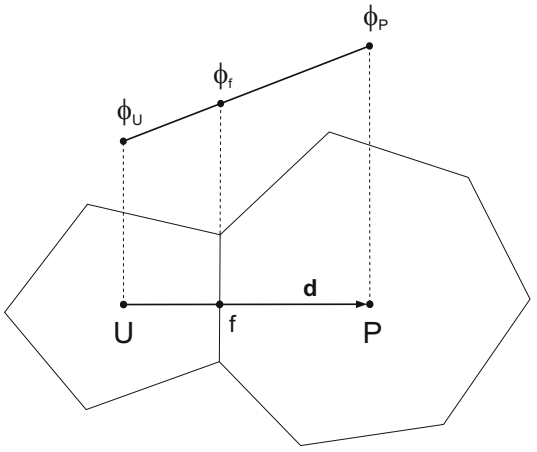

FIGURE 5.1: Interpolation of face values in the FVM .

Assuming a linear variation of the dependent variable ϕ between the cell centres U and P of two neighboring cells, the face value can be obtained by linear interpolation as

$$\phi_f = f_x\phi_P + (1 - f_x)\, \phi_U, \tag{5.6}$$

with the interpolation factor $f_x = \overline{fU}/\overline{PU}$. Note, the interpolated quantity $\overline{\boldsymbol{u}}_f$ must also satisfy the continuity constraint $\sum_f F = 0$. The linear interpolation of face quantities results in a second-order accurate scheme, which is commonly referred to as the Central-Differencing Scheme (CDS).

For problems where convection is the physically dominant mechanism in the flow the CDS may produce unbounded solutions and unphysical oscillations in the flow field. As the importance of convection increases the solution will become increasingly non-physical, which may then lead to divergence of the simulation. It is argued in Versteeg & Malalasekera (2007) that the major defect of CDS is the lack of sensitivity to the direction of the convection velocity. In strongly convective conditions the cell-centered value upstream of face f should have a stronger weighting than the value of the cell downstream. The upwind differencing scheme (UDS) takes account of the flow direction and computes the face values accordingly as

$$\phi_f = \begin{cases} \phi_P & \text{, if } F \geqslant 0 \\ \phi_U & \text{, if } F < 0. \end{cases} \tag{5.7}$$

The UDS is only first-order accurate but it considerable improves the stability characteristics by guaranteeing boundedness of the solution. Even though higher-order UDS can be derived the improved stability is always achieved at the expense of accuracy by introducing a significant amount of numerical diffusion. This is particularly problematic in the LES region of any hybrid RANS/LES approach where the modelled turbulence diffusivity may be very small or even of the same order of magnitude as the numerical diffusion. Any elevated level of numerical diffusion therefore inevitably contaminates the resolved flow field unless the modelled turbulence diffusivity is adjusted according to the numerical scheme employed in the simulation. Adjusting the modelled turbulence diffusivity is not a satisfying solution, since every turbulence model would have to be adjusted and re-calibrated for a large number of available convection discretisation schemes.

The small amount of numerical diffusion inherent in the CDS makes it well suited for performing simulations with resolved turbulent content. In simulations of practical interest it cannot alway be guaranteed that the mesh resolution Δ_x (in one dimensional problems) is sufficient to satisfy the boundedness requirement of a cell Peclet number (or sometimes called cell Reynolds number) $Pe = \overline{u}/(\Gamma/\Delta_x) < 2$ (see Versteeg & Malalasekera, 2007) of the CDS. Instead, it is necessary to introduce a small amount of additional numerical diffusion to the CDS such that the accuracy of the CDS is retained and stability and boundedness of the solution is improved. For this reason Peric (1985) has proposed a blended or hybrid convection scheme, which is obtained as a linear combination of a CDS and UDS scheme of the following form

$$\phi_f = (1 - \sigma_b)\, \phi_{f,CDS} + \sigma_b \phi_{f,UDS}. \tag{5.8}$$

The blending function σ_b controls the level of additional numerical diffusion. For $\sigma_b = 0$ a full CDS is recovered and for $\sigma_b = 1$ the interpolation follows a UDS. Travin *et al.* (2004*b*) use the blending technique to develop a hybrid convection scheme that is tailored to Detached Eddy Simulation. The hybrid convection scheme operates in a UDS mode in the RANS region and switches to a CDS mode in LES regions of the flow field. The blending function also depends on local flow quantities like turbulence viscosity ν_{sgs} and magnitude of strain and rotation rate S, Ω respectively. These quantities are used to detect flow regions with a well-resolved flow field ($\Omega > S$) where the CDS should be used and irrotational flow regions where UDS can be used. Since the hybrid convection scheme of Travin *et al.* (2004*b*) is used in this study in conjunction with Detached Eddy Simulation the constitutive relations are given here

$$\begin{aligned}
\sigma_b &= \tanh\left(A^{C_{h1}}\right), \quad A = C_{h2}\max\left[\frac{C_{DES}\Delta}{l_{turb}g} - 0.5, 0\right] \\
l_{turb} &= \sqrt{\frac{\nu_{sgs}+\nu}{C_\mu^{3/2}K}}, \quad K = \max\left(\sqrt{\frac{S^2+\Omega^2}{2}}, \frac{0.1}{\tau_{ref}}\right) \\
g &= \tanh\left(B^4\right), \quad B = \frac{C_{h3}\Omega\max\left[S,\Omega\right]}{\max\left[\frac{S^2+\Omega^2}{2}, 10^{-20}\right]} \\
C_{h1} &= 3, \quad C_{h2} = 1, \quad C_{h3} = 2.
\end{aligned} \tag{5.9}$$

and $\tau_{ref} = l_{ref}/u_{ref}$.

5.2.2 Flux-gradient Transport Term

Following a similar procedure as for the convection term the volume integral of the flux-gradient transport term can be converted into a surface integral as

$$\int_{CV} \nabla\cdot(\Gamma\nabla\phi)\,\mathrm{d}V = \sum_f \boldsymbol{A}\cdot(\Gamma\nabla\phi)_f = \sum_f \Gamma_f \boldsymbol{A}\cdot(\nabla\phi)_f\,. \tag{5.10}$$

The face value Γ_f can be determined by linear interpolation according to (5.6) and the face gradient is given by

$$\boldsymbol{A}\cdot(\nabla\phi)_f = |\boldsymbol{A}|\,\frac{\phi_P - \phi_U}{|\boldsymbol{d}|}, \tag{5.11}$$

where $\boldsymbol{d}$ is the vector connecting point U and P. This method is second-order accurate and provides bounded solutions, providing the face is orthogonal, i.e. $\boldsymbol{d}$

and $\boldsymbol{A}$ are parallel. In situations where the faces are non-orthogonal a correction (cross-diffusion) term needs to be introduced to (5.11) as follows

$$\boldsymbol{A} \cdot (\nabla\phi)_f = \boldsymbol{A}_d \frac{\phi_P - \phi_U}{|\boldsymbol{d}|} + \boldsymbol{A}_\theta \cdot (\nabla\phi)_f \,, \tag{5.12}$$

where $\boldsymbol{A}_d$ is the component parallel to $\boldsymbol{d}$ and $\boldsymbol{A}_\theta$ is component perpendicular to $\boldsymbol{A}$ such that $\boldsymbol{A} = \boldsymbol{A}_d + \boldsymbol{A}_\theta$. The term $(\nabla\phi)_f$ in (5.12) is obtained by interpolation of the cell-centered gradients according to (5.6). The cross-diffusion term may yield unbounded solutions on strongly non-orthogonal meshes. Therefore, the effect of the cross-diffusion term may have to be limited to ensure convergence of the solution. The gain in stability is again achieved at the expense of accuracy of the diffusion term.

5.2.3 Source Terms

All other source terms are linearised by decomposition into a constant part S_c and a part, which linearly depends on ϕ, i.e.

$$S_\phi = S_c + S_p\phi. \tag{5.13}$$

Since

$$\int_{CV} \phi \mathrm{d}V = \phi_P V_P, \tag{5.14}$$

the source term can be written as

$$\int_{CV} S_\phi \mathrm{d}V = S_c V_P + S_p V_P \phi_P. \tag{5.15}$$

5.3 Temporal Discretisation

Introducing the spatial discretisation into (5.2) yields the semi-discrestised form of the generic transport equation

$$\int_t^{t+\Delta t} \left[\left(\frac{\partial\phi}{\partial t} \right)_P V_P + \sum_f F\phi_f - \sum_f \Gamma_f \boldsymbol{A} \cdot (\nabla\phi)_f \right] \mathrm{d}t = \int_{t+\Delta t}^{t} \left[S_c V_P + S_p V_P \phi_P \right] \mathrm{d}t. \tag{5.16}$$

In order to maintain an overall second-order accuracy of the discretised transport equation the temporal derivative in (5.16) is discretised using the second-order accurate Backward Differencing (BD) scheme

$$\left(\frac{\partial\phi}{\partial t}\right)^n = \frac{(3/2)\phi^n - 2\phi^{n-1} + (1/2)\phi^{n-2}}{\Delta t}. \tag{5.17}$$

The BD scheme requires information from the three time levels $\phi^n = \phi(t + \Delta t)$, $\phi^{n-1} = \phi(t)$ and $\phi^{n-2} = \phi(t - \Delta t)$. Assuming that the temporal variation of the face fluxes ϕ_f and face gradients $(\nabla\phi)_f$ can be neglected a second-order accurate and fully implicit discretisation of the generic transport equation (5.1) is obtained as

$$\frac{(3/2)\phi^n - 2\phi^{n-1} + (1/2)\phi^{n-2}}{\Delta t}V_P + \sum_f F\phi_f^n - \sum_f \Gamma_f \boldsymbol{A}\cdot(\nabla\phi)_f^n = S_c V_P + S_p V_P \phi_P^n. \tag{5.18}$$

Note, although the BD scheme is second-order accurate, neglecting the temporal variation of the face fluxes and face gradients results in a larger truncation error as compared to, for example, the second-order Crank-Nicholson (CN) method (see Jasak, 1996). In the simulations performed in this work the time step and CFL number is generally small ($CFL < 1$), which minimises the effect of the larger truncation error and the resulting additional numerical diffusion.

In the final step, the new values for ϕ_P need to be determined. The discretisation of the face fluxes and face gradients introduces a dependency of ϕ_P on the values ϕ_N in the surrounding cells, which connect to the control volume under consideration. Equation (5.18) therefore can be written as an algebraic equation of the form

$$a_P\phi_P^n + \sum_N a_N\phi_N^n = R_P, \tag{5.19}$$

where a_P includes the contribution from all terms, which include ϕ_P^n, that is from the unsteady, convection and diffusion terms as well as from the linear part of the source terms. Similarly, a_N contains the coefficients ϕ_N^n of the neighboring cells. R_P contains all other terms, which do not depend on the new values ϕ^n. A system of algebraic equations of the form $A\phi = R$ is obtained by assembling one algebraic equation for each control volume. A is a sparse matrix containing the coefficients a_P and a_N, ϕ is the solution vector and R a vector containing the source terms. The system of equations is solved iteratively using the conjugate gradient method with preconditioning to accelerate convergence. More detail can be found in Jasak (1996) and de Villiers (2006).

5.4 Navier-Stokes Equation

When the discretisation procedure is applied to the Navier-Stokes equations some issues require special consideration. First, the incompressible Navier-Stokes equations are non-linear in nature due to the appearance of the quadratic product of velocities in the convection term. Second, the momentum equation constitutes a set of coupled equations and the pressure gradient term introduces another variable to the system. In incompressible flow the pressure cannot be computed from any transport or other equation and an iterative procedure needs to be employed to determine a pressure and velocity field such that the continuity and momentum equation are satisfied.

Convection Term

In order to make the non-linear convection term compatible with the linear system solver, a linearisation of the convection term is introduced. This is achieved by replacing one of the face values $\overline{\boldsymbol{u}}_f^n$ with the face value from the previous time step $\overline{\boldsymbol{u}}_f^{n-1}$. The linearised convection term is as follows

$$\int_{CV} \nabla \cdot (\overline{\boldsymbol{u}}\overline{\boldsymbol{u}})\, \mathrm{d}V = \sum_f \boldsymbol{A}\, (\overline{\boldsymbol{u}}\overline{\boldsymbol{u}})_f \approx \sum_f \left(\boldsymbol{A}\overline{\boldsymbol{u}}_f^{n-1}\right) \overline{\boldsymbol{u}}_f^n = \sum_f F^{n-1}\phi_f^n. \tag{5.20}$$

Pressure-velocity coupling

In compressible flow the continuity equation can be used to calculate the density and the pressure follows from the equation of state. For incompressible flows the continuity equation does not contain any information about the pressure and merely places an additional constraint on the flow field, which is determined from the momentum equations. However, combining the momentum and continuity equations an additional equation for the pressure can be derived. The momentum and pressure correction equations are solved in a sequential or segregated manner rather than in a fully coupled fashion. In order to achieve the pressure-velocity coupling, the SIMPLE algorithm Patankar (1981) is used for steady state problems and the PISO algorithm Issa (1986) for transient simulations.

Chapter 6

Baseline EASM

In this chapter the constitutive relations of the baseline EASM formulation are summarised and a range of different test and validation cases are presented. The first objective of this chapter is to evaluate the performance of the baseline EASM closure to predict complex and three-dimensional flows. This validation study has been found necessary for two reasons. First, the range of published validation cases for EASM models, particularly for three-dimensional mean flow, is very limited and second, the baseline EASM model employs a different pressure-strain correlation model compared to the widely used EASM model of Wallin & Johansen (2000) and Hellsten (2005). For the purpose of validating the baseline EASM closure, simulations are performed for the flow in a planar channel, the flow over the NASA hump configuration (Greenblatt *et al.*, 2004) and the flow in a three-dimensional diffuser (Cherry *et al.*, 2008) and the results are compared with reference data. In addition, the results are compared to predictions of the popular k-ω-SST and the recently proposed φ-α-UMIST model (Keshmiri *et al.*, 2008). The second objective of this chapter is to investigate potential differences between two-dimensional and three-dimensional EASM formulations for predicting complex three-dimensional flows. This investigation seems particularly relevant, since two-dimensional EASM closures are generally preferred, due to their simplicity and numerical efficiency, over the much more complex three-dimensional EASM formulation. However, three-dimensional EASM formulations use additional, higher-order, coupling terms in the stress-strain relationship, which may have the potential to improve the predicted results for cases with three-dimensional mean flow. Additional cases have been published by the author in Weinmann & Sandberg (2009) where the flow around an idealised wing-body junction and the flow over a three-dimensional axisymetric hill are considered.

6.1 Constitutive Relations

The baseline EASM is a high-Reynolds-number formulation, since neither the transport equations nor the quasi-homogeneous pressure-strain model used in the EASM includes modifications to account for various effects the wall exerts on the flow. The Reynolds-stress tensor $\overline{u_i' u_j'}$ of the EASM formulation constitutes a non-linear stress-strain relationship, which can be written as $\overline{u_i' u_j'} = (2/3)k\delta_{ij} + k a_{ij}$, where the anisotropy tensor is given by

$$a_{ij} = -2(\nu_T/k)S_{ij}^* + a_{ij}^{ex}, \tag{6.1}$$

with the mean strain rate tensor $S_{ij}^* = (1/2)\left(\partial\overline{u}_i/\partial x_j + \partial\overline{u}_j/\partial x_i\right)$ and the extra-anisotropy tensor a_{ij}^{ex}, which introduces anisotropy in addition to the anisotropy resulting form the mean strain rate S_{ij}^*. For a vanishing extra-anisotropy tensor $a_{ij}^{ex} = 0$, the stress-strain relationship reduces to the linear Boussinesq approximation. The most general form of the extra-anisotropy tensor, valid in three-dimensional mean flow, can be written in the following form:

$$\begin{aligned} a_{ij}^{ex} \;=\; & \beta_2\left(S_{ik}S_{kj} - (1/3)II_S\delta_{ij}\right) + \beta_3\left(\Omega_{ik}\Omega_{kj} - (1/3)II_\Omega\delta_{ij}\right) + \beta_4\left(S_{ik}\Omega_{kj} - \Omega_{ik}S_{kj}\right) \\ & + \beta_5\left(S_{ik}S_{kl}\Omega_{lj} - \Omega_{ik}S_{kl}S_{lj}\right) + \beta_6\left(S_{ik}\Omega_{kl}\Omega_{lj} + \Omega_{ik}\Omega_{kl}S_{lj} - (2/3)IV\delta_{ij}\right) \\ & + \beta_7\left(S_{ik}S_{kl}\Omega_{lm}\Omega_{mj} + \Omega_{ik}\Omega_{kl}S_{lm}S_{mj} - (2/3)V\delta_{ij}\right) \\ & + \beta_8\left(S_{ik}\Omega_{kl}S_{lm}S_{mj} - S_{ik}S_{kl}\Omega_{lm}S_{mj}\right) \\ & + \beta_9\left(\Omega_{ik}S_{kl}\Omega_{lm}\Omega_{mj} - \Omega_{ik}\Omega_{kl}S_{lm}\Omega_{mj}\right), \end{aligned} \tag{6.2}$$

with the invariants

$$II_S = \mathrm{tr}\left\{S_{ik}S_{kj}\right\}, \quad II_\Omega = \mathrm{tr}\left\{\Omega_{ik}\Omega_{kj}\right\}, \quad III = \mathrm{tr}\left\{S_{ik}S_{kl}S_{lj}\right\},$$

$$IV = \mathrm{tr}\left\{S_{ik}\Omega_{kl}\Omega_{lj}\right\}, \quad V = \mathrm{tr}\left\{S_{ik}S_{kl}\Omega_{lm}\Omega_{mj}\right\}. \tag{6.3}$$

The tensors S_{ij} and Ω_{ij} are the non-dimensionalised mean strain rate and rotation-rate tensors $S_{ij} = \tau S_{ij}^*$ and $\Omega_{ij} = (\tau/2)\left(\partial\overline{u}_i/\partial x_j - \partial\overline{u}_j/\partial x_i\right)$, respectively. The turbulence time scale is given by $\tau = 1/\beta^*\omega$ and is not limited by the viscous time scale, since this is not required in the present high-Reynolds-number formulation.

A detailed derivation of the explicit solution for a general quasi-linear Algebraic RSM can be found in Wallin & Johansen (2000) and is not repeated here. The β_i

coefficients are given as

$$\begin{aligned}
\beta_1 &= -0.5A_1N\left(30A_2IV - 21NII_\Omega - 2A_2^3III_S + 6N^3 - 3A_2^2II_SN\right)/Q,\\
\beta_2 &= -A_1A_2\left(6A_2IV + 12NII_\Omega + 2A_2^3III_S - 6N^3 + 3A_2^2II_SN\right)/Q,\\
\beta_3 &= -3A_1\left(2A_2^2III_S + 3NA_2II_S + 6IV\right)/Q,\\
\beta_4 &= -A_1\left(2A_2^3III_S + 3A_2^2NII_S + 6A_2IV - 6NII_\Omega + 3N^3\right)/Q,\\
\beta_5 &= 9A_1A_2N^2/Q, \quad \beta_6 = -9A_1N^2/Q, \quad \beta_7 = 18A_1A_2N/Q\\
\beta_8 &= 9A_1A_2^2N/Q, \quad \beta_9 = 9A_1N/Q,
\end{aligned} \tag{6.4}$$

where

$$\begin{aligned}
Q &= 3N^5 + \left(-(15/2)II_\Omega - (7/2)A_2^2II_S\right)N^3 + \left(21A_2IV - A_2^3III_S\right)N^2\\
&\quad + \left(3II_\Omega^2 - 8II_SII_\Omega A_2^2 + 24A_2^2V + A_2^4II_S^2\right)N + (2/3)A_2^5II_SIII_S\\
&\quad + 2A_2^3IVII_S - 2A_2^3II_\Omega A_2II_\Omega.
\end{aligned} \tag{6.5}$$

Wallin & Johansen (2000) (WJ) suggest using a modified version of the linear pressure-strain model of Launder *et al.* (1975). This pressure-strain model has also been adopted in the latest EASM of Hellsten (2005). The modification of WJ results in a simplified form of the Algebraic RSM and consequently in reduced complexity of the EASM approximation. Even though the resulting model is more compact and computationally slightly less expensive, it is achieved at the expense of predictive performance. For example, the EASM of WJ cannot predict the third normal-extra-anisotropy component, i.e. $a_{33}^{ex} = 0$. The baseline EASM used in this study is therefore based on the linear pressure-strain model of Speziale *et al.* (1991), which is able to predict all normal components of the extra-anisotropy tensor a_{ij}^{ex} and which also gives slightly better anisotropy predictions in homogeneous turbulence (see Speziale *et al.*, 1991). These features are believed to be favourable when predicting complex three-dimensional flows. The coefficients A_i appearing in (6.4) and (6.5) are directly determined from the model of Speziale *et al.* (1991) and are given as

$$A_1 = 1.22, \quad A_2 = 0.47, \quad A_3 = 0.88, \quad A_4 = 2.37.$$

The variable N appearing in (6.4) and (6.5) corresponds to the ratio of rates of turbulence kinetic energy production to dissipation ($N = A_3 + A_4P_k/\epsilon$) and is governed by a non-linear polynomial relation. For general three-dimensional mean flow, N is governed by a sixth-order polynomial equation and no explicit solution can be obtained. In the limit of two-dimensional mean flow N is governed by a cubic

polynomial relation for which an explicit solution can be obtained. In this work, the turbulence production to dissipation ratio in the three-dimensional EASM formulation is approximated using the solution for two-dimensional mean flow. For two-dimensional flows the non-linear equation has the explicit solution

$$N = \begin{cases} \frac{A_3}{3} + \left(P_1 + \sqrt{P_2}\right)^{1/3} + \left(P_1 - \sqrt{P_2}\right)^{1/3} & , P_2 \geqslant 0 \\ \frac{A_3}{3} + 2\left(P_1^2 - P_2\right)^{1/6} \cos\left[\frac{1}{3}\arccos\left(\frac{P_1}{\sqrt{P_1^2 - P_2}}\right)\right] & , P_2 < 0 \end{cases} \tag{6.6}$$

with

$$P_1 = \left[\frac{A_3^2}{27} + \left(\frac{A_1 A_4}{6} - \frac{2}{9}A_2^2\right) II_S - \frac{2}{3} II_\Omega\right] A_3, \tag{6.7}$$

$$P_2 = P_1^2 - \left[\frac{A_3^2}{9} + \left(\frac{A_1 A_4}{6} + \frac{2}{9}A_2^2\right) II_S + \frac{2}{3} II_\Omega\right]^3. \tag{6.8}$$

Finally, the relation for the turbulence viscosity takes the form

$$\nu_T = -0.5\left(\beta_1 + II_\Omega \beta_6\right) k\tau. \tag{6.9}$$

The constitutive relations for a_{ij}^{ex} provide a solution in three-dimensional mean flow. The resulting EASM obviously results in a large number of additional numerical operations to compute a_{ij}^{ex} and the coefficients β_i, compared to a linear two-equation model. In addition, the three-dimensional EASM formulation is not fully consistent, since the production to dissipation ratio P_k/ϵ is approximated using the solution for two-dimensional mean flows. Even though the full three-dimensional form might be required in some cases, two-dimensional EASM approximations are very appealing from a computational perspective and may provide a good compromise between predictive accuracy and computational expense. For the two-dimensional EASM the β_i coefficients reduce to

$$\begin{aligned} \beta_1 \;&=\; -A_1 N/Q, \quad \beta_2 = 2A_1 A_2/Q, \quad \beta_4 = -A_1/Q, \\ &\quad \beta_3 = \beta_5 = \beta_6 = \beta_7 = \beta_8 = \beta_9 = 0, \end{aligned} \tag{6.10}$$

where

$$Q = N^2 - 2II_\Omega - \frac{2}{3}A_2^2 II_S. \tag{6.11}$$

The anisotropy tensor $a_{ij} = F_{ij}\left(S_{ij}, \Omega_{ij}\right)$ (6.1) is expressed as an isotropic second-order tensor-valued function which depends on the two independent tensors S_{ij} and Ω_{ij}. The isotropic tensor function for a_{ij} satisfies the property $\boldsymbol{a}(\boldsymbol{Q}\boldsymbol{S}\boldsymbol{Q}^T, \boldsymbol{Q}\boldsymbol{\Omega}\boldsymbol{Q}^T) = \boldsymbol{Q}\boldsymbol{a}(\boldsymbol{S}, \boldsymbol{\Omega})\boldsymbol{Q}^T$, where $\boldsymbol{Q}$ is an orthogonal transformation matrix. Thus, the expression for a_{ij} is independent of the coordinate system used and hence, preserves

coordinate-frame invariance (see Gatski & Jongen, 2000). In the case of two-dimensional mean flow, only the two independent invariants II_S and II_Ω exist ($III = 0$, $IV = 0$ and $V = 0.5II_SII_\Omega$). This has the consequence that the isotropic tensor function for a_{ij} reduces to a three-term basis. Since all terms in the polynomial expansion of a_{ij} are linearly independent, any reduced basis will conserve the coordinate-frame invariance property of the isotropic tensor function for a_{ij}. In fact, the three-term basis is a very popular choice, since it provides an exact representation in two-dimensional mean flows, and provides an approximation, optimal in the least-squares sense, for the computation of three-dimensional mean flows (see Gatski & Jongen, 2000). In addition, the formulation is significantly simpler and numerically less expensive, compared to, for example, a ten-term basis.

Before the transport equations for the turbulence velocity-scale and length-scale variable are introduced, some further comments about the baseline EASM model are necessary. The baseline EASM is not used in conjunction with any streamline curvature modification as discussed, for example, in Wallin & Johansen (2002) and Hellsten (2002). The reasons for neglecting these modifications are twofold. First, curvature modifications significantly deteriorate the stability and convergence characteristics of the EASM (see, for example, Hellsten, 2005). Second, as pointed out in Wang *et al.* (2005), the success of curvature corrections is mainly limited to improved predictions in simple strongly curved flows, for example, the flow in a strongly curved two-dimensional U-duct. They are, however, less or even counter effective in more general three-dimensional flows, or flows with recirculation, due to over-prediction of the contribution from the curvature correction. For these two reasons curvature modifications are not included in the baseline EASM.

The relations above must be supplemented by a transport equation for the turbulence velocity and length-scale. The velocity scale is determined from a transport equation for the turbulence kinetic energy k. Many previous studies have independently demonstrated the importance of the length-scale equation in the framework of RANS modelling (see, for example, Wilcox, 1993). Due to the inability of the standard dissipation rate equation to produce correct length scales in adverse pressure gradient flows, the length-scale equation used in this work is based on the formulation proposed by Menter (1994), where the ω equation is used in the near-wall region and blended to the ϵ equation in the wake region of attached boundary layers. The blending retains the improved predictions of the ω formulation for adverse pressure gradient flows and at the same time avoids the spurious sensitivity of the specific turbulence dissipation rate equation to free-stream values. In addition, the ω-based formulation can be integrated to the wall without requiring ad-hoc

modification in order to recover the correct velocity profile. The transport equations used in this study are based on the re-calibrated version of Menter's blending approach as presented in Hellsten (2004, 2005). The aim of the recalibration effort of Hellsten (2005) is to take into account the non-constant C_{μ}^{eff} of the EASM formulation and to improve the model behaviour at the outer edge of a turbulent boundary layer as well as the spreading rate of wakes and mixing layers. In addition, the closure coefficients have been optimised to give satisfactory performance for a range of calibration cases, for example, zero and adverse pressure-gradient boundary layers, channel flow, wakes and mixing layers.

The transport equations for the turbulence kinetic energy k and the specific turbulence dissipation rate ω take the following form

$$\frac{Dk}{Dt} = P_k - \beta^* k\omega + \frac{\partial}{\partial x_j}\left[\left(\nu + \sigma_k \nu_T\right)\frac{\partial k}{\partial x_j}\right], \tag{6.12}$$

$$\frac{D\omega}{Dt} = \gamma\frac{\omega}{k}P_k - \beta\omega^2 + \frac{\partial}{\partial x_j}\left[\left(\nu + \sigma_\omega \nu_T\right)\frac{\partial \omega}{\partial x_j}\right] + \frac{\sigma_d}{\omega}\max\left(CD_{k\omega}, 0\right), \tag{6.13}$$

where $P_k = -\overline{u_i' u_j'}\partial\overline{u}_i/\partial x_j$ is the production of turbulence kinetic energy and $CD_{k\omega} = (\partial k/\partial x_j)(\partial\omega/\partial x_j)$ is a turbulent cross-diffusion term, arising from the formal transformation of the equation for the dissipation rate ϵ to a form based on the specific dissipation rate ω. The closure coefficients are obtained by blending the sets of coefficients from the ϵ and ω formulations

$$\phi = F_1\phi_1 + \left(1 - F_1\right)\phi_2. \tag{6.14}$$

The blending function F_1 used in this study follows the proposal of Hellsten (2005) but is slightly modified compared Menter's original formulation

$$F_1 = \tanh\left(1.5\Gamma^4\right), \tag{6.15}$$

with

$$\Gamma = \min\left[\max\left(\Gamma_1, \Gamma_2\right), \Gamma_3\right], \tag{6.16}$$

where

$$\Gamma_1 = \frac{\sqrt{k}}{\beta^*\omega y}, \quad \Gamma_2 = \frac{500\nu}{\omega y^2}, \quad \Gamma_3 = \frac{20k}{\max\left[y^2 CD_{k\omega}/\omega, 200k_\infty\right]}, \tag{6.17}$$

and k_∞ is the free-stream value of turbulence kinetic energy. The closure constants are given as:

Set 1: $\gamma_1 = 0.518, \quad \beta_1 = 0.0747, \quad \sigma_{K_1} = 1.1, \quad \sigma_{\omega_1} = 0.53, \quad \sigma_{d_1} = 1.0.$

Set 2: $\gamma_2 = 0.440, \quad \beta_2 = 0.0828, \quad \sigma_{K_2} = 1.1, \quad \sigma_{\omega_2} = 1.0, \quad \sigma_{d_2} = 0.4.$

6.2 Planar Channel Flow

In order to verify the correct implementation and to highlight the performance and deficiencies of the baseline EASM, the results for a fully developed turbulent channel flow are considered next. As a reference, the results of the k-ω-SST and φ-α-UMIST (Keshmiri *et al.*, 2008) turbulence model are also included.

6.2.1 Computational Setup

The flow in the planar channel is turbulent and fully developed with a Reynolds number of $Re_\tau = 590$, based on the skin friction velocity u_τ and the channel half-width $H = L_y/2$. The flow under consideration is essentially a 1D problem, since there is no variation of the mean flow field in the streamwise and the spanwise directions. For this reason periodic boundary conditions can be used in the spanwise and streamwise directions. In order to maintain a constant flow rate through the channel an additional momentum source is introduced to the momentum equations. The momentum source could iteratively be adjusted in order to yield the desired flow rate. Alternatively, the required pressure gradient can be computed exactly for the target Re_τ by considering the momentum balance in the streamwise direction. Simulations are conducted by imposing a fixed pressure gradient in the streamwise direction. The pressure gradient is computed from the relation $\mathrm{d}\overline{p}/\mathrm{d}x = \tau_w/H$ with the wall shear stress $\tau_w = \rho u_\tau^2$ and the skin friction velocity u_τ computed from the target Re_τ. The results are assessed and compared to DNS data of Moser *et al.* (1999).

Simulations are performed on a computational grid with a first wall-normal grid spacing of $y_1^+ \approx 0.2$ at the top and bottom wall and 200 cells in the wall-normal direction. Results have also been obtained on a computational grid with 400 cells in the wall-normal direction and they showed no significant differences. The convective fluxes are discretised using a second-order accurate upwind-difference scheme. The viscous terms use a second-order central-difference scheme. Steady-state results are obtained using the SIMPLE pressure-correction algorithm.

6.2.2 Results

The results shown in figure 6.1 are for the mean-velocity profile U^+, the normal components of the anisotropy tensor $a_{ij} = \overline{u_i' u_j'}/k - (2/3)\delta_{ij}$, the Reynolds-stress

components $\overline{u_i' u_j'}^+$, the asymptotic behaviour of the Reynolds-stress components, the III_a-II_a invariant map and the balance of the turbulence kinetic energy equation. The superscipt + denotes normalisation using the skin-friction velocity u_τ and viscosity ν.

All turbulence models predict the correct log-law behaviour of the velocity profile U^+. However, all turbulence model predict somewhat lower magnitudes of velocity in the buffer region $y^+ \approx 10-30$. The φ-α-UMIST is the only model, which predicts the correct velocity magnitude in the centre of the channel, whereas the k-ω-SST and EASM-2D predict somewhat too low values.

For the present case, the k-ω-SST and φ-α-UMIST model, which are both based on a linear constitutive stress-strain relationship fail to predict any anisotropy of the normal-Reynolds-stress components. This is, because the anisotropy is set by the strain rate tensor S_{ij}^* (recall that $a_{ij} = -2(\nu_T/k)S_{ij}^*$), and for this flow $S_{11}^* = S_{22}^* = S_{33}^* = 0$. The EASM-2D on the other hand, provides good predictions for all normal-anisotropy components in the log region. However, since the EASM formulation is based on a quasi-homogeneous pressure-strain model, the near-wall behaviour of the anisotropy tensor is largely in error, i.e. a_{22} does not approach the correct limit $a_{22} \to -2/3$ at the wall, and the near-wall peaks of a_{11} and a_{33} are not reproduced. This picture is confirmed by the anisotropy-invariant map in figure 6.1 (e), where only the EASM-2D is able to reproduce some parts of the locus predicted by DNS. However, the two-component line is not reached, which is a direct consequence of the incorrect wall limit of a_{22} and a non vanishing energy contained in the $\overline{v'v'}$ Reynolds-stress component. Further, at the centre of the channel, where the velocity gradient vanishes, the algebraic non-linear stress-strain relationship of the EASM fails to predict any anisotropy. In the centre of the channel, diffusion dominates the budget of $\overline{u_i' u_j'}$ and the failure of the EASM can be linked to the weak-equilibrium assumption employed in the derivation of the EASM, which effectively neglects all transport of $\overline{u_i' u_j'}$.

Concerning the components of the Reynolds-stress tensor in sub figures (c) and (d), all models predict the shear stress $\overline{u'v'}$ in good agreement with reference data. The normal components of the Reynolds-stress tensor show the same trend as the anisotropy tensor, i.e. the linear models predict the same magnitude for all normal components $\overline{u'u'} = \overline{v'v'} = \overline{w'w'} = (2/3)k$, which is clearly not correct. The EASM-2D is able to predict realistic levels of the normal-Reynolds-stress components in the log region. However, shortcomings can be observed in the near-wall region where the prediction of the normal-Reynolds-stress $\overline{u'u'}$ is largely in error. In addition, the

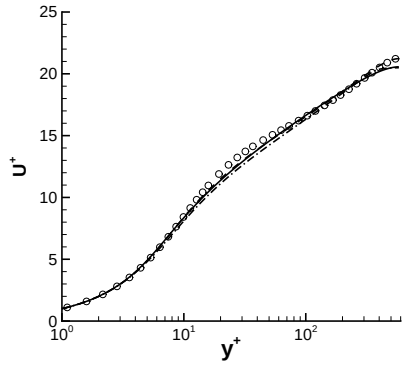

(a) Normalized velocity U^+.

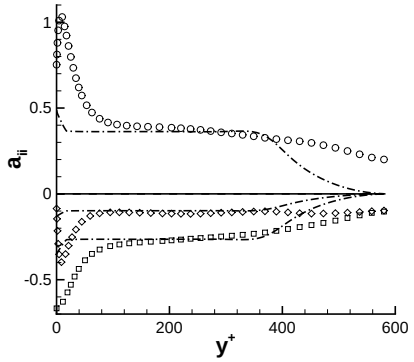

(b) Components of the anisotropy tensor , (○) a_{11} ; (□) a_{22} ; (◇) a_{33}.

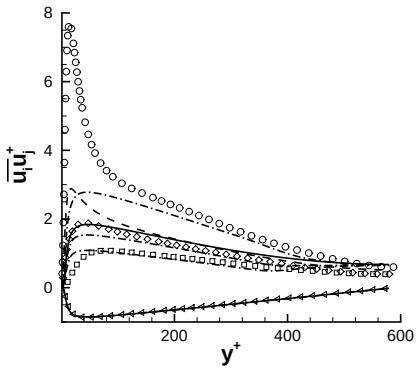

(c) Components of the Reynolds-stress tensor, (○) $\overline{uu}^+$; (□) $\overline{vv}^+$; (◇) $\overline{ww}^+$; (◁) $\overline{uv}^+$.

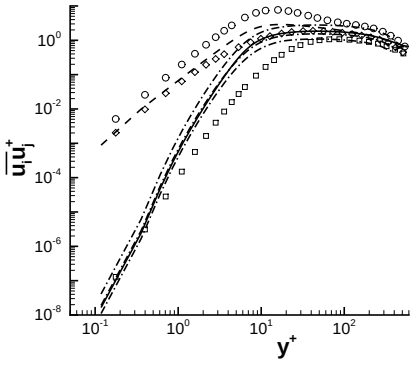

(d) Asymptotic behaviour of normal-Reynolds-stress components.

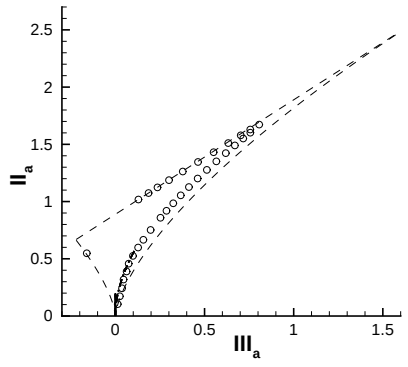

(e) Anisotropy-invariant map.

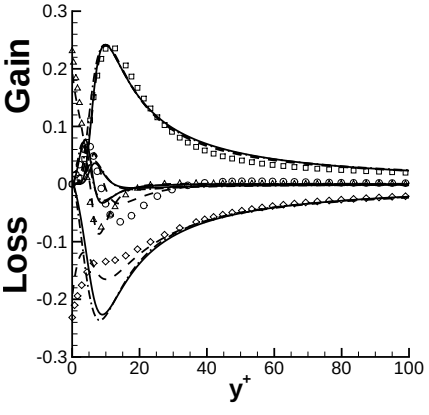

(f) Budget of the turbulence kinetic energy equation, (□) P_k^+; (△) $\nu\nabla^2 k^+$; (○) D_k^+; (◇) ϵ^+.

FIGURE 6.1: Predictions for a planar channel flow at $Re_\tau = 590$. Symbols correspond to DNS (Moser *et al.*, 1999), (—) k-ω-SST, (- - -) φ-α-UMIST, ($-\cdot-$) k-ω-EASM-2D.

asymptotic behaviours of the normal-Reynolds-stress components are not satisfactorily reproduced by any of the models considered here. The k-ω-SST predicts an asymptotic behaviour of $\overline{u_i' u_i'} \approx O(y^{+4.8})$, whereas the φ-α-UMIST model predicts $\overline{u_i' u_i'} \approx O(y^{+2})$. The leading-order asymptotic behaviour of the normal-Reynolds-stress components of the linear models is directly linked to the asymptotic behaviour of the evolution equation for the turbulence kinetic energy k. In the EASM formulation, the normal-Reynolds-stress components are additionally influenced by non-linear terms appearing in the constitutive stress-strain relationship.

The budget of the turbulence kinetic energy equation is shown in sub figure (f). Away from the wall, for $y^+ > 30$, the turbulence kinetic energy production P_k^+, transport D_k^+, viscous diffusion $\nu\nabla^2 k^+$ and dissipation rate ϵ^+ are in good agreement with reference data. The φ-α-UMIST model, which solves a transport equation for the dissipation rate ϵ, gives the best overall agreement with DNS data close to the wall. In particular, the dissipation rate ϵ^+ and viscous diffusion $\nu\nabla^2 k^+$, which are involved in the near-wall balance of k, are well reproduced. This explains why the φ-α-UMIST model is able to correctly predict the asymptotic behaviour $O(y^{+2})$ of turbulence kinetic energy as the wall is approached. The models based on the specific dissipation rate ω are not very successful in providing realistic prediction for ϵ^+ and $\nu\nabla^2 k^+$ close to the wall. Both terms go to zero rather than remaining finite at the wall. This explains the erroneous prediction of the asymptotic behaviour $O(y^{+4.8})$ of turbulence kinetic energy as the wall is approached.

The discussion above clearly highlights the deficiency of the baseline EASM constitutive relations to predict the highly anisotropic flow close to the wall ($y^+ < 100$). This is due to the lack of adequate modification of the quasi-homogeneous pressure-strain model and the high-Reynolds-number form of the transport equations for the turbulence quantities. The budget of turbulence kinetic energy shows that deficiencies exist in predicting the correct magnitude for the dissipation rate ϵ^+ and the viscous diffusion term $\nu\nabla^2 k^+$, which are both involved in the near-wall balance.

6.3 NASA Hump

The NASA wall-mounted hump is used here in order to evaluate the performance of the EASM model to capture important phenomena associated with separation from a smooth surface, recirculation and subsequent reattachment of the flow. This test case has also been used in the CFD validation workshops on turbulent separation control and refined turbulence modelling (Langley Research Center Workshop about CFD Validation of Synthetic Jets and Turbulent Separation Control 2004 and the 11th/12th ERCOFTAC/IAHR Workshop on Refined Turbulence Modelling 2005/2006). The configuration consists of a Glauert-Goldschmied type body, which is mounted on a splitter plate (see figure 6.2).

The model investigated in the experiment has a spanwise width of $L_z = 1.4c$, where c is the chord length. End plates are mounted on either side. At approximately $x/c = 0.65$ a slot opening extends over the entire spanwise width of the model in order to allow for separation control of the flow. In the following investigations only the baseline case will be considered with no-flow control.

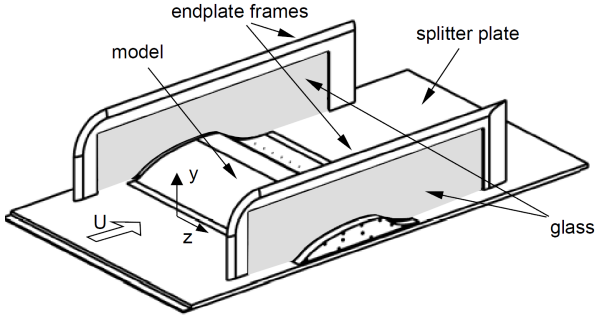

FIGURE 6.2: Geometry of the NASA hump, reproduced from Greenblatt *et al.* (2004).

The flow is tripped at the splitter plate leading edge in order to yield a fully developed flow approaching the hump. The Reynolds number based on the chord c is $Re_c = 9.36 \times 10^5$ and corresponds to the experimental data of Greenblatt *et al.* (2004, 2006). Detailed information about the velocity field and Reynolds stress are available for the separated flow region as well as surface pressure and wall shear stress measurements on the model. As a reference, the results of the k-ω-SST and φ-α-UMIST turbulence models are also included and compared to the experimental data.

6.3.1 Computational Setup

The computational domain used here does not include the slot for flow control (see figure 6.3), and has an extended upstream section of $x/c = 6.39$ in order to generate a fully turbulent boundary layer approaching the hump. The upstream extent is chosen such that the velocity profile of the approaching turbulent boundary layer matches experimental data at the location $x/c = -2.14$. At the outlet, located at $x/c = 4$ downstream of the hump, zero-gradient boundary conditions are specified for all quantities. The end plates used in the experiment introduced some undesired three-dimensional effects near the end plate. The effect of the side walls are approximated in the two-dimensional computational domain by a modified contour of the upper inviscid boundary (see Rumsey & Greenblatt, 2009, for details). All simulations are performed on a grid using 840×216 cells and a maximum first wall-normal grid spacing of $y_1^+ \approx 0.2$. Grid convergence has been verified using a coarser computational grid with every other grid point removed. The convective fluxes are discretised using a second-order accurate upwind-difference scheme. The viscous terms use a second-order central-difference scheme. Steady-state results are obtained using the SIMPLE pressure-correction algorithm.

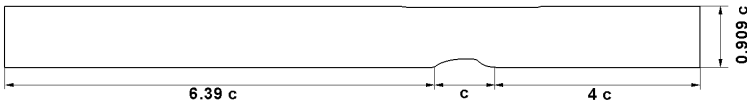

(a) Computational domain.

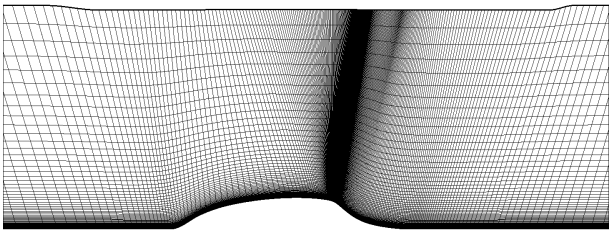

(b) Coarse grid.

FIGURE 6.3: Computational setup of the NASA hump.

6.3.2 Results

The predicted streamwise velocity contour U/U_0 and computed streamlines are shown in figure 6.4 for the three turbulence models investigated and experimental data. It is evident that the recirculation region in the experiment is significantly smaller compared to the predictions of all three turbulence models. The experimental data show the separation and reattachment point to be located at approximately $x_s/c = 0.66 - 0.67$ and $x_r/c = 1.1$, respectively. The k-ω-SST and k-ω-EASM-2D predict the separation point at $x_s/c = 0.655$. The φ-α-UMIST model, which is based on a transport equation for the turbulence dissipation rate ϵ, predicts separation at $x_s/c = 0.660$, which is in good agreement with the reference data. The defect common to turbulence models based on the turbulence dissipation rate ϵ, to delay separation, is not observed here.

The location of the reattachment point is predicted very similar by all three turbulence models. The k-ω-SST predicts the longest recirculation zone with reattachment occurring at $x_r/c = 1.28$, the φ-α-UMIST gives $x_r/c = 1.26$ and the EASM-2D $x_r/c = 1.24$, giving the best agreement with reference data. The better agreement of the EASM-2D might be linked to a more realistic prediction of the reattachment process by providing improved predictions for the normal-Reynolds-stress components. Further, the reattachment streamline of the experiment shows a steep inclination to the wall, which is reproduced by the EASM-2D model. Both, the k-ω-SST and φ-α-UMIST model, show a shallower inclination of the reattachment streamline.

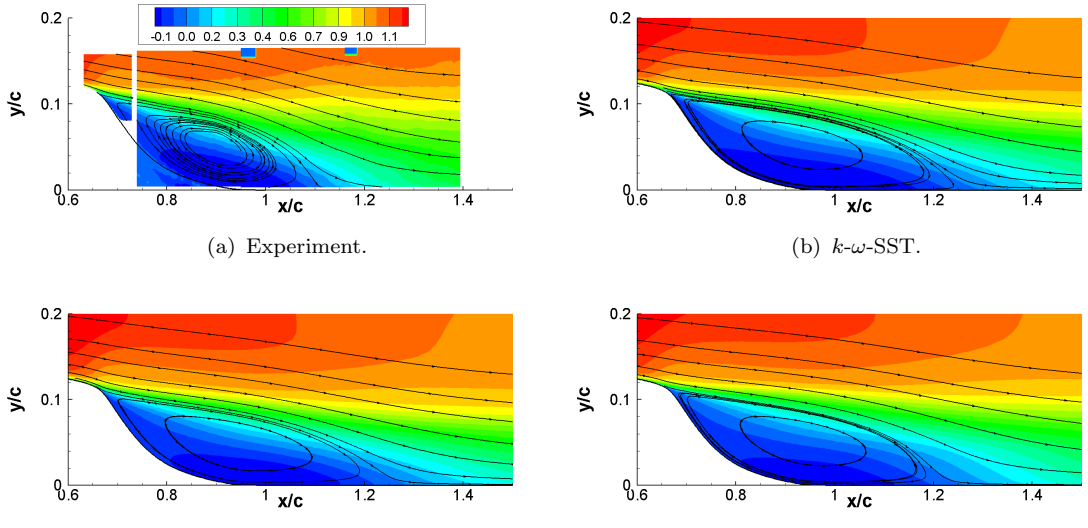

(a) Experiment.

(b) k-ω-SST.

(c) φ-α-UMIST.

(d) EASM-2D.

FIGURE 6.4: Streamwise velocity contours U/U_0 and streamlines for the NASA hump case.

Figure 6.5 shows predictions for the surface-pressure coefficient $C_p = (p - p_{ref})/(0.5\rho U_0^2)$ and the skin-friction coefficient $C_f = \tau_w/(0.5\rho U_0^2)$ distributions. The surface-pressure distribution of the k-ω-SST and EASM-2D are very similar with only negligible differences. Both under-predict the low pressure peak on the model upstream of the separation point. The φ-α-UMIST model provides somewhat better predictions in this region. On the other hand, the magnitude of the surface pressure in the recirculation region is better predicted by the k-ω-SST and EASM-2D models. Further, all three turbulence models predict too slow a rate of pressure recovery downstream of the reattachment point. The skin-friction coefficient distribution is more sensitive to the turbulence model formulation. In the region upstream of the separation point the k-ω-SST and φ-α-UMIST models predict a much lower magnitude of skin-friction compared to the EASM-2D model. It is difficult to judge, due to the scatter in the experimental data, which model performs better. The situation is much clearer downstream of the separation point. Inside the recirculation region the k-ω-SST and k-ω-EASM-2D models predict the skin-friction magnitude in much better agreement with the reference data than the φ-α-UMIST model, which significantly over-estimates the magnitude of skin friction. None of the turbulence models is capable of predicting the correct location of maximum skin friction in the recirculation region. This is linked to the erroneous prediction of the extent of the recirculation zone. After reattachment, only the EASM-2D model is able to recover the correct magnitude of skin-friction. The skin-friction predicted by the k-ω-SST after reattachment remains too low, whereas the φ-α-UMIST model shows somewhat too high levels of skin friction.

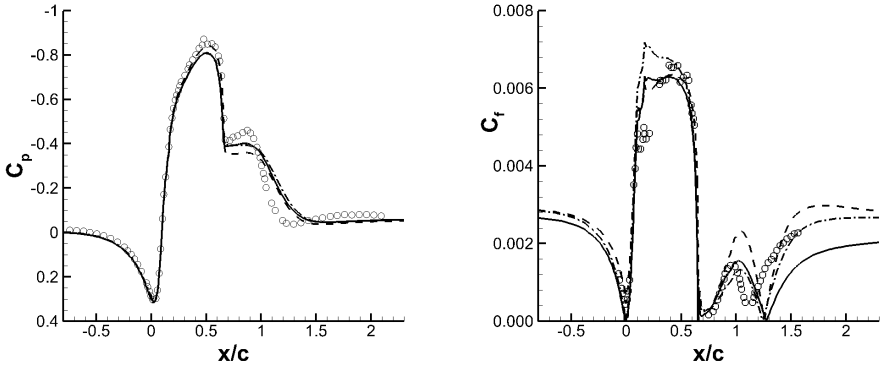

(a) Surface-pressure coefficient C_p. (b) Skin-friction coefficient C_f.

FIGURE 6.5: Surface-pressure coefficient C_p and skin-friction coefficient C_f distribution. Symbols correspond to experimental data of Greenblatt *et al.* (2004, 2006). (—) k-ω-SST, (- - -) φ-α-UMIST, (−·−) EASM-2D.

The velocity profiles for the streamwise and vertical velocity component U/U_0 and V/U_0 are shown in figure 6.6, for the stations $x/c = 0.65$, $x/c = 0.8$, $x/c = 1.0$ and $x/c = 1.2$. The velocity profiles reflect what has been said in the preceding discussion. At the first station, $x/c = 0.65$, which is immediately upstream of the separation point, the φ-α-UMIST model predicts both components of the velocity profile in excellent agreement with experimental data. The k-ω-SST and EASM-2D show too strong a retardation of the streamwise velocity component close to the wall. This behaviour explains the somewhat too early separation from the hump observed for those two models. At the second station, $x/c = 0.8$, the better upstream predictions of the φ-α-UMIST model is reflected in the predictions of the streamwise velocity component, which is still in good agreement with reference data. The k-ω-SST and EASM-2D also predict the velocity profiles, but with somewhat larger departure from the reference data. At the next location farther downstream, $x/c = 1.0$, which is located just upstream of the reattachment point, the departure from experimental data, mainly away from the wall, becomes slightly more pronounced. Close to the wall, the reverse flow magnitude is in good agreement with reference data. The rapid flow reattachment and flow recovery occurring between $x/c = 1.0$ and $x/c = 1.2$ is not adequately predicted by any of the three turbulence models. Consequently, the near-wall region at the last station, $x/c = 1.2$, is rather poorly predicted by all models, but the EASM-2D showing somewhat improved predictions.

The final quantities for which reference data are available are the components of the Reynolds-stress and anisotropy tensor. The shear stress $\overline{u'v'}$ and normal-stress components $\overline{u'u'}$ and $\overline{v'v'}$ are shown in figure 6.7. The anisotropy tensor components a_{11} and a_{22} are shown in figure 6.8. It is noted that the uncertainty in the experimental data for the turbulence quantities is as much as 14%-20% at maximum, which makes a comparisson of absolute values difficult. The shear stress at station $x/c = 0.65$, where the flow is still attached, is well predicted by all models even though the EASM-2D predicts a slightly too large magnitude close to the wall. At the next two stations downstream, which are located in the recirculation region, the shear stress in the free-shear layer is under-predicted by all models. There is also a significant offset in peak-value location at $x/c = 1.0$. In the separated flow region, the models based on the specific dissipation rate ω seem to predict somewhat higher levels of shear stress compared to the φ-α-UMIST model. It is interesting to note that the EASM-2D predicts the highest levels of shear stress of all models even though the constant $C_\mu^{eff} = -0.5\beta_1 \approx 0.055$, in the eddy viscosity relation, is significantly reduced compared to the generally accepted value of $C_\mu^{eff} = 0.09$ or the prediction of the φ-α-UMIST model, which gives $C_\mu^{eff} = C_\mu^{\nu}\varphi \approx 0.095$. The

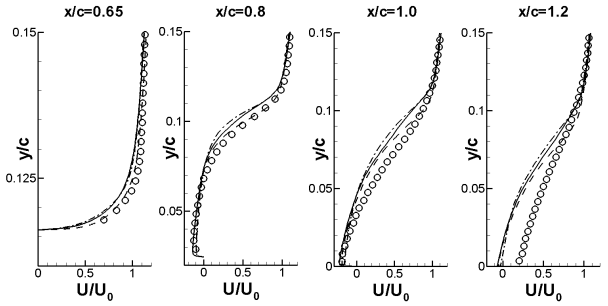

(a) Streamwise velocity component U/U_0

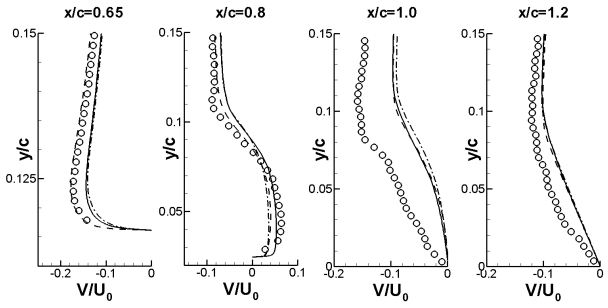

(b) Vertical velocity component V/U_0

FIGURE 6.6: Velocity profiles at different stations in the flow field. Symbols correspond to experimental data of Greenblatt *et al.* (2004, 2006). (—) k-ω-SST, (- - -) φ-α-UMIST, $(- \cdot -)$ EASM-2D.

rather low value predicted by the EASM relations is a consequence of the sensitivity of C_μ^{eff} to strain and rotation rate. The overall insufficient levels of shear stress in the free-shear layer consequently results in an over-prediction of the recirculation length.

In the prediction of the normal-Reynolds-stress and anisotropy components a clear trend becomes noticeable. At almost all stations in the flow field the EASM-2D is clearly superior in predicting the correct magnitude of the normal-Reynolds-stress components away from the wall. The same holds for the anisotropy tensor components, where significant improvements of the EASM-2D over the models based on a linear stress-strain relationship can be observed. Even though the near-wall behaviour of the wall-normal fluctuations $\overline{v'v'}$ seems to be in agreement with reference data at most locations, predictions of the streamwise fluctuations $\overline{u'u'}$ and both anisotropy components are largely in error. This behaviour is consistent to what has been observed in the prediction of the planar channel flow in section 6.2.

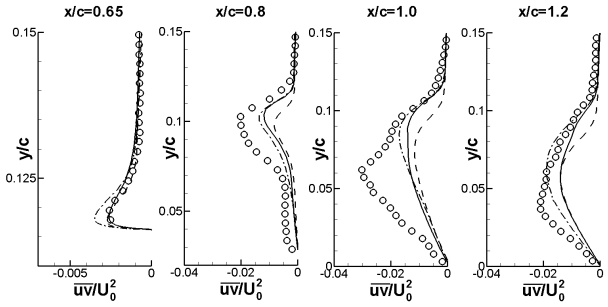

(a) Reynolds-stress component $\overline{u'v'}$

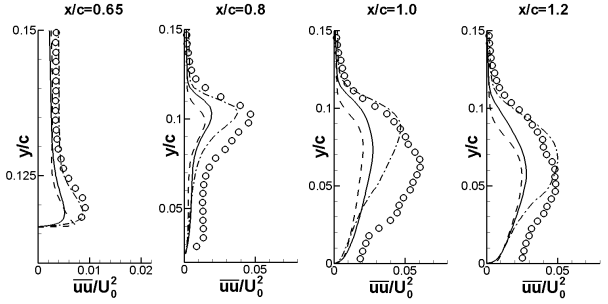

(b) Reynolds-stress component $\overline{u'u'}$

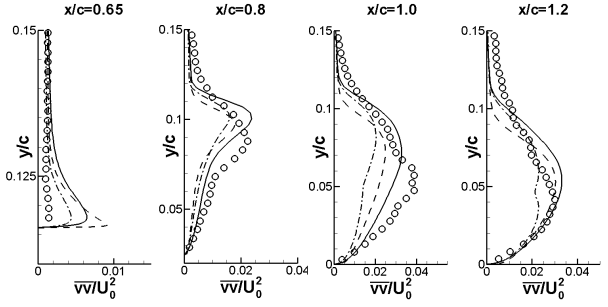

(c) Reynolds-stress component $\overline{v'v'}$

FIGURE 6.7: Components of the Reynolds-stress tensor. Symbols correspond to experimental data of Greenblatt *et al.* (2004, 2006). (—) k-ω-SST, (- - -) φ-α-UMIST, ($-\cdot-$) EASM-2D.

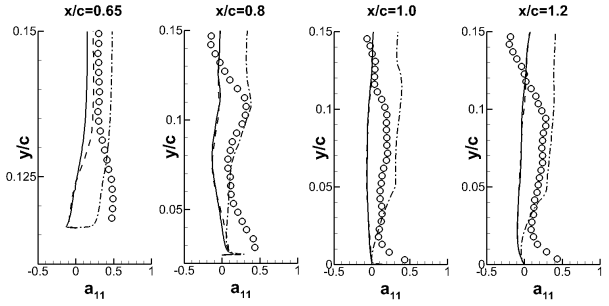

(a) Anisotropy tensor component a_{11}

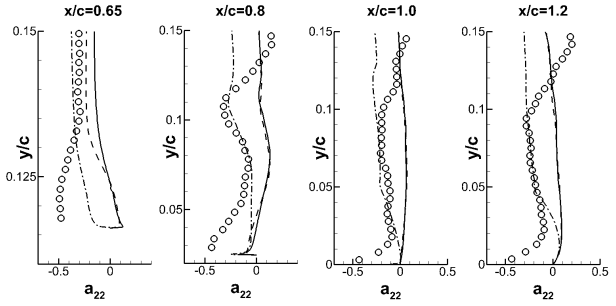

(b) Anisotropy tensor component a_{22}

FIGURE 6.8: Components of the anisotropy tensor. Symbols correspond to experimental data of Greenblatt *et al.* (2004, 2006). (—) k-ω-SST, (- - -) φ-α-UMIST, (– · –) EASM-2D.

6.4 Three-Dimensional Diffuser

The last test case considered is the flow in an asymmetric three-dimensional diffuser. The flow in the diffuser includes three-dimensional boundary-layer separation and turbulence-driven secondary motion in the corners of the diffuser, which makes it a challenging test case for any RANS turbulence model, but especially for models based on a linear stress-strain relationship. This case has been subject to the 13th/14th ERCOFTAC/IAHR Workshop on Refined Turbulence Modelling. The diffuser has a rectangular cross section, as depicted in figure 6.9, with a geometric expansion of 11.3° and 2.56°, respectively. The Reynolds number is $Re_H = 10000$, based on the channel height H and bulk velocity U_b, or approximately $Re_\tau \approx 588$ at the diffuser inflow. In the experiments of Cherry *et al.* (2008, 2009) a long rectangular channel has been used upstream of the diffuser, which results in a fully developed turbulent flow at the diffuser inlet. Magnetic-resonance velocimetry has been used to measure the three-dimensional velocity field in the entire diffuser volume. In addition, surface-pressure measurements at the bottom wall and streamwise velocity fluctuations are also available for comparison. The experimental data show an uncertainty of as much as 10% at maximum. Simulations are performed with the EASM-2D and EASM-3D and the results of the k-ω-SST and φ-α-UMIST turbulence model are included as a reference.

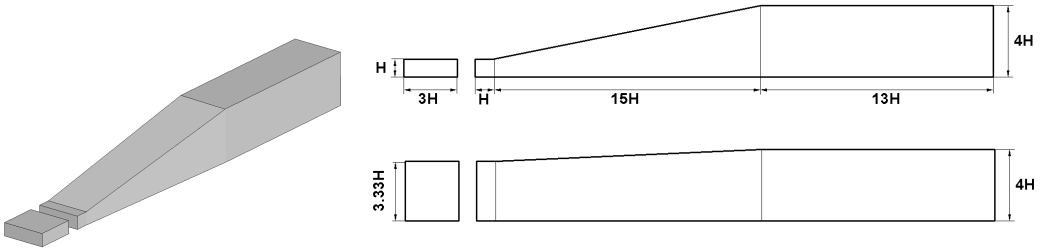

(a) Isometric view

(b) Top: x-y plane. Bottom: x-z plane.

FIGURE 6.9: Three-dimensional diffuser geometry.

6.4.1 Computational Setup

The simulations are performed on a computational grid with approximately 2.1×10^6 cells ($335 \times 65 \times 97$) for the diffuser domain. In order to generate fully developed turbulent inflow conditions a short rectangular channel is computed simultaneously and the flow is mapped to the inlet of the diffuser domain. The boundary conditions

of the inflow channel are periodic in the streamwise direction and the flow is driven by an imposed pressure gradient. The pressure gradient is adjusted iteratively to yield the desired bulk velocity U_b. The computational grid of the separate channel-flow domain has approximately 400000 cells. The convective fluxes are discretised using a second-order accurate upwind-difference scheme. The viscous terms use a second-order central-difference scheme. Steady-state results are obtained using the SIMPLE pressure-correction algorithm. No-slip boundary conditions are specified for all walls and zero-gradient boundary conditions are used at the diffuser outlet. It should also be mentioned that the diffuser used in the experiment joins the inflow duct by a small radius. The small radius is not modelled here and approximated by a sharp corner, which considerably simplifies the grid generation process. A grid convergence study was conducted on a computational grid with a 50% increase in cells in each coordinate direction ($502 \times 98 \times 145$) and with a total number of approximately 7×10^6 cells for the diffuser domain. Since the velocity field predicted by the coarser computational collapses with predictions on the finer mesh, all results presented subsequently are obtained on the coarse computational grid.

6.4.2 Results

The presentation of results is split into two parts. First, a comparison of the flow field at the spanwise location $z/L_z = 0.5$, where $L_z = 3.33H$ is the spanwise width of the inflow channel, is presented. This is followed by an analysis of the streamwise evolution of the three-dimensional flow.

Centre Plane $z/L_z = 0.5$

The predictions of the surface-pressure distribution $C_p = (p - p_{ref})/(0.5\rho U_b^2)$ at the bottom wall ($y/H = 0$) is shown in figure 6.10. The reference pressure p_{ref} is evaluated at the bottom wall, where the geometric expansion starts, $x/L = 0$, where $L = 15H$ is the length of the diffuser. It is obvious that none of the turbulence models investigated here is capable of predicting the correct pressure recovery observed in the experiment. All of the turbulence models have difficulties in predicting particularly the initial, rapid pressure recovery, which extents up to the location $x/L \approx 0.5$. For the streamwise locations $x/L > 0.5$, all models predict the reduced, slower rate of pressure recovery, which agrees with the trend observed in the experiment. However, the magnitude of C_p remains significantly too low for $x/L > 0.5$. The k-ω-SST shows the largest departure from reference data. The EASM-2D and φ-α-UMIST give very similar results, which are in better agreement

with the experimental data. The EASM-3D, which might be expected to be better suited for predicting truly three-dimensional flows, gives a surface-pressure distribution, which is less accurate compared to EASM-2D. Most of the turbulence models investigated in the 13th/14th ERCOFTAC/IAHR Workshop, including more sophisticated DRSM closures, show a similar trend with an under-prediction of C_p, as observed here.

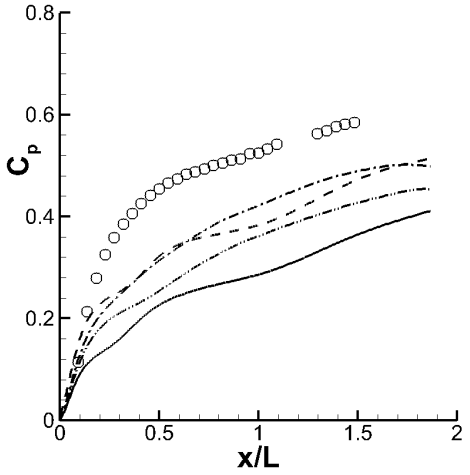

FIGURE 6.10: Surface-pressure coefficient C_p at the bottom wall. Symbols correspond to experimental data of Cherry *et al.* (2008, 2009). (—) k-ω-SST, (- - -) φ-α-UMIST, (−·−) EASM-2D and (−··−) EASM-3D.

Some more insight into the flow field predictions can be gained from figure 6.11, which shows the streamwise velocity contour U/U_b at the centre plane $z/L_z = 0.5$. The figure also includes a thick line, which corresponds to the zero-velocity contour line and gives the extent of the separated flow region. The experimental data show a large separation zone, which extents approximately from $x/H \approx 7$ to $x/H \approx 19$. It is now obvious that the initial, rapid, pressure recovery occurs in the region $x/H < 7$, where the flow is still attached. The region of a slowed pressure recovery corresponds to the separated flow region downstream of $x/H \approx 7$. It is important to note that the boundary-layer separation is a three-dimensional process and starts much further upstream in the corner of the diffuser. None of the turbulence models predicts the extent of the recirculation zone in satisfactory agreement with reference data. The φ-α-UMIST model fails to predict any separation apart from the tiny recirculations zone just downstream of the sharp corner, where the geometric expansion starts. This is also predicted by all other models. The main recirculation zone predicted by the k-ω-SST starts too far upstream, at $x/H \approx 4$, and only extents to $x/H \approx 11$. The EASM-2D predicts a very small recirculation zone ranging from $x/H \approx 13$ to

$x/H \approx 18$. The location of the recirculation zone predicted by EASM-3D is closest to the reference data, even though the extent from $x/H \approx 11$ to $x/H \approx 17$ is still too small. Another fundamental difference becomes obvious from the velocity contour plots. The experiment shows that the flow discharged into the diffuser propagates towards the centre of the diffuser, away from the bottom wall. All turbulence models predict the flow to remain too close to the bottom wall.

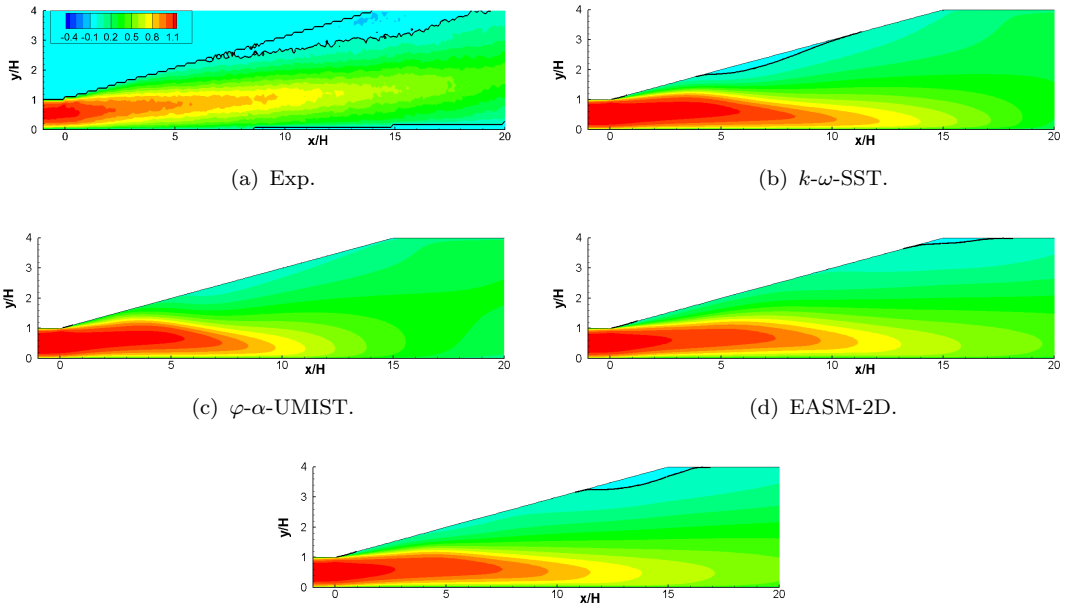

(a) Exp.

(b) k-ω-SST.

(c) φ-α-UMIST.

(d) EASM-2D.

(e) EASM-3D.

FIGURE 6.11: Streamwise velocity contours U/U_b at the plane $z/L_z = 0.5$.

A more detailed comparison of the flow field on the centre plane is shown in figures 6.12 and 6.13, where the velocity profile U/U_b, Reynolds-stress and anisotropy tensor components are plotted at the four streamwise locations, $x/H = 1$, $x/H = 5$, $x/H = 12$ and $x/H = 16$. The flow at the diffuser inlet, $x/H = 0$, was also analysed but the results are not shown here. The diffuser inflow condition are better predicted by the EASM-2D and EASM-3D model, which predict 5% less streamwise velocity magnitude in the centre of the channel and hence show better agreement with the reference data. It may be argued that improved inflow conditions are a consquence of the non-linear stress-strain relationship of the EASM, which is able to resolve the anisotropy-induced secondary motion developing in the corners of the inflow duct. The experimental data show a slight asymmetry in the velocity profile at the inflow, which is not captured by any of the turbulence models investigated here. It is not clear whether the flow at the diffuser inlet in the experiment is indeed asymmetric or whether the asymmetry stems from inaccuracies of the measurements. It should be kept in mind that the flow in the diffuser is sensitive to the

inflow boundary conditions and the asymmetry in the velocity profile may cause the flow in the diffuser to develop differently compared to a symmetric velocity profile. At the location $x/H = 1$, the same trend as for the inflow is still visible. Both EASM models predict the velocity magnitude, in the centre of the diffuser, in better agreement with the experimental data than the k-ω-SST and φ-α-UMIST. Further downstream, at station $x/H = 5$, the location of peak velocity has moved away from the bottom wall towards the centre of the diffuser. A similar trend is captured by all turbulence models. However, the location of peak velocity remains too close to the bottom wall. In addition, the magnitude of streamwise velocity is significantly over-predicted with a difference of the order of 15% of U_b. At the top wall, overall good agreement is observed for most turbulence models, apart from the k-ω-SST, which already shows separated flow at this station. The error in predicting the location of peak velcoity becomes more pronounced for the stations farther downstream, $x/H = 12$ and $x/H = 16$. The measurements show that the location of peak velocity is close to the centre of the diffuser, whereas the predicted peak velocity location remains too close to the bottom wall. The φ-α-UMIST model shows overall the greatest departure in the velocity profile from reference data. It not only fails in predicting the location of peak velocity, but it also significantly under-predicts the velocity magnitude. In fact, at the station $x/H = 16$, the flow is almost uniform over the entire diffuser height. The k-ω-SST model does somewhat better in predicting the peak velocity magnitudes, but it also fails in predicting the flow close to the top wall. The EASM-2D and EASM-3D show overall the best, but not satisfying, agreement with the reference data. Improvements are not only observed for the location of peak velocity and velocity magnitude, the EASM models also predict the flow at the top wall, at $x/H = 16$, in good agreement with the reference data.

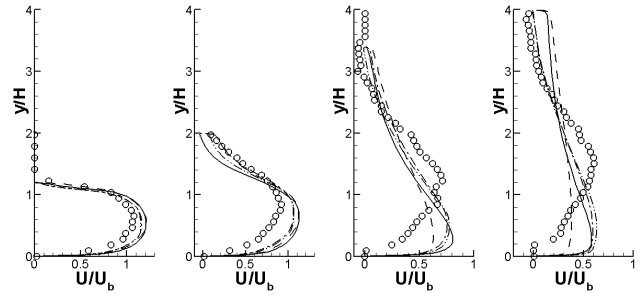

(a) Velocity component U/U_b

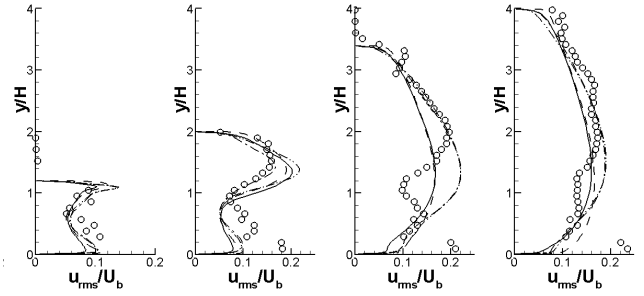

(b) $\overline{u'}_{rms}/U_b$

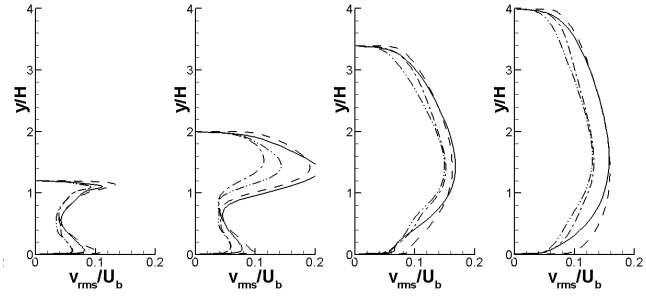

(c) $\overline{v'}_{rms}/U_b$

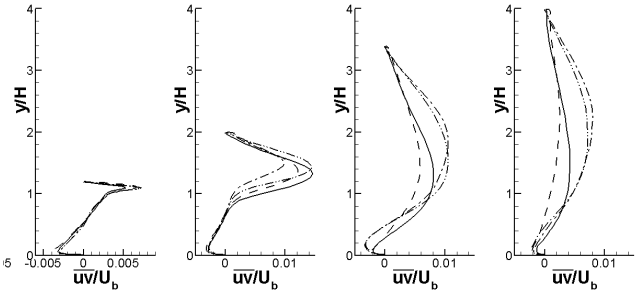

(d) $\overline{u'v'}/U_b^2$

FIGURE 6.12: Velocity and Reynolds-stress components at the centre plane $z/L_z = 0.5$. Locations from left to right: $x/H = 1$, $x/H = 5$, $x/H = 12$ and $x/H = 16$. Symbols correspond to experimental data of Cherry *et al.* (2008, 2009). (—) k-ω-SST, (- - -) φ-α-UMIST, $(- \cdot -)$ EASM-2D and $(- \cdot\cdot -)$ EASM-3D.

The predictions of the Reynolds-stress and anisotropy tensor are discussed next. Unfortunately, experimental data are only available for the component $\overline{u'}_{rms}/U_b$. It is obvious from figure 6.12, that there is a significant difference in the predictions for the streamwise and wall-normal velocity fluctuations predicted by the EASM models and by the models based on a linear stress-strain relationship. The non-linear stress-strain relationship of the EASM formulation clearly provides improved predictions for the streamwise velocity fluctuations $\overline{u'}_{rms}/U_b$. The linear models tend to under-predict the intensity of the streamwise fluctuations and over-predict the intensity of wall-normal fluctuations, similar to the predictions for the channel flow in section 6.2. This is particularly visible at stations $x/H = 12$ and $x/H = 16$. The EASM models provide higher levels of streamwise velocity fluctuations and a lower magnitude for the wall-normal fluctuations, which is in better agreement with the reference data. For the predictions of shear stress $\overline{u'v'}/U_b^2$ in sub figure (f), another difference between the EASM and the k-ω-SST and φ-α-UMIST models becomes apparent. The shear stress predicted by both EASM models is larger in magnitude, even though the variable $C_\mu^{eff} = -0.5\beta_1$ reduces the contribution of the linear term in the stress-strain relationship to the shear stress of the order 10-20% compared to a constant $C_\mu = 0.09$.

The ability of the EASM models to predict more realistic levels of normal-Reynolds-stress components is reflected in the predictions of the anisotropy tensor, shown in figure 6.13. The linear stress-strain relationship of the k-ω-SST and φ-α-UMIST models only predicts a very weak anisotropy state for the normal components a_{11} and a_{22} at all stations in the flow field. This is not too surprising, since linear model are not intended to predict anisotropy, unless the anisotropy is directly induced through the strain-rate tensor ($a_{ij} = -2(\nu_T/k)S_{ij}^*$). Unfortunately, no reference data are available for the anisotropy tensor. However, both EASM models predict much higher levels of anisotropy throughout, which seem more realistic. Nevertheless, the EASM models are not capable of predicting the correct limiting state $a_{22} \rightarrow -2/3$ as the wall is approached.

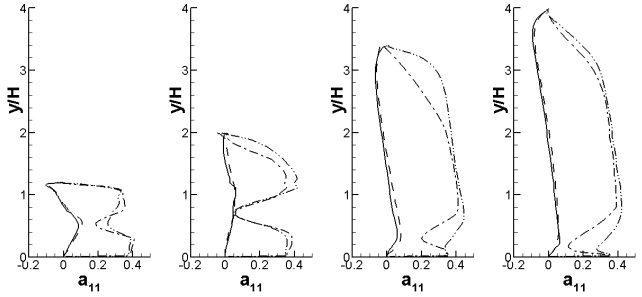

(a) Anisotropy component a_{11}.

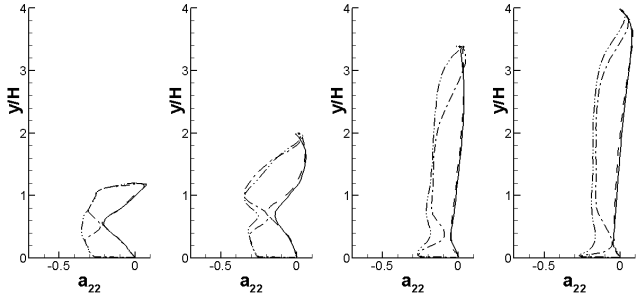

(b) Anisotropy component a_{22}.

FIGURE 6.13: Components of the anisotropy tensor a_{ij} at the centre plane $z/L_z = 0.5$. Locations from left to right: $x/H = 1$, $x/H = 5$, $x/H = 12$ and $x/H = 16$. (—) k-ω-SST, (- - -) φ-α-UMIST, $(- \cdot -)$ EASM-2D and $(- \cdot\cdot -)$ EASM-3D.

Three-Dimensional Flow Field

Further insight into the predictions of the three-dimensional flow field can be gained from figures 6.14 and 6.15, which show contour plots of streamwise velocity component U/U_b and streamwise velocity fluctuations $\overline{u'}_{rms}/U_b$ at the streamwise locations $x/H = 1$, $x/H = 5$, $x/H = 12$ and $x/H = 16$. Figure 6.14 also includes the contour line with zero velocity in order to visualise the extent of the separated flow region. At the first cross section, $x/H = 1$, the experimental data show incipient boundary-layer separation emanating from the two upper corners in the diffuser. The same trend is reproduced by all turbulence models with the tendency of a too large separation zone in the corners. At the next station downstream, $x/H = 5$, the separation is limited to the top right corner in the diffuser. All turbulence models are able to capture this trend. However, the shape and extent of the recirculation zone depart somewhat from the reference data. In the predictions of the k-ω-SST model the flow is already completely detached from the side wall. At the next two stations downstream, $x/H = 12$ and $x/H = 16$, the flow in the experiment has completely detached from the top wall and the recirculation zone has become almost two-dimensional with no variation in the spanwise direction. In the predictions of the k-ω-SST and φ-α-UMIST models the flow fully separates from the right wall and not from the top wall. It is somewhat surprising and counter-intuitive, that separation is predicted at the side wall, where the geometrical expansion is much smaller (2.56°) compared to the top wall with an expansion of 11.3°. One possible explanation for the departure from reference data might be the failure of the linear stress-strain relationship to predict the anisotropy-induced secondary motion in the corners of the inflow duct. Even though the magnitude of the secondary motion is relatively weak, approximately 3.5% of the bulk velocity, it was demonstrated in Schneider *et al.* (2010*a*) by means of LES, that the flow topology in the diffuser is sensitive to the secondary motion in the corners of the inflow duct. The EASM-2D and EASM-3D models both resolve the secondary motion in the inflow duct and the predictions are indeed somewhat improved, although not entirely satisfying. The EASM-2D predicts the flow to remain attached in parts to the side wall and only separates fully from the top wall at the location $x/H \approx 16$. The separation zone remains fully three-dimensional and does not show much resemblance with the separation zone observed in the experiment. The EASM-3D also predicts a fully three-dimensional separation zone where parts of the flow remain attached to the top wall and the side wall is fully separated. Even though the secondary motion is resolved by the EASM, the magnitude of the secondary motion is less than 1%

of the bulk velocity and therefore quite different to what is observed in the experiment. This might be an explanation for the improved, but not fully satisfactory predictions of the flow topology in the diffuser by the EASM. It would be intersting to investigate the sensitivity of the flow in the diffuser by artificially enhacing the magnitude of the secondary motion, similarly to what has been done by Schneider *et al.* (2010*a*) using LES. This study is left for future investigation.

The contours of streamwise velocity fluctuations $\overline{u'}_{rms}/U_b$ in figure 6.15 are predicted very similar by all turbulence models investigated here. As discussed before, the EASM models predict a somewhat too high intensity of streamwise velocity fluctuations compared to the k-ω-SST and φ-α-UMIST model and hence, shows better agreement with the reference data.

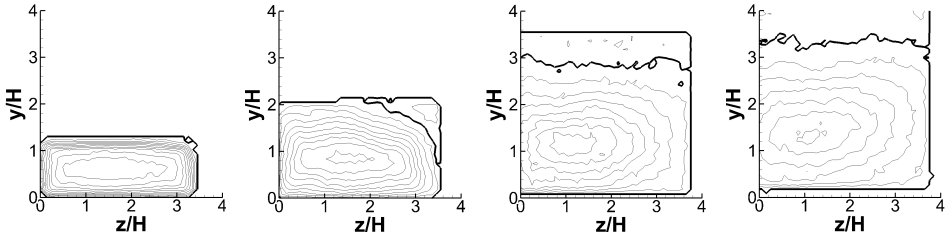

(a) Experiment ($x/H = 1$) (b) Experiment ($x/H = 5$) (c) Experiment ($x/H = 12$) (d) Experiment ($x/H = 16$)

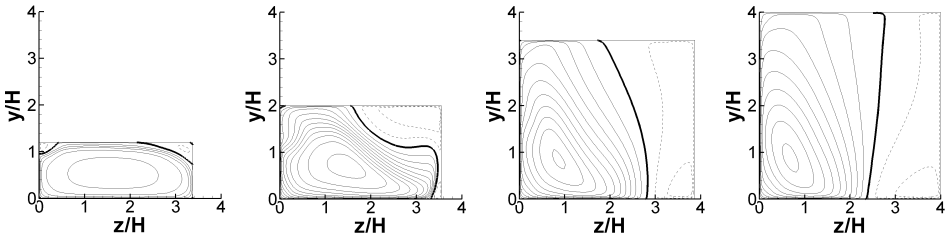

(e) k-ω-SST ($x/H = 1$) (f) k-ω-SST ($x/H = 5$) (g) k-ω-SST ($x/H = 12$) (h) k-ω-SST ($x/H = 16$)

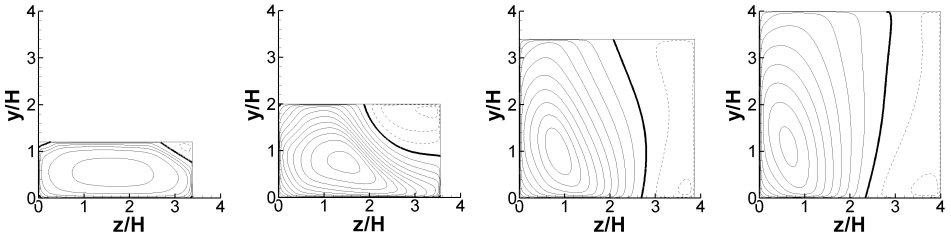

(i) φ-α-UMIST ($x/H = 1$) (j) φ-α-UMIST ($x/H = 5$) (k) φ-α-UMIST ($x/H = 12$) (l) φ-α-UMIST ($x/H = 16$)

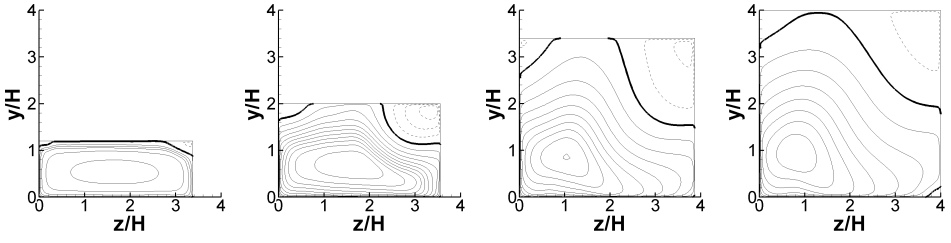

(m) EASM-2D ($x/H = 1$) (n) EASM-2D ($x/H = 5$) (o) EASM-2D ($x/H = 12$) (p) EASM-2D ($x/H = 16$)

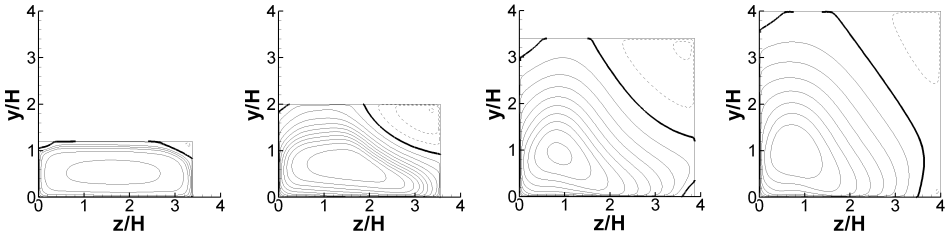

(q) EASM-3D ($x/H = 1$) (r) EASM-3D ($x/H = 5$) (s) EASM-3D ($x/H = 12$) (t) EASM-3D ($x/H = 16$)

FIGURE 6.14: Streamwise velocity contours predicted by the k-ω-SST, φ-α-UMIST, EASM-2D, EASM-3D and experimental data of Cherry *et al.* (2008, 2009). Thick line corresponds to zero-velocity contour line. The spacing between contour lines corresponds to $\Delta U/U_b = 0.1$ and dashed lines denote negative velocities.

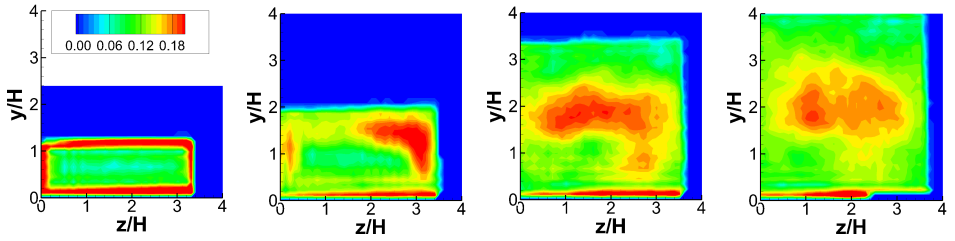

(a) Experiment ($x/H = 1$) (b) Experiment ($x/H = 5$) (c) Experiment ($x/H = 12$) (d) Experiment ($x/H = 16$)

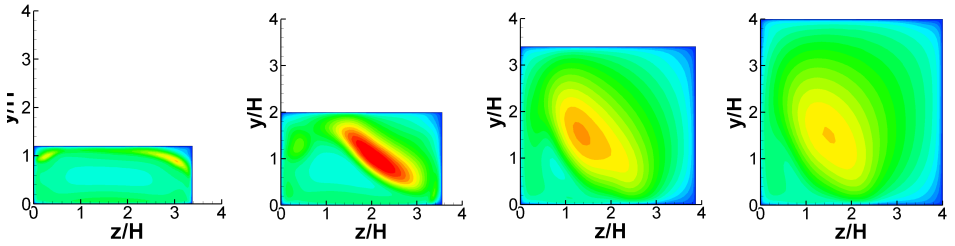

(e) k-ω-SST ($x/H = 1$) (f) k-ω-SST ($x/H = 5$) (g) k-ω-SST ($x/H = 12$) (h) k-ω-SST ($x/H = 16$)

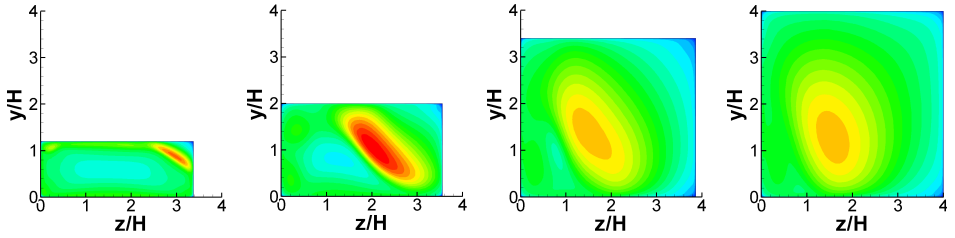

(i) φ-α-UMIST ($x/H = 1$) (j) φ-α-UMIST ($x/H = 5$) (k) φ-α-UMIST ($x/H = 12$) (l) φ-α-UMIST ($x/H = 16$)

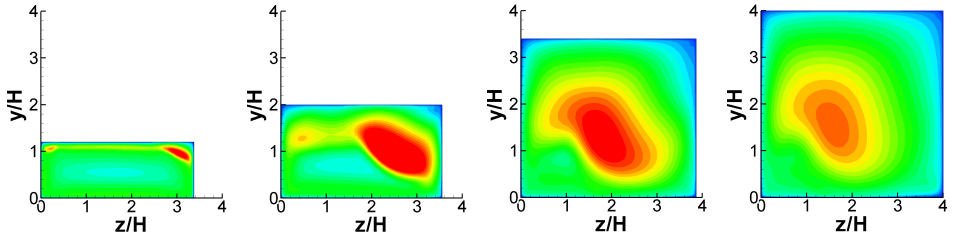

(m) EASM-2D ($x/H = 1$) (n) EASM-2D ($x/H = 5$) (o) EASM-2D ($x/H = 12$) (p) EASM-2D ($x/H = 16$)

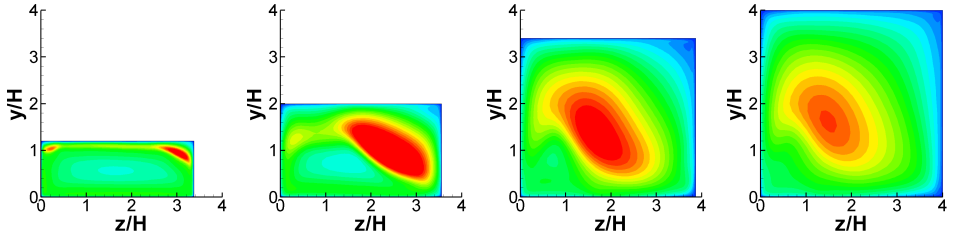

(q) EASM-3D ($x/H = 1$) (r) EASM-3D ($x/H = 5$) (s) EASM-3D ($x/H = 12$) (t) EASM-3D ($x/H = 16$)

FIGURE 6.15: Streamwise velocity fluctuations $\overline{u'}_{rms}/U_b$ predicted by the k-ω-SST, φ-α-UMIST, EASM-2D, EASM-3D and experimental data of Cherry *et al.* (2008, 2009).

6.5 Summary

Based on the test cases considered a fairly consistent picture of the performance of the EASM closure is emerging. The two- and three-dimensional EASM closures are capable of providing improved predictions for the flow in the three-dimensional diffuser, over turbulence models based on a linear stress-strain relationship. Improvements are not limited to predictions of the Reynolds-stress and anisotropy tensor but are also reflected in more realistic predictions of the mean-velocity field. However, the EASM closures show deficiencies in predicting the near-wall behaviour of turbulence kinetic energy and the Reynolds-stress and anisotropy tensor when compared to the reference data. The EASM closures also failed to provide improved predictions for the mean-velocity field of the massively separated flow around the NASA hump configuration despite improved predictions of normal-Reynolds-stress components. This shortcoming is attributed to the behaviour of the variable $C_{\mu}^{eff} = -0.5\beta_1$ in the free-shear layer, which is sensitive to strain- and rotation-rate, and which reduces the contribution of the linear term in the stress-strain relationship to the shear stress. This has the consequence that the extent of the recirculation zone is over-predicted. The test cases also reveal that the two- and three-dimensional formulations of the EASM closure predict equivalent or very similar results in three-dimensional flows. The three-dimensional EASM closure is not found to give improved or significantly different predictions, which suggests that the considerable additional numerical expense compared to the two-dimensional formulation is not justified.

Chapter 7

Accounting for Wall-Induced Anisotropy

The baseline EASM, as presented in chapter 6, is from a theoretical point of view only valid for high-Reynolds-number flows and away from solid boundaries, since neither the transport equations nor the quasi-homogeneous pressure-strain model used in the EASM formulation include modifications to account for various effects the wall exerts on the flow. Nevertheless, a distinct advantage of the EASM based on the k-ω framework is that it can be used on fine near-wall grids, which resolve the viscous sublayer and low-Reynolds-number region close to the wall, despite the lack of appropriate near-wall and low-Reynolds-number modifications. It has been shown in chapter 6 and in Weinmann & Sandberg (2009), where the baseline EASM closure is applied to a range of test cases, that the EASM is capable of providing significantly improved predictions of the normal-Reynolds-stress and anisotropy tensor away from solid walls, over turbulence models based on a linear stress-strain relationship. Nevertheless, room for improvements exists for both, modelling the transport equations and predictions of the Reynolds-stress and anisotropy tensor close to the wall.

In this chapter several strategies are presented, which aim at improving the predictions of the Reynolds-stress and anisotropy tensor of the baseline EASM close to the wall. Possible improvements in the near-wall region may be beneficial for a range of applications, since not only most of the turbulence kinetic energy is generated in this region but also, because it influences predictions of separation, aerodynamic drag and heat and mass transfer. The correct asymptotic near-wall behaviour of the components of the Reynolds-stress and anisotropy tensor close to the wall are

discussed first. This is followed by a review of existing near-wall modifications and different strategies to improve the predictions of the baseline EASM close to the wall.

7.1 Asymptotic Near-Wall Behaviour

It was argued in section 3.4.5, that the two different mechanisms of viscous damping and non-viscous, kinematic wall-blocking both affect the turbulence close to the wall. In order to ensure the correct physical behaviour close to the wall, any near-wall modification needs to be designed such that the asymptotic behaviour of the fluctuating velocities is correctly reproduced as the wall is approached. Therefore, the characteristic asymptotic near-wall behaviour is introduced in this section. The asymptotic near-wall behaviour of the mean and the fluctuating velocity components can be derived using Taylor-series expansions in terms of the wall-normal distance y. The no-slip condition at the wall removes the contribution of the zero-order terms in the series expansions of the fluctuating velocity components. Additionally, the continuity constraint requires, that the coefficient of the linear contribution of the fluctuating velocity $v^{'}$ vanishes as well, thus

$$\begin{aligned} u^{'} &= a_u y + b_u y^2 + O(y^3), \\ v^{'} &= b_v y^2 + c_v y^3 + O(y^4), \\ w^{'} &= a_w y + b_w y^2 + O(y^3), \end{aligned} \tag{7.1}$$

where a, b and c are free coefficients. The asymptotic near-wall behaviours of the Reynolds-stress components can now be written as

$$\begin{aligned} \overline{u'u'} &= \overline{a_u^2} y^2 + 2\overline{a_u b_u} y^3 + O(y^4), \\ \overline{v'v'} &= \overline{b_v^2} y^4 + 2\overline{b_v c_v} y^5 + O(y^6), \\ \overline{w'w'} &= \overline{a_w^2} y^2 + 2\overline{a_w b_w} y^3 + O(y^4), \\ \overline{u'v'} &= \overline{a_u b_v} y^3 + (\overline{b_u b_v} + \overline{a_u c_v}) y^4 + O(y^5), \\ \overline{u'w'} &= \overline{a_u a_w} y^2 + (\overline{a_u b_w} + \overline{b_u a_w}) y^3 + O(y^4), \\ \overline{v'w'} &= \overline{b_v a_w} y^3 + (\overline{b_v b_w} + \overline{c_v a_w}) y^4 + O(y^5). \end{aligned} \tag{7.2}$$

It also follows directly, that the turbulence kinetic energy and dissipation rate are

$$\begin{aligned} k &= \frac{1}{2}(\overline{a_u^2} + \overline{a_w^2})y^2 + O(y^3), \\ \epsilon &= \nu(\overline{a_u^2} + \overline{a_w^2}) + O(y). \end{aligned} \tag{7.3}$$

From the above, the near-wall asymptotic behaviour of the anisotropy tensor components, which are relevant for this work, can be derived as

$$\begin{aligned} a_{11} &= -\frac{2}{3} + \frac{\overline{a_u^2}}{0.5(\overline{a_u^2} + \overline{a_w^2})} + O(y), \\ a_{22} &= -\frac{2}{3} + O(y^2), \\ a_{33} &= -\frac{2}{3} + \frac{\overline{a_w^2}}{0.5(\overline{a_u^2} + \overline{a_w^2})} + O(y), \\ a_{12} &= O(y). \end{aligned} \tag{7.4}$$

It is now obvious that the a_{12} anisotropy component scales linearly with the wall distance y and has to vanish at the wall. The wall-normal component a_{22} of the anisotropy tensor has a limiting value of $a_{22} = -2/3$ at the wall and the limiting value is approached to order $O(y^2)$. The behaviour of a_{22} is a direct consequence of the wall blocking effect and the limiting value of $a_{22} \to -2/3$ is a requirement for reproducing the two-component state of turbulence very close to the wall. The wall-limiting values of the other two normal components a_{11} and a_{33} depend on the constants $\overline{a}_u$ and $\overline{a}_w$ and therefore, on the flow under consideration. Typical values for $\overline{a}_u$ and $\overline{a}_w$ in plane channel flow, boundary layers and pipe flow are summarised in So *et al.* (1991). Also note that the characteristic variation of a_{11} and a_{33} is of order $O(y)$, which is different compared to the $O(y^2)$ variation of a_{22}.

The near-wall behaviour of the baseline EASM can now be examined and compared to the correct physical behaviour of the Reynolds-stress and anisotropy tensor close to the wall. In order to understand the near-wall behaviour of the baseline EASM, the assumption of one-dimensional parallel shear flow is invoked, where $\mathrm{d}\overline{u}/\mathrm{d}y$ is the only non-zero component of the velocity-gradient tensor. In this specific case, the components of the anisotropy tensor predicted by the baseline EASM reduces

to

$$\begin{aligned} a_{11} &= \left(\frac{1}{3}\beta_2 - \frac{1}{3}\beta_3 - 2\beta_4\right)\sigma^2 - \left(\frac{2}{3}\beta_7 + 2\beta_8 + 2\beta_9\right)\sigma^4, \\ a_{22} &= \left(\frac{1}{3}\beta_2 - \frac{1}{3}\beta_3 + 2\beta_4\right)\sigma^2 - \left(\frac{2}{3}\beta_7 - 2\beta_8 - 2\beta_9\right)\sigma^4, \\ a_{33} &= \left(-\frac{2}{3}\beta_2 + \frac{2}{3}\beta_3\right)\sigma^2 + \frac{4}{3}\beta_7\sigma^4, \\ a_{12} &= \beta_1\sigma - 2\beta_6\sigma^3, \end{aligned} \tag{7.5}$$

where $\sigma = (1/2)(k/\epsilon)\mathrm{d}\overline{u}/\mathrm{d}y$. The quantity σ becomes very large close the wall and has an asymptotic near-wall behaviour, which is of the order $O(y^2)$. It is therefore instructive to investigate the near-wall behaviour of the baseline EASM by assuming a large value for σ. In this case, the variable N, which represents the ratio of rate of turbulence kinetic energy production to its dissipation, scales as $N \propto \sigma$, and the invariants scale as $II_S, II_\Omega \propto \sigma^2$, $III_S = IV = 0$ and $V \propto \sigma^4$. The behaviour of the β_i coefficients can now be estimated as

$$\beta_1 \propto 1/\sigma, \quad \beta_2, \beta_3, \beta_4 \propto 1/\sigma^2, \quad \beta_5, \beta_6 \propto 1/\sigma^3, \quad \beta_7, \beta_8, \beta_9 \propto 1/\sigma^4. \tag{7.6}$$

Substituting this into equations 7.5 confirms the picture, that was emerging from the channel-flow simulation in section 6.2 (figure 6.1), namely that the level of normal-anisotropy close to the wall is approximately constant. This behaviour is not consistent with the physically correct asymptotic limits.

The relations (7.5) are also useful, since they allow identification of the contribution of each term in the tensorial expansion to each component of the anisotropy tensor. For example, the coefficients β_1, β_5 and β_6 do not contribute to the normal components of the anisotropy tensor and, therefore, do not need any alteration when modifications for the normal-anisotropy components are introduced. Further, the contribution to the shear stress is not limited to the linear term associated with the β_1 coefficient, but the higher-order term associated with the β_6 coefficient also contributes to the shear stress and therefore, requires special treatment. It is interesting to note that the contribution of the β_6 term to the shear stress is only present if the full three-dimensional EASM approximation is used; for the two-dimensional EASM approximation, this coefficient, amongst others, vanishes.

7.2 Review of Existing Near-Wall Modifications

Possibly the best and most consistent way to include near-wall effects into an EASM closure is to start the derivation from a DRSM, which includes appropriate modifications of the quasi-homogeneous pressure-strain model, such that the presence of solid boundaries is adequately accounted for. This approach has been pursued by Manceau (2003), who derived a k-ϵ-α EASM model from the elliptic-blending DRSM of Manceau & Hanjalic (2002). The variable α is governed by an elliptic equation, which modifies the redistribution term in the DRSM, such that the two-component limit is achieved at the wall. This approach allows the correct near-wall behaviour to be included into a two-equation model. Although initial results for channel flow seem very promising, the resulting model is extremely complex and a fourth-order polynomial equation needs to be solved using an iterative procedure. In addition, the derivation of the EASM was limited to a three-term tensorial expansion for a_{ij}, i.e. to two-dimensional mean flow. Due to the complexity of the resulting model an extension to three-dimensional mean flow seems too cumbersome. At present it is not clear whether the k-ϵ-α EASM provides improved robustness at a lower computational cost when compared to a full DRSM.

The second approach is to derive the EASM based on a quasi-homogeneous pressure-strain model and subsequently modify the β_i coefficients to reproduce the correct near-wall behaviour. Wallin & Johansen (2000) (WJ) introduce viscous blending and damping functions where the anisotropy predicted from the quasi-homogeneous EASM is blended towards a fixed anisotropy state at the wall. WJ chose to fix the limiting anisotropy values at the wall such that they correspond to the limiting values in a planar channel flow. Since the anisotropy state at the wall is fixed, it cannot adjust itself for different types of flows. This must be considered a disadvantage and limits the application to channel flow-type cases. The correct asymptotic near-wall behaviour is achieved by the blending functions, which reproduce the correct asymptotic behaviour at the wall. Karlatiras & Papadakis (2006) used the elliptic-blending function of Manceau & Hanjalic (2002) to replace the viscosity-based blending/damping function in the approach of WJ. Rahman *et al.* (2001) extended the EASM of Gatski & Speziale (1993) by a low-Reynolds-number correction. They introduced viscosity-dependent damping functions, in the same way, as is commonly done for two-equation models. However, they neglected the fact that additional modifications are required to rectify the erroneous predictions of the quasi-homogeneous EASM for the highly anisotropic state of turbulence close to the wall.

Some NLEVM, which seem particularly suitable for providing improved and more accurate predictions for the Reynolds-stress and anisotropy close to the wall are introduced next. Note that other NLEVM are also discussed in the literature review in section 3.7. Durbin (1995*b*) and Lien & Durbin (1996) proposed a non-linear stress-strain relationship for the elliptic-relaxation k-ϵ-v^2 model. The stress-strain relationship is derived by imposing the constraints $a_{11} = \alpha_s a_{22}$ and $a_{22} = v^2/k - 2/3$, where the velocity scale v^2 is obtained from the transport equation. The empirical function $\alpha_s = -1 - 6\left|S^*_{ij}\right| / (15 + \left|S^*_{ij}\right|)$ is designed by reference to shear flow data and approximately gives the correct behaviour of the anisotropy component a_{11}. Suga & Abe (2000) proposed a cubic nonlinear k-ϵ-A model, where A denotes the use of a transport equation for Lumley's flatness parameter, $A = 1 - (9/8)\,(II_a - III_a)$. The flatness parameter A vanishes at the two-component state close to the wall and is unity in isotropic turbulence. The flatness parameter A is used to modify the NLEVM such that it produces the correct two-component limit at the wall. Apsley & Leschziner (1998) derived a cubic NLEVM where the free coefficients of the model were modified to reproduce the correct near-wall behaviour of turbulent boundary layers and channel flow. Abe *et al.* (2003) modified the model of Abe *et al.* (1997) by introducing additional terms and wall-direction indicators, which enhance the anisotropy state close to the wall and hence, provide improved predictions of Reynolds stress and anisotropy close to the wall.

7.3 Near-Wall Modifications for the Baseline EASM

In this section three different strategies are presented, which improve the predictions of the normal-Reynolds-stress and anisotropy components of the baseline EASM close to the wall. The near-wall modifications are to some extent based on modelling concepts that can be found in the literature, but all of them require adjustment or re-calibration to work in conjunction with the present baseline EASM. In addition, modifications to the transport equations are introduced such that the turbulence kinetic energy is correctly predicted as the wall is approached. In order to highlight the performance of the resulting modified EASM, predictions for the planar channel flow configuration of section 6.2 are presented.

7.3.1 Near-Wall Anisotropy Modifications

The near-wall modifications are initially introduced for the two-dimensional EASM formulation and may be extend later to the full three-dimensional EASM formulation, if required. This decision is motivated by the observation that the predictive capabilities of the two-dimensional EASM may be very similar in a range of complex three-dimensional flows when compared to the much more complex three-dimensional EASM formulation. In addition, the two-dimensional EASM is numerically much more efficient and only requires slightly more resources (approx. 7%) compared to standard two-equation models.

For one-dimensional mean flow the anisotropy tensor (7.5) reduces to the simplified form

$$a_{12} = \beta_1 \sigma, \quad a_{11} = \left(\frac{1}{3}\beta_2 - 2\beta_4 \right) \sigma^2,$$
$$a_{22} = \left(\frac{1}{3}\beta_2 + 2\beta_4 \right) \sigma^2, \quad a_{33} = -\frac{2}{3}\beta_2 \sigma^2. \tag{7.7}$$

The correct near-wall behaviour for the normal and off-diagonal components of the anisotropy tensor can now be imposed by modifying the β_i coefficient such that the correct asymptotic behaviour is reproduced. Since β_1 only influences the predictions of the a_{12} component, the modification for the off-diagonal and normal-anisotropy components can be performed independently of each other.

7.3.1.1 Anisotropy Component a_{12}

It has been shown above that the coefficient $\beta_1 \propto 1/\sigma$ as σ becomes large, which results in an approximately constant value of a_{12} close to the wall. In order to achieve the correct asymptotic behaviour of $a_{12} = O(y)$, the coefficient can be modified by a damping function, which imposes the correct near-wall behaviour. The damping function needs to be of $O(y)$ as the wall is approached. Thus, the near-wall corrected coefficient β_1 is given by

$$\beta_1 = f_1 \beta_1^h, \tag{7.8}$$

where β_1^h is obtained from the baseline EASM relations, which are derived from a quasi-homogeneous pressure strain model. Multiplication with a van-Driest-like damping function of the form $f_1 = 1 - \exp(-y^+/A^+)$ would introduce the correct near-wall behaviour. However, using y^+ is problematic, especially in situations where the wall shear stress vanishes. It is therefore preferred to base the damping

function on quantities like $Re_y = \sqrt{k}y/\nu$ or $Re_T = k^2/\nu\epsilon$. The damping function initially used here is obtained from Wallin & Johansen (2000) and takes the form

$$f_1 = 1 - \exp\left(-C_y^1\sqrt{Re_y} - C_y^2 Re_y^2\right), \tag{7.9}$$

where $C_y^1 = 2.4/26$ and $C_y^2 = 0.003/26$.

Figure 7.1 shows predictions of C_μ^{eff} and the anisotropy component $a_{12} = -2C_\mu^{eff}\sigma$ for the baseline EASM ($C_\mu^{eff} = -0.5\beta_1^h$), the modified EASM ($C_\mu^{eff} = -0.5 f_1\beta_1^h$) and a standard k-ϵ two-equation model without near-wall damping ($C_\mu^{eff} = 0.09$) using a priori study, based on the DNS data of Moser *et al.* (1999) for a planar channel flow at $Re_\tau = 590$. It is obvious that a constant C_μ^{eff} is not applicable close

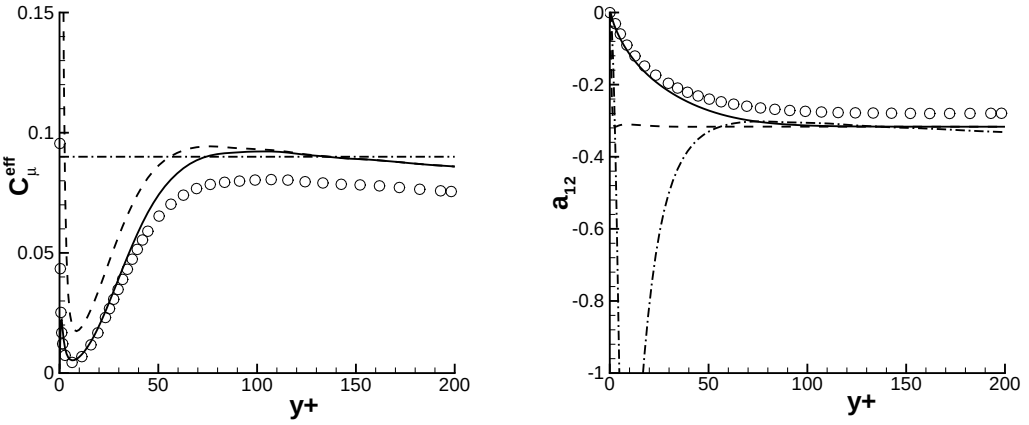

(a) C_μ^{eff} (b) $a_{12} = -2C_\mu^{eff}\sigma$

FIGURE 7.1: A priori study for predictions of C_μ^{eff} and a_{12} in a planar channel flow at $Re_\tau = 395$. (○) DNS data of Moser *et al.* (1999). (—) modified EASM , (- - -) baseline EASM, ($-\cdot-$) k-ϵ model.

to the wall and will result in non-realisable values ($|a_{12}| \leqslant 1.0$) for the anisotropy component a_{12}. It can be argued that the damping for standard two-equation turbulence models is required in order to eliminate non-realisable values at large strain-rate (see, for example, Hanifi *et al.*, 1999). The damping of C_μ^{eff} is more naturally included in the baseline EASM, since the coefficient β_1^h is sensitive to the strain-rate invariant II_S, which results in an approximately constant value for the a_{12} component at the wall. The correct asymptotic near-wall behaviour for C_μ^{eff} and a_{12} is eventually recovered by using the modified $f_1\beta_1^h$ coefficient.

7.3.1.2 Normal Anisotropy Components

Three different possibilities are introduced next to account for the highly anisotropic region close to the wall. The first one is a generalisation of the blending approach of Wallin & Johansen (2000). The second and third approaches are largely based on the ideas of Abe *et al.* (2003), where additional terms are used to locally enhance the anisotropy close to the wall. The difference between the second and third approach is the use of additional wall-direction-dependent terms.

Blending Functions

The first EASM model, which has been proposed including near-wall modifications is the model of Wallin & Johansen (2000). Their approach has been discussed above and is not repeated here. Wallin & Johansen have chosen the constants in the pressure-strain model such that a simplified form of the tensorial expansion for a_{ij} is obtained. In the course of the present work, the near-wall modifications of Wallin & Johansen have been extended to EASM formulations, which use a three-term expansion for a_{ij}. Since the extension to a three-term basis cannot be found in the literature, such a formulation is given here. Following the idea of Wallin & Johansen, the blending approach can be written as

$$
\begin{aligned}
a_{11} &= \left(\frac{1}{3}\beta_2 - 2\beta_4\right)\sigma^2 = f_2 a_{11}^h + (1-f_2)\,(B_{11} - 2/3)\,, \\
a_{22} &= \left(\frac{1}{3}\beta_2 + 2\beta_4\right)\sigma^2 = f_2 a_{22}^h + (1-f_2)\,(-2/3)\,, \\
a_{33} &= -\frac{2}{3}\beta_2\sigma^2 = f_2 a_{33}^h + (1-f_2)\,(B_{33} - 2/3)\,,
\end{aligned}
\tag{7.10}
$$

where $B_{11} = \overline{a_u^2}/(0.5(\overline{a_u^2} + \overline{a_w^2})) = 1.8$, $B_{33} = \overline{a_w^2}/(0.5(\overline{a_u^2} + \overline{a_w^2}))$ and f_2 is a blending function. Note that quantities with superscript h are computed from the EASM relations presented in chapter 6 and are based on a quasi-homogeneous form of the pressure-strain model, for example, $a_{11}^h = \left((1/3)\beta_2^h - 2\beta_4^h\right)\sigma^2$.

In order to achieve the correct behaviour of the normal components of the anisotropy tensor, only the coefficients β_2 and β_4 are available to impose the correct behaviour. In other words, the system of equations (7.10) is overdetermined, since there are two unknowns in three equations. The modifications introduced subsequently are derived by imposing the correct near-wall behaviour on a_{11} and a_{22}. This seems justified, since the component a_{11} is the largest in magnitude for shear flows and a_{22} is crucial in achieving a two-component state at the wall. Solving the equations

for the unknown coefficients β_2 and β_4 gives

$$\beta_2 = f_2\beta_2^h + (1-f_2)\,\frac{3B_{11}-4}{\max\left[II_S, II_S^{eq}\right]}, \tag{7.11}$$

$$\beta_4 = f_2\beta_4^h - (1-f_2)\,\frac{B_{11}}{2\max\left[II_S, II_S^{eq}\right]}. \tag{7.12}$$

A few points should be made here. First, the variable σ^2 is replaced and generalised by $\sigma^2 = II_S/2$. Second, the invariant II_S in the denominator would result in a numerically ill-behaved model, since II_S vanishes at points where the strain rate vanishes. Singular behaviour is avoided by introducing the equilibrium value $II_S^{eq} = 5.05$ as a lower bound. Last, the blending function f_2 needs to be designed such that the correct asymptotic near-wall behaviour of the normal components is obtained. Since it is not possible to satisfy the correct asymptotic behaviour for all normal-anisotropy components, Wallin & Johansen chose $f_2 = f_1^2$, which makes f_2 behave as $f_2 = O(y^2)$, and hence reproduces the correct asymptotic behaviour of the a_{22} component.

Local Enhancement of Anisotropy

The idea here is to retain the behaviour of the β_i^h coefficients close to the wall, but to use additional terms to compensate for the erroneous near-wall behaviour. This idea has also been used in Abe *et al.* (2003). The tensor a_{ij}^w is added to the anisotropy tensor obtained from the baseline EASM model a_{ij}^h and the total anisotropy tensor is as follows:

$$a_{ij} = a_{ij}^h + (1-f_2)\,a_{ij}^w. \tag{7.13}$$

The activation of a_{ij}^w needs to be restricted to the near-wall region. This is achieved by the function f_2, which shuts off the additional term away from solid boundaries. In order to introduce a $O(y^2)$ behaviour, the function f_2 is taken to be $f_2 = f_1^2$. The additive fragment a_{ij}^w is expressed in the following form

$$\begin{aligned} a_{ij}^w = \left(1-f_r^2\right)\Bigg[&\frac{\alpha_2}{1+II_S}\left(S_{ik}S_{kj} - \frac{1}{3}II_S\delta_{ij}\right) \\ &+\frac{\alpha_4}{1+\sqrt{-II_\Omega II_S}}\left(S_{ik}\Omega_{kj} - \Omega_{ik}S_{kj}\right)\Bigg]. \end{aligned} \tag{7.14}$$

The function $f_r = (II_\Omega + II_S)/(II_\Omega - II_S)$ is used to ensure an activation of the near-wall correction for shear-dominated flows only, i.e. $f_r = 0$ for pure shear flow. The calibration constants α_i could be determined from an apriori study using DNS data. In present study, the constants α_i are obtained by optimisation for a planar

channel flow at $Re_\tau = 590$ and take the following values

$$\alpha_2 = 0.9, \qquad \alpha_4 = -0.49. \tag{7.15}$$

Rearranging equation (7.13) gives the modified, near-wall improved coefficients

$$\beta_2 = \beta_2^h + (1 - f_2)\left(1 - f_r^2\right)\frac{\alpha_2}{1 + II_S}, \tag{7.16}$$

$$\beta_4 = \beta_4^h - (1 - f_2)\left(1 - f_r^2\right)\frac{\alpha_4}{1 + \sqrt{-II_\Omega II_S}}. \tag{7.17}$$

Local and Directional Enhancement of Anisotropy

The near-wall modifications based on a local enhancement of the near-wall anisotropy obviously relies on the invariants II_S and II_Ω. In order to improve the anisotropy predictions in situations where the invariants vanish, it is suggested in Abe *et al.* (2003) to use an additional term, which modifies the anisotropy state independent of the invariants II_S and II_Ω. The model from above can therefore be extended to

$$a_{ij} = a_{ij}^h + (1 - f_2)\left[a_{ij}^w - 0.5M_{ij}\right], \tag{7.18}$$

where $M_{ij} = N_{ij} - (1/3)\delta_{ij}$ is the deviatoric part of the tensor obtained from taking the outer product of the wall-normal vector $N_{ij} = n_i n_j$. Different possibilities exist for how the wall-normal vector can be evaluated. The formulation used here avoids the computation of the distance to the closest wall, which cannot uniquely be defined in complex geometries involving multiple walls. Instead, the wall-normal vector can be obtained with sufficient accuracy from a variable, which shows a characteristic wall-normal variation. In this study, the damping function f_1 is used to compute the wall-normal vector using the relation $n_i = (\nabla f_1)_i / \|\nabla f_1\|$. The calibration constants α_i are again determined by optimization for a planar channel flow at $Re_\tau = 590$. The values are given as

$$\gamma_2 = 1.4, \qquad \gamma_4 = -0.23. \tag{7.19}$$

7.3.2 Near-Wall Consistent Transport Equation

It has been shown in section 6.2, that the high-Reynolds-number form of the transport equations for k and ω fail in predicting the correct near-wall asymptotic behaviour of turbulence kinetic energy k. As a consequence, the asymptotic behaviour of all other derived quantities, such as $\epsilon = \beta^* k\omega$ or $\tau = k/\epsilon$, will also be largely

in error close to the wall. In order for the near-wall modifications to work as intented, it is crucial that the near-wall asymptotic behaviour of k and ω is correctly reproduced. In the following, modifications to the transport equation of turbulence kinetic energy are introduced, which rectify the erroneous predictions close to the wall and yield the correct asymptotic behaviour for k as the wall is approached.

The balance of the k and ω equations very close to the wall reduces to

$$\nu\frac{\partial^2 k}{\partial x_j^2} - \epsilon = 0, \qquad \nu\frac{\partial^2 \omega}{\partial x_j^2} - \beta\omega^2 = 0. \tag{7.20}$$

It is easy to show that close to the wall the solution to the ω equation is given by $\omega = a_\omega/y^2$. The constant a_ω can be determined from (7.20) as $a_\omega = 6\nu/\beta$. Hence, the near-wall balance of the ω equation is satisfied providing $\omega \to 6\nu/\beta y^2$ as the wall is approached. In order to ensure the correct behaviour of ω close to the wall it is common practice to prescribe the solution of ω at the first grid point (or cell) adjacent to walls as $\omega_1 = 6\nu/\beta y_1^2$, where y_1 is the distance of the first grid point to the closest wall. Alternatively, the somewhat arbitrary wall boundary condition $\omega_w = 10 \cdot 6\nu/\beta y_1^2$ (see, for example, Menter, 1994) can be used. From experience gained in this work, the specification of the boundary conditions ω_1 or ω_w may not always be sufficient to fully reproduce the correct asymptotic behaviour of ω close to the wall, particularly if the grid resolution near the wall is not adequate. In order to ensure that ω behaves correctly as the wall is approached, the present formulation prescribes the asymptotic solution $\omega = 6\nu/\beta y^2$ in the near-wall region, where $y^* = \beta^{*1/4}k^{1/2}y/\nu \leqslant 2.0$.

Next, the near-wall balance of the turbulence kinetic energy equation is considered. Assuming the turbulence kinetic energy behaves as $k = a_k y^2$ close to the wall and using the model for the dissipation rate $\epsilon = \beta^* k\omega$, the near-wall balance reduces to $1-3\beta^*/\beta = 0$. This constraint is obviously not fulfilled in the high-Reynolds number formulation, and explains the incorrect asymptotic behaviour of k. In order to take this constraint into account, the first option would be to apply a damping function to the closure coefficient β (see Speziale *et al.*, 1992). In the present formulation a damping function f_{β^*} is applied to the model for the dissipation rate $\epsilon = f_{\beta^*}\beta^* k\omega$. The function f_{β^*} needs to satisfy the limiting value of $f_{\beta^*} \to \beta/3\beta^*$. This ensures that the near-wall balance is satisfied. The damping function follows the proposal of Wilcox (1998) and depends on the turbulence Reynolds number $Re_T = k/\nu\omega$, thus

$$f_{\beta^*} = \frac{\beta/3\beta^* + (Re_T/R_\beta)^4}{1 + (Re_T/R_\beta)^4}. \tag{7.21}$$

The constant R_β controls the turbulence kinetic energy dissipation rate close to the wall and has to be adjusted to give the correct log-law behaviour of a turbulent boundary layer. For the present formulation the correct behaviour is reproduced for $R_\beta = 8$. Note that the other two functions of Wilcox (1998) k-ω model for transitional flows, which multiply the eddy viscosity and production of specific dissipation rate, are not needed here.

7.4 Planar Channel Flow

In order to highlight the performance of these near-wall modifications, the modified EASM formulations are applied to the planar channel flow configuration of section 6.2. The results are summarised in figure 7.2 and show the mean-velocity profile U^+, the normal components of the anisotropy tensor $a_{ij} = \overline{u_i' u_j'}/k - (2/3)\delta_{ij}$, the Reynolds-stress components $\overline{u_i' u_j'}^+$, the asymptotic behaviour of the Reynolds-stress components, the III_a-II_a invariant map and the balance of the turbulence kinetic energy equation.

The predictions of the mean-velocity profile are the same as for the baseline EASM formulation. The small under-prediction of velocity magnitude in the buffer region, and centre of the channel, is still present. Very clear improvements can be observed for the predictions of the Reynolds-stress and anisotropy tensors. Good agreement is now achieved in the near-wall regions for both the Reynolds-stress and anisotropy tensor components. The asymptotic behaviours of the normal-Reynolds-stress components, particularly for $\overline{u'u'}$ and $\overline{v'v'}$, show significant improvements. The $\overline{w'w'}$ component departs slightly from the reference data. Even though the near-wall behaviour of the normal-anisotropy components are in much better agreement with the reference data, none of the modifications are able to resolve the reduction of the anisotropy components a_{11} and a_{33} between the peak locations and the wall. This deficiency is also reflected in the anisotropy-invariant map (e), where all near-wall modifications predict a two-components state at the wall, but none is able to predict the correct variation along the two-component line. The budget of turbulence kinetic energy (f) also shows significant improvements close to the wall. The damping function $f_{\beta*}$ is effective in reducing the artificial peak of the dissipation rate ϵ^+ close to the wall, which eliminates the severe under-prediction of turbulence kinetic energy k^+ observed for the baseline EASM. The damping function not only improves the predictions of k^+ close to the wall, but it also improves predictions of the viscous and turbulent diffusion terms.

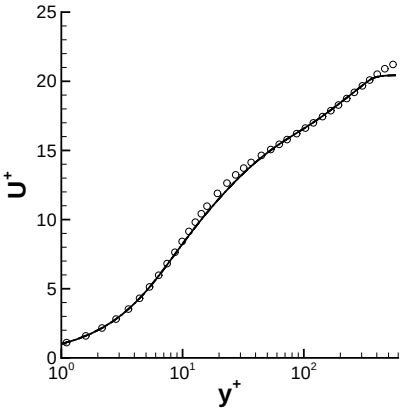

(a) Normalised velocity U^+.

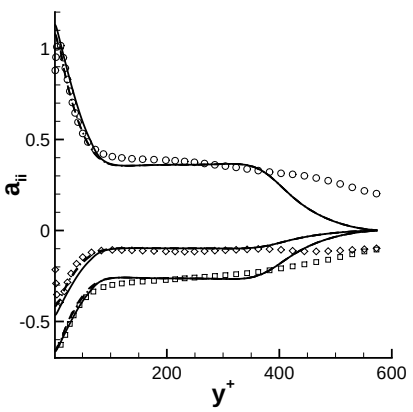

(b) Components of the anisotropy tensor , (○) a_{11} ; (□) a_{22} ; (◇) a_{33}.

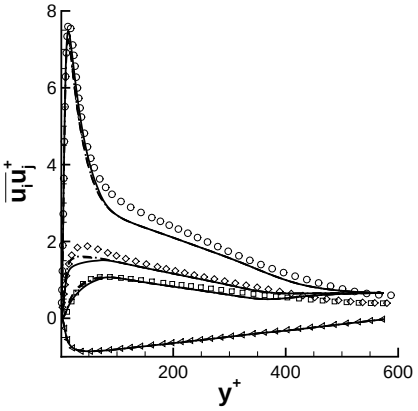

(c) Components of the Reynolds-stress tensor, (○) $\overline{uu}^+$; (□) $\overline{vv}^+$; (◇) $\overline{ww}^+$; (◁) $\overline{uv}^+$.

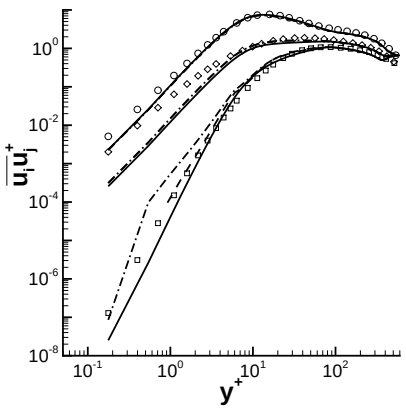

(d) Asymptotic behaviour of normal-Reynolds-stress components.

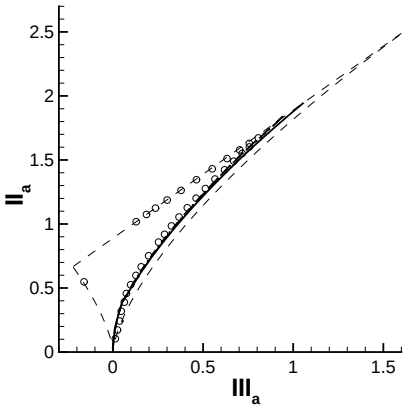

(e) Anisotropy-invariant map.

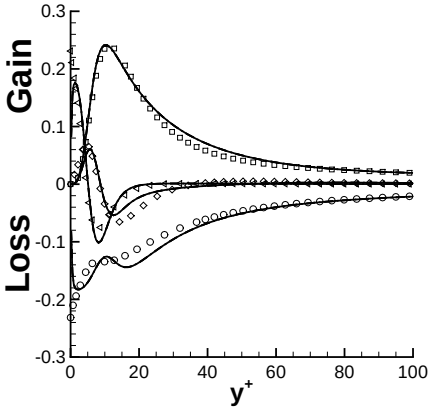

(f) Budget of the turbulence kinetic energy equation, (□) P_k^+; (△) $\nu\nabla^2 k^+$; (○) D_k^+; (◇) ϵ^+.

FIGURE 7.2: Predictions for a planar channel flow at $Re_\tau = 590$. Symbols correspond to DNS (Moser *et al.*, 1999). (—) EASM based on the blending approach, (- - -) EASM based on local enhancement of anisotropy , $(- \cdot -)$ EASM based on local and directional enhancement of anisotropy.

Chapter 8

A Novel Non-Linear Elliptic-Blending RANS Model

In this chapter, a new approach is presented, which aims at combining the advantages of the elliptic-blending approach for modelling near-wall flows with the advantages of a non-linear stress-strain relationship to provide more accurate predictions of the Reynolds-stress and anisotropy field in complex flows. The resulting non-linear elliptic-blending RANS model contains several novelties. First of all, any viscosity-dependent blending or damping functions as they are used for the near-wall anisotropy modifications and for modelling the transport equations in section 7 are abandoned and their effect is more naturally included based on the elliptic-blending approach. Second, the elliptic-blending approach of Keshmiri *et al.* (2008) is used in conjunction with a k-ω framework and not, as usual, in conjunction with a k-ϵ model. This seams a reasonable decision due to the previously discussed superiority of the ω equation to predict the flow in adverse pressure gradient or strong non-equilibrium conditions. Finally, a non-linear stress-strain relationship is proposed, which recovers the normal-Reynolds-stress and anisotropy predictions of the baseline EASM model away from the wall, where the quasi-homogeneous pressure-strain model of Speziale *et al.* (1991) provides good predictions for the Reynolds-stress and anisotropy tensor. A near-wall-consistency constraint and additional near-wall anisotropy modification are introduced in order to improve the predictions of the quasi-homogeneous pressure-strain model close to the wall, such that the highly anisotropic state of turbulence and the limiting two-component state is correctly reproduced as the wall is approached. In order to assess the performance of the new turbulence model, simulations are performed for the flow in a planar channel,

the flow over the NASA hump configuration and the flow in a three-dimensional diffuser and the results are assessed by comparing to reference data.

8.1 Transport Equations

The proposed RANS model is based on a transport equation for the inverse turbulent time scale or specific turbulence dissipation rate ω. The transport equation from the baseline EASM can be retained and do not require re-calibration or further modifications. The transport equations for the turbulence kinetic energy k and the specific dissipation rate ω take the following form (see Hellsten, 2004, 2005)

$$\frac{Dk}{Dt} = P_k - \epsilon + \frac{\partial}{\partial x_j}\left[\left(\nu + \sigma_k \nu_T\right)\frac{\partial k}{\partial x_j}\right], \tag{8.1}$$

$$\frac{D\omega}{Dt} = \gamma\frac{\omega}{k}P_k - \beta\omega^2 + \frac{\partial}{\partial x_j}\left[\left(\nu + \sigma_\omega \nu_T\right)\frac{\partial \omega}{\partial x_j}\right] + \frac{\sigma_d}{\omega}\max\left(CD_{k\omega}, 0\right), \tag{8.2}$$

where $P_k = -\overline{u_i' u_j'}\partial\overline{u}_i/\partial x_j$ is the rate of production of turbulence kinetic energy and $CD_{k\omega} = (\partial k/\partial x_j)(\partial\omega/\partial x_j)$ is the turbulent cross-diffusion term, which stems from the transformation of the standard k-ϵ model to a k-ω framework. The cross-diffusion term is effective in reducing the model sensitivity to free-stream values of ω. The turbulence kinetic energy dissipation rate is now modelled as

$$\epsilon = f_{\beta^*}\beta^* k\omega, \tag{8.3}$$

where f_{β^*} is a novel damping function, which relies on the wall-normal fluctuation ratio $\varphi = \overline{v^2}/k$, as predicted by the elliptic-blending approach, rather than using the turbulence Reynolds number Re_T. A damping function, which satisfies the constraint $\beta^*/\beta \to 1/3$ as the wall is approached is given by

$$f_{\beta^*} = \frac{\beta/3\beta^* + \left(\varphi/\beta^*\right)^3}{1 + \left(\varphi/\beta^*\right)^3}. \tag{8.4}$$

The constants in f_{β^*} are chosen such that the correct log-layer behaviour of the mean-velocity profile is reproduced. The present formulation employs the φ-α model of Keshmiri *et al.* (2008), which is based on the elliptic-blending concept of Manceau & Hanjalic (2002). The φ-α model solves a transport equation for the normalised wall-normal fluctuating velocity scale $\varphi = \overline{v^2}/k$ and an elliptic equation for the

parameter α. The constitutive equations for φ and α take the form

$$\frac{D\varphi}{Dt} = (1-\alpha^p)\, f_{wall} + \alpha^p f_{hom} - \frac{\varphi}{k}P_k + \frac{2}{k}\left(\sigma_k \nu_T\right)\frac{\partial k}{\partial x_j}\frac{\partial \varphi}{\partial x_j} + \frac{\partial}{\partial x_j}\left[\left(\nu + \sigma_\varphi \nu_T\right)\frac{\partial \varphi}{\partial x_j}\right],$$

$$L^2\nabla^2\alpha - \alpha = -1. \tag{8.5}$$

The redistribution term f_{hom} is based on the quasi-homogeneous pressure-strain model of Speziale *et al.* (1991), thus

$$f_{hom} = -(1/\tau)\left(C_1 - 1 + C_2 P_k/\epsilon\right)\left(\varphi - 2/3\right), \quad f_{wall} = -\frac{\varphi\epsilon}{k}. \tag{8.6}$$

The damping function $f_{\beta*}$ in the model for the turbulence kinetic energy dissipation rate not only ensures that the turbulence kinetic energy is correctly predicted of the order $k = O(y^2)$ as the wall is approached. It also guarantees, that the near-wall balance of the φ equation is satisfied, and that the correct behaviour $\varphi = O(y^2)$ is reproduced.

The eddy viscosity, which contains the correct near-wall damping through the normalised velocity scale φ, is as follows

$$\nu_T = C_\mu^\nu \varphi k \tau. \tag{8.7}$$

In order to take viscous effects into account, a lower bound on the viscous time τ and length scales L is introduced. In addition, the realisability constraint of Durbin (1996) is imposed, such that

$$\tau = \max\left[\min\left(\frac{k}{\epsilon}, \frac{0.6}{\sqrt{6}C_\mu\varphi\left|S_{ij}^*\right|}\right), C_\tau\sqrt{\frac{\nu}{\epsilon}}\right], \tag{8.8}$$

$$L = C_L \max\left[\min\left(\frac{k^{3/2}}{\epsilon}, \frac{k^{1/2}}{\sqrt{6}C_\mu\varphi\left|S_{ij}^*\right|}\right), C_\eta\left(\frac{\nu^3}{\epsilon}\right)^{1/4}\right]. \tag{8.9}$$

8.2 Non-linear Stress-Strain Relationship

The Reynolds-stress tensor $\overline{u_i' u_j'}$ of the new RANS model constitutes a non-linear stress-strain relationship, which can be written as $\overline{u_i' u_j'} = (2/3)k\delta_{ij} + k a_{ij}$, where the anisotropy tensor is given by

$$a_{ij} = -2(\nu_T/k)S_{ij}^* + a_{ij}^{ex}. \tag{8.10}$$

The most general form of the extra-anisotropy tensor in the limit of two-dimensional mean flow is given by the following relation:

$$a_{ij}^{ex} = \beta_2 \left(S_{ik}S_{kj} - \frac{1}{3} II_S \delta_{ij} \right) + \beta_4 \left(S_{ik}\Omega_{kj} - \Omega_{ik}S_{kj} \right), \tag{8.11}$$

with the invariants

$$II_S = \mathrm{tr}\left\{ S_{ik}S_{kj} \right\}, \quad II_\Omega = \mathrm{tr}\left\{ \Omega_{ik}\Omega_{kj} \right\}. \tag{8.12}$$

Recall that it was demonstrated in chapter 6 and in Weinmann & Sandberg (2009) that the baseline EASM, which is based on the quasi-homogeneous pressure-strain model of Speziale *et al.* (1991) (SSG), is capable of providing realistic predictions for the Reynolds-stress and anisotropy tensor in complex three-dimensional flows away from solid boundaries. It was also found that the SSG model fails to predict the highly anisotropic state of turbulence and the limiting two-component state as the wall is approached.

In order to improve the predictions of the quasi-homogeneous pressure-strain model close to the wall, a near-wall-consistency constraint and additional near-wall anisotropy modification are introduced. These constraints result in a set of modified coefficients β_i, which include the correct near-wall behaviour, and which recover the solution of the quasi-homogeneous EASM model away from solid boundaries. Thus, away from solid boundaries, the new model recovers the coefficients β_i^h of the quasi-homogeneous EASM. The coefficients β_i^h are given by

$$\beta_2^h = 2A_1A_2/Q, \quad \beta_4^h = -A_1/Q \tag{8.13}$$

where

$$Q = N^2 - 2II_\Omega - \frac{2}{3}A_2^2 II_S. \tag{8.14}$$

The constants A_i are directly determined from the model of Speziale *et al.* (1991), and are given as

$$A_1 = 1.22, \quad A_2 = 0.47, \quad A_3 = 0.88, \quad A_4 = 2.37.$$

The variable N appearing in (8.14) corresponds to the ratio of turbulence kinetic energy production to dissipation rate and is governed by a non-linear relation. For

two-dimensional flows the non-linear equation has the explicit solution

$$N = \begin{cases} \frac{A_3}{3} + \left(P_1 + \sqrt{P_2}\right)^{1/3} + \left(P_1 - \sqrt{P_2}\right)^{1/3} & , P_2 \geqslant 0 \\ \frac{A_3}{3} + 2\left(P_1^2 - P_2\right)^{1/6} \cos\left[\frac{1}{3}\arccos\left(\frac{P_1}{\sqrt{P_1^2 - P_2}}\right)\right] & , P_2 < 0 \end{cases} \tag{8.15}$$

with

$$P_1 = \left(\frac{A_3^2}{27} + \left(\frac{A_1 A_4}{6} - \frac{2}{9}A_2^2\right) II_S - \frac{2}{3} II_\Omega\right) A_3, \tag{8.16}$$

$$P_2 = P_1^2 - \left(\frac{A_3^2}{9} + \left(\frac{A_1 A_4}{3} + \frac{2}{9}A_2^2\right) II_S + \frac{2}{3} II_\Omega\right)^3. \tag{8.17}$$

Near-Wall Consistency and Anisotropy Modifications

The main objective for the proposed model is to introduce the ability to account for the highly anisotropic state of turbulence close to a wall. The correct near-wall behaviour of the coefficients β_i is achieved by imposing the following constraints on the anisotropy tensor:

$$a_{11} = a_{11}^h + f_w a_{11}^w, \quad a_{22} = f_b\left(\varphi - 2/3\right) + \left(1 - f_b\right) a_{22}^h. \tag{8.18}$$

That is, the a_{11} anisotropy component is obtained as the sum of the contribution from the quasi-homogeneous EASM model a_{11}^h, and the extra component a_{11}^w, which enhances the anisotropy state close to the wall. The function f_w ensures that the anisotropy modifications are only activated close to the wall. The a_{22} anisotropy component is designed such that the anisotropy state obtained from the wall-normal velocity scale $(\varphi - 2/3)$ is used in the near-wall region and blended towards the anisotropy state predicted by the EASM relations a_{22}^h away from solid boundaries. The blending is achieved by the specifically designed blending function f_b. The present formulation ensures that the Reynolds-stress and anisotropy predictions of the baseline EASM model are recovered away from solid boundaries. Note that no constraint is placed on a_{33}, since only two relations are required to determine the new coefficients β_2 and β_4.

New expressions for the coefficients β_2 and β_4 are derived by considering two-dimensional parallel mean flow, where (8.10) reduces to

$$a_{12} = -2C_\mu^{eff}\sigma, \quad a_{11} = \left((1/3)\beta_2 - 2\beta_4\right)\sigma^2,$$

$$a_{22} = \left((1/3)\beta_2 + 2\beta_4\right)\sigma^2, \quad a_{33} = -(2/3)\beta_2\sigma^2, \tag{8.19}$$

where $\sigma = (1/2)\tau \mathrm{d}\overline{u}/\mathrm{d}y$ and $C_\mu^{eff} = C_\mu^\nu \varphi$. Using the relations (8.19) to rewrite the tensor a_{ij}^h and the wall anisotropy modification tensor a_{ij}^w in terms of β_i^h and β_i^w, and substituting both into (8.18) yields a system of equations that can be solved. The result is

$$\beta_2 = \beta_2^h + \frac{3 f_b \left(\varphi - 2/3\right)}{\max\left[II_S, 5.05\right]} - f_b \left(\frac{1}{2}\beta_2^h + 3\beta_4^h\right) + f_w \left(\frac{1}{2}\beta_2^w + 3\beta_4^w\right), \tag{8.20}$$

$$\beta_4 = \beta_4^h + \frac{f_b \left(\varphi - 2/3\right)}{2\max\left[II_S, 5.05\right]} - f_b \left(\frac{1}{12}\beta_2^h + \frac{1}{2}\beta_4^h\right) - f_w \left(\frac{1}{12}\beta_2^w + \frac{1}{2}\beta_4^w\right). \tag{8.21}$$

The strain rate σ has been replaced and generalised using the relation $\sigma^2 = 0.5 II_S$, and is limited to the equilibrium value in order to avoid numerical difficulties in situations where II_S vanishes. The coefficients β_i^w for the near-wall-anisotropy corrections are taken as

$$\beta_2^w = \frac{\alpha_2}{1 + II_S}, \quad \beta_4^w = \frac{\alpha_4}{1 + \sqrt{-II_S II_\Omega}}. \tag{8.22}$$

The constants α_i are calibrated using planar channel flow and take the values $\alpha_2 = 0.9$ and $\alpha_4 = 0.49$. The auxiliary function f_b is a modified version of Menter's blending function F_1 and ensures that the consistency constraint is only invoked in a region close to the wall, where the stress and anisotropy state predicted by the baseline EASM model is largely in error. Alternatively, the region where the consistency constraint is invoked could easily be extended to a region of almost the entire boundary layer by using Menter's original functions $f_b = F_1$ or $f_b = F_2$. The function f_w, which ensures that the near-wall-anisotropy modifications are only activated close to the wall, uses the elliptic-blending variable α to detect the presence of solid boundaries. Since the near-wall modifications are derived by assuming parallel shear flow, the function $f_r = \left(II_\Omega + II_S\right) / \left(II_\Omega - II_S\right)$ is introduced to f_w, in order to ensure that the modifications are only active in shear-dominated flows for which $f_r \to 0$. The auxiliary functions take the form

$$f_b = \tanh\left(16\Gamma_2^4\right), \quad f_w = \left(1 - \alpha^2\right)\left(1 - f_r^2\right)\frac{\widetilde{II}_S + 100}{II_S + 100}, \tag{8.23}$$

where $\Gamma_2 = 500\nu/\omega y^2$. The invariant $\widetilde{II}_S = \mathrm{tr}\left\{\widetilde{S}_{ik}\widetilde{S}_{kj}\right\}$ is determined from $\widetilde{S}_{ij} = \widetilde{\tau} S_{ij}^*$ using the time scale $\widetilde{\tau} = \min\left(k/\epsilon, 0.6/\sqrt{6}C_\mu\varphi\left|S_{ij}^*\right|\right)$, which does not impose a lower viscous limit. The invariant $\widetilde{II}_S$ is necessary in order to correctly model the variation of the anisotropy components a_{11} and a_{33} between the peak location and the wall.

The suggested closure coefficients for the new φ-α-EASM can be summarised as

Set 1:	$\gamma_1 = 0.518$	$\beta_1 = 0.0747$	$\sigma_{K_1} = 1.1$	$\sigma_{\omega_1} = 0.53$	$\sigma_{d_1} = 1.0$
Set 2:	$\gamma_2 = 0.440$	$\beta_2 = 0.0828$	$\sigma_{K_2} = 1.1$	$\sigma_{\omega_2} = 1.00$	$\sigma_{d_2} = 0.4$
$C_\mu^\nu = 0.22$	$C_1 = 1.7$	$C_2 = 1.2$	$p = 3$	$\sigma_\varphi = 1$	$C_L = 0.161$
$C_\tau = 6$	$C_\eta = 90$	$\alpha_2 = 1.0$	$\alpha_4 = 0.49$	$R_\alpha = 0.01$	$\beta^* = 0.09$

TABLE 8.1: Closure constants for the φ-α-EASM

8.3 Discussion

The new φ-α-EASM differs from the baseline EASM in the following ways: 1) the inclusion of additional near-wall-anisotropy modifications, which are used in conjunction with a near-wall-consistency constraint and 2) the redefinition of C_μ^{eff}, which is given here as $C_\mu^{eff} = C_\mu^\nu \varphi$, and for the baseline EASM as $C_\mu^{eff} = -0.5\beta_1^h$ with $\beta_1^h = -A_1 N/Q$. With the present formulation, several shortcomings of the coefficient β_1^h are obviated. Consider, for example, two-dimensional parallel shear flow. It can be shown that for large strain rates σ, the coefficient β_1^h behaves as $\beta_1^h \propto 1/\sigma$, with the consequence that a_{12} is approximately constant close to the wall. Therefore, the damping inherent in β_1^h is not sufficient and additional damping functions are required in order to achieve the correct behaviour of $a_{12} = O(y)$ as the wall is approached. In the present formulation the wall damping is naturally included and $a_{12} = O(y^2)$. Note that the behaviour $a_{12} = O(y^2)$ is a spurious feature of the elliptic-blending/-relaxation technique and is tantamount to a turbulence viscosity ν_T, that behaves as $O(y^4)$ instead of $O(y^3)$, as it should, as the wall is approached. This is not considered a problem, since ν_T is sufficiently small close to the wall such that the total effective viscosity $\nu_{eff} = \nu + \nu_T$ is correctly reproduced (see Durbin, 1991). Second, in case of vanishing strain rate, $\sigma \to 0$, the coefficient β_1^h takes excessive values. For example, the predicted $C_\mu^{eff} = -0.5\beta_1^h$ at the centerline of a planar channel flow reaches values close to $C_\mu^{eff} \approx 0.7$. This is clearly in contradiction to the generally accepted value of $C_\mu^{eff} = 0.09$. The present formulation does not suffer from this issue.

Finally, the authors recent experience has shown that for separated flows the EASM formulation is sometimes inferior to traditional linear two-equation models. One source of deficiency of the EASM framework was identified to be the coefficient β_1^h, which reduces the contribution of the linear term in the stress-strain relationship to the shear stress in the separated shear layer, through $C_\mu^{eff} = -0.5\beta_1^h$, by up

to 30% (when compared to $C_\mu^{eff} = 0.09$). The insufficient level of shear stress in the separated shear layer consequently leads to an over-prediction of the separation or recirculation zone. These observations are confirmed by Jang *et al.* (2002) who investigated the performance of several NLEVMs and EASMs in massively separated flows. The model presented here avoids this issue by using $C_\mu^{eff} = C_\mu^\nu \varphi$, which does not reduce in free shear layers. This feature effectively shortens excessive recirculation zones frequently observed with EASM models.

Even though the present modifications solve some of the common issues related to EASM models in shear-dominated flows, it might do so by sacrificing some of the capabilities inherent in β_1^h, particularly the sensitivity to rotational effects through the invariant II_Ω, to predict flows with strong streamline curvature or imposed system rotation. However, the present formulation has been tested for the strongly curved flow in a two-dimensional U-duct and the predicted results for the mean flow and turbulence quantities were found to be very similar to the baseline EASM. For this reason, no further action has been taken to retain the original coefficient β_1^h of the baseline EASM formulation for rotational flows.

8.4 Planar Channel Flow

In order to highlight the performance of the new φ-α-EASM model, it is applied to the planar channel flow configuration of section 6.2. The results are summarised in figure 8.1, which shows the mean-velocity profile U^+, the normal components of the anisotropy tensor $a_{ij} = \overline{u_i' u_j'}/k - (2/3)\delta_{ij}$, the Reynolds-stress components $\overline{u_i' u_j'}^+$, the III_a-II_a invariant map and the balance of the turbulence kinetic energy equation.

The mean-velocity profile U^+ follows the same trends, which were observed for the baseline EASM formulation, i.e. a slight under-prediction of velocity magnitude at the centre of the channel and in the buffer region ($y^+ \approx 10 - 30$). The predictions of the components of the anisotropy tensor has improved over the baseline EASM and over the modified EASM, as discussed in section 7.3. The present model is able to capture the reduction of the normal components a_{11} and a_{33} between the peak locations and the wall. It is also able to maintain higher levels of anisotropy as the centre of the channel is approached. This is related to the fact, that the erroneous behaviour of C_μ^{eff} for $\sigma \to 0$ is eliminated in the new φ-α-EASM model. The components of the Reynolds-stress tensor and the asymptotic behaviour of the normal components are both in excellent agreement with the reference data. Only

the $\overline{w'w'}$ component shows a small kink close to the wall. Note that the k-ϵ-α of Manceau (2003) shows a similar dip for $\overline{w'w'}$ at approximately the same location. The excellent predictions of the anisotropy tensor are also reflected in the III_a-II_a invariant map, where the new model is able to fully reproduce the DNS data. The predictions of the near-wall budget of the turbulence kinetic energy equation has not changed much. This is not too surprising, since the k and ω equations remain the same as for the near-wall modified EASM of section 7.3, apart from the newly designed damping function $f_{\beta*}$.

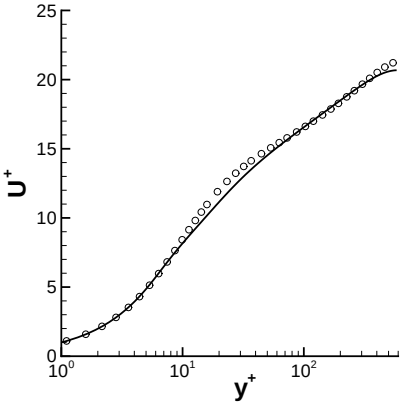

(a) Normalised velocity U^+.

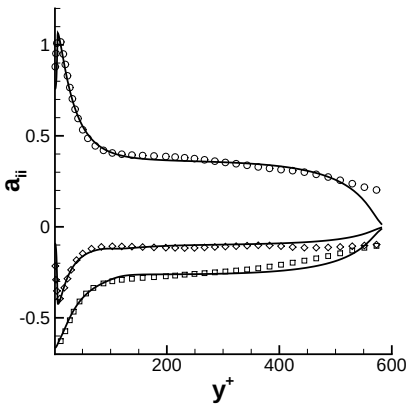

(b) Components of the anisotropy tensor , (○) a_{11} ; (□) a_{22} ; (◇) a_{33}.

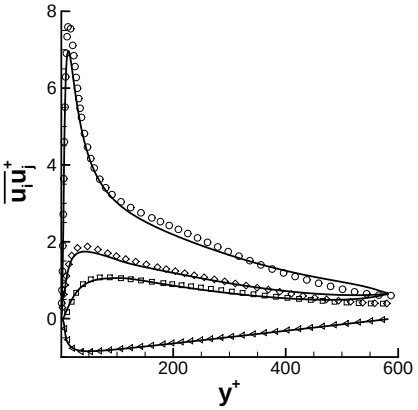

(c) Components of the Reynolds-stress tensor, (○) $\overline{uu}^+$; (□) $\overline{vv}^+$; (◇) $\overline{ww}^+$; (◁) $\overline{uv}^+$.

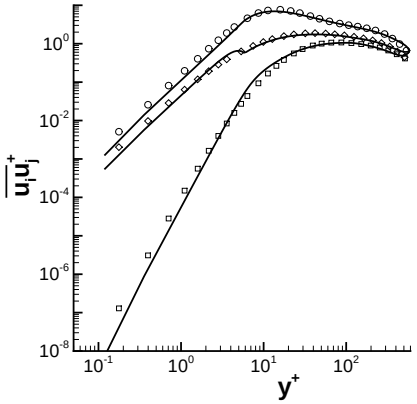

(d) Asymptotic behaviour of normal-Reynolds-stress components.

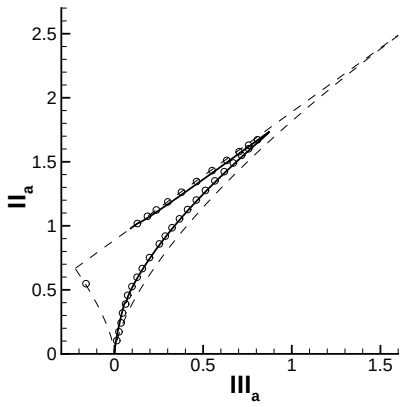

(e) Anisotropy-invariant map.

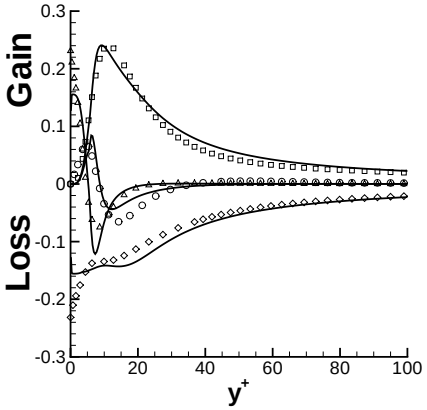

(f) Budget of the turbulence kinetic energy equation, (□) P_k^+; (△) $\nu\nabla^2 k^+$; (○) D_k^+; (◇) ϵ^+

FIGURE 8.1: Predictions for a planar channel flow at $Re_\tau = 590$. Symbols correspond to DNS (Moser *et al.*, 1999). (—) new φ-α-EASM model.

8.5 NASA Hump

The NASA wall-mounted hump has already been introduced in section 6.3 and is used here again in order to evaluate the performance of the new φ-α-EASM model to predict separation from a smooth surface, recirculation and subsequent reattachment of the flow. As a reference, the results of the EASM-2D and φ-α-UMIST models are also included in the compassion with the experimental data of Greenblatt *et al.* (2004, 2006).

The predicted streamwise velocity contour U/U_0 and computed streamlines are shown in figure 8.2. The φ-α-EASM model predicts the separation point at the location $x_s/c = 0.665$, which is identical to the locations predicted by the EASM-2D. The reattachment point is located at $x_r/c = 1.16$ and has moved much closer to the reattachment location of the experiment $x_r/c = 1.1$. The error in the reattachment location has reduced from approximately 13% of chord of the EASM-2D to 5% of chord of the φ-α-EASM. As a consequence, the small recirculation zone observed in the experiment is now much better predicted by the φ-α-EASM compared to the other turbulence models. The shortening of the recirculation zone is a direct consequence of the redefinition of $C_\mu^{eff} = C_\mu^\nu \varphi$, which does not reduce the contribution of the linear term in the stress-strain relationship to the shear stress in the free-shear layer. This is in contrast to the baseline EASM, where the sensitivity of C_μ^{eff} to strain and rotation reduces the shear stress in the free-shear layer.

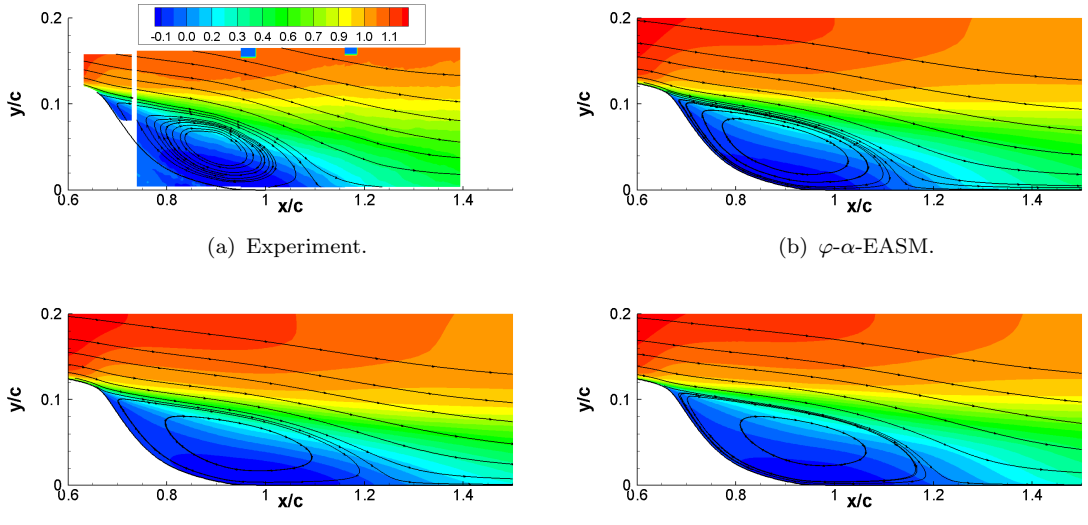

(a) Experiment.

(b) φ-α-EASM.

(c) φ-α-UMIST.

(d) EASM-2D.

FIGURE 8.2: Streamwise velocity contours and streamlines for the NASA hump case.

Figure 8.3 shows predictions of the surface-pressure coefficient $C_p = (p - p_{ref})/(0.5\rho U_0^2)$ and skin-friction coefficient $C_f = \tau_w/(0.5\rho U_0^2)$ distributions. Upstream of the separation point, the surface-pressure distribution of the φ-α-EASM matches the results of the φ-α-UMIST and reference data, whereas the baseline EASM shows a small under-prediction of the low-pressure peak. In the separated flow region, the surface-pressure distribution is slightly improved over the φ-α-UMIST, but remains somewhat higher compared to the EASM-2D. After reattachment, the φ-α-EASM shows recovery of surface pressure, which is in better agreement with the reference data. The skin-friction distribution of the φ-α-EASM closely follows that of the EASM-2D. In the region upstream of the separation point, the φ-α-UMIST model shows a much lower magnitude of skin friction compared to the φ-α-EASM and EASM-2D models. Within the recirculation zone, the φ-α-EASM and EASM-2D predict much lower levels of skin friction, which is in better agreement with the reference data, whereas the φ-α-UMIST model shows excessive levels of skin friction. The EASM-2D seems to be slightly superior in predicting the correct magnitude of skin friction in the recirculation zone. Downstream of the reattachment point, only the φ-α-EASM and EASM-2D models are able to recover the correct magnitude of skin friction.

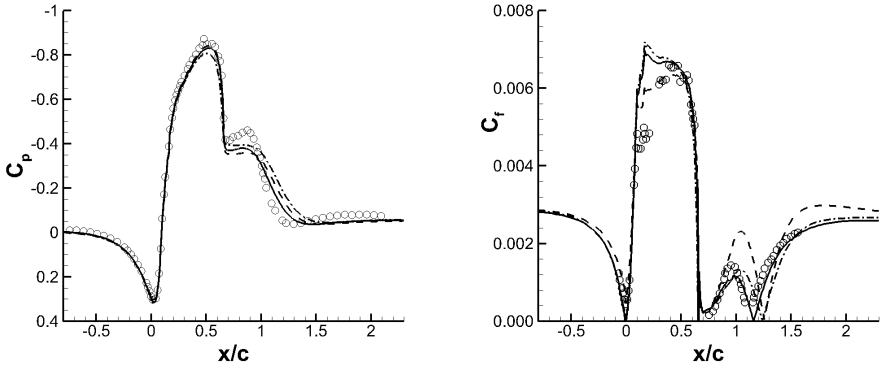

(a) Surface-pressure coefficient C_p (b) Skin-friction coefficient C_f

FIGURE 8.3: Surface-pressure coefficient C_p and skin-friction coefficient C_f distribution. Symbols correspond to experimental data of Greenblatt *et al.* (2004, 2006). (—) φ-α-EASM, (- - -) φ-α-UMIST, ($- \cdot -$) EASM-2D.

The velocity profiles for the streamwise and vertical velocity components U/U_0 and V/U_0 are shown in figure 8.4 for the stations $x/c = 0.65$, $x/c = 0.8$, $x/c = 1.0$ and $x/c = 1.2$. At the first station, $x/c = 0.65$, immediately upstream of the separation point, the φ-α-EASM model predicts both components of the velocity in excellent

agreement with the experimental data and does not show the defect of the EASM-2D of too strong a retardation of the streamwise velocity component close to the wall. At the second and third stations, $x/c = 0.8$ and $x/c = 1.0$, the φ-α-EASM and φ-α-UMIST predict the streamwise velocity component very similar and in good agreement with corresponding measurements. Some advantages can be observed for the φ-α-EASM in predicting the velocity component V/U_0. At the last station, $x/c = 1.2$, just after reattachment, the superiority of the new φ-α-EASM becomes clearly visible in the predictions of the streamwise velocity profile. Both the EASM-2D and φ-α-UMIST show a small amount of reverse flow close to the bottom wall, whereas the flow of the φ-α-EASM has already reattached. The earlier reattachment reflects significant improvements of the velocity profile close to the wall.

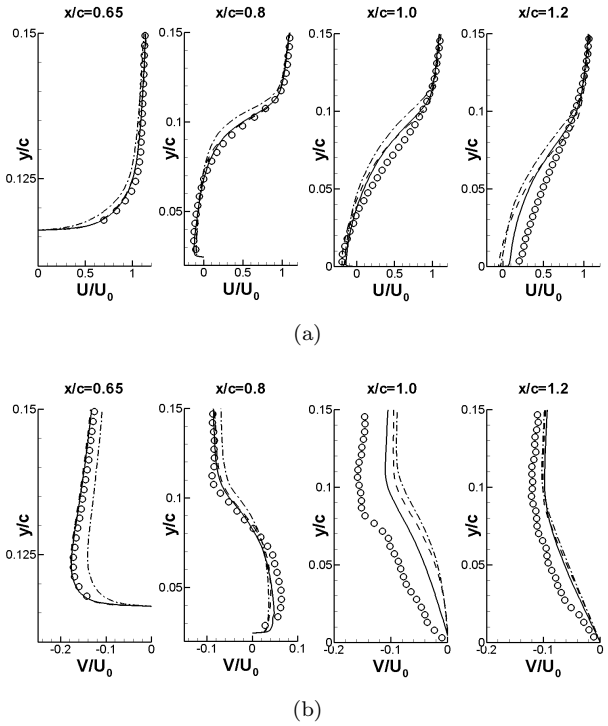

FIGURE 8.4: Velocity profiles at different stations in the flow field. Symbols correspond to experimental data of Greenblatt *et al.* (2004, 2006). (—) φ-α-EASM, (- - -) φ-α-UMIST, (– · –) EASM-2D.

The shear stress $\overline{u'v'}$ and normal-stress components $\overline{u'u'}$ and $\overline{v'v'}$ are shown in figure 8.5. The shear-stress prediction at $x/c = 0.65$ by the φ-α-EASM model has now a pronounced peak close to the wall, which is absent in the predictions of the other models and from the reference data. In the region of the free-shear layer, the φ-α-EASM model predicts higher overall shear stress, which is in better agreement with the experimental data. The location of the shear-stress peak value has also moved towards the location of maximum shear stress found in the experiment. The higher overall levels of shear stress are responsible for the shortening of the recirculation

zone. At the last station, $x/c = 1.2$, the new φ-α-EASM recovers the predictions of the EASM-2D.

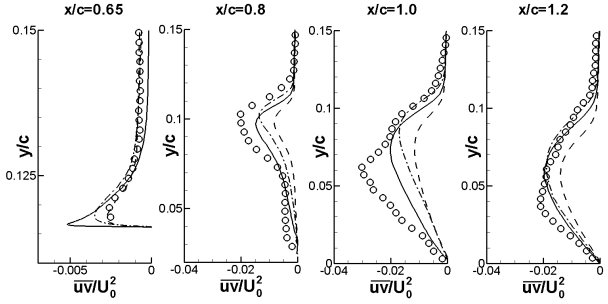

(a) Reynolds-stress tensor component $\overline{u'v'}$

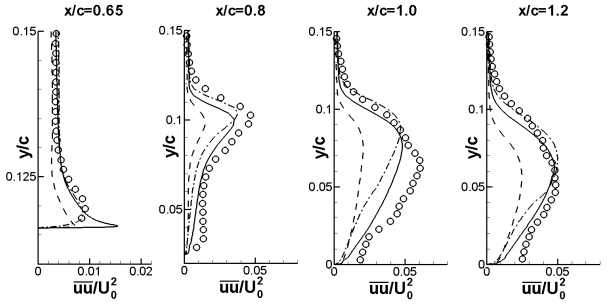

(b) Reynolds-stress tensor component $\overline{u'u'}$

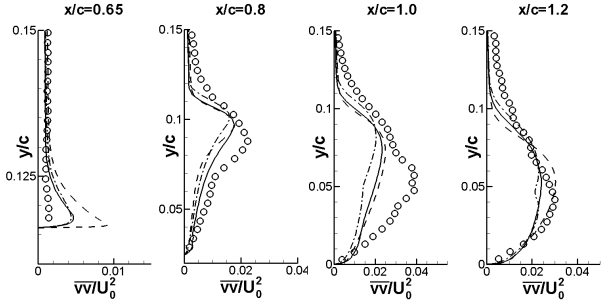

(c) Reynolds-stress tensor component $\overline{v'v'}$

FIGURE 8.5: Components of the Reynolds-stress tensor. Symbols correspond to experimental data of Greenblatt *et al.* (2004, 2006). (—) φ-α-EASM, (- - -) φ-α-UMIST, (– · –) EASM-2D.

Similar to the shear stress, the normal-stress component $\overline{u'u'}$ at station $x/c = 0.65$ of the φ-α-EASM shows a large peak close to the wall, which is not predicted by the other models, and which is not observed in the experimental data. This peak stems from the normal-anisotropy modifications of the φ-α-EASM and seems to be too intense. At all other stations, the normal-stress component $\overline{u'u'}$ has improved over the EASM-2D and the φ-α-UMIST models. The φ-α-EASM model shows higher intensities of normal stress $\overline{u'u'}$ close to the wall and in the free-shear layer. The location of the peak normal stress has also slightly improved.

The predictions of the normal-stress component $\overline{v'v'}$ show less scatter. At station $x/c = 0.65$, the φ-α-EASM and EASM-2D show significantly better predictions, even though the intensity of $\overline{v'v'}$ remains too high close to the wall. At all other stations, the results are very similar and good agreement is observed with the reference data.

In order to illustrate the effect of the near-wall consistency and anisotropy modifications used in the φ-α-EASM, it is convenient to analyse the components of the anisotropy tensor. The a_{11} and a_{22} components of the anisotropy tensor are shown in figure 8.6. It is again obvious, that the φ-α-EASM and EASM-2D model provide good agreement with the reference data for the region away from the wall. It should be emphasised that the anisotropy predictions away from the wall of both models are very similar, as expected, since the φ-α-EASM recovers the normal anisotropy of the EASM-2D model, as desired. At $x/c = 0.65$ and $x/c = 0.8$, the effect of the near-wall consistency and anisotropy modification becomes apparent. The a_{11} components show a large peak close to the wall, and the a_{22} component approaches the correct limiting value of $a_{22} \to -2/3$ at the wall. The rate at which the wall limit is approached is somewhat too rapid compared to the reference data. At the last two stations, $x/c = 1.0$ and $x/c = 1.2$, it is much harder to detect the effect of the near-wall consistency and anisotropy modifications, since they are limited to a region very close to the wall.

Finally, the anisotropy-invariant map is presented in figure 8.7. The first to notice is that all anisotropy states are bound inside the triangle. This indicates that the φ-α-EASM model predicts physically realisable results. Second, the new model is able to reproduce the physically correct two-component state of turbulence at the wall. This is linked to the correct limit of $a_{22} \to -2/3$. Unfortunately, no reference data are available, which prevents further comparison and evaluation.

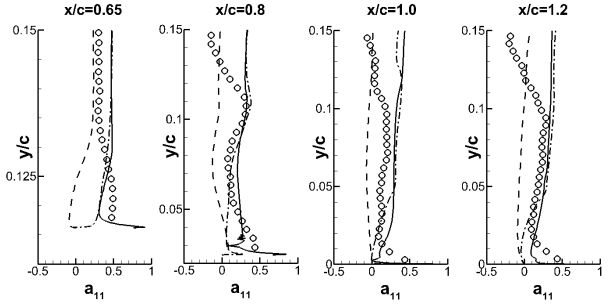

(a) Anisotropy tensor component a_{11}

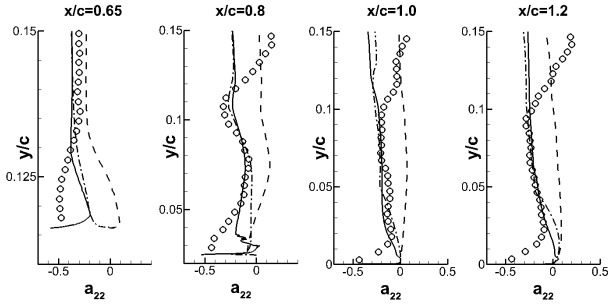

(b) Anisotropy tensor component a_{22}

FIGURE 8.6: Components of the anisotropy tensor. Symbols correspond to experimental data of Greenblatt *et al.* (2004, 2006). (—) φ-α-EASM, (- - -) φ-α-UMIST, (– · –) EASM-2D.

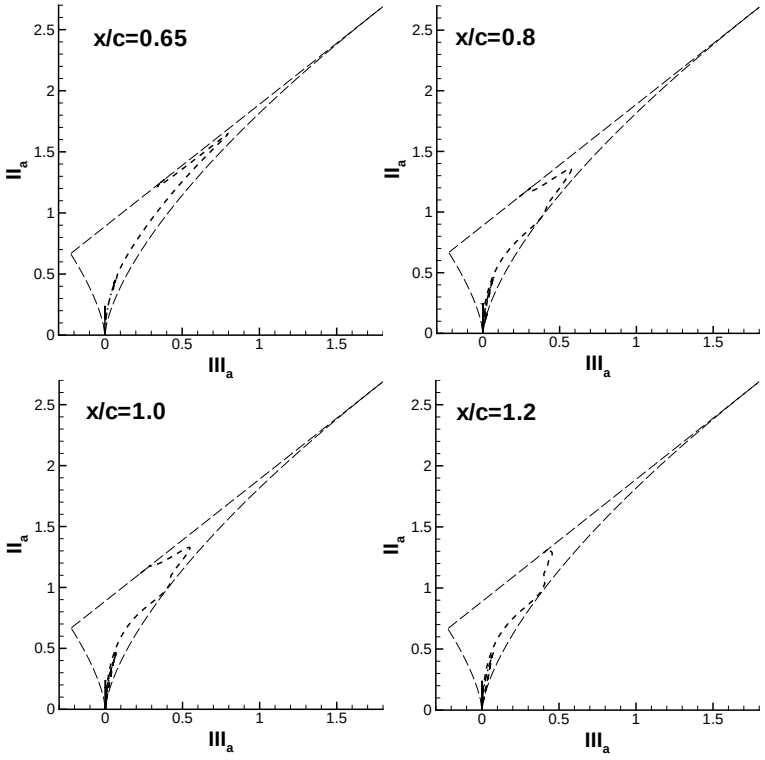

FIGURE 8.7: Anisotropy-invariant map. (- - -) φ-α-EASM, (—) φ-α-UMIST, (– · –) EASM-2D.

8.6 Three-Dimensional Diffuser

The three-dimensional diffuser has already been introduced in section 6.4 and is used here again in order to evaluate the performance of the new φ-α-EASM model to predict three-dimensional flow including boundary-layer separation. As a reference, the results of the EASM-2D and φ-α-UMIST turbulence models are also included in the comparison with experimental data of Cherry *et al.* (2008, 2009).

The flow field at the spanwise location $z/L_z = 0.5$ is presented first. This is followed by a more detailed analysis of the streamwise evolution of the three-dimensional flow field.

Centre Plane $z/L_z = 0.5$

The predictions of the surface-pressure distribution $C_p = (p - p_{ref})/(0.5\rho U_b^2)$ at the bottom wall, $y/H = 0$, are shown in figure 8.8. The new φ-α-EASM model clearly shows improved predictions over the EASM-2D and φ-α-UMIST models for the surface-pressure distribution downstream of $x/L \approx 0.3$. The φ-α-EASM model shows the highest magnitude of C_p throughout and is therefore in better agreement with the reference data. The other models more severely under-predict the surface-pressure distribution. All of the models exhibit the same difficulties in reproducing the initial, rapid pressure recovery, which extents up to the location $x/L \approx 0.5$. The φ-α-EASM model is slightly superior in this respect and predicts the correct trend up to approximately $x/L \approx 0.2$.

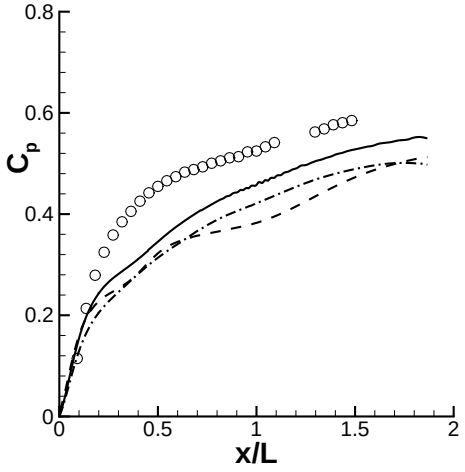

FIGURE 8.8: Surface-pressure coefficient C_p at the bottom wall. Symbols correspond to experimental data of Cherry *et al.* (2008, 2009). (—) φ-α-EASM, (- - -) φ-α-UMIST, ($- \cdot -$) EASM-2D.

More insight into the flow field predictions can be gained from figure 8.9, which shows the streamwise velocity contour U/U_b at the centre plane $z/L_z = 0.5$. The figure also includes a thick line, which corresponds to the zero-velocity contour line and gives the extent of the separated flow region. The experimental data show a large separation zone, which extents from approximately $x/H \approx 7$ to $x/H \approx 19$. The φ-α-EASM and φ-α-UMIST both predict no separation at the centre plane, apart from a very small recirculation zone just downstream of the sharp corner at $x/H = 0$. The EASM-2D gives a more realistic picture of the separation zone, even though agreement is also not fully satisfactory. Similar to the other models, the φ-α-EASM model fails to predict the spreading of the flow away from the bottom wall, towards the centre of the diffuser.

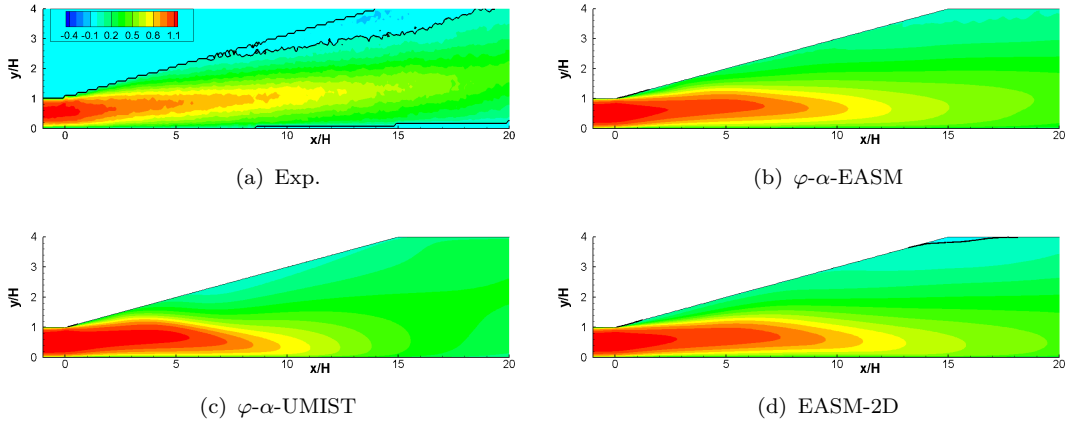

(a) Exp. (b) φ-α-EASM

(c) φ-α-UMIST (d) EASM-2D

FIGURE 8.9: Streamwise velocity contour U/U_b at the centre plane $z/L_z = 0.5$.

A more detailed comparison of the flow field in the centre plane is shown in figures 8.10 and 8.11, where the velocity profiles and Reynolds-stress tensor components are plotted at the four streamwise locations $x/H = 1$, $x/H = 5$, $x/H = 12$ and $x/H = 16$. Although not shown in the figures, the diffuser inflow conditions are better predicted by the φ-α-EASM, similar to the EASM-2D. Both predict the centre-line velocity in better agreement with reference data than the φ-α-UMIST model, which over-predicts the streamwise velocity in the centre of the channel. At $x/H = 1$ and $x/H = 5$, the same trend as for the inflow is still visible, in that, both the φ-α-EASM and EASM-2D predict the velocity magnitude in the centre of the diffuser in better agreement with experimental data. Further downstream, at $x/H = 12$ and $x/H = 16$, the over-prediction of streamwise velocity magnitude is considerably reduced and the magnitudes are closer to the reference data. Nevertheless, the location of the streamwise velocity peak remains too close to the bottom wall, and does not move towards the centre of the diffuser as observed in the experiment. The φ-α-EASM gives the best agreement near the bottom wall and

the location of the peak streamwise velocity is at all stations predicted further away from the bottom wall. However, the overall agreement with reference is still not entirely satisfactory. The streamwise velocity near the top wall is best reproduced by the EASM-2D model. As discussed before, the φ-α-EASM and φ-α-UMIST model do not predict any flow separation at the top wall. This is reflected in the velocity profiles, which show a too large streamwise velocity magnitude at the top wall.

For the streamwise velocity fluctuations $\overline{u'}_{rms}/U_b$ close to the wall, clear differences can be observed between the φ-α-EASM and EASM-2D model (figure 8.10 (d)). The differences are most pronounced at $x/H = 1$ and $/H = 5$, where the φ-α-EASM shows a significantly higher intensity close to the wall. The higher level of streamwise velocity fluctuations can be attributed to the near-wall-anisotropy modifications used in the φ-α-EASM model. Further downstream, at $x/H = 1$ and $x/H = 5$, the influence of the near-wall modifications is less pronounced compared to the stations upstream. Away from the wall, φ-α-EASM predicts the streamwise velocity fluctuations in close agreement with the EASM-2D. This behaviour is expected, since the φ-α-EASM model recovers the normal-Reynolds-stress and anisotropy predictions of the EASM-2D away from the wall. The non-linear stress-strain relationship of both EASM-based models shows clearly more realistic predictions compared to the φ-α-UMIST model. However, the φ-α-EASM model predicts wall-normal velocity fluctuations $\overline{v'}_{rms}/U_b$ that are similar to the EASM-2D model, and which are significantly lower in intensity than from φ-α-UMIST model. Even though the lower intensity seems more realistic, no experimental data are available to confirm this.

Predictions for the $\overline{u'v'}$ shear stress reveal that the φ-α-EASM closely follows the predictions of the EASM-2D. Both models show significantly higher values of shear stress, particularly at $x/H = 12$ and $/H = 16$. It is somewhat surprising, that at the last two stations, the EASM-2D model predicts higher levels of shear stress compared to the φ-α-EASM model, even though the non-constant coefficient $C_\mu^{eff} = -0.5\beta_1$ reduces the contribution of the linear term in the stress-strain relationship to the shear stress.

The ability of the EASM-based models to predict more realistic levels of normal-Reynolds-stress components is also reflected in the predictions of the anisotropy tensor, as shown in figure 8.11. The difference between the φ-α-EASM and the EASM-2D model and the effectiveness of the near-wall consistency and anisotropy modifications becomes more obvious in predictions of the anisotropy tensor. The

near-wall-anisotropy modifications introduce a peak in the a_{11} anisotropy component close to the wall, which is not predicted by the baseline EASM model. In addition, the near-wall-consistency constraint ensures that the a_{22} anisotropy component approaches the correct limit of $a_{22} \rightarrow -2/3$ at both walls. It is also obvious that the anisotropy components from the φ-α-EASM model away from the wall, reduce to the predictions of the baseline EASM-2D model. Even though no reference data are available for the anisotropy tensor, the significantly higher anisotropy of the φ-α-EASM and EASM-2D models seem more realistic than the predictions of the φ-α-UMIST model.

Finally, the anisotropy-invariant map is presented in figure 8.12. The first to notice is that, for this internal flow case, all anisotropy states are bound within the triangle. This indicates that the φ-α-EASM model predicts physically realisable results. Second, the new model is able to predict the physically correct two-component state of turbulence at both walls. This is a direct consequence of predicting the correct limit $a_{22} \rightarrow -2/3$ as the wall is approached.

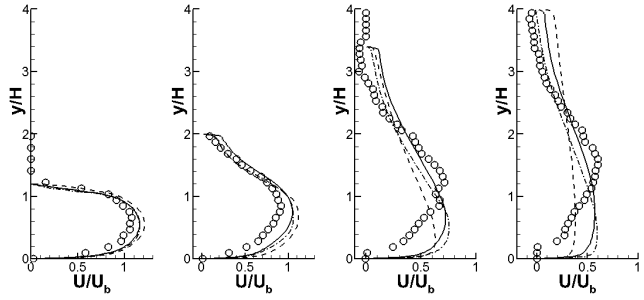

(a) Velocity component U/U_b

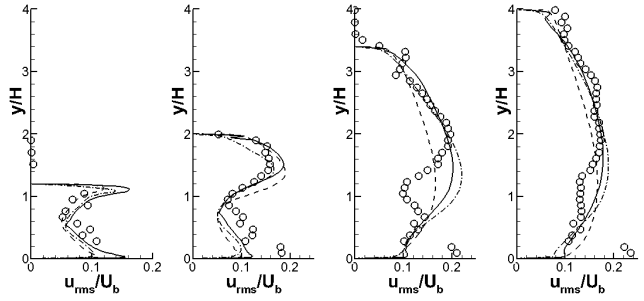

(b) $\overline{u'}_{rms}/U_b$

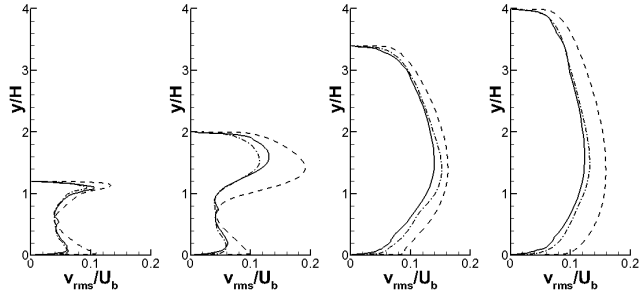

(c) $\overline{v'}_{rms}/U_b$

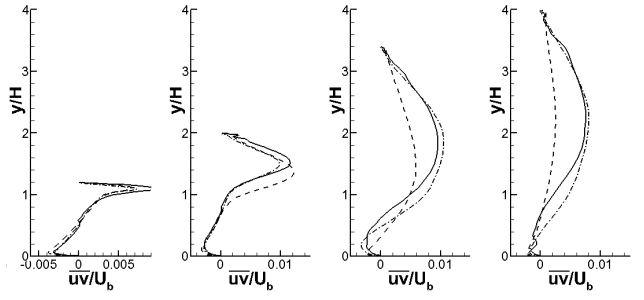

(d) $\overline{u'v'}/U_b^2$

FIGURE 8.10: Velocity and Reynolds-stress tensor components at the centre plane $z/L_z = 0.5$. Locations from left to right: $x/H = 1$, $x/H = 5$, $x/H = 12$ and $x/H = 16$. Symbols correspond to experimental data of Cherry *et al.* (2008, 2009). (—) φ-α-EASM, (- - -) φ-α-UMIST, ($- \cdot -$) EASM-2D.

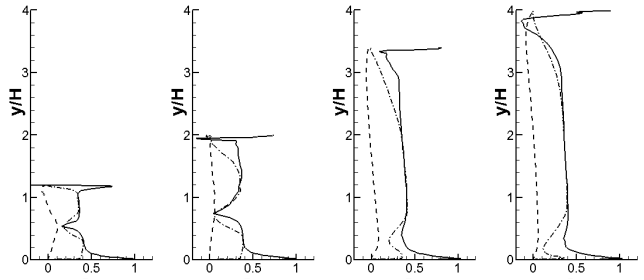

(a) a_{11}

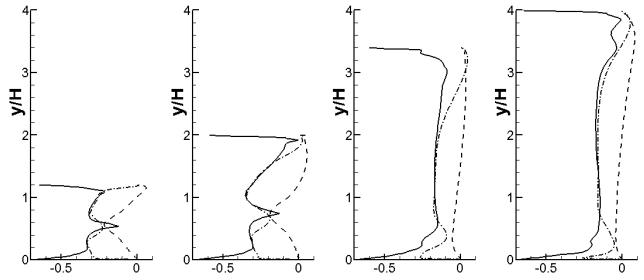

(b) a_{22}

FIGURE 8.11: Components of the anisotropy tensor a_{ij} at the centre plane $z/L_z = 0.5$. Locations from left to right: $x/H = 1$, $x/H = 5$, $x/H = 12$ and $x/H = 16$. (—) φ-α-EASM, (- - -) φ-α-UMIST, (– · –) EASM-2D.

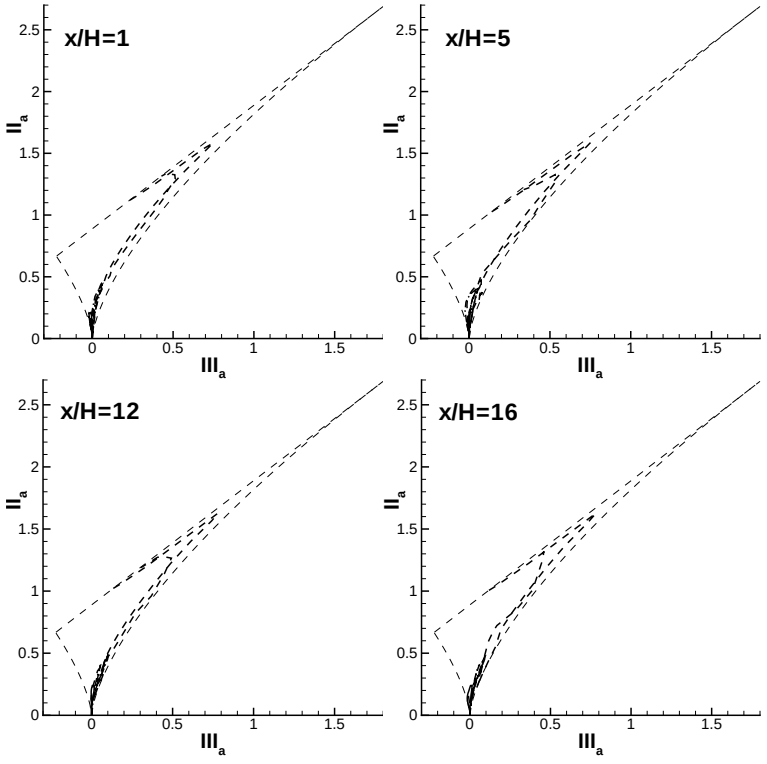

FIGURE 8.12: Anisotropy-invariant map. (- - -) φ-α-EASM, (—) φ-α-UMIST, (– · –) EASM-2D.

Three-Dimensional Flow Field

Further insight into the predictions of the three-dimensional flow field can be gained from figures 8.13 and 8.14, which show contour plots of streamwise velocity component U/U_b and streamwise velocity fluctuations $\overline{u'}_{rms}/U_b$ at the streamwise locations $x/H = 1$, $x/H = 5$, $x/H = 12$ and $x/H = 16$. Figure 8.13 also includes the contour line with zero velocity in order to visualise the extent of the separated-flow region.

At the first cross section, $x/H = 1$, the experimental data show incipient boundary-layer separation emanating from the two upper corners in the diffuser. The same trend is reproduced by all turbulence models with a small tendency to over-predict the amount of separation in the corners. At the next station downstream, $x/H = 5$, the separation is limited to the top right corner and again, all turbulence models are able to capture this trend. However, the shape and extent of the recirculation zone departs slightly from the reference data. The EASM-2D shows separation in the top left corner, which is not observed in the experiment or by the φ-α-EASM and φ-α-UMIST models. At the next two stations downstream, $x/H = 12$ and $x/H = 16$, the flow in the experiment has completely detached from the top wall, and the recirculation zone has become almost two dimensional, with no variation in spanwise direction. Only the EASM-2D model is able to predict the complete flow separation from the top wall, even though this occurs far too late, at approximately $x/H \approx 16$. Both the φ-α-EASM and φ-α-UMIST models show separation from the right wall, which is in contradiction to the experimental data. The shape of the recirculation zone is slightly different between both models. The φ-α-EASM additionally shows flow separation in the top left corner, similarly to the EASM-2D model. It is somewhat surprising that the φ-α-EASM provides improved predictions for the surface-pressure distribution and the velocity profiles at the centre plane, even though, the three-dimensional flow topology is better predicted by the EASM-2D. It is also worth mentioning that the intensity of the secondary motion in the corners of the inflow duct of the φ-α-EASM has almost doubled, to 1.7% of U_b, compared to the baseline EASM-2D. This is in better agreement to reference data, but did not result in improved results for the three-dimensional flow topology.

The contours of streamwise velocity fluctuations $\overline{u'}_{rms}/U_b$ in figure 8.14 are again predicted very similar by all turbulence models investigated here. As discussed before, the EASM models predict a somewhat higher intensity of streamwise velocity fluctuations compared to the φ-α-UMIST model. This is in better agreement with the reference data.

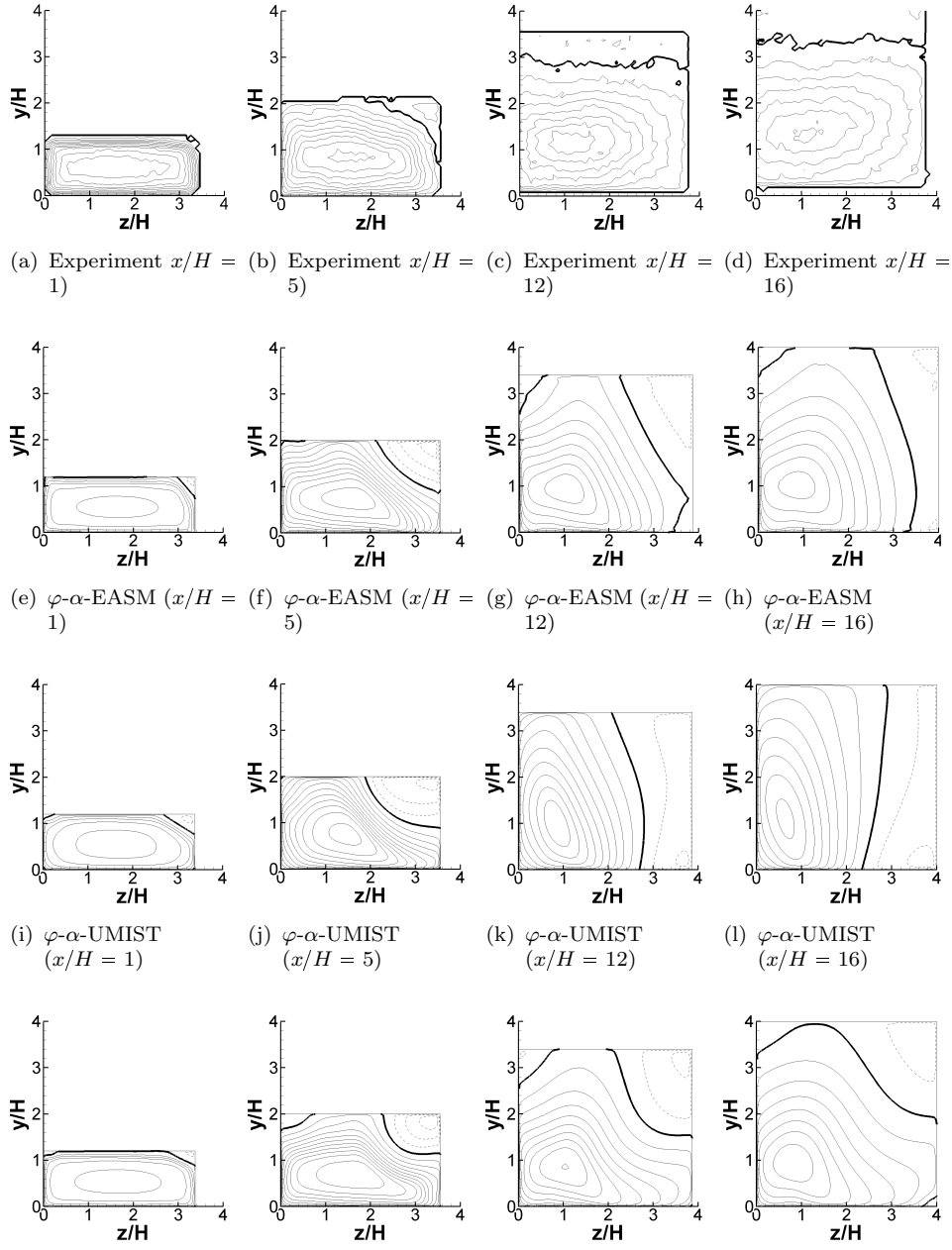

(a) Experiment $x/H = 1$) (b) Experiment $x/H = 5$) (c) Experiment $x/H = 12$) (d) Experiment $x/H = 16$)

(e) φ-α-EASM ($x/H = 1$) (f) φ-α-EASM ($x/H = 5$) (g) φ-α-EASM ($x/H = 12$) (h) φ-α-EASM ($x/H = 16$)

(i) φ-α-UMIST ($x/H = 1$) (j) φ-α-UMIST ($x/H = 5$) (k) φ-α-UMIST ($x/H = 12$) (l) φ-α-UMIST ($x/H = 16$)

(m) EASM-2D ($x/H = 1$) (n) EASM-2D ($x/H = 5$) (o) EASM-2D ($x/H = 12$) (p) EASM-2D ($x/H = 16$)

FIGURE 8.13: Streamwise velocity contours predicted by the φ-α-EASM, φ-α-UMIST, EASM-2D and experimental data of Cherry *et al.* (2008, 2009). Thick line corresponds to zero-velocity contour line. The spacing between contour lines corresponds to $\Delta U/U_b = 0.1$ and dashed lines denote negative velocities.

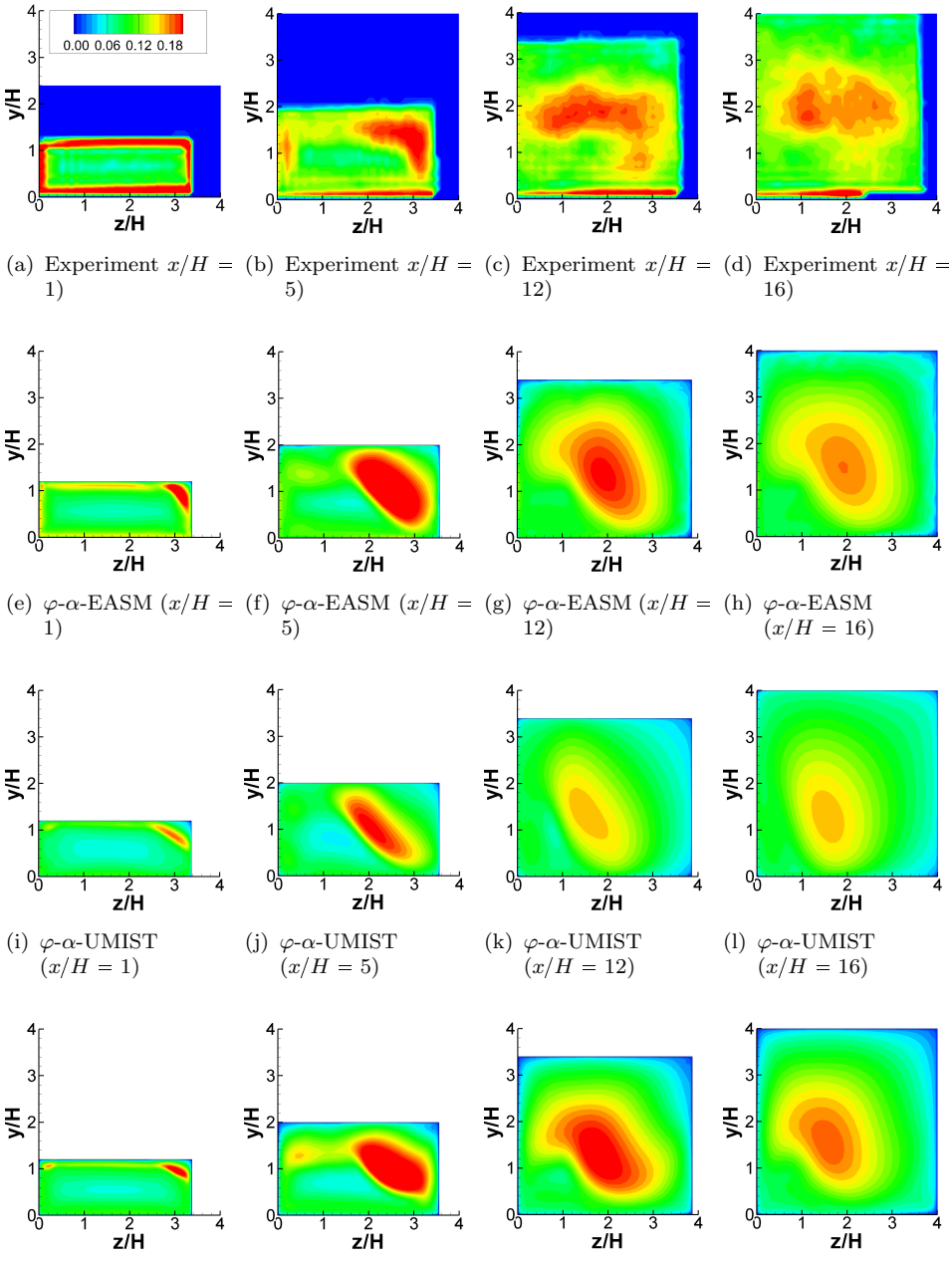

(a) Experiment $x/H = 1$) (b) Experiment $x/H = 5$) (c) Experiment $x/H = 12$) (d) Experiment $x/H = 16$)

(e) φ-α-EASM ($x/H = 1$) (f) φ-α-EASM ($x/H = 5$) (g) φ-α-EASM ($x/H = 12$) (h) φ-α-EASM ($x/H = 16$)

(i) φ-α-UMIST ($x/H = 1$) (j) φ-α-UMIST ($x/H = 5$) (k) φ-α-UMIST ($x/H = 12$) (l) φ-α-UMIST ($x/H = 16$)

(m) EASM-2D ($x/H = 1$) (n) EASM-2D ($x/H = 5$) (o) EASM-2D ($x/H = 12$) (p) EASM-2D ($x/H = 16$)

FIGURE 8.14: Streamwise velocity fluctuations $\overline{u'}_{rms}/U_b$ predicted by the φ-α-EASM, φ-α-UMIST, EASM-2D and experimental data of Cherry *et al.* (2008, 2009).

Chapter 9

A Modified Flow Simulation Methodology

In this section a modified Flow Simulation Methodology (FSM) is presented, which is expected to provide the required amount of turbulence modelling for any mesh resolution, and seamlessly operate between RANS and DNS mode. In order to further enhance the reliability and predictive accuracy of the FSM approach, a hybrid convection discretisation scheme is proposed. The free parameters in the FSM approach are calibrated for stationary homogeneous isotropic turbulence, in order to provide proper LES behaviour and a physically consistent energy cascade. The FSM approach is proposed in conjunction with three different underlying RANS closures of different levels of sophistication. The turbulence models include the k-ω-SST, EASM-2D and φ-α-EASM model.

9.1 The Hybrid RANS/LES Model Formulation

In the combined RANS/LES approach of Speziale (1998b,a) (see also discussion in section 4.5.4) the unresolved-stress components are computed by damping the Reynolds-stress tensor predicted from a state-of-the-art RANS turbulence model. Hence, the unresolved-stress components are given by

$$\overline{u_i' u_j'} = F \cdot \overline{u_i' u_j'}^{RANS}, \tag{9.1}$$

where F is a damping function. The damping function F allows for a continuous blending between RANS and DNS mode, depending on the local and instantaneous

grid resolution, and hence is expected to provide the required amount of turbulence modelling for any mesh resolution. This feature seems highly desirable for any hybrid RANS/LES method to be successfully employed in a commercial solver environment, because it may automatically compensate for inadequate grid resolution by elevated contribution of the unresolved-stress tensor. In general, the blending function needs to be designed such that $F \to 0$, if the grid resolution is sufficient to perform DNS and to resolve the smallest scales of turbulence. In the coarse-grid or infinite-Reynolds-number limit, F needs to approach unity to recover a RANS closure. For values $0 \leqslant F \leqslant 1$, the model is able to operate in LES mode, where most of the turbulence kinetic energy is resolved in the simulation, or in a VLES mode, where large amounts of turbulence kinetic energy are not resolved and are statistically represented by the turbulence model.

Consistency of FSM

The consistency issue of FSM has been addressed in section 4.5.4. Recall that at least two possibilities exist for the computation of the Reynolds-stress tensor. The first approach is to determine the Reynolds-stress tensor by performing explicit averaging of the flow field and only use averaged quantities as an input in the RANS model. This could be achieved by an a-priori RANS simulation, or by computing averaged quantities 'on the fly' as the simulation progresses. Computing the average as the simulation progresses seems not desirable, since accuracy is only achieved for long-time averages and additional averaging may be required for cases, which are statistically unsteady. In addition, the averaging operation removes all information about the local and instantaneous state of the flow and modelling the unresolved component of the local and instantaneous velocity field based on mean-flow quantities seems questionable. Therefore, if mean-flow quantities were used to compute $\overline{u_i' u_j'}^{RANS}$, at least one additional element needs to be introduced, such that the turbulence model may adjust its contribution to the local and instantaneous nature of the flow field, but without influencing the mean-flow field determined by $\overline{u_i' u_j'}^{RANS}$. The hybrid RANS/LES approach of Uribe *et al.* (2010) is based on an idea similar to this. The present FSM approach is designed such that the turbulence-model contribution adjusts to the local and instantaneous state of the flow. This is achieved by using the local and instantaneous filtered flow field to determine the Reynolds-stress tensor $\overline{u_i' u_j'}^{RANS}$. The instantaneous flow field provides sufficient information to model the unresolved scales at a certain instant in time and space. In this case, the resulting Reynolds-stress tensor should be considered as a subgrid-stress tensor and the turbulence kinetic energy k and dissipation rate ϵ computed from the transport equation, turn into the subgrid quantities k_{sgs} and ϵ_{sgs}, respectively.

The main problem of traditional URANS is that the length-scale-providing equation is designed and calibrated to reproduce mean-flow quantities. Therefore, URANS does not predict the correct length scale or turbulence dissipation rate if resolved turbulence fluctuations exist in the flow field. On dimensional grounds, the turbulence viscosity and the turbulence kinetic energy dissipation rate are given by

$$\nu_T = C_\mu V_T L_T, \quad \epsilon = V_T^3 / L_\epsilon, \tag{9.2}$$

where L_T and L_ϵ are two characteristic turbulence length scales and V_T is a characteristic velocity scale. In traditional RANS predictions, L_T and L_ϵ are characteristic length scales of the mean flow, which are too large and therefore not adequate in the presence of resolved turbulence. This has the consequence that the magnitude of ϵ is too small and the resulting magnitude of ν_T is too high. In order to make the URANS equations resolve or sustain turbulence fluctuations, the magnitude of the characteristic length scales L_T and L_ϵ needs to be consistent with the smallest turbulence length scales present in the flow. Since the un-resolved turbulence length scales are much smaller than the length scale of the mean flow, the turbulence dissipation rate is naturally increased and the turbulence viscosity is decreased. The characteristic velocity scale V_T depends on the characteristic turbulence length scale L_T. In the simplest case of a mixing-length RANS model, $V_T = L_T \overline{S}^*_{ij}$, or when obtained from a transport equation for the turbulence kinetic energy, $V_T = k^{1/2}$. It is important to note that the velocity scale V_T is sensitive to the resolved flow field through $\overline{S}^*_{ij}$ or through the production term P_k in the turbulence kinetic energy equation. V_T also has the correct order of magnitude providing the length scale L_T is consistent with the smallest resolved length scale in the flow field. Therefore, in order to make the URANS equations resolve turbulence, only the characteristic turbulence length scales or turbulence dissipation rate ϵ needs to be modified, but not the way the turbulence velocity scale V_T is obtained.

In two-equation DES models, the length scale L_ϵ is modified to be of the order of the grid resolution Δ, which corresponds to the smallest turbulence scales that can be resolved. However, this is not fully consistent, since the length scale L_T in the turbulence viscosity relation is left unchanged. This not only increases the turbulence viscosity, but it also affects the magnitude of the diffusion terms, which are usually modelled using the turbulence viscosity. In contrast, FSM aims at rescaling the Reynolds-stress tensor, which using the Boussinesq approximation 3.10, can be written as $F \cdot \overline{u_i' u_j'}^{RANS} = (2/3) F k \delta_{ij} - 2 F \nu_T \overline{S}^*_{ij}$. From the discussion above, the first term on the right-hand side should not be damped, since it has the correct magnitude, providing the correct length scale is used in the transport equation for

k. The second term on the right-hand side suggests that F can be used to rescale the characteristic length scale L_T in the turbulence viscosity relation to a smaller magnitude $F \cdot L_T$. However, this is again not fully consistent, since the length scale L_ϵ in the turbulence dissipation rate ϵ is left unchanged. Another argument, to limit the damping function F to the turbulence viscosity only and not to damp the entire Reynolds-stress tensor, is that the diffusion terms are computed consistently, i.e. with a turbulence viscosity of the correct magnitude. Yan *et al.* (2009) investigated different hybrid RANS/LES formulations by replacing the turbulence length scales following the idea of DES and FSM and a consistent formulation where both L_T and L_ϵ are modified. The application to a coaxial jet clearly demonstrated the superior performance of the consistent formulation.

Therefore, the URANS equations can be transformed into a subgrid-scale model by modifying both length scales L_T and L_ϵ. The simplest of such a modification is to take $L_T \propto \Delta$ and $L_\epsilon \propto \Delta$, which would reduce the URANS equations to exactly the same form as a typical one-equation SGS model for LES (see, for example, Menon *et al.*, 1996)

$$\frac{Dk_{sgs}}{Dt} = -\overline{u_i' u_j'} \frac{\partial \overline{u}_i}{\partial x_j} - C_\epsilon \frac{k_{sgs}^{3/2}}{\Delta} + \frac{\partial}{\partial x_j} \left[\left(\nu + \frac{\nu_{sgs}}{\sigma_k} \right) \frac{\partial k_{sgs}}{\partial x_j} \right], \tag{9.3}$$

with $\nu_{sgs} = C_\mu k_{sgs}^{1/2} \Delta$ and $\tau_{ij} = (2/3) k_{sgs} \delta_{ij} - 2\nu_{sgs} \overline{S}_{ij}^*$. Note, the closure constants of the RANS model are designed to predict a statistically steady mean-flow field. In the present formulation, the standard RANS closure constants C_μ and $C_{\epsilon 1}$ in (9.3) are modified by the calibration procedure discussed in section 9.4 such that FSM provides proper turbulence resolving capabilities with a physically correct energy cascade.

The original proposal of Speziale to rescale the Reynolds-stress tensor is reduced to a damping of the characteristic length scale $L_T = k^{1/2}/\beta^* \omega$, computed from the RANS equations. Thus, the effective, or hybrid, length scale in FSM is given as $L_{hyb} = F \cdot L_T$. The way this is implemented into a two-equation RANS model is discussed in the next section.

A New Damping Function

The damping function F is particularly important for the success of the FSM approach. The original damping function by Speziale was based on the ratio of grid

spacing to Kolmogorov length scale Δ/L_η and was given by

$$F = f_\eta = \left[1 - \exp\left(\frac{-\beta\Delta}{L_\eta}\right)\right]^n. \tag{9.4}$$

This function is expected to provide the correct behaviour in the DNS limit. However, the Kolmogorv length scale is not a relevant characteristic length scale when performing LES. Therefore, there is no guarantee that this damping function will provide the correct magnitude of damping in LES mode. It seems even more questionable how this damping function would recover a RANS mode in case of too-coarse grids. The first modification to the FSM approach, that has been made in this work, is to retain the original damping function f_η to ensure that FSM reaches the DNS limit. Another advantage of this approach is that the two free parameters n and β can more easily be tuned. Figure 9.1 shows the dependency of the damping function f_η on the parameters n and β. For example, the values $n = 4$ and $\beta = 0.5$ yield a damping function, which rapidly goes to zero as the ratio Δ/L_η drops below 10. The issue of choosing β is revisited in section 9.4, where the modified FSM approach is calibrated for homogeneous isotropic turbulence.

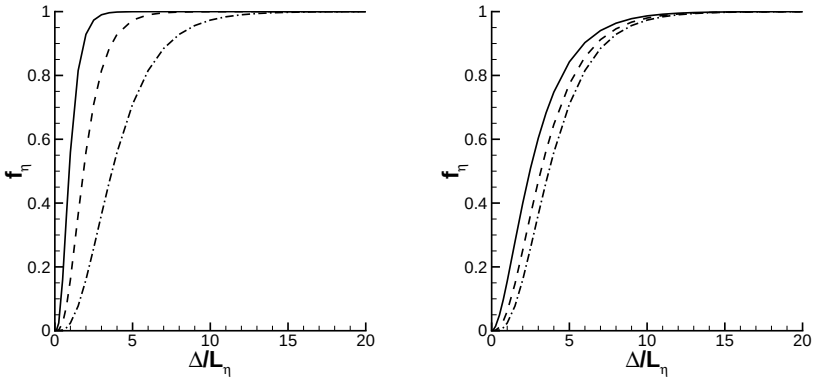

(a) β dependency ($n = 4$), (—) $\beta = 2$, (- - -) $\beta = 1$, (– · –) $\beta = 0.5$

(b) n dependency ($\beta = 0.5$), (—) $n = 2$, (- - -) $n = 3$, (– · –) $n = 4$

FIGURE 9.1: Dependency of f_η on the parameters n and β.

The second modification ensures that FSM provides the correct damping in LES mode. In the LES region, most of the turbulence kinetic energy production and turbulence kinetic energy is explicitly resolved by the simulation. This requires a grid resolution such that the resolution cut-off is located in the inertial subrange of the energy spectrum. In LES the grid size represents the characteristic length scale of the unresolved turbulence, with $L_{hyb} \propto \Delta$. Therefore, the additional element $f_\Delta = C_\alpha \Delta/L_T$ is introduced to the damping function F, where C_α is a constant that needs to be calibrated. With the modifications so far, the damping function F

can be written as

$$F = f_\eta f_\Delta = \left[1 - \exp\left(-\frac{\beta\Delta}{L_\eta}\right)\right]^n \frac{C_\alpha \Delta}{L_T}. \tag{9.5}$$

The filter length scale is defined in this work as the cube root of the cell volume, i.e. $\Delta = \mathrm{d}V^{1/3}$. Note that many other definitions are possible, but this one is suitable for cells of arbitrary polyhedral shapes.

If the filter width is smaller than the local characteristic length scale, $C_\alpha\Delta < L_T$, the FSM approach will operate in LES mode, with $F < 1$. This usually occurs away from the wall where the grid size is sufficiently fine to resolve turbulence fluctuations. As the wall is approached, the length scale L_T goes to zero, since the turbulence kinetic energy vanishes at the wall, $k_w = 0$. As a consequence, $C_\alpha\Delta > L_T$ close to the wall, which gives $F > 1$. A damping function larger than unity is not desirable, since its need to be able to recover the RANS mode. Thus,

$$F = \min\left[f_\eta f_\Delta, 1\right] = \min\left[\left(1 - \exp\left(-\frac{\beta\Delta}{L_\eta}\right)\right)^n \frac{C_\alpha\Delta}{L_T}, 1\right]. \tag{9.6}$$

This modification ensures that the hybrid formulation operates in a URANS mode for $C_\alpha\Delta > L_T$. Recall that for $C_\alpha\Delta < L_T$ the FSM approach reduces to the exact form as a one-equation subgrid-scale model for LES. It is not very likely that the present formulation would return to URANS mode away from the wall, even if the grid resolution becomes too coarse to resolve turbulence fluctuations. On too-coarse grids the length scale definition $L_{hyb} \propto \Delta$ becomes increasingly inappropriate, and the FSM approach effectively operates as a sort of badly calibrated one-equation RANS model. In order to completely revert back to RANS mode, or to enter the VLES regime, another element needs to be introduced to the damping function, such that F approaches unity. The v. Karman length scale L_{vK} may be a suitable candidate. However, this issue has not been investigated in the current work due to time constraints.

The present FSM formulation suffers from the same grid sensitivity issues as DES. It is therefore essential to introduce another element to the damping function F, which ensures that the switch from RANS to LES occurs outside the boundary layer. This is easily achieved by the function

$$f_z = \frac{1}{1 - F_z}. \tag{9.7}$$

The 'shielding' function can be chosen as $F_z = F_1$ or $F_z = F_2$, where F_1 and F_2 are blending functions, which are required for the underlying k-ω turbulence model described in the next section. Therefore, the resulting new formulation of the damping function, including a boundary-layer shield, is given as

$$F = \min\left[f_\eta f_\Delta f_z, 1\right] = \min\left[\left(1 - \exp\left(-\frac{\beta\Delta}{L_\eta}\right)\right)^n \frac{C_\alpha \Delta}{L_T}\left(\frac{1}{1-F_z}\right), 1\right]. \quad (9.8)$$

9.2 Choice of underlying RANS model

It is natural to assume that a more sophisticated RANS model will provide improved predictions in the RANS region within a hybrid RANS/LES framework. This offers enough incentive to employ a state-of-the-art RANS turbulence model with, for example, a non-linear constitutive stress-strain relationship and strain- and rotation-dependent coefficients within a hybrid RANS/LES method. Such features are likely to provide more realistic predictions of the Reynolds-stress and anisotropy tensor, and better performance in non-equilibrium flows.

The benefits of using a more sophisticated RANS model will also be reflected in the quality of the predictions in the LES region, where the RANS model functions as a subgrid-scale model. A more sophisticated RANS model will presumably provide a more realistic representation of the modelled subgrid-stress and hence will improve the predictions in the LES region. Improvements are expected to be most pronounced in situations where the unresolved subgrid flow is not in equilibrium and contains a significant degree of anisotropy. Such situations are likely to be encountered in engineering and industrial applications where the mesh quality and resolution is sometimes sacrificed in favour of short turnaround times. For example, on anisotropic computational grids the resolved turbulence structures will contain a forced anisotropy, which is also reflected in anisotropy of the modelled subgrid-stress. Close to the wall, the turbulence is highly anisotropic and so will be the unresolved subgrid-stress. In situations where the computational grid is too coarse and the resolution cut-off is located in the large scales, the unresolved turbulence will not be in equilibrium and will be anisotropic. In all these cases a sophisticated turbulence model, which contains advanced elements to accurately predict the subgrid flow is considered highly desirable.

In fact, a range of LES subgrid-scale models have been developed with the intention of providing a more realistic representation of the unresolved turbulence as it is possible with a linear stress-strain relationship. For example, scale-similarity models

explicitly filter the resolved flow field in order to obtain a more accurate description of the structure of the unresolved turbulence. Similarly, non-linear and differential subgrid-scale models (see, for example, Deardorff (1973) or Lund & Novikov (1992)) have been introduced with the intention of providing a more realistic representation of the subgrid-stress and anisotropy field. Fureby *et al.* (1997*a*,*c*) have investigated differential subgrid-scale models and confirmed that improved mean-velocity predictions and second-order statistics could be obtained. Marstropp *et al.* (2009) proposed an explicit algebraic subgrid-stress model and found that for coarse resolution the mean velocity and Reynolds stresses were better than those given by the dynamic Smagorinsky model. In addition, the predictions were found to be much less sensitive to the resolution of the computational grid. These findings were confirmed in Rasam *et al.* (2011).

In order to investigate the sensitivity of results with respect to the underlying RANS model, the Flow Simulation Methodology is used in conjunction with three different RANS turbulence models of different levels of sophistication. The first RANS model is the k-ω-SST model, which is based on a linear stress-strain relationship. The second model is the baseline EASM-2D model, which contains strain- and rotation-dependent coefficients and is based on a non-linear constitutive stress-strain relationship. The last model is the φ-α-EASM model, which includes consistency and anisotropy modifications for improved predictions of the flow close to the wall.

FSM-k-ω-SST

The transport equations for the turbulence kinetic energy k and the specific dissipation rate ω of the k-ω-SST model are unchanged and take the form:

$$\frac{Dk}{Dt} = \tilde{P}_k - \epsilon + \frac{\partial}{\partial x_j}\left[\left(\nu + \sigma_k \nu_T\right)\frac{\partial k}{\partial x_j}\right], \tag{9.9}$$

$$\frac{D\omega}{Dt} = \gamma \frac{1}{\nu_T}\tilde{P}_k - \beta\omega^2 + \frac{\partial}{\partial x_j}\left[\left(\nu + \sigma_\omega \nu_T\right)\frac{\partial \omega}{\partial x_j}\right] + 2(1-F_1)\sigma_{\omega 2}\frac{1}{\omega}\frac{\partial k}{\partial x_i}\frac{\partial \omega}{\partial x_i}. \tag{9.10}$$

Within the hybrid FSM approach the turbulence kinetic energy dissipation rate is given by

$$\epsilon = F^{-1}\beta^* k\omega, \tag{9.11}$$

and the turbulence viscosity is obtained as

$$\nu_T = F\frac{a_1 k}{\max(a_1\omega, SF_2)}. \tag{9.12}$$

Note that this formulation is consistent with replacing the characteristic turbulence length scale in the definition of the dissipation rate and in the turbulence viscosity, with $L_{hyb} = FL_T$, where $L_T = k^{1/2}/\beta^*\omega$.

FSM-k-ω-EASM

The transport equations for the turbulence kinetic energy k and the specific dissipation rate ω of the baseline EASM-2D model take the following form:

$$\frac{Dk}{Dt} = P_k - \epsilon + \frac{\partial}{\partial x_j}\left[\left(\nu + \sigma_k \nu_T\right)\frac{\partial k}{\partial x_j}\right], \tag{9.13}$$

$$\frac{D\omega}{Dt} = \gamma\frac{\omega}{k}P_k - \beta\omega^2 + \frac{\partial}{\partial x_j}\left[\left(\nu + \sigma_\omega \nu_T\right)\frac{\partial \omega}{\partial x_j}\right] + \frac{\sigma_d}{\omega}\max\left(CD_{k\omega}, 0\right). \tag{9.14}$$

Within the hybrid FSM approach the dissipation rate is given by

$$\epsilon = F^{-1}\beta^* k\omega, \tag{9.15}$$

and the turbulence viscosity is

$$\nu_T = F(-0.5\beta_1 k\tau). \tag{9.16}$$

Note that the turbulence time scale is given by $\tau = 1/\beta^*\omega$ and is not limited by the viscous time scale. The non-linear stress-strain relationship of the EASM model $\overline{u_i' u_j'} = (2/3)k\delta_{ij} + ka_{ij}$, also requires that the damping function is applied to the extra-anisotropy tensor according to

$$a_{ij} = -2(\nu_T/k)S_{ij}^* + F \cdot a_{ij}^{ex}. \tag{9.17}$$

FSM-φ-α-EASM

The transport equations for the turbulence kinetic energy k and the specific dissipation rate ω of the new φ-α-EASM model take the following form:

$$\frac{Dk}{Dt} = P_k - \epsilon + \frac{\partial}{\partial x_j}\left[\left(\nu + \sigma_k \nu_T\right)\frac{\partial k}{\partial x_j}\right], \tag{9.18}$$

$$\frac{D\omega}{Dt} = \gamma\frac{\omega}{k}P_k - \beta\omega^2 + \frac{\partial}{\partial x_j}\left[\left(\nu + \sigma_\omega \nu_T\right)\frac{\partial \omega}{\partial x_j}\right] + \frac{\sigma_d}{\omega}\max\left(CD_{k\omega}, 0\right), \tag{9.19}$$

where the turbulence dissipation rate is given by

$$\epsilon = F^{-1} f_{\beta^*}\beta^* k\omega. \tag{9.20}$$

In addition, the transport equation for the wall-normal velocity scale ratio and the elliptic operator are given as

$$\frac{D\varphi}{Dt} = (1-\alpha^p)\, f_{wall} + \alpha^p f_{hom} - \frac{\varphi}{k} P_k + \frac{2}{k}\left(\sigma_k \nu_T\right) \frac{\partial k}{\partial x_j}\frac{\partial \varphi}{\partial x_j} + \frac{\partial}{\partial x_j}\left[\left(\nu + \sigma_\varphi \nu_T\right)\frac{\partial \varphi}{\partial x_j}\right],$$

$$L^2 \nabla^2 \alpha - \alpha = -1. \tag{9.21}$$

The homogeneous and wall redistribution term are computed using the RANS dissipation rate ϵ. It has been found that in this way the near-wall modifications remain inactive away from the wall, in case of resolved turbulence. Therefore, the redistribution terms are given by

$$f_{hom} = -(1/\tau)\left(C_1 - 1 + \frac{C_2 P_k}{f_{\beta^*}\beta^* k\omega}\right)\left(\varphi - \frac{2}{3}\right), \quad f_{wall} = -\varphi f_{\beta^*}\beta^*\omega. \tag{9.22}$$

In order to avoid a double-damping of the turbulence viscosity

$$\nu_T = F \cdot C_\mu^\nu \varphi k \tau, \tag{9.23}$$

the turbulence time and length scale are also computed using the RANS dissipation rate, thus

$$\tau = \max\left[\min\left(\frac{1}{f_{\beta^*}\beta^*\omega}, \frac{0.6}{\sqrt{6}C_\mu \varphi \left|S_{ij}^*\right|}\right), C_\tau \sqrt{\frac{\nu}{f_{\beta^*}\beta^* k\omega}}\right], \tag{9.24}$$

$$L = C_L \max\left[\min\left(\frac{k^{1/2}}{f_{\beta^*}\beta^*\omega}, \frac{k^{1/2}}{\sqrt{6}C_\mu \varphi \left|S_{ij}^*\right|}\right), C_\eta \left(\frac{\nu^3}{f_{\beta^*}\beta^* k\omega}\right)^{1/4}\right]. \tag{9.25}$$

The same holds for the time scale $\widetilde{\tau}$ used in the near-wall consistency and anisotropy modification.

The non-linear stress-strain relationship of the φ-α-EASM model $\overline{u_i' u_j'} = (2/3)k\delta_{ij} + k a_{ij}$ also requires that the damping function is applied to the extra-anisotropy tensor, according to

$$a_{ij} = -2(\nu_T/k) S_{ij}^* + F \cdot a_{ij}^{ex}. \tag{9.26}$$

9.3 A tailored Hybrid Convection Scheme

In this section a tailored hybrid convection scheme is proposed, where the face fluxes are obtained by a linear combination of the central-difference scheme (CDS) and a second-order upwind scheme, using a flow-dependent flux-blending function. This scheme is intended to be used in conjunction with the modified FSM approach. A similar hybrid convection scheme tailored to Detached Eddy Simulation has been presented in Travin *et al.* (2004*b*).

The motivation for using a hybrid convection scheme stems from the conflicting demands RANS and LES place on the discretisation scheme. In LES applications, the subgrid-scale (SGS) model has to provide an adequate amount of dissipation, such that the energy cascade is correctly reproduced and no energy accumulates at the smallest resolved scales. The amount of dissipation provided by the SGS model is usually very small, with the consequence that any elevated level of numerical dissipation will inevitably contaminate the resolved flow field. Therefore, higher-order schemes with low levels of numerical dissipation, such as the CDS, are the preferred choice in LES. The unboundedness of CDS may result in spurious oscillations if the stability constraints are not satisfied. According to Hirsch (1994), the following constraints need to be satisfied: $Pe \cdot \sigma < 2$ and $2\beta < 1$, where the Peclet number is defined as $Pe = \sigma/\beta = \overline{u}/(\Gamma/\Delta_x)$, the variable $\sigma = \overline{u}\Delta t/\Delta_x$ corresponds to the Courant–Friedrichs–Lewy number and the diffusion number $\beta = \Gamma\Delta t/\Delta_x^2$, where Δt denotes the time step and Δ_x the grid spacing. Since fine grids are required for LES and the diffusivity Γ is small, the pure CDS is often applicable. However, in strongly convective conditions it may be necessary to introduce a very small amount, say 5%, of second-order upwind in order to stabilise the solution. In general, higher-order upwind or TVD schemes are not recommended for turbulence resolving simulations, since the additional numerical dissipation introduced by these schemes is significant, and will contaminate the resolved flow field. It will be shown later, in section 9.4 and chapter 10, that when higher-order upwind or TVD schemes are used in the LES region, the results will inevitably deteriorate. In RANS applications, the source terms and high-order nonlinearities present in the transport equations for turbulence quantities require more robust, yet less accurate, upwind or TVD schemes to ensure numerical stability. The increased levels of numerical dissipation induced by the second-order upwind or TVD schemes is usually smaller than the large diffusivity Γ provided by the RANS model and hence, will not affect the predictions as much as in the case of LES.

Based on this discussion, a second-order accurate hybrid convection scheme is proposed, which employs the linear-upwind (LUD) scheme in the RANS region and the CDS scheme in the LES region. Alternatively, the LUD scheme could be replaced by a TVD scheme. The face fluxes of the hybrid convection scheme are obtained from a linear combination of the form

$$\phi_f = (1 - \sigma_b)\, \phi_{f,CDS} + \sigma_b \phi_{f,LUD}, \tag{9.27}$$

where σ_b is a flow-dependent blending function. The blending function is designed such that $\sigma_b = 1$ if FSM operates in RANS mode ($F = 1$) and rapidly drops to zero if the damping function is $F < 1$. The following function provides the desired behaviour

$$\sigma_b = \tanh\left(A^3\right), \quad A = \max\left[f_\eta f_\Delta f_z - 0.6, 0\right]. \tag{9.28}$$

Note that other possibilities exist to combine CDS and LUD/TVD schemes, for example, a switch or blending between both schemes based on the local Peclet number would be a viable option. Since the FSM scheme has been found to work as intended, no further effort has been devoted to the implementation and testing of other numerical schemes.

Figure 9.2 shows contours of the blending function σ_b for the flow around two inline tandem cylinders and the flow in a diffuser, using the modified FSM approach. Both cases are described in more detail in chapter 10. It is obvious that the free-stream and boundary layers on both cylinder are computed using the upwind-difference scheme ($\sigma_b = 1$). In the wake of the first and second cylinder, σ_b drops sharply to zero and the resolved flow is computed using the central-difference scheme. It should be noted that no stable solution could be obtained for the tandem cylinder case if the central-difference scheme was employed everywhere in the domain. The blending function also works as intended for the flow in the diffuser. The near-wall RANS region is computed using the upwind-difference scheme whereas the flow away from the wall is computed using the central-difference scheme. It will be shown in chapter 10 that the hybrid FSM schemes provides almost identical results to those obtained using the central-difference scheme.

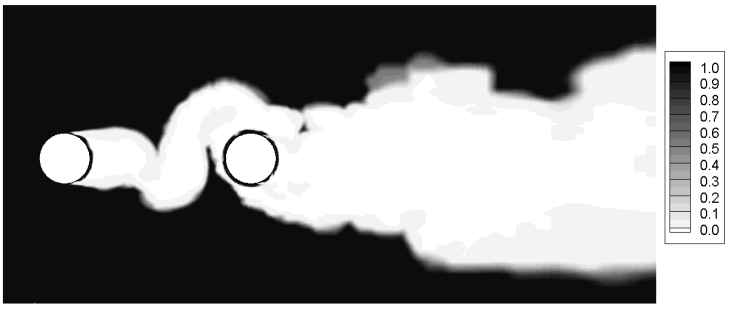

(a) Tandem Cylinders.

(b) Diffuser.

FIGURE 9.2: Flux blending function σ_b.

9.4 Calibration of the modified FSM approach

The remaining task to complete the model formulation is to determine suitable values for the free parameters C_α, β and n, which appear in the damping function F. Homogeneous isotropic turbulence (HIT) is used to calibrate and validate the LES capabilities of the proposed modified FSM approach. In the calibration process the total turbulence kinetic energy dissipation rate $\epsilon = \epsilon_{sgs} + \epsilon_\nu + \epsilon_{num}$, resulting form the combined effect of turbulence model formulation, viscosity and numerical framework, is optimised such, that the FSM approach provides proper LES capabilities with resolved turbulence, as depicted in figure 9.3, and with a physically consistent energy cascade. It is important that the numerical dissipation is included in the calibration study, since the magnitude may be of the same order as the dissipation provided by the turbulence model. For this reason, the calibration is performed in conjunction with the hybrid FSM convection scheme presented in section 9.3.

HIT is probably the most simple turbulent flow conceivable. In HIT the spatial gradients of mean flow and turbulence statistics vanish and with that all production and transport processes. This has the consequence that the turbulence kinetic energy decays according to $\mathrm{d}k/\mathrm{d}t = -\epsilon$. Typically, decaying HIT is used for the calibration of virtually all trusted turbulence-resolving approaches such as, DES, SAS and many LES sugbrid-scale models. In the calibration process the model

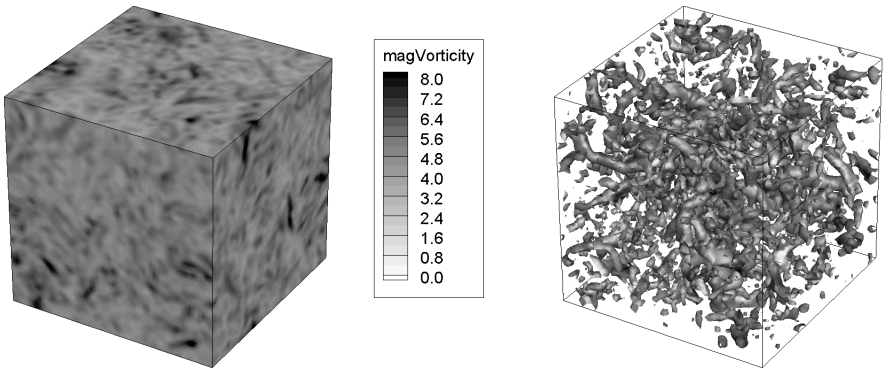

(a) Vorticity magnitude (b) $Q = (1/2)(\Omega^*_{ij}\Omega^*_{ij} - S^*_{ij}S^*_{ij}) = 3(1/s^2)$

FIGURE 9.3: Homogeneous isotropic turbulence.

constants are adjusted and results for the energy spectra are matched to experimental or DNS data. One of the major difficulties associated with temporal simulation of decaying homogeneous isotropic turbulence is that physically realistic initial conditions are required for the three-dimensional velocity field. With the availability of reference DNS data, the three-dimensional velocity field from DNS can be re-sampled/truncated to the grid resolution used for the calibration study. The situation is slightly more difficult when experimental data are used as a reference. Usually only energy spectra are available from experiments, which need to be converted into a three-dimensional flow field using inverse Fourier transform. Even though the spectral energy distribution of the flow field can be re-created, the resulting velocity field lacks physically consistent spatial correlations. In the calibration procedure the simulation is started from the initial flow field and after a certain time has elapsed, the instantaneous energy spectra is compared to reference data. The simulation time, of course, needs to be long enough such, that the flow field recovers from unphysical initial conditions and to allow the flow to adapt to the contributions from the turbulence model.

In the calibration study conducted here, the potential sensitivity of the results to initial conditions is avoided by performing simulations of stationary homogeneous isotropic turbulence, where the natural decay of turbulence is circumvented by adding an artificial forcing term to the momentum equations. The forcing term maintains a certain level of turbulence kinetic energy. This procedure not only allows to achieve arbitrarily high Reynolds numbers, with a significant inertial subrange, it also allows to obtain statistically converged turbulence statistics.

9.4.1 Computational Setup

The forcing scheme employed in this work follows the proposal of Eswaran & Pope (1988) and has previously been used in Fureby *et al.* (1997*b*). The energy is only added to wavenumbers below $\kappa = |\boldsymbol{\kappa}| \leqslant 2.5[1/m]$. This ensures that the statistics of the small-scale motion close to the grid cut-off wavenumber are not contaminated by the artificial forcing mechanism, which mainly consists of spatially random white noise. Even though some of the small-scale quantities are set by the large-scale motion, e.g. dissipation rate, it has been shown in Eswaran & Pope (1988), that forcing at low wavenumbers does not significantly influence the dynamics of the small-scale motion and hence the statistics at high wavenumbers.

Simulations are performed in a cubic box with a side length of $L = 2\pi[m]$ and with periodic boundary conditions in all directions. The Reynolds number investigated here is $Re_\lambda = u_{rms}\lambda_T/\nu = 732$, with $u_{rms} = \sqrt{(2/3)\langle k\rangle}$, $\langle k\rangle = (1/2)\langle u_i u_i\rangle$ and the Taylor length scale $\lambda_T = \left(\langle u_i u_i\rangle / \left\langle (\nabla u_j)^2 \right\rangle\right)^{1/2}$, where the brackets $\langle\rangle$ denotes space-averaged quantities. This Reynolds number is also studied in Kaneda *et al.* (2003) using DNS, and their results are used here as a reference.

In order to assess potential grid dependencies of the calibration constants, the calibration study is conducted for two different grid resolutions using 32 (HIT32) and 64 (HIT64) cells in each direction of the cubic box. The physical time step is set to $\Delta t = 0.05[sec]$ for the coarse mesh and $\Delta t = 0.025[sec]$ for the fine mesh and yields a CFL number of $CFL < 0.4$. The resulting energy spectra are averaged over more than 30 samples, which are sufficiently separated in time to ensure that they are not correlated. In all simulations the integral length scale $L_I = (\pi/2u_{rms}) \int_0^{\kappa_{max}} \kappa^{-1} E(\kappa) \mathrm{d}\kappa$ did not exceed $L_I < 0.2L$, such that the use of periodic boundary conditions is justified.

9.4.2 Calibration of C_α

The closure constant C_α is the most important one and controls the behaviour of FSM for an LES-like resolution of the flow. Recall that the Taylor-scale Reynolds number is $Re_\lambda = 732$ and the ratio of grid spacing to Kolmogorov length scale is $\Delta/L_\eta = 187$ for the coarse mesh and $\Delta/L_\eta = 93$ for the finer mesh, where the Kolmogorov length scale L_η is obtained from DNS data. This high ratio is reflected in the damping function f_η, which controls the behaviour of FSM close to the DNS limit. For the two grid resolutions f_η remains inactive ($f_\eta = 1$). As a

consequence, only the constant C_α for the damping function f_Δ can be determined, and the constant β appearing in f_η has to be determined using a different strategy or smaller Reynolds number.

Before the results of the calibration study are presented some additional comments about the calibration strategy are necessary. It is important to note again that all underlying RANS models used here are based on a set of closure constants, which are obtained by blending between the k-ω and k-ϵ framework using the blending function F_1. The blending function F_1 is designed to be unity close to the wall and to decay to zero away from the wall. For the case $F_1 = 1$ the closure constants of the k-ω framework are active and for $F_1 = 0$ the closure constants of the k-ϵ framework are active. The present calibration case does not involve any walls and the closure constants of the RANS model therefore corresponds to the k-ϵ model. It would seem natural to perform the calibration for both limits $F_1 = 1$ and $F_1 = 0$, and to obtain two constants C_{α_1} and C_{α_2}, which are blended according to F_1. However, this has been found not to be necessary for the following reason. Consider the cases where parts of the boundary layer are shielded using either $f_z = 1/(1 - F_1)$ or $f_z = 1/(1 - F_2)$. In both cases FSM will be operating in a RANS mode in regions where $F_1 = 1$ or $F_2 = 1$ with the consequence, that the value of C_{α_1} becomes irrelevant. In case f_z is not used to shield parts of the boundary layer, it might potentially occur that the damping function F reduces the model contribution to LES mode and the blending function F_1 is still close to unity. Only in this specific case would it be beneficial to have an optimised value of C_{α_1}, since FSM will try to resolve turbulence with the baseline RANS model operating in the k-ω regime. However, it has been observed in practical applications that when FSM reduces the model contribution to an LES level, the blending function F_1 also sharply drops to zero. This means that the k-ω regime is almost exclusively used in a pure RANS mode, which does not require the constant C_{α_1}. For this reason and for the sake of reducing the complexity of the FSM approach, a blending function for C_α is not considered here.

Results

The constants C_α resulting from the optimisation study are summarised in table 9.1 for all three underlying RANS models and for both mesh resolutions. Figure 9.4 shows the corresponding three-dimensional energy spectra $E(\kappa)$, which are obtained by performing integration over spherical shells and where $\kappa = |\boldsymbol{\kappa}|$ is the wavenumber

magnitude. For comparison, results of IDDES, SAS and with no subgrid-scale model (UDNS), are shown as well.

FSM	C_α (HIT 32)	C_α (HIT 64)
SST	1.0	0.85
EASM	2.4	2.1
φ-α-EASM	1.0	0.85

TABLE 9.1: Model constants C_α for the FSM approach.

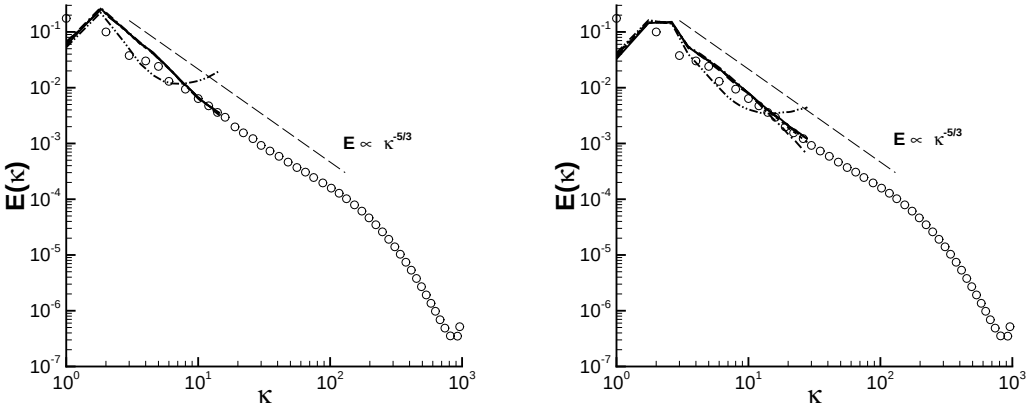

(a) HIT 32 (b) HIT 64

FIGURE 9.4: Energy spectra $E(\kappa)$. Symbols correspond to DNS of Kaneda *et al.* (2003). (—) FSM-SST, (- - -) FSM-EASM, (– – –) FSM-φ-α-EASM, ($\cdots$) IDDES , (– · –) SAS, (– · ·–) UDNS .

The simulations with no sub-grid scale model are clearly not very successful in reproducing the correct energy cascade at the cut-off and show an spurious accumulation of energy at the high wavenumbers. The energy spectra for the low resolution case (HIT32) is predicted consistently by all models in good agreement with DNS data. The small discrepancies at low wavenumbers can be attributed to the artificial forcing mechanism, which is active in this range. It is interesting to note that the constant C_α of the FSM-EASM model is significantly larger compared to the values for the FSM-SST and FSM-φ-α-EASM models. This implies that the dissipative nature of the FSM-EASM model is significantly less compared to the other two RANS models and needs to be compensated by a larger value of C_α. The difference in the dissipative nature is explained by the sensitivity of C_μ^{eff} to strain and rotation rate. In the present case C_μ^{eff} of the FSM-EASM reduces to $\left\langle C_\mu^{eff} \right\rangle = 0.028$, where brackets $\langle\rangle$ denote averaging in time and space. This value is significantly less compared to the generally accepted value of $C_\mu^{eff} = 0.09$ (away from solid walls). The FSM-EASM model introduces a dynamic response to the

flow field under consideration through the sensitivity of C_μ^{eff} to strain and rotation rate. It is generally acknowledged that the closure constants in LES subgrid-scale models, for example, C_S in the Smagorinsky model, are not universal and take significantly different values for different types of flow. The flow dependency of the calibration constants C_S explains the success of dynamic subgrid-scale models, which dynamically adjust the model constants to the flow under consideration. It might be argued that the behaviour of the FSM-EASM model is somewhat similar to a dynamic subgrid-scale model in the sense of providing the capability to adapt to different types of flows depending on strain and rotation-rate. This seems a very appealing feature and makes it worthwhile to explore in more detail.

The φ-α-EASM can also adapt to the flow through $C_\mu^{eff} = 0.22\varphi$. However, the variable φ does not reduce much in the case of a resolved flow field and predicts $\left\langle C_\mu^{eff} \right\rangle \approx 0.09$. This results in almost the same dissipative behaviour as the FSM-SST formulation. Note that the wall-damping function $f_{\beta*}$ in the turbulence kinetic energy equation used in the φ-α-EASM model is also based on the variable φ. This damping function maintains a value of unity in the resolved flow field, and does not erroneously activate the near-wall damping, as observed for low-Reynolds-number turbulence model formulations, where viscosity-dependent parameters such as Re_T are used. The similar dissipative behaviour of the FSM-SST and FSM-φ-α-EASM also suggests that the extra non-linear terms in the stress-strain relationship do not significantly alter the dissipative behaviour of the model.

The calibration constants C_α for the higher resolved case (HIT64) are optimised to reproduce a $-5/3$ slope at the cut-off wavenumber. Note that the DNS of Kaneda *et al.* (2003) predicts a slope of the inertial range close to -1.77 rather than exactly $-5/3$. In order to achieve the correct dissipative behaviour in the HIT64 case, all constants C_α have to be reduced compared to the HIT32 case. The IDDES and SAS model show a similar resolution sensitivity. On the fine grid, the SAS model shows too large a damping of the smallest resolved scales with insufficient energy in the smallest scales. IDDES predicts a slope at the cut-off wavenumber, which is somewhat too step, -1.95, even though this is not clearly visible in figure 9.4. The dependence of the results of IDDES to the grid resolution has also been observed in Mockett (2009).

These findings are worrying, since the calibration constant does not only depend on the flow under investigation but also on the level of resolution of the flow field. Perhaps the most promising way to tackle this issue would be to introduce a dynamic procedure to determine the constant C_α. This, however, adds considerable

complexity and is therefore not considered at this stage. Nevertheless, to complete the calibration effort a constant C_α needs to be chosen. It could be argued that the calibration constants corresponding to the lower resolution (HIT32) would be more appropriate for practical applications, since the computational cost associated with fine meshes are currently often not affordable. On the other hand, it could be argued that on coarse meshes the application of low dissipative schemes, as they are used in the calibration study, are often problematic and some upwinding may be required to stabilise the simulation. As mentioned before, any form of upwinding inevitably introduces additional numerical dissipation. With that in mind, the larger values of C_α combined with upwinding stabilised numerical schemes might be too dissipative. For this reason the lower values of the constants C_α will be used in the simulations to follow in chapter 10.

9.4.3 Calibration of β

A straightforward approach to determine the constant β would be to choose a value such that f_η approaches zero for a certain ratio of Δ/L_η, say $\Delta/L_\eta \approx 10$. However, this approach does not take into account the uncertainty associated with determining the Kolmogorov length scale L_η using the subgrid dissipation rate ϵ_{sgs}. It has been found that for the high-Reynolds-number case $Re_\lambda = 732$, the estimated ratio of grid length scale to Kolmogorov length scale is $\langle \Delta/L_\eta \rangle = 26.2$, which is a factor 7 smaller compared to DNS, which gives $\Delta/L_\eta = 187$. In order to obtain a suitable value for the constant β, a Taylor-scale Reynolds number of $Re_\lambda = 35$ is considered here. This Reynolds number is low enough to achieve DNS resolution on the the HIT32 and HIT64 grids. For example, Jimenez *et al.* (1993) performed DNS of isotropic turbulence at $Re_\lambda = 35$ using a box of 64 cubed cells. Eswaran & Pope (1988) used a box of 32 cells for DNS at $Re_\lambda \approx 30$. Therefore, the parameter β will be determined here such that the FSM contribution function reduces to $F = 0$ for the HIT32 and HIT64 resolutions at a Taylor-scale Reynold number of $Re_\lambda = 35$. Since the energy spectra do not provide any additional insights, only the resulting constant β is given for which the contribution function approaches zero. The result of this study is that a value of $\beta \leqslant 1.0$ is sufficient to ensures that all FSM models approach the DNS limit. For all following simulation a value of $\beta = 0.75$ will be used, unless stated otherwise.

9.4.4 Influence of Numerical Discretisation

The calibration study presented above gives suitable values of the calibration constants of the FSM approach when used in conjunction with the hybrid FSM convection scheme. Since it is not possible to repeat the calibration study for all possible numerical discretisation schemes, this section investigates the dissipative behaviour and the error introduced when FSM is used in conjunction with other convection discretisation schemes. For this purpose, five different convection schemes, which are all formally second-order accurate, will be assessed for the same calibration case. All tested schemes are likely to be employed in unsteady simulation of turbulence using commercial finite-volume codes. The schemes considered are the central-difference scheme (CDS), a bounded central-difference scheme with 20% TVD conformity (TVD), the hybrid convection scheme of Travin *et al.* (2004*b*), a second-order linear upwind scheme (LUD), a blend between LUD and CDS with 20% upwinding (BDS20) and the new hybrid FSM convection scheme (FSM scheme). It should be noted that the hybrid convection scheme of Travin *et al.* (2004*b*) has been designed for the combination of a fourth-order CDS and third/fifth-order upwind scheme. It is used here in conjunction with a second-order accurate CDS and LUD schemes.

The resulting energy spectra at $Re_\lambda = 732$ are shown in figure 9.5 for a box of 32 and 64 cells, obtained by FSM-SST using the optimised constants C_α from section 9.4.2.

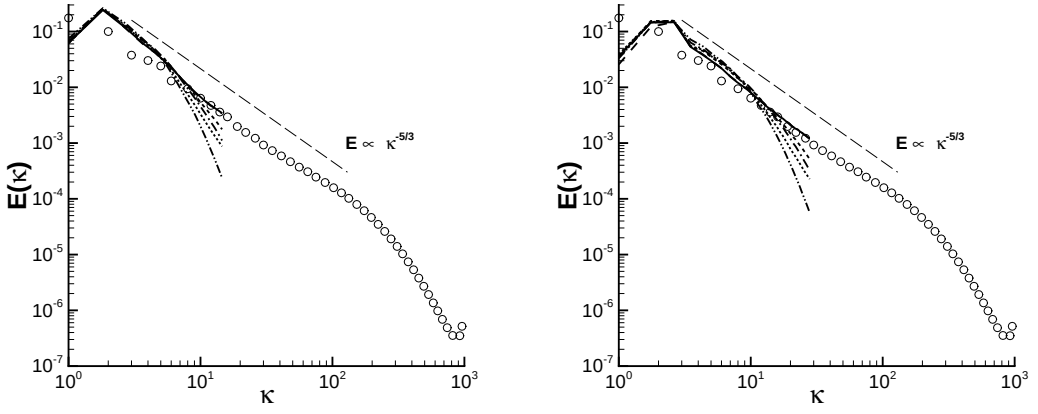

(a) HIT 32 (b) HIT 64

FIGURE 9.5: Energy spectra $E(\kappa)$. Symbols correspond to DNS of Kaneda *et al.* (2003). (—) CDS, (· · ·) TVD , (- - -) Travin *et al.* (2004*b*), (– · –) BDS20, (– · ·–) LUD, (– – –) new hybrid FSM scheme .

The numerical schemes with the smallest amount of numerical dissipation are the CDS and the new hybrid FSM convection scheme. The new blending function σ_b of the FSM convection scheme is zero for both mesh resolutions, with the consequence that the hybrid FSM scheme operates in pure CDS mode. The hybrid scheme of Travin *et al.* (2004*b*) is somewhat more dissipative and shows a small departure from the $-5/3$ energy cascade at the cut-off. This behaviour can be traced back to the blending function σ_b, which takes a non-zero value $\langle\sigma_b\rangle \approx 0.03$ and which exhibits localised regions where σ_b is close to unity; see figure 9.6. The non-zero value of σ_b might be necessary in terms of stability requirements when the hybrid scheme is used in conjunction with a fourth-order accurate CDS, as suggested in Travin *et al.* (2004*b*). However, the small amount of upwinding is not required in the present case in order to stabilise the full second-order CDS. The new hybrid FSM convection scheme is preferred in this respect, since it recovers a full CDS and avoids contamination of the resolved small scales of turbulence.

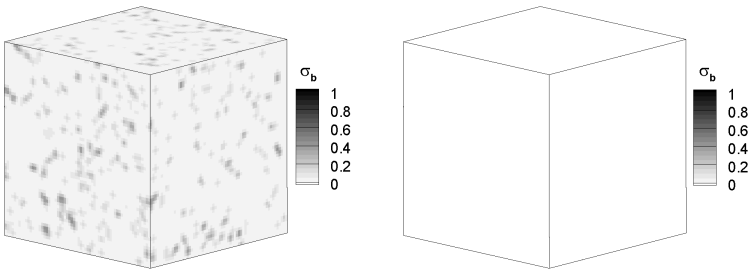

(a) Blending function of Travin *et al.* (2004*b*)

(b) Blending function of the FSM convection scheme

FIGURE 9.6: Blending function σ_b of the hybrid convection scheme.

The BDS20 and the TVD scheme are slightly more dissipative than the hybrid scheme of Travin *et al.* (2004*b*) and the departure from a $-5/3$ energy cascade at the cut-off wavenumber is clearly visible. It also turns out that the TVD variant is slightly more dissipative than the BDS20 scheme. The LUD scheme provides the most damping of the small-scales of turbulence. Even though the LUD is second-order accurate it cannot be recommended for the use within the hybrid RANS/LES environment unless the constant C_α is significantly lowered.

Chapter 10

Applications of the FSM Approach

In this chapter the proposed modifications and extensions to the Flow Simulation Methodology (FSM) are assessed on a range of test cases, which cover both internal and external flows. The flow around a tandem cylinder configuration is used to investigate the performance of FSM when operated in its basic, 'natural', mode, where the entire attached boundary layer is treated in RANS mode and the massively separated flow outside the boundary layer is treated in LES mode. The use of the basic FSM may become overly restrictive for many internal flows where it is beneficial to resolve some turbulence in the outer layer of the boundary layer. The other two test cases are selected to investigate the performance of FSM when operated in an 'extended' mode, where only the near-wall region is treated in RANS mode and the flow away from the wall, both inside and outside the boundary layer, is treated in LES mode. This extended mode can be referred to as wall-modelled LES (WMLES), where the computationally expensive near-wall region is bridged using a state-of-the-art RANS model. The first internal flow case considered is the flow in a planar channel. This case is mainly used to investigate the extent of the log-layer mismatch frequently observed when the switch from RANS to LES occurs inside the boundary. The second case is the flow in a three-dimensional diffuser, where the incoming fully developed turbulent duct flow experiences a three-dimensional boundary-layer separation.

Simulations are performed with FSM based on three different underlying RANS closures with different levels of sophistication, that is, the k-ω-SST, EASM-2D and the new φ-α-EASM model. All cases include an assessment of the statistical convergence of results, investigations of the sensitivity and influence of the resolution

of the computational grid and numerical convection discretisation scheme. The results are compared to reference data and to results obtained with other hybrid RANS/LES methods, such as IDDES and SAS.

10.1 Planar Channel Flow

The flow in a planar channel is used here in order to investigate the performance of the FSM framework to provide basic WMLES capabilities. In addition, a parameter and sensitivity study is conducted to investigate the influence of the convection discretisation scheme and the calibration parameters C_α and β of the FSM model. Simulations are performed for both low and high-Reynolds-number channel flow at $Re_\tau = 395$ and $Re_\tau = 18000$, respectively. The simulations are conducted without the function f_z included in the damping function F of the FSM, unless stated otherwise. Results are compared to the DNS of Moser *et al.* (1999) and to the correlation of Reichardt (1951) for the mean-velocity profile. In order to improve the predictions of the mean-velocity profile in WMLES mode, an additional modification is introduced to the FSM framework.

10.1.1 Computational Setup

Planar channel flow can be considered as the flow between two parallel plates. It is approximated here as the flow through a domain with the streamwise extent of $L_x = 2\pi H$, the spanwise width of $L_z = \pi H$ and a channel height of $L_y = 2H$, where H is the channel half-height. These dimensions correspond to the channel used by Moser *et al.* (1999) for DNS at $Re_\tau = 395$. Periodic boundary conditions are used in the spanwise and streamwise directions. The domain size is large enough to accommodate the streamwise streaks close the wall with $\Delta_x^+ = 1000 - 1600$, and to allow the spanwise and streamwise correlations to reduce to a sufficiently small magnitude in order for periodic boundary conditions to be applicable. The simulation at the lower Reynolds number $Re_\tau = 395$ is performed on a computational grid with $54 \times 54 \times 54$ cells. This corresponds to a maximum resolution in wall units of $\Delta_x^+ = 46$, $\Delta_{y_1}^+ = 0.8$ and $\Delta_z^+ = 23$, where $\Delta_{y_1}^+$ is the first grid spacing adjacent to walls. The simulations for the higher Reynolds number case, $Re_\tau = 18000$, are performed on a computational grid with $96 \times 124 \times 96$ cells. This provides a resolution of $\Delta_x^+ = 1178$, $\Delta_{y_1}^+ = 0.8$ and $\Delta_z^+ = 588$ in wall units.

The convective fluxes in the flow equations are discretised using the hybrid FSM difference scheme and a second-order upwind scheme is used for the turbulence transport equations. The viscous terms use a second-order central-difference scheme. Time stepping is performed using an implicit second-order accurate backward-difference scheme and the coupling between the pressure and velocity is achieved by the PISO algorithm. The time step is set as $1.6 \times 10^{-3} H/u_\tau$ such that the CFL number does not exceed 0.5.

In order to maintain a constant flow rate through the channel, an additional momentum source term is introduced to the streamwise momentum equation. In the present simulations, the pressure gradient required to yield the desired Re_τ is computed from the momentum balance in the streamwise direction. The required pressure gradient is obtained from the relation $\mathrm{d}\overline{p}/\mathrm{d}x = \tau_w/H$, with the wall shear stress $\tau_w = \rho u_\tau^2$ and the skin-friction velocity u_τ.

Initialisation

Without special consideration of the initial flow field the transition process from the initial flow field to a fully turbulent state may require a large number of channel flow-through times. In order to speed up the transition process the following strategy has been found very effective in quickly generating turbulence structures. The same strategy has also been employed in de Villiers (2006). The velocity field is initialised by prescribing a laminar parabolic velocity profile, where the streamwise velocity component near the wall is perturbed with parallel streaks of high- and low-speed streamwise velocity. These streamwise streaks are further modified by introducing a periodic spanwise perturbation of approximately +/-10% of the bulk velocity. This procedure is applied only to the first simulation of this series. Every following simulation is re-started from an instantaneous solution of the previous run.

10.1.2 Averaging and Statistical Convergence

Before any results are presented, the averaging procedure and statistical convergence is discussed. For all simulations the flow is allowed to develop from the initial flow field for approximately $15H/u_\tau$ time units. After the initial settling period, statistical quantities are computed by averaging over $80H/u_\tau$ time units, which approximately corresponds to 200 flow through times. For post-processing purposes the time-averaged quantities are additionally averaged over both homogeneous directions.

In order to verify the statistical convergence of the flow field, results for the mean velocity U^+, the modelled, resolved and total turbulence kinetic energy k^+ and the modelled, resolved and total shear stress $\overline{u'v'}^+$, are presented in figure 10.1, after averaging over $23H/u_\tau$, $43H/u_\tau$,$63H/u_\tau$ and $80H/u_\tau$ time units. It is obvious that after averaging over only $23H/u_\tau$ time units the mean-velocity profile is already converged. However, the statistics for the shear stress and turbulence kinetic energy are not yet fully converged. When averaging over more than $43H/u_\tau$ time units the statistics for the shear stress and turbulence kinetic energy are also fully converged.

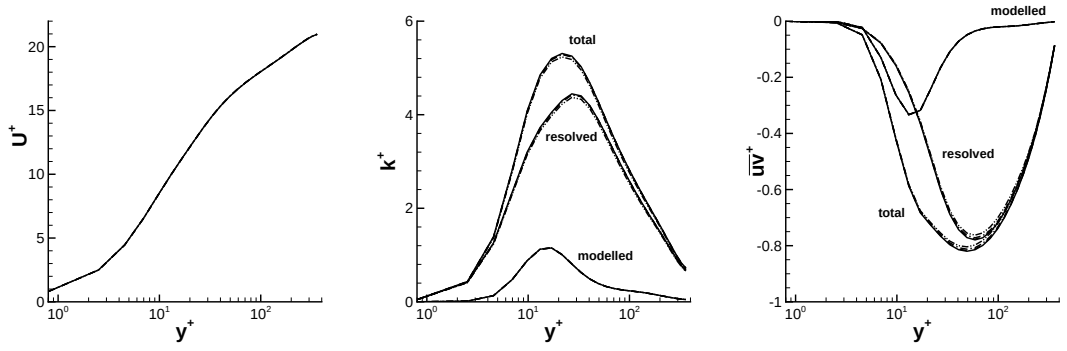

(a) Mean velocity profile U^+. (b) Turbulence kinetic energy k^+. (c) Shear-stress $\overline{u'v'}^+$.

FIGURE 10.1: Statistical convergence of the flow field. $(- \cdot \cdot -)$ $t = 23H/u_\tau$, $(- \cdot -)$ $t = 43H/u_\tau$, (- - -) $t = 63H/u_\tau$ and (—) $t = 80H/u_\tau$.

10.1.3 Influence of Convection Discretisation

The sensitivity of results with respect to the numerical convection discretisation scheme is investigated next. Four different second-order accurate schemes are considered in this study. The numerical schemes include the central-difference scheme (CDS), the hybrid FSM convection scheme (FSM) with a flow-dependent model for the flux-blending function, a bounded central-difference scheme with 20% TVD coformity (BCD20) and the linear upwind scheme (LUD). Simulations are performend using the FSM-SST formulation and $C_\alpha = 0.85$, $\beta = 0.75$ and $n = 4$. Results for the mean velocity U^+, damping function F and the modelled, resolved and total shear stress $\overline{u'v'}^+$ are shown in figure 10.2.

The results clearly demonstrate that the mean-velocity profile and shear stress exhibit a large sensitivity to the convection discretisation scheme, even though the resulting damping function F is considerably less sensitive to the numerical scheme. All damping functions collapse onto one curve close to the wall and take slightly

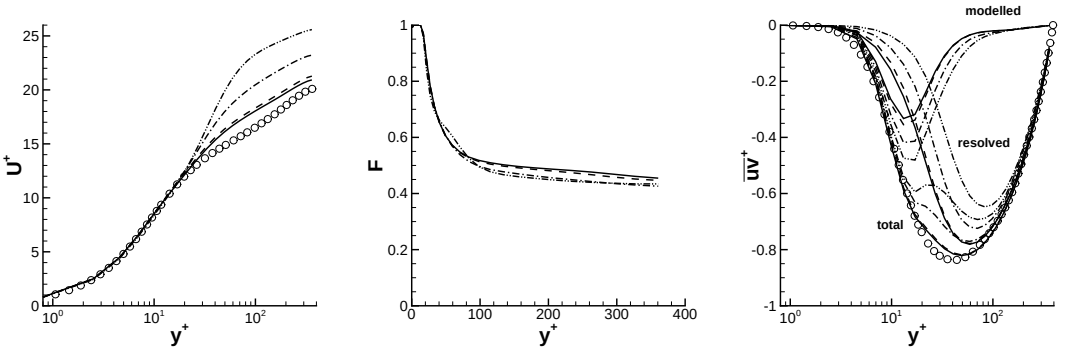

(a) Mean velocity profile U^+. (b) Damping function F. (c) Shear stress $\overline{u'v'}^+$.

FIGURE 10.2: Sensitivity with respect to the convection discretisation scheme. Symbols correspond to DNS of Moser *et al.* (1999). (—) CDS, (- - -) hybrid FSM scheme, (– · –) BCD20, (– ··–) LUD .

different values away from the wall. It is obvious that with increasing level of numerical dissipation inherent in the discretisation scheme the results increasingly depart from the reference data. The LUD scheme predicts a mean-velocity profile, which grossly departs from the reference data and which is not within typical predictive tolerances required for engineering applications. The situation is slightly improved with the BCD20 scheme, which predicts the velocity profile and shear stress in better agreement with reference data. However, the overall accuracy of the BCD20 scheme is still not satisfying. Both the LUD and BCD20 schemes predict reduced levels of resolved shear stress when compared to the more accurate CDS scheme. The reduced resolved shear stress is not compensated by a sufficient increase in modelled shear stress, such that reasonable predictions for the total shear stress and hence the velocity profile are obtained. Only the CDS and hybrid FSM scheme are capable of predicting results in reasonable agreement with the reference data. It should be noted that the FSM-SST formulation is not optimised for WMLES. That is why the CDS and hybrid FSM scheme over-predict the velocity magnitude in the log layer by a small margin. The results of the hybrid FSM scheme are very encouraging and are in close agreement with the CDS. This indicates that the numerical dissipation of the hybrid FSM scheme in the resolved flow region is of similar magnitude to that of the CDS. It also indicates that the enhanced numerical dissipation of the LUD scheme employed in the RANS region does not adversely affect the flow in the LES region. For this reason, the hybrid FSM convection scheme will be used for all further studies, unless stated other wise.

10.1.4 Sensitivity to the Underlying RANS Model

The sensitivity of the results with respect to the underlying RANS model is investigated in this section. Simulations are performed using the FSM-SST, FSM-EASM and FSM-φ-α-EASM formulation in conjunction with the hybrid FSM convection scheme. Results for the mean velocity U^+, damping function F and the modelled, resolved and total shear stress $\overline{u'v'}^+$ are presented in figure 10.3.

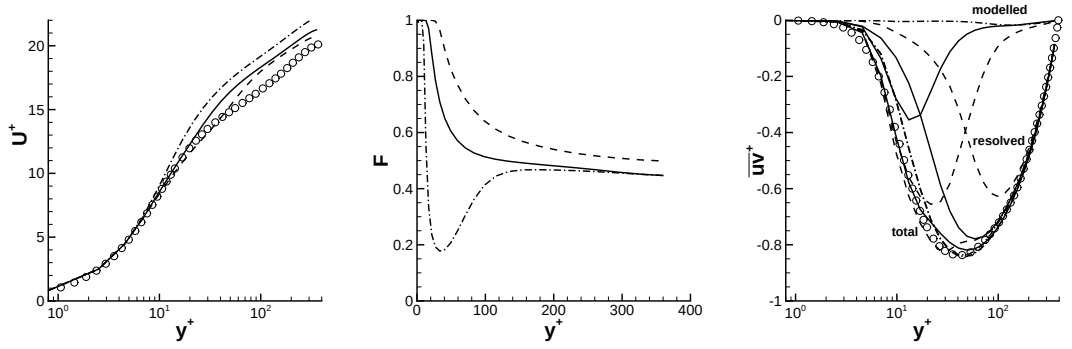

(a) Mean velocity profile U^+. (b) Damping function F. (c) Shear stress $\overline{u'v'}^+$.

FIGURE 10.3: Sensitivity of FSM with respect to the underlying RANS model. Symbols correspond to DNS of Moser *et al.* (1999). (—) FSM-SST, (- - -) FSM-EASM, (– · –) FSM-φ-α-EASM.

At first sight the predictions for the channel flow are clearly sensitive to the underlying RANS model. However, the differences in the predictions are mainly caused by the damping function F, which takes significantly different shapes and values depending on the underlying RANS model. The different shapes of the damping functions are caused by differences in the predictions of k and ω, which are both used to compute the relevant length scales in the damping function.

The damping function resulting from the supposedly most sophisticated RANS model, the φ-α-EASM, seems not very well suited for the channel flow predictions and the results for the mean-velocity profile in the log-layer region show the greatest departure from the reference data. This is caused by a large reduction of the damping function close to the wall, which results in a vanishing modelled shear stress and in a general under-estimation of the total shear stress between the wall and approximately $y^+ \approx 30$. The FSM-SST and FSM-EASM models predict a thicker RANS layer ($F = 1$) close to the wall, which results in elevated levels of modelled shear stress and in reduced levels of resolved shear stress. The total shear stress is now better predicted in the near-wall region, which is also reflected in improved predictions for the mean-velocity profile in the log-layer region. The FSM-EASM shows the largest extent of the near-wall RANS layer and provides the

best overall agreement with the reference data. It is important to note that both the FSM-SST and FSM-EASM show too low levels of total shear stress between the locations $y^+ \approx 20$ and $y^+ \approx 80$. This defect is responsible for the too high velocity magnitude in the log layer. In order to reduce the velocity magnitude in the log layer it is necessary to enhance the modelled shear stress at the switching location from RANS to LES, such that the total shear stress is not under-predicted in this region.

Since the predictions strongly depend on the shape of the damping function, it is unfortunately not very clear to what extend the non-linear stress-strain relationship of the EASM model, or the improved near-wall treatment of the φ-α-EASM, influences the predictions. The influence of the underlying RANS model can only be rigorously assessed if the same damping function is used for all three underlying turbulence models. This study is left for future investigations.

10.1.5 Sensitivity to the Constant C_α

The sensitivity to the calibration constant C_α appearing in the damping function F is investigated next. The sensitivity study is conducted using the FSM-SST formulation in conjunction with the hybrid FSM convection scheme. Simulations are performed with $C_\alpha = 0.7$, $C_\alpha = 0.85$ and $C_\alpha = 1.0$. The results for the mean velocity U^+, damping function F and the modelled, resolved and total shear stress $\overline{u'v'}^+$ are presented in figure 10.4. The same sensitivity study was conducted for the FSM-EASM and FSM-φ-α-EASM models. Since the results show exactly the same trend as for the FSM-SST formulation, they are not presented here.

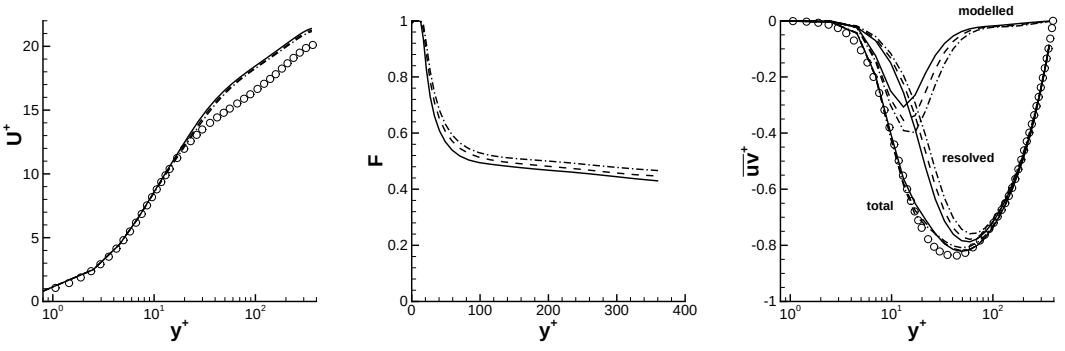

(a) Mean velocity profile U^+. (b) Damping function F. (c) Shear stress $\overline{u'v'}^+$.

FIGURE 10.4: Sensitivity of the results to the calibration constant C_α. Symbols correspond to DNS of Moser *et al.* (1999). (—) $C_\alpha = 0.7$, (- - -) $C_\alpha = 0.85$, $(- \cdot -)$ $C_\alpha = 1.0$.

The different values for C_α are reflected in different magnitudes of the damping function F in the LES region. However, the overall differences in the resulting magnitude of F are rather small. Nevertheless, the variation of C_α would be enough to observe a noticeable difference in the energy spectra for isotropic turbulence (see section 9.4). Lower values of C_α result in a reduction of modelled shear stress and in an increase of resolved shear stress, such that the total shear stress remains approximately the same for all values of C_α. Since the total shear stress does not change significantly the velocity profile is very similar for all values of C_α investigated here.

10.1.6 Sensitivity to the Constant β

The sensitivity of results to the calibration constant β appearing in the damping function F is investigated next. The sensitivity study is conducted using the FSM-SST formulation in conjunction with the hybrid FSM convection scheme. Simulations are performed with $\beta = 1.0$, $\beta = 0.75$, $\beta = 0.5$ and $\beta = 0.25$. The results for the mean velocity U^+, damping function F and the modelled, resolved and total shear stress $\overline{u'v'}^+$ are presented in figure 10.5.

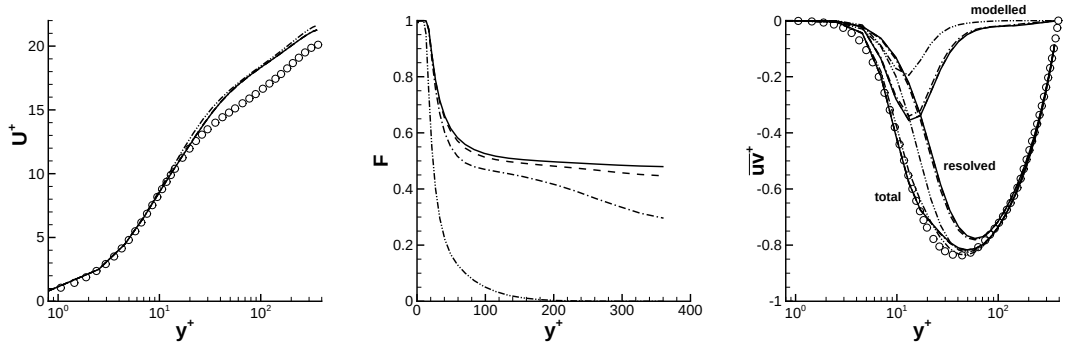

(a) Mean velocity profile U^+. (b) Damping function F. (c) Shear stress $\overline{u'v'}^+$.

FIGURE 10.5: Sensitivity of the results to the calibration constant β. Symbols correspond to DNS of Moser *et al.* (1999). (—) $\beta = 1.0$, (- - -) $\beta = 0.75$, $(- \cdot -)$ $\beta = 0.5$, $(- \cdot\cdot -)$ $\beta = 0.25$.

The calibration constant β is much more effective in modifying the level of damping in the LES region than C_α. For values of β smaller than $\beta \approx 0.25$, the FSM-SST formulation reduces to a quasi-DNS for large parts of the channel, while the extent of the RANS region ($F = 1$) is not much altered by different values of β. It is somewhat surprising that the three constants, $\beta = 1.0$, $\beta = 0.75$ and $\beta = 0.5$, result in the same levels of resolved and modelled shear stress and consequently in the same velocity profile. At first sight this seems not very intuitive, since the magnitude of

the damping function F away from the wall is significantly different. In addition, the sensitivity study of the calibration constant C_α has shown that different values of F away from the wall result in different levels of resolved and modelled shear stress. However, a closer inspection of the damping function F reveals that close to the wall ($y^+ < 30$) different values of β collapse onto one curve, with the exception of $\beta = 0.25$. This is not the case in the sensitivity study for the calibration constant C_α, where different values of C_α result in a different distribution of the damping function close to the wall ($y^+ < 30$). It seems that the level of damping in the near-wall region ($y^+ < 30$) controls the magnitude of resolved fluctuations away from the wall. The magnitude of the damping function away from the wall seems to have a negligible effect on the resolved shear stress. This is probably only true for sufficiently small values of the damping function, such that the flow field away from the wall is not contaminated by overly large levels of modelled dissipation. Even though the levels of damping differ significantly for different values of β, the velocity profile is not significantly affected by the values of β investigated here.

10.1.7 Introducing f_z for WMLES

The sensitivity study so far has revealed that the resulting damping function may take significantly different shapes and values depending on the underlying RANS model. The FSM-φ-α-EASM, for example, shows a significant reduction of the damping function close to the wall, which results in an almost vanishing modelled shear stress and in an over-prediction of the velocity magnitude in the log-layer region. It was also shown, that the damping function close to the wall controls the levels of resolved and modelled shear stress. In addition, changing the calibration constants C_α and β is not an effective way to improve the predictions of the velocity profile in the log-layer region. In the following, an attempt is presented, which aims at modifying the damping function close to the wall such that it takes a more consistent shape for all underlying turbulence models and also provides improved predictions of the velocity profile. For this purpose, the function f_z is introduced, which effectively controls the extent of the RANS region ($F = 1$) close to the wall. The shielding function f_z is given by

$$f_z = \frac{1}{1 - F_z}, \tag{10.1}$$

where

$$F_z = \tanh(C_z \Gamma_2^4), \qquad \Gamma_2 = \frac{500\nu}{\omega y^2}. \tag{10.2}$$

The constant C_z controls the extent of the RANS region close to the wall. The resulting damping function is now given as

$$F = \min\left[f_\eta f_\Delta f_z, 1\right]. \tag{10.3}$$

In order to illustrate the effect of the shielding function, simulations are performed with the FSM-SST, FSM-EASM and FSM-φ-α-EASM formulation using the new function f_z and the optimised constant $C_z = 16$. Results for the mean velocity U^+, damping function F, the modelled, resolved and total shear stress $\overline{u'v'}^+$ and the total (resolved plus modelled) normal-Reynolds-stress components are presented in figure 10.6. In addition, results of the IDDES model based on the k-ω-SST are also included as a reference.

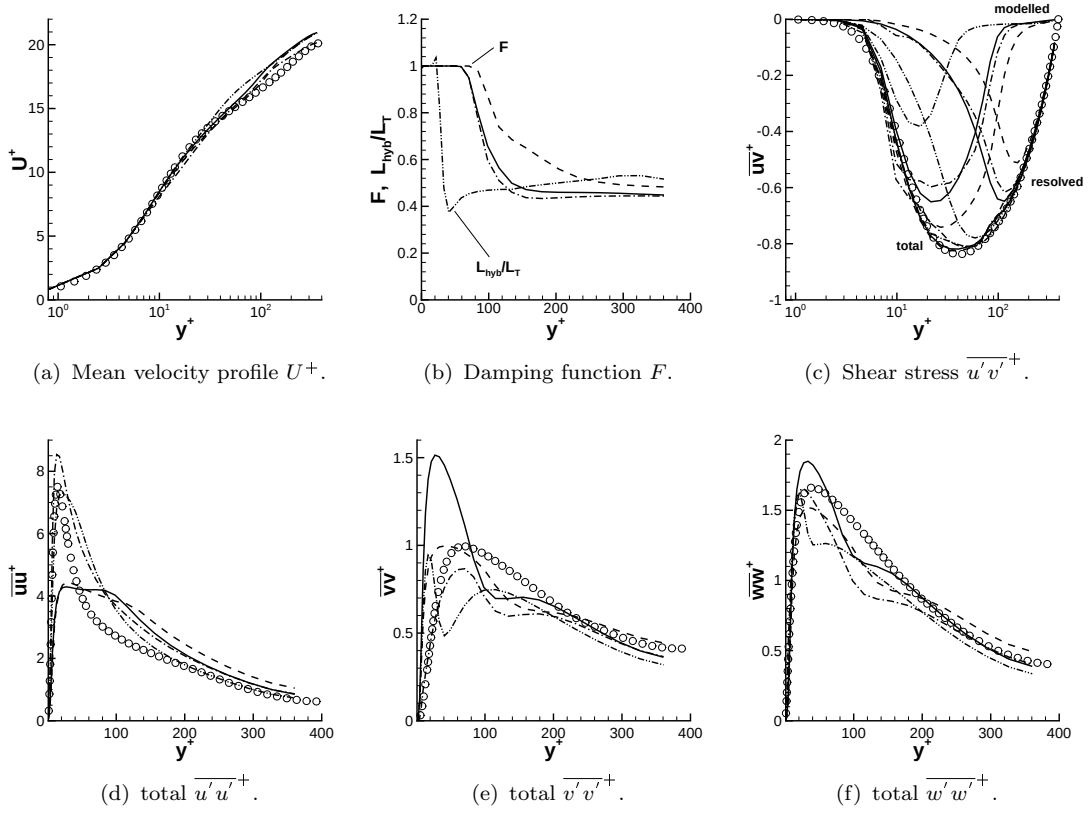

(a) Mean velocity profile U^+. (b) Damping function F. (c) Shear stress $\overline{u'v'}^+$.

(d) total $\overline{u'u'}^+$. (e) total $\overline{v'v'}^+$. (f) total $\overline{w'w'}^+$.

FIGURE 10.6: Influence of the shielding function f_z. Symbols correspond to DNS of Moser *et al.* (1999). (—) FSM-SST, (- - -) FSM-EASM, (– · –) FSM-φ-α-EASM, (– · · –) IDDES .

It is obvious that the shielding function f_z is effective in modifying the damping function F close to the wall. The RANS region close to the wall is generally enlarged and all three underlying turbulence models now show a more consistent distribution of F. As a consequence of the enlarged RANS region, the modelled shear stress is

increased close to the wall, and the resolved shear stress is reduced away from the wall, when compared to simulations without f_z, as seen in figure 10.3.

The enlarged RANS region, which now extends up to $y^+ \approx 100$, significantly improves predictions of the velocity profile in the buffer and log-layer region. Recall that predictions without f_z show a large over-prediction of the velocity profile in the log-layer regions. Even though the velocity profile is generally improved, the onset of a secondary, resolved log layer becomes visible in the results. Again, this is caused by an under-prediction of the total shear stress around the switching location from RANS to LES mode. When the shielding function is included, the most sophisticated RANS model, the φ-α-EASM, provides the best predictions of the velocity profile and matches the centerline velocity of the reference data. Surprisingly, the IDDES formulation also over-predicts the velocity magnitude in the log-layer region, even though, it includes the function f_e, which is designed to enhance the modelled shear stress at the switching location and hence compensates for the drop of total shear stress. The effect of the function f_e is visible in figure 10.6 (b) as a small peak in the predictions of the length-scale ratio L_{hyb}/L_T.

The total normal-Reynolds-stress components are discussed next. Note that the results are normalised by the skin-friction velocity u_τ, which is the same for all simulations, since the pressure gradient is fixed in the simulation, which gives $u_\tau = \sqrt{(H/\rho)(\mathrm{d}p/\mathrm{d}x)}$. Therefore, the differences between the predictions are solely caused by the turbulence model formulation and not by the scaling with u_τ. The FSM-SST, which is based on a linear-constitutive stress-strain relationship, shows the greatest overall departure from the reference data. The $\overline{u'u'}^+$ component is significantly under-predicted in the near-wall region, whereas the other two normal components, $\overline{v'v'}^+$ and $\overline{w'w'}^+$, are over-predicted. The FSM-EASM shows more realistic wall-normal fluctuations $\overline{v'v'}^+$ compared to the FSM-SST. The FSM-φ-α-EASM more accurately reproduces the near-wall peak of the streamwise velocity fluctuations $\overline{u'u'}^+$, which is a consequence of the near-wall anisotropy modifications employed in the φ-α-EASM model. In addition, the FSM-φ-α-EASM shows improved asymptotic near-wall behaviours of all normal-Reynolds-stress components. The IDDES formulation results in a much smaller RANS region close to the wall. As a consequence, IDDES shows the lowest levels of modelled shear stress and the highest levels of resolved shear stress. Additionally, the smaller RANS region allows turbulence fluctuations to penetrate much more deeply into the near-wall region, which is reflected in a larger intensity of streamwise velocity fluctuations $\overline{u'u'}^+$ close to the wall. It is also obvious that all models show a reduction of total normal-Reynolds-stress components $\overline{v'v'}^+$ and $\overline{w'w'}^+$ around the interface location.

The turbulence activity in the RANS region at $y^+ = 10$ and in the LES region at $y^+ = 200$ is visualised in figures 10.7 and 10.8, using the instantaneous vorticity magnitude $|\omega| H/u_\tau$. Note that the resolution of the computational grid is relatively high and should be able to the resolve the dominant near-wall turbulence structures. This is achieved by IDDES, which shows more turbulence structures at the wall distance $y^+ = 10$. All FSM models damp most of the turbulence fluctuations close to the wall, and show un-physically large 'super' streaks, similar to what has been observed in Baggett (1998). The difference in the level of turbulence activity stems from the extent of the RANS region close to the wall, which for the FSM models, is significantly larger and extents up to $y^+ \approx 100$. Nevertheless, fluctuations from the LES zone penetrate deep into the RANS zone and result in an over-prediction of total (modelled plus resolved) Reynolds stress. Clearly, IDDES is superior in resolving as much as possible of the near-wall turbulence structures on the same computational grid. However, since the velocity profile is reasonably reproduced by the FSM models, no further modifications are introduced at this stage. In the log layer, at the wall distance $y^+ = 200$, the resolved turbulence activity is overall very similar for all models. The FSM-EASM and FSM-φ-α-EASM both show the presence of a large streamwise structure. The existence of very large structures in the log layer was experimentally observed by Hutchins & Marusic (2007) and was referred to as 'superstructures'. The superstructures present in the log layer are much larger than the near-wall streaky structure and are reported to be of the streamwise extent $20H$ and of a spanwise width $0.3-0.5H$ (see Hutchins & Marusic, 2007). Whether the observed structure in the simulations of the FSM-EASM and FSM-φ-α-EASM corresponds to such superstructures, or whether they are linked to the near-wall super streaks has not been investigated further.

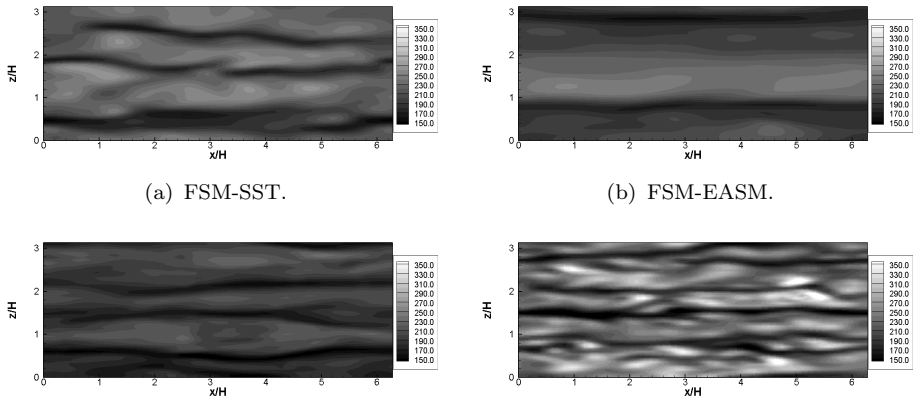

(a) FSM-SST. (b) FSM-EASM.

(c) FSM-φ-α-EASM. (d) IDDES.

FIGURE 10.7: Instantaneous vorticity magnitude $|\omega| H/u_\tau$ at the plane $y^+ = 10$.

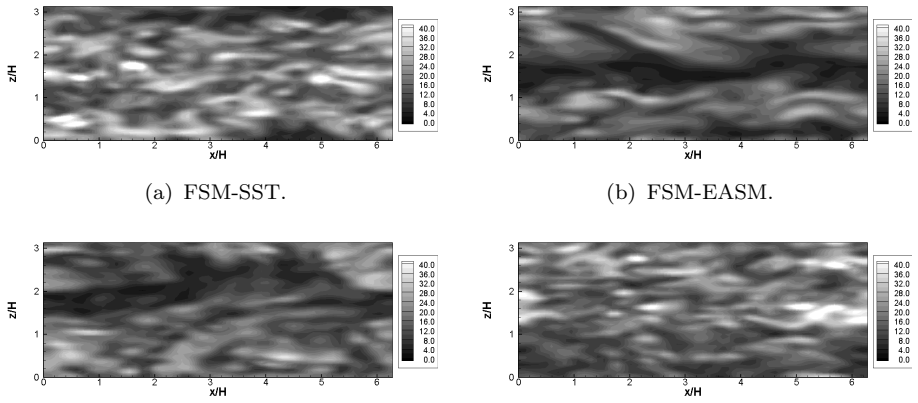

(a) FSM-SST. (b) FSM-EASM.

(c) FSM-φ-α-EASM. (d) IDDES.

FIGURE 10.8: Instantaneous vorticity magnitude $|\omega|\, H/u_\tau$ at the plane $y^+ = 200$.

10.1.8 Performance at High Reynolds Number

In the final investigation of this flow, the FSM-SST, FSM-EASM and FSM-φ-α-EASM formulations to provide WMLES capabilities at a much higher Reynolds number is evaluated. All FSM models include the shielding function f_z in the damping function F. The Reynolds number under consideration is $Re_\tau = 18000$. The results are compared to the correlation of Reichardt (1951) for the velocity profile. In addition, results obtained from IDDES based on the k-ω-SST model are also included as a reference. Results for the mean velocity U^+, damping function F and the modelled, resolved and total shear stress $\overline{u'v'}^+$ are shown in figure 10.9.

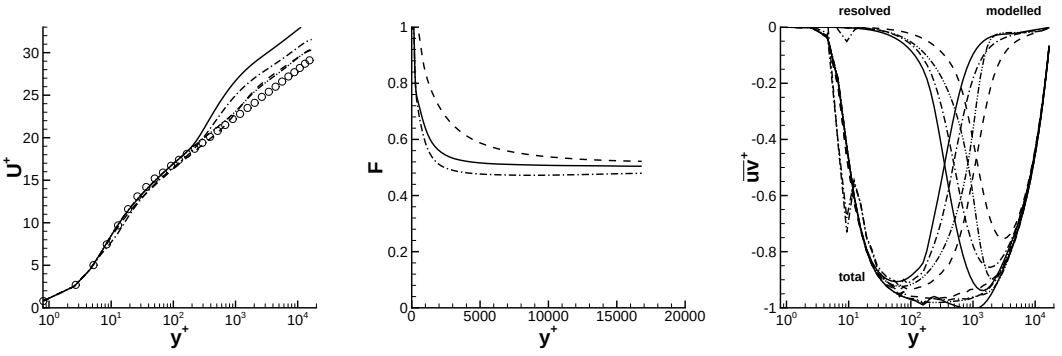

(a) Mean velocity profile U^+. (b) Damping function F. (c) Shear stress $\overline{u'v'}^+$.

FIGURE 10.9: Planar channel flow at $Re_\tau = 18000$. Symbols correspond to the correlation of Reichardt (1951). (—) FSM-SST, (- - -) FSM-EASM, (– · –) FSM-φ-α-EASM, (– · ·–) IDDES .

Even though all FSM formulations include the shielding function f_z, the resulting distribution of the damping function F is quite different, particularly in the near-wall region. The FSM-SST and FSM-φ-α-EASM formulations both show a RANS zone close to the wall, which extents up to $y^+ \approx 160$. For $y^+ > 160$ the damping function drops sharply to a lower value. The FSM-EASM, on the other hand, shows a RANS zone, which extents up to $y^+ \approx 450$ and the damping function drops relatively slower to lower magnitude. This difference is reflected in the predictions of the velocity profile as well as in the modelled and resolved shear stress. The FSM-SST predicts the smallest level of modelled shear stress and the highest level of resolved shear stress. It also shows the most pronounced log-layer mismatch of all models investigated here. The FSM-φ-α-EASM gives the highest levels of modelled shear stress and the lowest level of resolved shear stress, which results in a reduced log-layer mismatch. The FSM-EASM and IDDES formulations show intermediate levels of resolved and modelled shear stress and provide more accurate results of the velocity profile, with a smaller log-layer mismatch. The result of the FSM-EASM is particularly encouraging, since it matches the prediction of IDDES. Note that the IDDES implementation used here shows a slightly more pronounced log-layer mismatch than the results of Shur *et al.* (2008). However, Shur *et al.* (2008) employ a fourth-order accurate numerical scheme, which might explain the observed differences.

10.1.9 Summary

It is demonstrated that the elevated level of numerical dissipation of the upwind and TVD schemes results in reduced levels of resolved shear stress when compared to the more accurate Central-Difference Scheme. The reduced resolved shear stress is not compensated by a sufficient increase in modelled shear stress, such that reasonable predictions for the total shear stress, and hence the mean-velocity profile, are obtained. Both schemes results are beyond the level of accuracy normally required in engineering applications. Only the new hybrid FSM convection scheme delivers results in close agreement with predictions from the CDS. This shows that the numerical dissipation of the hybrid FSM scheme is of a similar magnitude to that of the CDS in the resolved-flow region, and that the enhanced numerical dissipation of the upwind scheme employed in the RANS region, does not adversely affect the flow in the LES region.

It is also shown that the mean-velocity predictions are insensitive to the choice of the calibration constants C_α and β. Although the shape of the damping function

F depends on the calibration constants, the total shear-stress and mean-velocity predictions are very similar, almost independent of the value of the calibration constants. On the other hand, the results are very sensitive to the underlying RANS model. It is argued that the sensitivity with respect to the RANS model is mainly caused by different distributions of the damping function F. For this reason, an extension to FSM is introduced, which modifies the damping function close to the wall, such that it has a more consistent shape for all underlying turbulence models and also provides improved predictions of the mean-velocity profile. With this modification included, the most sophisticated underlying RANS model, the φ-α-EASM, provides the best predictions of the mean-velocity profile and asymptotic near-wall behaviour of all normal-Reynolds-stress components for the $Re_\tau = 395$ case. The small log-layer mismatch present in the results is caused by an under-prediction of total (resolved plus modelled) shear stress at the switching location; this mismatch could potentially be eliminated by enhancing either the resolved or modeled contribution to the shear stress at the switching location. For the high-Reynolds-number channel flow ($Re_\tau = 18000$), the FSM-EASM and FSM-φ-α-EASM models provide improved predictions over FSM based on the k-ω-SST model. The FSM-EASM model shows the best prediction, with minimal log-layer mismatch and good agreement with predictions from IDDES. Nevertheless, more testing is required, particularly in more complex flows, in order to confirm the good performance of the FSM-EASM.

10.2 Three-Dimensional Diffuser

The next test case is the flow in an asymmetric three-dimensional diffuser. This case has already been introduced in section 6.4. In was demonstrated in sections 6.4 and 8.6, as well as in the 13th/14th ERCOFTAC/IAHR Workshop on Refined Turbulence Modelling, that even the most sophisticated RANS model exhibits difficulties in predicting the correct boundary-layer separation and flow topology in the three-dimensional diffuser. Even though the Reynolds number is moderate and would allow for wall-resolved LES (Schneider *et al.*, 2010*b*) and even DNS (Ohlsson *et al.*, 2010), this case is used here in order to investigate the performance of the FSM approach to provide WMLES capabilities for complex internal flows.

10.2.1 Computational Setup

In order to generate fully developed turbulent inflow conditions, a periodic, rectangular channel of the streamwise extent $3H$ is computed simultaneously and the flow mapped to the inlet of the diffuser domain. This approach is computationally relative cheap and provides physically correct turbulence fluctuations to the diffuser domain. However, the relatively short streamwise extent of the periodic inflow channel has the consequence that a spurious periodicity is induced in the diffuser domain. The primary recycling frequency, determined by the convection speed in the centre of the channel and channel length, is approximately $0.4[Hz]$. The undesirable recycling frequency and higher harmonics can be observed in the diffuser domain. The alternative is to use a much longer section upstream of the diffuser in order to achieve a fully developed flow field at the inlet. Ohlsson *et al.* (2010), for example, use a development section of $63H$ and specify laminar flow at the upstream boundary.

The boundary conditions of the rectangular inflow channel are periodic in the streamwise direction and the flow is driven by an imposed pressure gradient, which is adjusted iteratively to yield the desired bulk velocity U_b. Convective boundary conditions of the form $\partial\phi/\partial t + \overline{u}\partial\phi/\partial n = 0$, where n is the outward pointing normal direction, are used at the diffuser outlet. The convective boundary condition is placed $13H$ downstream of the diffuser. It is therefore expected that the boundary condition at the outlet is not significantly influencing the flow in the diffuser.

The simulations are performed on a computational grid with approximately 2.1×10^6 cells ($335 \times 65 \times 97$) for the diffuser domain and approximately 400000 cells for the

separate duct flow domain. The average first wall-normal grid spacing is around $y_1^+ = 0.5$ and the maximum value is $y_1^+ = 0.8$. The convective fluxes in the flow equations are discretised using the hybrid FSM difference scheme and a second-order upwind scheme is used for the turbulence transport equations. The viscous terms use a second-order central-difference scheme. Time stepping is performed using an implicit second-order accurate backward-difference scheme, and the coupling between the pressure and velocity is achieved by the PISO algorithm. The time step is set to $0.007H/U_b$ such that the CFL number does not exceed 0.5.

Initialisation

The initial conditions of the inflow duct require special attention, in order to speed up the transition to a fully developed turbulent flow. The parabolic initial velocity field in the periodic inflow channel is perturbed in the same way as described for the planar channel flow simulation in section 10.1. This procedure is applied only to the first simulation of this series. Every following simulation is re-started from an instantaneous solution of the first run.

10.2.2 Averaging and Statistical Convergence

The statistical convergence of the flow field is discussed first. For all simulations, the flow is allowed to develop for approximately $200D/U_b$ time units. After the initial settling period, statistical quantities are computed by averaging over $2300D/U_b$ time units. In order to verify the statistical convergence of the flow field, results for the surface-pressure coefficient C_p distribution on the bottom wall, as well as the streamwise velocity component U/U_b and the streamwise velocity fluctuations $\overline{u'}_{rms}$ on the centre plane at $z/L_z = 0.5$, are presented in figures 10.10 and 10.11, for averaging intervals of $600D/U_b$, $1100D/U_b$, $1700D/U_b$ and $2300D/U_b$ time units.

It is obvious that after averaging over only $600D/U_b$ time units the surface-pressure distribution $C_p = (p - p_{ref})/(0.5\rho U_b^2)$ at the bottom wall ($y/H = 0$), at $z/L_z = 0.5$, is already converged. However, the streamwise velocity profile and velocity fluctuations at the last two stations, $x/H = 12$ and $x/H = 16$, are not yet fully converged. Even averaging over $1100D/U_b$ does not provided fully converged results for the streamwise turbulence intensity. Averaging over more than $1700D/U_b$ time units is required for the mean flow and turbulence statistics to be fully converged.

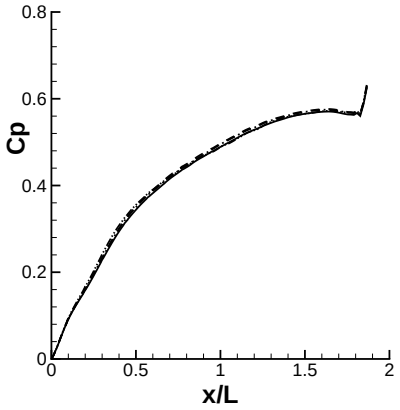

FIGURE 10.10: Surface-pressure coefficient C_p at the bottom wall. $(- \cdot \cdot -)$ $t = 600D/U_b$, $(- \cdot -)$ $t = 1100D/U_b$, (- - -) $t = 1700D/U_b$, (—) $t = 2300D/U_b$.

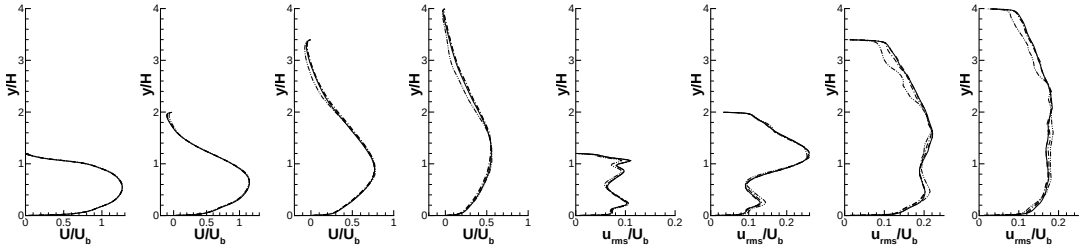

(a) Velocity component U/U_b (b) $\overline{u'}_{rms}/U_b$

FIGURE 10.11: Streamwise velocity and turbulence fluctuations at the centre plane $z/H = 0.5$. Locations from left to right: $x/H = 1$, $x/H = 5$, $x/H = 12$ and $x/H = 16$. $(- \cdot \cdot -)$ $t = 600D/U_b$, $(- \cdot -)$ $t = 1100D/U_b$, (- - -) $t = 1700D/U_b$, (—) $t = 2300D/U_b$.

10.2.3 Inflow Duct Results

The quality of the predictions provided by the inflow duct is assessed. For this purpose, the streamwise velocity profile and streamwise turbulence fluctuations $\overline{u'}_{rms}/U_b$ at the spanwise location $z/L_z = 0.5$ are shown in figure 10.12, for the predictions of the FSM-SST, FSM-EASM, FSM-φ-α-EASM and IDDES models. All models predict a very similar velocity profile with a too high velocity magnitude in the centre of the duct compared to corresponding measurements. In addition, the experimental data show a asymmetry of the velocity profile, which is not reproduced by any of the simulations. In the centre of the duct, the resolved streamwise turbulence fluctuations are in good agreement with the reference data. The differences in the near-wall treatment becomes noticeable close to the wall. All FSM model resolve much lower turbulence intensities close to wall than the IDDES model. As

discussed before, this is linked to the larger RANS region of the FSM models, which damps the turbulence fluctuations close to the wall.

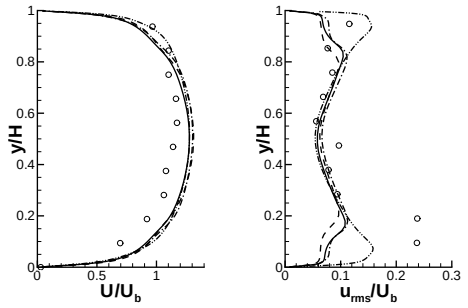

(a) Velocity component U/U_b (b) $\overline{u'}_{rms}/U_b$

FIGURE 10.12: Streamwise velocity profile and turbulence fluctuations in the inflow duct, at the centre plane $z/L_z = 0.5$. Symbols correspond to experimental data of Cherry *et al.* (2008, 2009). (—) FSM-SST, (- - -) FSM-EASM, (−·−) FSM-φ-α-EASM, (−··−) IDDES.

10.2.4 Influence of Convection Discretisation

The sensitivity of results with respect to the numerical convection discretisation scheme is investigated. Three second-order accurate schemes are considered in this study. The numerical schemes include the hybrid FSM convection scheme (FSM) with a flow-dependent model for the flux-blending function, a bounded central-difference scheme with 20% TVD conformity (BCD20) and the central-difference scheme (CDS). All simulations are performed using the FSM-SST model with $C_\alpha = 0.85$, $\beta = 0.75$ and $n = 4$.

The prediction of the surface-pressure distribution C_p at the bottom wall ($y/H = 0$) is shown in figure 10.13. There are significant differences in the predictions of the surface-pressure distribution. The CDS and hybrid-FSM scheme give similar results in reasonable agreement with the reference data, whereas the bounded BCD20 scheme significantly over-predicts the pressure recovery in the diffuser. Note that the jump in C_p at $x/L = 1.86$ is caused by the boundary conditions specified at the outlet. The results for the pressure distribution suggest that the velocity field predicted by the BCD20 scheme also differs from the predictions of the other two convection schemes. This is confirmed in figure 10.14, which shows the streamwise velocity contour U/U_b at the centre plane, $z/L_z = 0.5$. The figures also include a thick line, which corresponds to the zero-velocity contour and gives the extent of

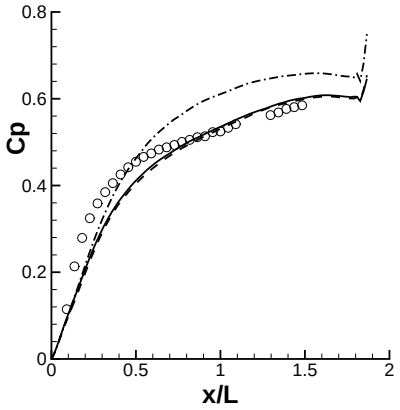

FIGURE 10.13: Surface pressure coefficient C_p at the bottom wall. Symbols correspond to experimental data of Cherry *et al.* (2008, 2009). (—) CDS, (- - -) hybrid FSM scheme, (– · –) BCD20.

the separated-flow region. The hybrid FSM scheme and CDS again give a very similar picture of the separated-flow region. Both show a separated-flow region, which extents from approximately $x/H \approx 1$ to $x/H \approx 18$. On the other hand, BCD20 only predicts very shallow separation at the top wall. Even though separation occurs too early with the CDS and hybrid FSM scheme, the agreement with reference data is much better than with the BCD20 scheme.

A more detailed comparison of the flow field on the centre plane is shown in figure 10.15, where the streamwise velocity profile and streamwise turbulence fluctuations $\overline{u'}_{rms}/U_b$ are plotted at the four streamwise locations $x/H = 1$, $x/H = 5$, $x/H = 12$ and $x/H = 16$. The CDS and hybrid FSM scheme again predict similar results for both streamwise velocity and streamwise turbulence fluctuations. At $x/H = 12$ and $x/H = 16$, where the differences in the velocity profiles are most pronounced, the CDS and hybrid-FSM scheme are clearly in much better agreement with the reference data. A similar trend is evident in the streamwise velocity fluctuations. The CDS and hybrid-FSM scheme again predict similar results, that agree better with the reference data, whereas the BCD20 scheme over-predicts the magnitude of velocity fluctuations at the bottom wall for the first two stations. At the last two stations, the turbulence streamwise intensity predicted by BCD20 is overall smaller in magnitude and the agreement with the reference data deteriorates.

The three-dimensional velocity field in the diffuser has also been analysed, but is not shown here. Predictions of the three-dimensional flow field reflect what has already been said above. The CDS and hybrid-FSM scheme predict the flow field in much better agreement with the reference data. On the other hand, the BCD20 scheme

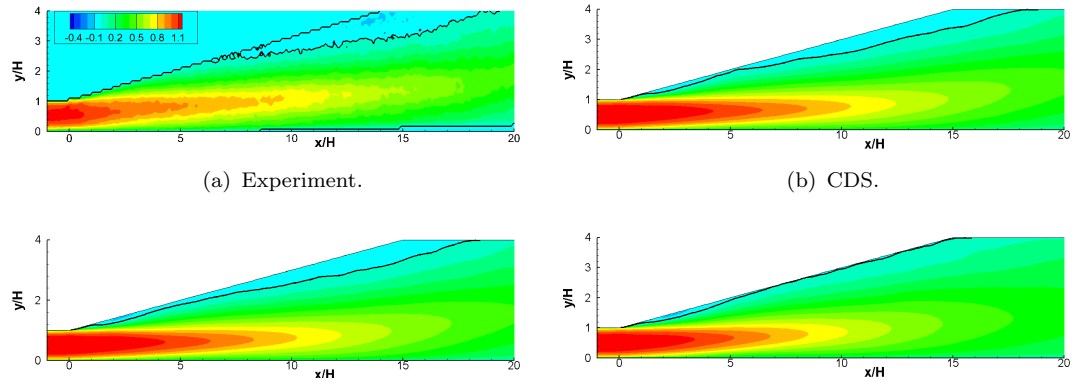

(a) Experiment. (b) CDS.

(c) Hybrid FSM scheme. (d) BCD20.

FIGURE 10.14: Streamwise velocity contours U/U_b at the plane $L_z/H = 0.5$.

almost completely suppresses flow separation at the top wall and hence shows a greater departure from the reference data.

Figure 10.16 shows the frequency power spectral density distribution of the streamwise velocity component at the locations $x/H = 8, y/H = 1$ and $x/H = 14, y/H = 2$ in the centre plane ($z/L_z = 0.5$). The CDS and hybrid-FSM scheme both allow for a physically realistic energy cascade $\propto St^{-5/3}$, where the Strouhal number is defined as $S_t = fH/U_b$, over approximately one decade at both locations. This suggests that the resolution of the computational grid is in principle adequate to resolve a fair amount of turbulence structures. The bounded central-difference scheme BCD20 only sustains a very short $St^{-5/3}$ region and shows an overly large damping of the high-frequency content. The damping originates from the additional numerical dissipation introduced by the BCD20 scheme. The study of the numerical convection scheme illustrates that the hybrid-FSM convection scheme provides results as accurate as the CDS with significantly improved robustness in the RANS region. It also indicates that boundedness of the numerical scheme inevitably contaminates the resolved flow and hence deteriorates the results.

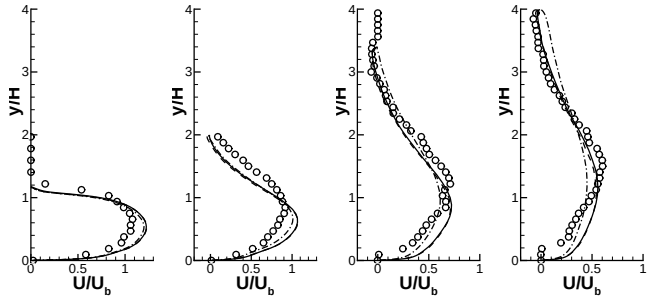

(a) Velocity component U/U_b

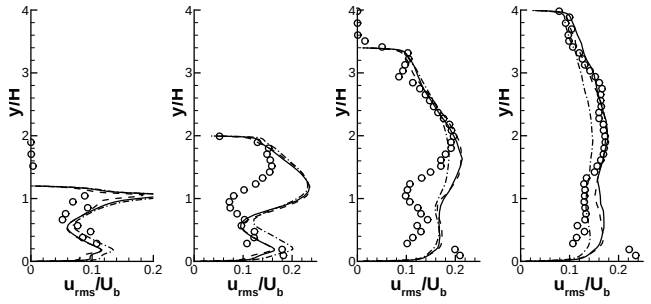

(b) $\overline{u'}_{rms}/U_b$

FIGURE 10.15: Velocity and Reynolds-stress components at the centre plane $z/H = 0.5$. Locations from left to right: $x/H = 1$, $x/H = 5$, $x/H = 12$ and $x/H = 16$. Symbols correspond to experimental data of Cherry *et al.* (2008, 2009). (—) CDS, (- - -) hybrid FSM scheme, (– · –) BCD 20.

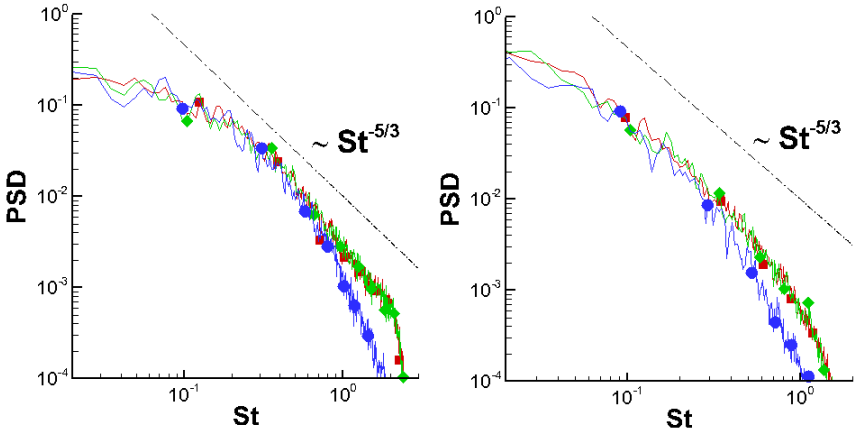

FIGURE 10.16: Power spectral density of streamwise velocity at two different locations. Left: $x/H = 8, y/H = 1, z/H = 1.665$; right: $x/H = 14, y/H = 2, z/H = 1.665$. (▪—▪) CDS, (◆—◆) hybrid-FSM scheme, (●—●) BCD 20.

10.2.5 Grid and Parameter Sensitivity Study

In this section the influence of the resolution of the computational grid is investigated together with the effect of the shielding function f_z, as developed in section 10.1.7 for improved WMLES capabilities of FSM. In order to assess the effectiveness of the shielding function for WMLES, simulations with and without the shielding function are performed and compared. The grid sensitivity is investigated by performing a simulation on a computational grid with a 50% increase in cells in each coordinate direction ($502 \times 98 \times 145$), which gives a total number of approximately 7×10^6 cells within the diffuser. All simulations are performed using the FSM-SST model and with $C_\alpha = 0.85$, $\beta = 0.75$ and $n = 4$.

An instantaneous snapshot of the spanwise vorticity $\omega_z H/U_b$ contour at the centre plane, $z/L_z = 0.5$, is shown in figure 10.17. The shielding function f_z enforces a significantly enlarged RANS layer, which suppresses turbulence fluctuations close to the wall. The reduced turbulence activity in the RANS layer has the consequence that the incoming boundary layer at the top wall requires much longer streamwise distances before the flow breaks down into fine-scale turbulence. When the shielding function f_z is not used, turbulence fluctuations are allowed to penetrate much closer to the wall, with the effect of a much faster breakdown into turbulence downstream of the sharp corner. The same effect is achieved on the fine grid, where resolved turbulence fluctuations develop much faster downstream of the sharp corner. Moreover, the computational grid with the higher resolution clearly allows finer turbulence structures to develop, compared to the relatively coarse baseline computational grid.

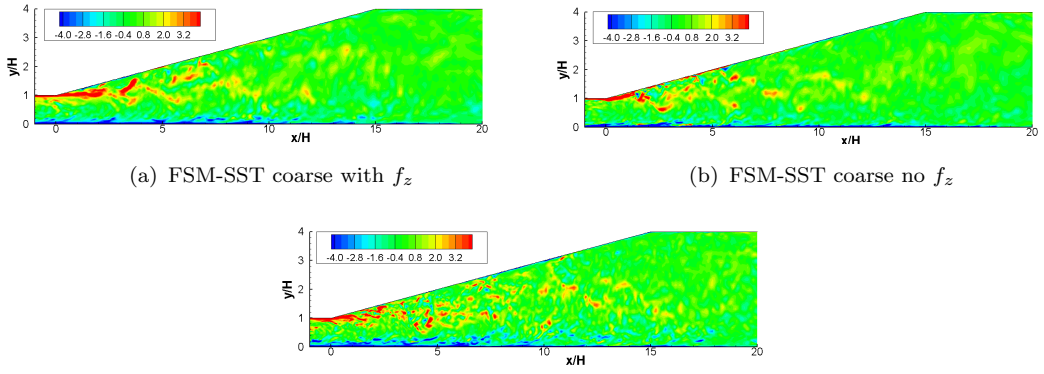

(a) FSM-SST coarse with f_z

(b) FSM-SST coarse no f_z

(c) FSM-SST fine with f_z

FIGURE 10.17: Instantaneous spanwise vorticity $\omega_z H/U_b$ contour at the plane $z/L_z = 0.5$.

The predictions of the surface-pressure distribution C_p at the bottom wall ($y/H = 0$), at $z/L_z = 0.5$, are shown in figure 10.18. The simulation on the coarse grid and including the shielding function shows the greatest departure of the rapid pressure recovery, up to $x/L \approx 0.5$. However, further downstream, at $x/L > 0.5$, it provides the best agreement with reference data. The simulations on the fine grid and the simulation on the coarse grid without the shield function better predict the rapid initial pressure rise in the diffuser. The fine resolution case also provides good agreement of surface pressure at $x/L > 0.5$. The simulation without the shielding function shows overly large surface-pressure values downstream of $x/L \approx 0.5$. The shielding function developed for improved WMLES is also effective in the present case and improves the overall quality of the predictions.

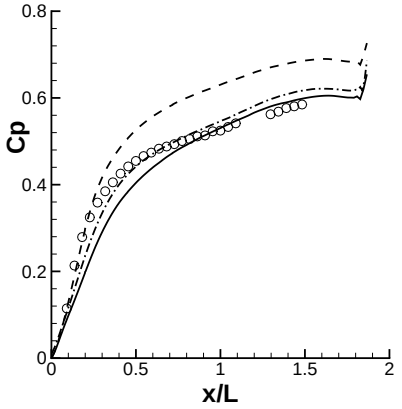

FIGURE 10.18: Surface-pressure coefficient C_p at the bottom wall. Symbols correspond to experimental data of Cherry *et al.* (2008, 2009). (—) FSM-SST coarse with f_z, (- - -) FSM-SST coarse no f_z, (– · –) FSM-SST fine with f_z.

The differences in the surface-pressure distribution can be explained from the streamwise velocity U/U_b contour in the centre plane, $z/L_z = 0.5$, which is shown in figure 10.19. The figure also includes a thick line, which corresponds to the zero-velocity contour and gives the extent of the separated-flow region. In the predictions on the coarse grid and including the shielding function, flow separation occurs almost immediately downstream of the sharp corner and extents up to $x/H \approx 18$. The premature separation from the top wall explains the relatively slow pressure recovery downstream of the sharp corner. This is probably a consequence of the delayed breakdown of the flow from the RANS layer into resolved turbulence fluctuations. The simulations on the fine grid and the simulation without the shielding function, both predict a shallow recirculation region just downstream of the diffuser inlet. This results in better predictions of the initial, rapid, pressure rise in the diffuser. The improved predictions are likely related to the much faster breakdown of the flow

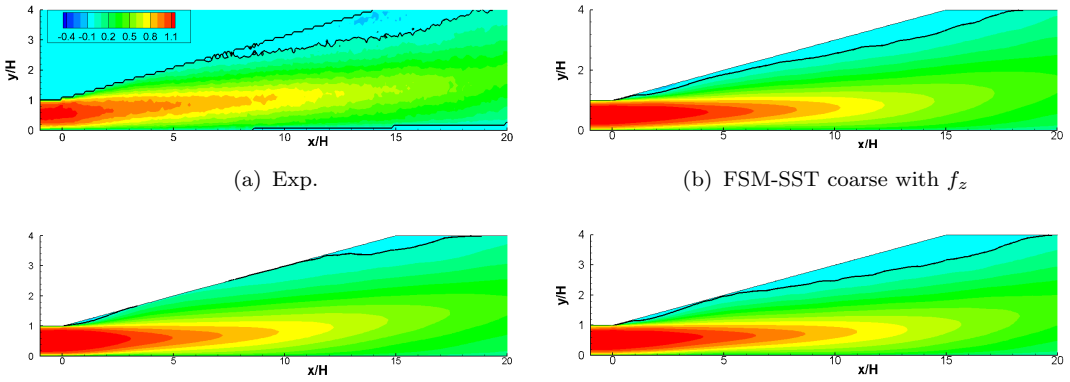

(a) Exp.

(b) FSM-SST coarse with f_z

(c) FSM-SST coarse no f_z

(d) FSM-SST fine with f_z

FIGURE 10.19: Streamwise velocity contours U/U_b at the plane $z/L_z = 0.5$.

from the RANS layer into resolved turbulence fluctuations. The flow in the simulation without shielding function reattaches to the top wall and separates again at $x/H \approx 12$. This is significantly delayed compared to the reference data, and results in a too-small recirculation zone. The fine resolution case provides the best overall agreement with the reference data, in terms of predicting the correct extent of the recirculation region. This is reflected in good agreement of the surface-pressure distribution.

A more detailed comparison of the flow field on the centre plane is shown in figure 10.20, where the streamwise velocity profile and streamwise fluctuations $\overline{u'}_{rms}/U_b$ are plotted at the four streamwise locations $x/H = 1$, $x/H = 5$, $x/H = 12$ and $x/H = 16$. The velocity profile at the first station, $x/H = 1$, is predicted very similarly by all simulations. At the second station, $x/H = 5$, the fine- and coarse-resolution cases show the same velocity distribution close to the bottom wall and under-predict the streamwise velocity magnitude at the top wall. The case without shielding function shows improved agreement at the top wall, which is not much of a surprise, since it predicts no flow separation at this station, which is in agreement with the reference data. The flow close to the top wall, at $x/H = 12$ and $x/H = 16$, is better reproduced if the shielding function is included. This is linked to a more realistic prediction of the extent of the recirculation zone. At the bottom wall the two cases with shielding function exhibit a somewhat higher streamwise velocity magnitude compared to the case without shielding function. The lower magnitude is in better agreement with the reference data.

It has been discussed before, that without the shielding function included, turbulence fluctuations are allowed to penetrate much closer to the wall. This is reflected in significantly increased streamwise fluctuations $\overline{u'}_{rms}/U_b$ at $x/H = 1$, close to

the wall. At the other stations, farther downstream, this difference is much less pronounced or even non existent. The coarse-grid simulation using the shielding function shows the highest level of streamwise fluctuations throughout. The simulations on the fine grid and the simulation without the shielding function show a smaller intensity of the streamwise fluctuations, particularly at the centre of the diffuser, and hence provide better agreement with the reference data.

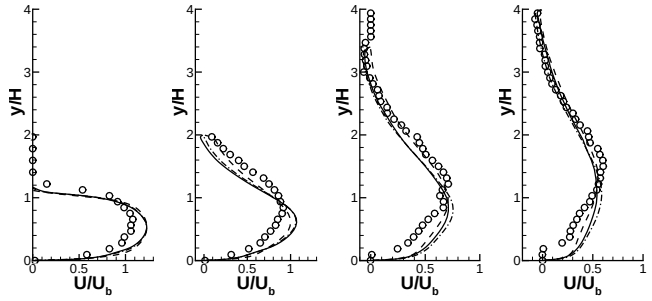

(a) Velocity component U/U_b

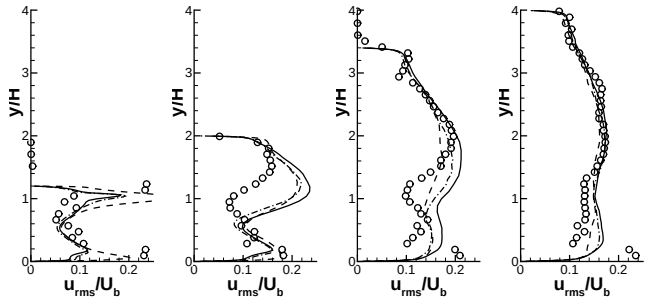

(b) $\overline{u'}_{rms}/U_b$

FIGURE 10.20: Velocity component U/U_b and streamwise velocity fluctuations $\overline{u'}_{rms}/U_b$ at the centre plane $z/L_z = 0.5$. Locations from left to right: $x/H = 1$, $x/H = 5$, $x/H = 12$ and $x/H = 16$. Symbols correspond to experimental data of Cherry *et al.* (2008, 2009). (—) FSM-SST coarse with f_z, (- - -) FSM-SST coarse no f_z, $(- \cdot -)$ FSM-SST fine with f_z.

10.2.6 Sensitivity to the Turbulence Model

The sensitivity of results to the underlying RANS model is investigated. Simulations are performed using the FSM-SST, FSM-EASM and FSM-φ-α-EASM formulation in conjunction with the hybrid FSM convection scheme. In addition, results obtained by IDDES based on the k-ω-SST model are also included in the comparison with the reference data. Simulations have also been performed using the Scale-Adaptive Simulation (SAS) methodology. However, SAS was not able to sustain any turbulence fluctuations in the inflow duct and in the diffuser, and are therefore not included in the subsequent discussion.

The presentation of results is split into three parts. First, the instantaneous flow field is discussed, followed by a comparison of the mean-flow field at the spanwise location $z/L_z = 0.5$. Finally, analysis of the streamwise evolution of the three-dimensional flow field is presented.

Instantaneous flow field at the centre plane $z/L_z = 0.5$

An instantaneous snapshot of the spanwise vorticity contours $\omega_z H/U_b$, at the centre plane $z/L_z = 0.5$, is shown in figure 10.21. It is evident, that all FSM models resolve very long streamwise structures at the bottom wall. In the predictions of the IDDES model these elongated turbulence structure do not exist and instead, many more fine-grained turbulence structures are resolved close to the wall. As previously discussed, this is related to the extent of the RANS region adjacent to the wall, which is much smaller for IDDES than for the FSM models, where the function f_z enforces a larger RANS layer. The excessive damping in the RANS region eliminates most of the turbulence structures, that are observed in the IDDES predictions close to the wall. This issue has already been discussed in section 10.1 and is clearly visualised in figure 10.7 for the flow in a planar channel. The suppression of turbulence fluctuations close to the wall by the FSM models has the consequence, that the incoming boundary layer at the top wall requires much longer streamwise distances before the breakdown into fine-scale turbulence occurs.

Mean flow field at the centre plane $z/L_z = 0.5$

The surface-pressure distribution C_p at the bottom wall ($y/H = 0$), is shown in figure 10.22. All of the employed hybrid RANS/LES models have difficulties in reproducing both, the initial rapid pressure recovery, which extents up to $x/L \approx 0.5$, and the correct magnitude of surface pressure downstream of $x/L \approx 0.5$. The IDDES model gives good predictions for the initial, rapid, pressure recovery in the

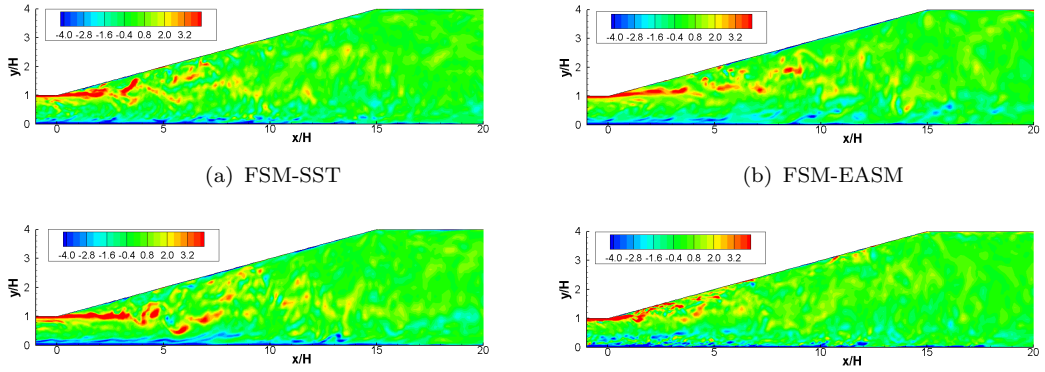

(a) FSM-SST (b) FSM-EASM

(c) FSM-φ-α-EASM (d) IDDES

FIGURE 10.21: Spanwise vorticity $\omega_z H/U_b$ at the plane $z/L_z = 0.5$.

diffuser but over-predicts the magnitude of C_p for $x/L > 0.5$. On the other hand, all FSM models show deficiencies in predicting the correct pressure recovery up to the location $x/L \approx 0.5$. Downstream of $x/L \approx 0.5$, the predictions of the FSM models improve and the FSM-SST and FSM-EASM models achieve reasonable agreement with the reference data. The FSM-φ-α-EASM model under-predicts the magnitude of C_p and therefore provides least agreement with the reference data, compared to the other FSM models. Note that many of the LES and hybrid RANS/LES simulation presented at the 13th/14th ERCOFTAC/IAHR Workshop show trends similar to that observed here. They show either good agreement for the initial, rapid, pressure recovery with over-prediction of C_p for $x/L > 0.5$, or they fail to predict the rapid pressure rise but predict a more realistic magnitude of C_p farther downstream.

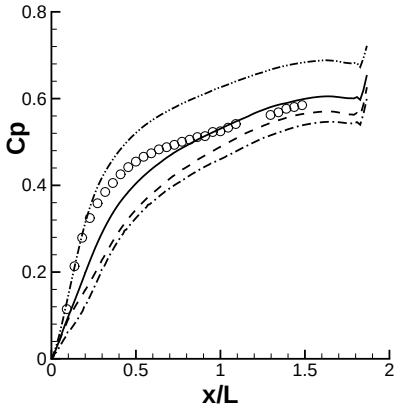

FIGURE 10.22: Surface-pressure coefficient C_p at the bottom wall. Symbols correspond to experimental data of Cherry *et al.* (2008, 2009). (—) FSM-SST, (- - -) FSM-EASM, (– · –) FSM-φ-α-EASM, (– · · –) IDDES.

Some more insight into the flow-field predictions can be gained from figure 10.23, which shows the streamwise velocity contour U/U_b at the centre plane $z/L_z = 0.5$. The figure also includes a thick line, which corresponds to zero-velocity contours, which reveal the extent of the separated flow region. The streamwise velocity contour and particularly the amount of separation explains the departure in the predictions of the surface-pressure distribution from the reference data. The experimental data show a large separation zone, which extends from approximately $x/H \approx 7$ to $x/H \approx 19$. It is now obvious that the initial, rapid, pressure recovery occurs in the region $x/H < 7$, where the flow is still attached. Downstream of $x/H \approx 7$, the recirculation zone reduces the effective cross section, which is responsible for the observed reduced rate of pressure recovery in the diffuser. The IDDES model predicts a very shallow recirculation zone just downstream of the sharp corner and the main separation from the top wall occurs far too late, at approximately $x/H \approx 11$. The fact that the flow remains attached to the top wall is consistent with the reference data, and is reflected in accurate predictions of the surface-pressure distribution in this region. The erroneous prediction of the location and size of the recirculation zone is again reflected in an over-prediction of the magnitude of C_p in this region. On the other hand, all FSM models predict flow separation to occur almost immediately downstream of the sharp edge, at approximately $x/H \approx 1$, and the thickness of the recirculation zone to be much larger and hence in better agreement with the reference data. This explains the departure observed in the predictions of the surface-pressure distribution by the FSM models up to $x/L \approx 0.5$, and the better agreement further downstream.

A more detailed comparison of the flow field on the centre plane is shown in figure 10.24, where the mean-velocity profiles and resolved Reynolds-stress components are plotted at the four streamwise locations $x/H = 1$, $x/H = 5$, $x/H = 12$ and $x/H = 16$. The quality of the streamwise velocity component at the first location, $x/H = 1$, is similar for all hybrid RANS/LES models. All models show a too high streamwise velocity magnitude in the centre of the diffuser. At the second station, $x/H = 5$, the flow predicted by the IDDES model is still attached to the top wall, which is reflected in good agreement of the velocity profile with the reference data at the top wall. All FSM models predict flow separation at this location, and for this reason, show a departure in the streamwise velocity profile at the top wall. All hybrid models show too large peak values of streamwise velocity magnitude near the bottom wall. The models, which predict the thickest recirculation zone at this station consequently predict the largest peak value of streamwise velocity. That is, the IDDES model shows, relative to the other models, the lowest peak value and

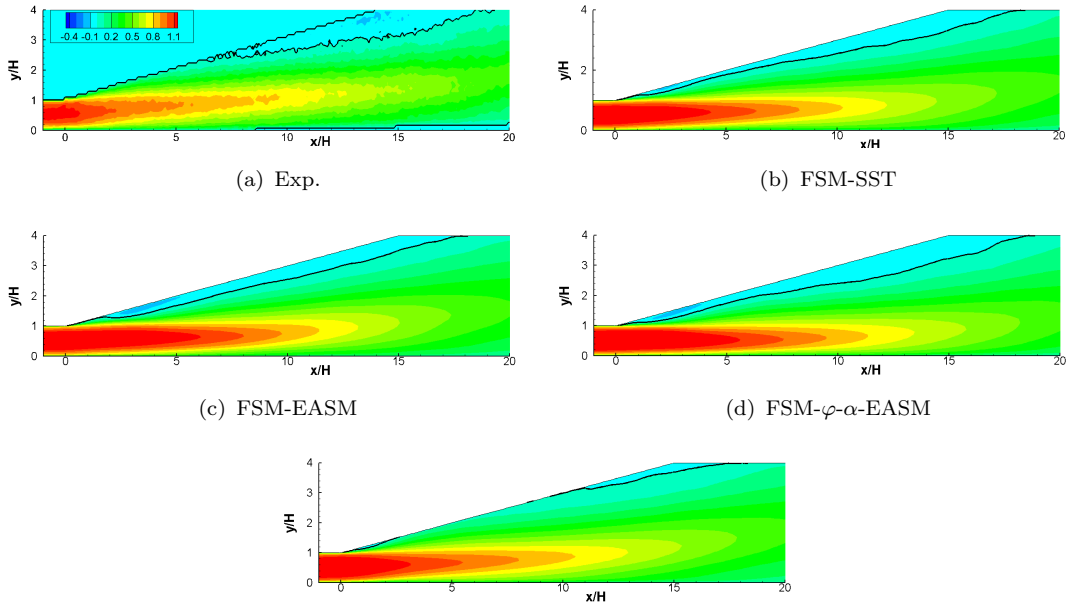

(a) Exp.

(b) FSM-SST

(c) FSM-EASM

(d) FSM-φ-α-EASM

(e) IDDES

FIGURE 10.23: Streamwise velocity contours U/U_b at the plane $z/L_z = 0.5$.

the FSM-EASM and FSM-φ-α-EASM models predict the highest peak values. In addition, all hybrid RANS/LES predict the location of maximum streamwise velocity too close to the bottom wall. At the last two stations, $x/H = 12$ and $x/H = 16$, all hybrid RANS/LES models show significantly improved predictions compared to the RANS results (see section 6.4). Close to the bottom wall, the IDDES and FSM-EASM models provide better agreement for the location of maximum streamwise velocity. The peak streamwise velocity location of the FSM-SST and FSM-φ-α-EASM models remain too close to the bottom wall and the velocity magnitude is generally over-predicted. The FSM formulation with the most sophisticated underlying RANS model (φ-α-EASM) shows the greatest departure from the reference data at the bottom wall. The streamwise velocity profile at the top wall confirms what has been said in the discussion about the size of the recirculation zone. The IDDES model predicts the least amount of reverse flow and therefore slightly overestimates the streamwise velocity. It should be noted that the streamwise velocity profiles obtained by the wall-resolved LES of Schneider *et al.* (2010*b*) and the DNS of Ohlsson *et al.* (2010) also do not achieve perfect agreement with the experimental data, particularly for the stations downstream of $x/H \approx 15$.

The predictions of the resolved Reynolds-stress components are discussed next. At the first station, $x/H = 1$, the IDDES model predicts significantly higher values of streamwise velocity fluctuations, $\overline{u'}_{rms}/U_b$, wall-normal velocity fluctuations, $\overline{v'}_{rms}/U_b$ and shear stress, $\overline{u'v'}/U_b^2$, compared to the FSM approaches. The reason

for the more intense fluctuations of IDDES is, that more turbulence structures are allowed to develop close to the wall. The FSM models employ a larger RANS zone, where resolved turbulence fluctuations are strongly suppressed. At the next station downstream, at $x/H = 5$, the IDDES model shows the lowest levels of resolved turbulence fluctuations in the centre of the channel, which is in better agreement with the reference data. This is probably linked to the more rapid breakdown into smaller-scale turbulence fluctuations of the incoming boundary layer at the top wall. On the other hand, the FSM models show a delayed breakdown of the flow from the RANS layer into turbulence fluctuations, which results in more energetic large-scale turbulence motion at that location. This trend continues throughout to the downstream stations, $x/H = 12$ and $x/H = 16$, where the IDDES model consistently shows lower levels of turbulence fluctuations than the FSM approaches. It is also obvious that the FSM-φ-α-EASM model consistently predicts the highest levels of resolved turbulence fluctuations. The FSM-SST and FSM-EASM formulations show very similar levels of resolved turbulence fluctuations with an intensity lower than the FSM-φ-α-EASM model, but higher than the IDDES model.

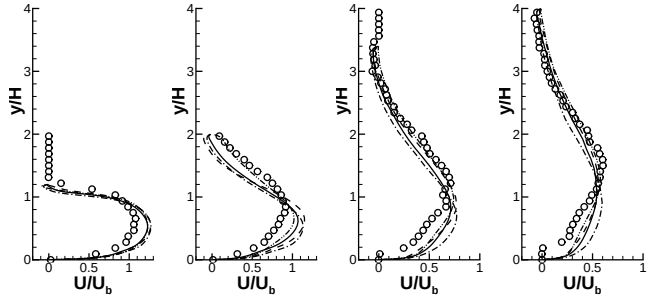

(a) Velocity component U/U_b

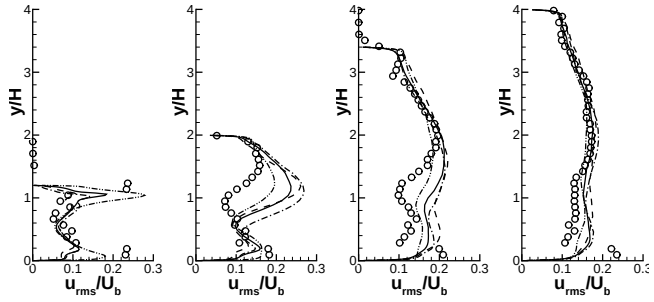

(b) $\overline{u'}_{rms}/U_b$

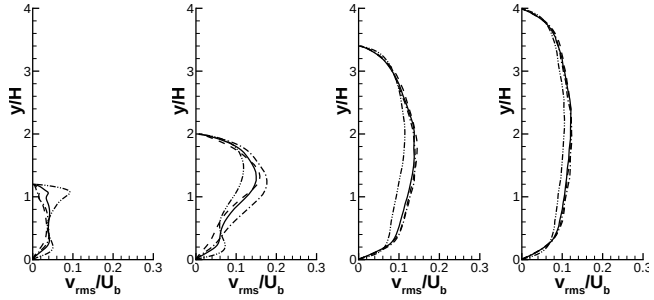

(c) $\overline{v'}_{rms}/U_b$

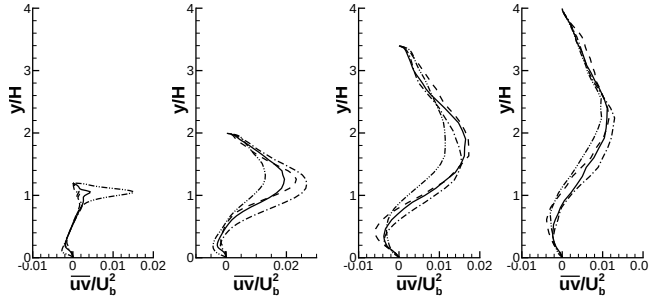

(d) $\overline{u'v'}/U_b^2$

FIGURE 10.24: Velocity and Reynolds-stress components at the centre plane $z/L_z = 0.5$. Locations from left to right: $x/H = 1$, $x/H = 5$, $x/H = 12$ and $x/H = 16$. Symbols correspond to experimental data of Cherry *et al.* (2008, 2009). (—) FSM-SST, (- - -) FSM-EASM, $(- \cdot -)$ FSM-φ-α-EASM, $(- \cdots -)$ IDDES.

Three-Dimensional Flow Field

Further insight into the predictions of the three-dimensional flow field can be gained from figures 10.25 and 10.26, which show contour plots of streamwise velocity U/U_b and resolved streamwise velocity fluctuations $\overline{u'}_{rms}/U_b$ at the streamwise locations $x/H = 1$, $x/H = 5$, $x/H = 12$ and $x/H = 16$. Figure 10.25 also includes the contour line with zero-velocity, in order to visualise the extent of the separated-flow region. The flow field at the first station, $x/H = 1$, is well predicted by the FSM-SST and FSM-EASM models. Both show a small recirculation region in the top left and top right corners. FSM-φ-α-EASM and IDDES both predict flow separation at the entire top wall at this station, which is not consistent with the reference data. At the second station, $x/H = 5$, the size of the recirculation zone in the top right corner has grown significantly, but the flow still remains attached on parts at the top wall. All three FSM models predict the flow to be completely separated from the top wall at this station. The flow predicted by IDDES has re-attached at the top wall, and shows a recirculation zone in the top right corner, consistent with the experimental data. The extent of the recirculation zone is slightly under-predicted. At the last two stations, $x/H = 12$ and $x/H = 16$, the flow has completely detached from the top wall and the recirculation zone has become almost two-dimensional, with no variation in the spanwise direction. All hybrid models are able to correctly predict the flow separation from the top wall. The shape of the recirculation region exhibits some variation in the spanwise direction and hence does not fully match the reference data. Nevertheless, all hybrid models predict the mean-flow topology in satisfying agreement with the reference data, and are therefore clearly superior to the RANS predictions of section 6.4, which completely failed to predict a realistic flow topology in the diffuser.

The contour plots of resolved streamwise velocity fluctuations $\overline{u'}_{rms}/U_b$ in figure 10.26 illustrate again the differences in resolved turbulence fluctuations between the FSM and IDDES approach. The levels of resolved turbulence fluctuations predicted by the IDDES, at the plane $x/H = 1$, is significantly higher, particularly close to the wall, compared to the FSM models, and hence in better agreement with the reference data. At the second plane, $x/H = 5$, the opposite trend can be observed. All FSM models predict higher intensities of streamwise velocity fluctuations, whereas the IDDES model predicts lower intensities, which is, again, in better agreement with the reference data. At the last two planes, $x/H = 12$ and $x/H = 16$, the IDDES model consistently predicts lower resolved streamwise fluctuations, compared to the FSM models. The higher levels of streamwise fluctuations of the FSM models now

better matches the reference data. Although, the FSM-EASM and FSM-φ-α-EASM models predict still somewhat too high intensities at the plane $x/H = 12$.

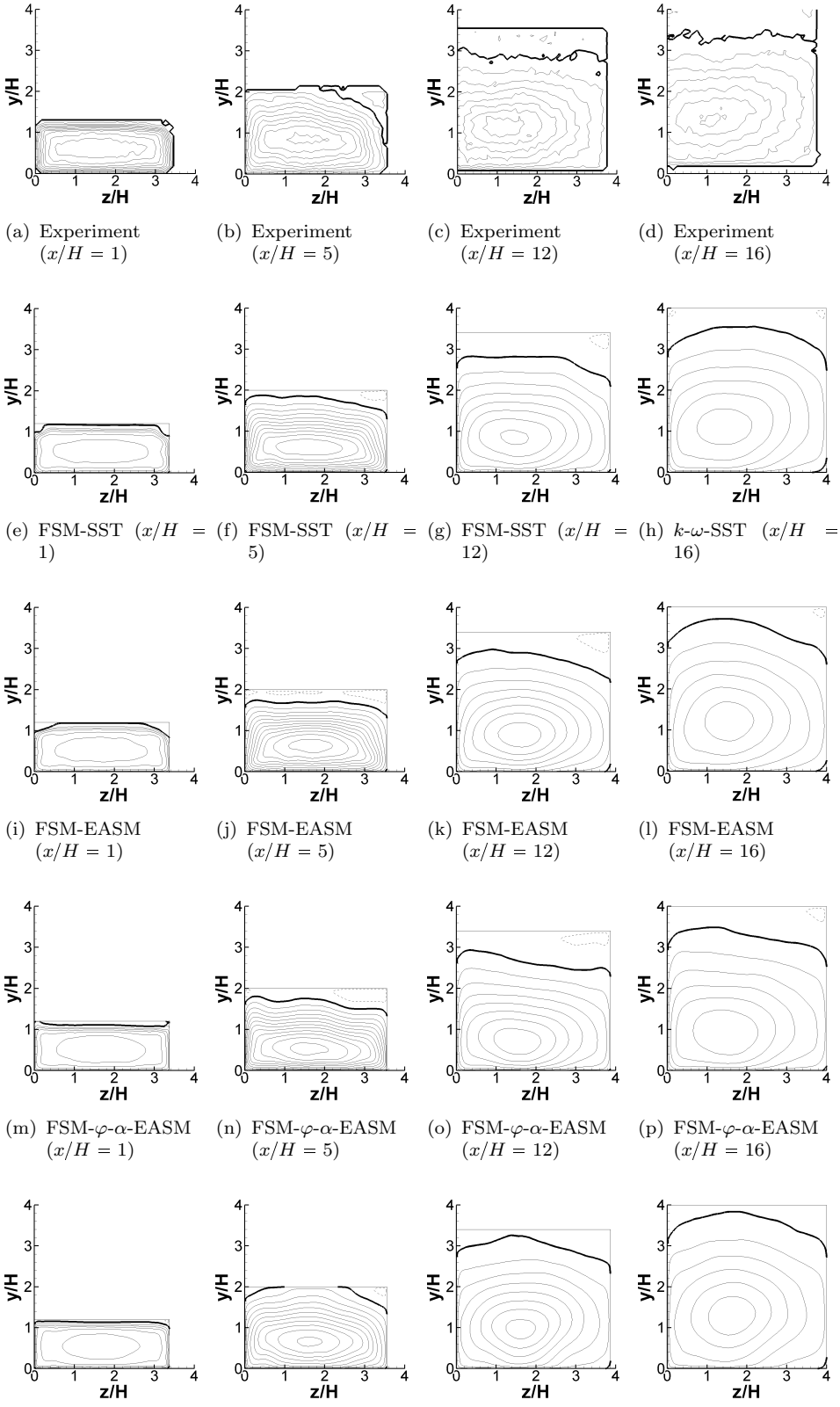

(a) Experiment ($x/H = 1$) (b) Experiment ($x/H = 5$) (c) Experiment ($x/H = 12$) (d) Experiment ($x/H = 16$)

(e) FSM-SST ($x/H = 1$) (f) FSM-SST ($x/H = 5$) (g) FSM-SST ($x/H = 12$) (h) k-ω-SST ($x/H = 16$)

(i) FSM-EASM ($x/H = 1$) (j) FSM-EASM ($x/H = 5$) (k) FSM-EASM ($x/H = 12$) (l) FSM-EASM ($x/H = 16$)

(m) FSM-φ-α-EASM ($x/H = 1$) (n) FSM-φ-α-EASM ($x/H = 5$) (o) FSM-φ-α-EASM ($x/H = 12$) (p) FSM-φ-α-EASM ($x/H = 16$)

(q) IDDES ($x/H = 1$) (r) IDDES ($x/H = 5$) (s) IDDES ($x/H = 12$) (t) IDDES ($x/H = 16$)

FIGURE 10.25: Streamwise velocity contours predicted by the FSM-SST, FSM-EASM, FSM-φ-α-EASM, IDDES and experimental data of Cherry *et al.* (2008, 2009). Thick line corresponds to zero velocity contour line. The spacing between contour lines corresponds to $\Delta U/U_b = 0.1$ and dashed lines denote negative velocities.

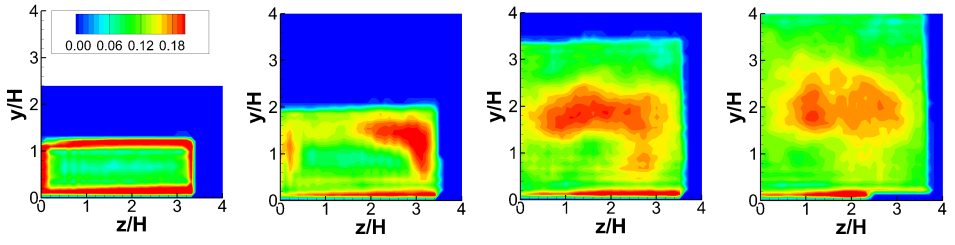

(a) Experiment ($x/H = 1$) (b) Experiment ($x/H = 5$) (c) Experiment ($x/H = 12$) (d) Experiment ($x/H = 16$)

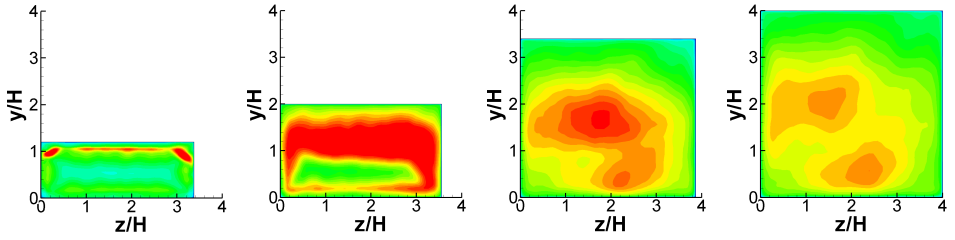

(e) FSM-SST ($x/H = 1$) (f) FSM-SST ($x/H = 5$) (g) FSM-SST ($x/H = 12$) (h) FSM-SST ($x/H = 16$)

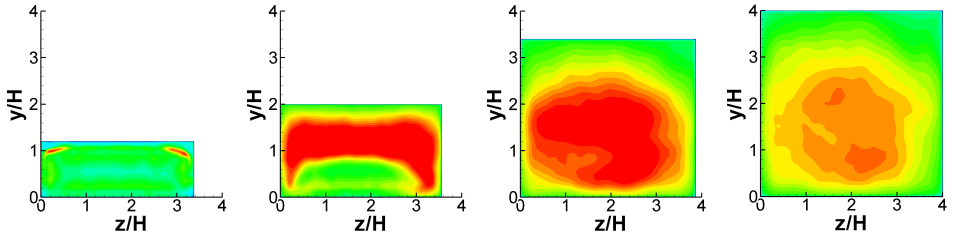

(i) FSM-EASM ($x/H = 1$) (j) FSM-EASM ($x/H = 5$) (k) FSM-EASM ($x/H = 12$) (l) FSM-EASM ($x/H = 16$)

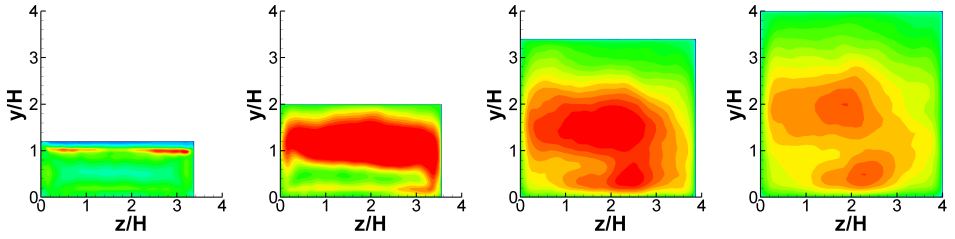

(m) FSM-φ-α-EASM ($x/H = 1$) (n) FSM-φ-α-EASM ($x/H = 5$) (o) FSM-φ-α-EASM ($x/H = 12$) (p) FSM-φ-α-EASM ($x/H = 16$)

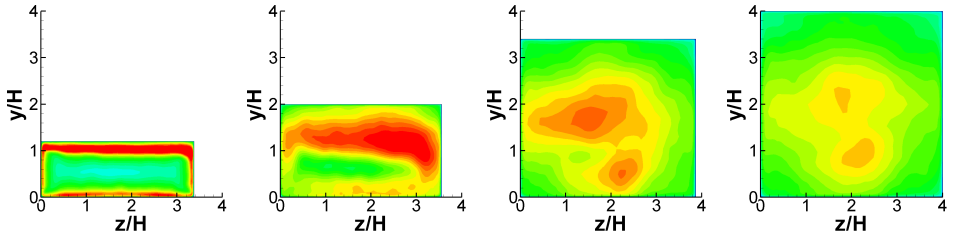

(q) IDDES ($x/H = 1$) (r) IDDES ($x/H = 5$) (s) IDDES ($x/H = 12$) (t) IDDES ($x/H = 16$)

FIGURE 10.26: Streamwise velocity fluctuations $\overline{u'}_{rms}/U_b$ predicted by the FSM-SST, FSM-EASM, FSM-φ-αEASM, IDDES and experimental data of Cherry *et al.* (2008, 2009).

10.2.7 Summary

The simulations of the flow in a three-dimensional diffuser confirm that a bounded convection discretisation scheme in the LES region adversely affects the results. The bounded scheme almost completely suppresses flow separation on the centre plane, whereas the CDS and hybrid FSM schemes give a similar picture of the separated flow region, in much better agreement with the reference data. In addition, both schemes allow for a more realistic spectral distribution of velocity fluctuations and show a more distinct $-5/3$ energy cascade.

All hybrid RANS/LES models considered here provide significantly improved results over pure RANS predictions, and are able to predict the correct flow topology in the diffuser. However, for the simulations on the relatively coarse baseline grid, none of the investigated turbulence models provides a satisfactory prediction of the flow field, in good agreement with the corresponding measurements. The SAS method is not able to sustain any turbulence fluctuations in the diffuser. In the predictions of the IDDES model, separation from the top wall occurs too late and results in too small a recirculation zone. On the other hand, all FSM models exhibit premature separation just downstream of the sharp corner. The differences in the predictions are related to the capabilities of each model to resolve turbulence fluctuations close to the wall. The IDDES model resolves more turbulence structures close to the wall than does FSM, which influences the predictions of the boundary-layer separation in the diffuser. It is shown that grid refinement improves the predictions of the separated-flow region just downstream of the sharp corner, and provides better agreement with the reference data. Concerning the sensitivity of results with respect to the underlying RANS model, the FSM-SST and FSM-EASM models give slightly better overall predictions, compared to the more sophisticated FSM-φ-α-EASM, which shows a pronounced over-prediction of streamwise velocity close to the bottom wall.

10.3 Tandem Cylinders

The configuration consists of two in-line, tandem cylinders, where the first cylinder creates an unsteady wake, which interacts with the downstream cylinder. For this reason, tandem cylinder flows are classed as a problem of wake interference (see Zdravkovich, 1987). The separation between the cylinders sets the type of wake interaction. When the cylinders are close to each other, vortex shedding from the upstream cylinder has been found to be suppressed. As the cylinder spacing is increased, a variety of flow modes are encountered, with upstream shear layer reattachment occurring first on the downstream cylinder, followed by the re-establishment of vortex shedding behind the upstream cylinder. This canonical wake/bluff-body interaction problem has recently received much attention in an effort to improve the understanding of sound generation mechanisms of landing-gear components, and has been subject of a workshop on Benchmark problems for Airframe Noise Computations (BANC) (see Lockard, 2011). Most tandem-cylinder studies have been performed at relatively low Reynolds number. However, a recent experimental program has been performed at high Reynolds number (1.66×10^5) by Lockard *et al.* (2007), Khorrami *et al.* (2007) and Jenkins *et al.* (2006), that provides one of the most comprehensive data sets available for aerodynamic and aeroacoustic simulation validation.

The tandem cylinder configuration is used here to investigate the performance of FSM and other hybrid RANS/LES methods when operated in its basic, 'natural', mode, where the entire attached boundary layer is treated in RANS mode and the massively separated flow outside the boundary layer is treated in LES mode. The tandem cylinder configuration has a gap spacing of $x/D = 3.7$ (from centre to centre) and a Reynolds number of $Re_D = 1.66 \times 10^5$ based on the cylinder diameter D and free-stream velocity U_0. The cylinder spacing of $x/D = 3.7$ is large enough, such that regular vortex shedding occurs on the front cylinder. The boundary layer on the upstream cylinder was tripped in the experiments of the QFF and BART facilities (Lockard *et al.* (2007), Khorrami *et al.* (2007) or Jenkins *et al.* (2006)). The boundary-layer tripping ensures, that the flow is fully turbulent prior to separation and hence corresponds to a super-critical flow regime. It is argued in Lockard (2011), that due to the tripping, the resulting pressure distribution of the single front cylinder corresponds to a Reynolds number greater than 8×10^6. The boundary-layer tripping justifies the use of a fully turbulent simulation approach, where all boundary layers are fully turbulent and transition is not accounted for. It also facilitates a comparison between experiment and CFD.

In order to successfully reproduce the experimental data, it is important to correctly predict the boundary layer, flow separation and the development free-shear layer from the front cylinder, since any error in the predictions may significantly alter the downstream development of the flow. The main challenge associated with the flow around the downstream cylinder is to accurately capture the interaction of the wake and the cylinder, as well as, the development of the boundary layer on the downstream cylinder. Experimental data show that the wake of the rear cylinder strongly depends on the state of the boundary layer and associated separation points. Recall that the front cylinder is tripped in all experiments. Two data sets are available, with and without tripping of the boundary layer on the rear cylinder. The fully turbulent simulation approach more closely resembles the experimental data with tripping of the boundary layer on both cylinders.

10.3.1 Computational Setup

The computational setup consists of a three-dimensional C-type domain with a spanwise extend of $z/D = 3$. The up-stream boundary is placed $25D$ away from the cylinders and the outflow boundary is located at $x/D = 30$ downstream of the centre of the first cylinder. Periodic boundary conditions are used in the spanwise direction, and zero-gradient boundary conditions on the outflow boundary. Each two-dimensional plane (x-y) (see figure 10.27) is discretised with approximately 52000 cells using an average first wall-normal grid spacing, on both cylinders, of around $y_1^+ = 0.7$ and a maximum value of $y_1^+ = 1.7$. The number of cells in the spanwise direction is 40, so as to achieve almost isotropic cells in the gap region between the cylinders. The total cell count is approximately 2×10^6 cells. Note that the total number of cells of the baseline grid is significantly less compared to what was used in other contributions to the BANC I workshop (typically $7 - 133 \times 10^6$ cells). The turbulence kinetic energy and specific dissipation rate at the inflow are respectively prescribed as $k_\infty = 10^{-6} U_0^2$ and $\omega_\infty = 5U_0/D$ (see Spalart & Rumsey, 2007) such that immediate transition occurs in the boundary layer.

The convective fluxes in the flow equations are discretised using the hybrid FSM difference scheme and a second-order upwind scheme is used for the turbulence transport equations. The viscous terms use a second-order central-difference scheme. Time stepping is performed using an implicit second-order backward-difference scheme, and the coupling between the pressure and velocity is achieved by the PISO algorithm. The time step is set to $0.003D/U_0$ such that the CFL number does not exceed 0.5.

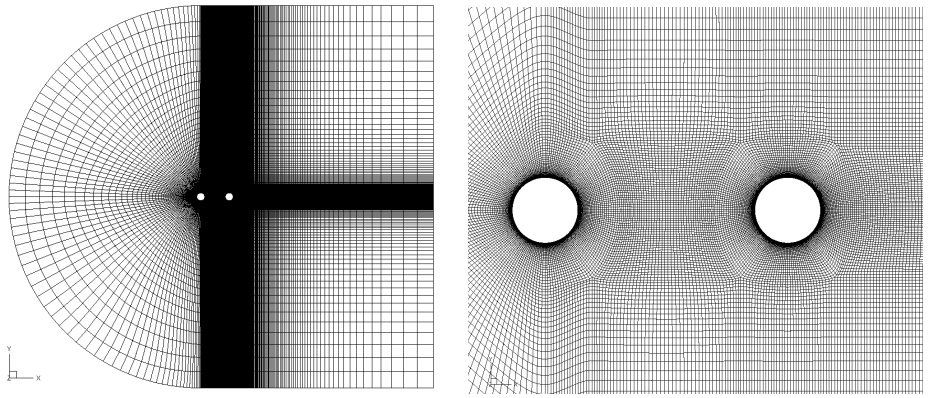

(a) (b)

FIGURE 10.27: Computational grid.

10.3.2 Averaging and Statistical Convergence

Before any results are presented the averaging procedure and statistical convergence is discussed. For all simulations, the flow is allowed to develop from the initial flow field for approximately $115D/U_0$ time units. After the initial settling period, statistical quantities are computed by averaging over $700D/U_0$ time units. For post-processing purposes the time-averaged quantities are additionally averaged over the homogeneous spanwise direction.

In order to verify the statistical convergence, the distributions of mean-surface-pressure coefficient C_p and fluctuating-surface-pressure coefficient $C_{p'_{rms}}$ are shown in figure 10.28, for both cylinders, for averaging over $230D/U_0$, $460D/U_0$ and $690D/U_0$ time units. In addition, the predictions of mean streamwise velocity and resolved two-dimensional turbulence kinetic energy $k_{res}^{2D} = (1/2)\left(\overline{u'u'} + \overline{v'v'}\right)/U_0^2$ on the centerline, $y/D = 0$, are shown in figure 10.29. It is obvious that the mean-surface-pressure distribution is already converged after averaging over $230D/U_0$ time units. The fluctuating-surface-pressure distribution requires time-averaging over at least $460D/U_0$ time units before adequately converged statistics are obtained. The same holds for the streamwise velocity and turbulence kinetic energy distributions. Averaging over more than $460D/U_0$ time units does not change the statistics.

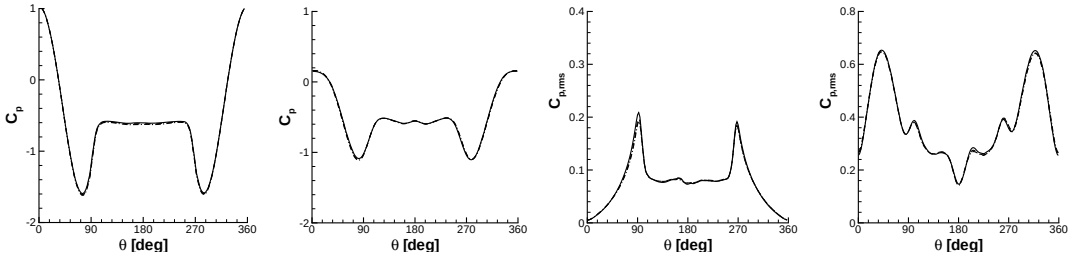

(a) C_p front cylinder. (b) C_p rear cylinder. (c) $C_{p'_{rms}}$ front cylinder. (d) $C_{p'_{rms}}$ rear cylinder.

FIGURE 10.28: Mean-surface-pressure C_p and fluctuating-surface-pressure coefficient $C_{p'_{rms}}$. (—) $t = 230D/U_0$, (- - -) $t = 460D/U_0$, $(- \cdot -)$ $t = 690D/U_0$.

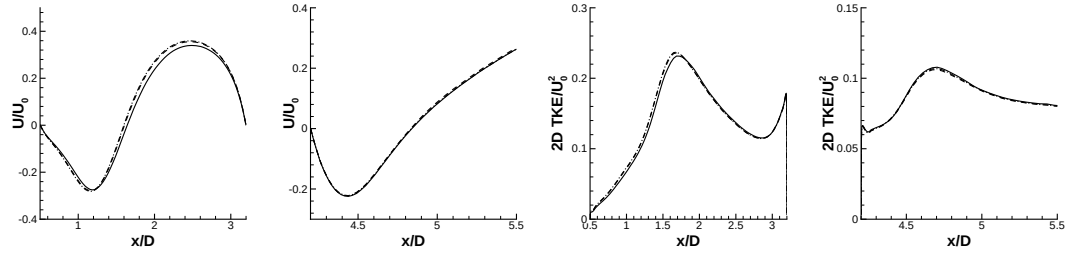

(a) U/U_0 gap region. (b) U/U_0 aft of rear cylinder. (c) TKE gap region. (d) TKE aft of rear cylinder.

FIGURE 10.29: Streamwise velocity profiles U/U_0 and 2D TKE at $y/D = 0$. (—) $t = 230D/U_0$, (- - -) $t = 460D/U_0$, $(- \cdot -)$ $t = 690D/U_0$.

10.3.3 Influence of Convection Discretisation

The sensitivity of results to the convection discretisation scheme is investigated. Three different second-order schemes are considered in this study. The numerical schemes include the hybrid FSM convection scheme (FSM) with a flow-dependent model for the flux-blending function, a central-difference scheme with 20% TVD conformity (BCD20) and a fully TVD conformal central-difference scheme (BCD). Unfortunately, no results could be obtained using the unbounded central-difference scheme, due to the presence of severe numerical oscisllations in the flow field. This highlights the advantages of an accurate hybrid scheme, such as the newly developed FSM scheme. The results presented here are obtained using the FSM-SST formulation and the baseline grid. This study focuses on differences in the predictions between each numerical scheme and is thus not so much concerned with the discussion of the overall agreement with reference data.

The distributions of mean-surface-pressure coefficient C_p and fluctuating-surface-pressure coefficient $C_{p'_{rms}}$ are shown in figure 10.30, for the upstream and downstream cylinder. The three convection schemes show negligible differences in mean-surface-pressure distribution on both cylinders. The fluctuating-surface-pressure distribution is predicted very similarly by the FSM and BCD20 schemes. Only the BCD scheme predicts overall higher levels of surface-pressure-fluctuations, which is particularly pronounced on the upstream cylinder, and which deteriorates the agreement with the reference data.

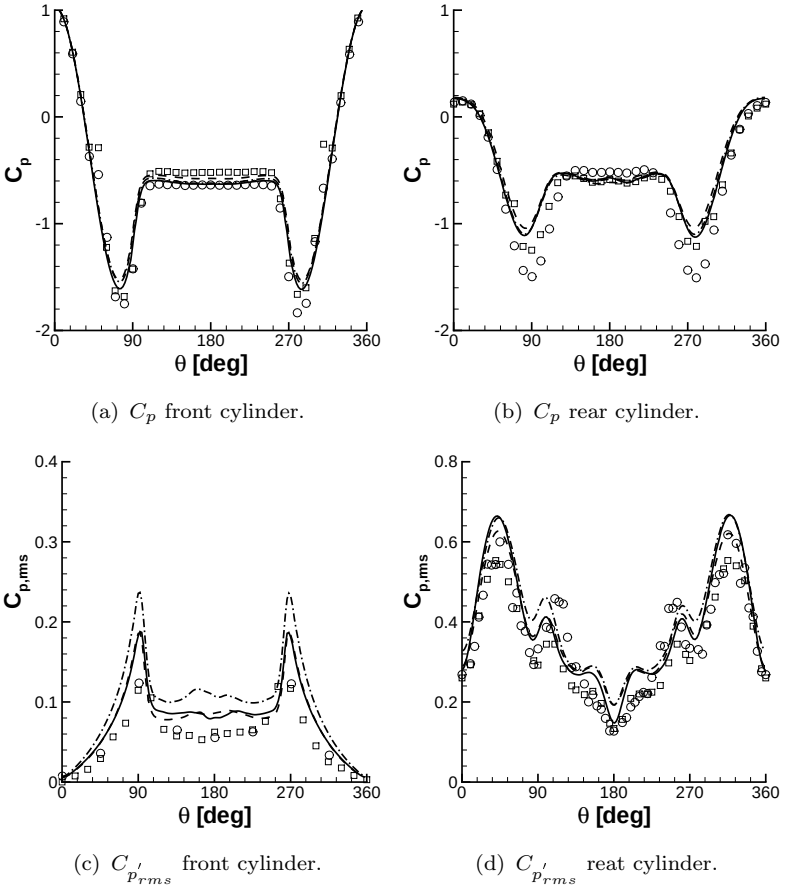

(a) C_p front cylinder.

(b) C_p rear cylinder.

(c) $C_{p'_{rms}}$ front cylinder.

(d) $C_{p'_{rms}}$ reat cylinder.

FIGURE 10.30: Mean-surface-pressure C_p and fluctuating-surface-pressure coefficient $C_{p'_{rms}}$. Front cylinder: (○) BART, (▫) QFF. Rear Cylinder: (○) BART, (▫) BART (rear cylinder tripped). (—) new FSM convection scheme, (- - -) BCD20, (– · –) BCD.

The predictions of mean streamwise velocity and resolved two-dimensional turbulence kinetic energy k_{res}^{2D} on the centerline, $y/D = 0$, are shown in figure 10.31. Significant differences can be observed for the velocity distribution in the gap region. Only the hybrid FSM scheme is able to provide predictions in excellent agreement with the reference data. Both bounded central-difference schemes, BCD20 and BCD, over-predict the size of the recirculation zone and predict lower intensities

of maximum streamwise velocity in the gap region at around $x/D = 2.5$. It seems that the additional numerical dissipation of the BCD20 and BCD schemes damps the natural shear layer instability mechanism, which results in a delayed breakdown of the separated shear layer. This results in an over-prediction of the recirculation zone behind the upstream cylinder, and in reduced entrainment of free-stream fluid, into the gap region, which manifests as an under-prediction of maximum streamwise velocity. Even though the velocity distribution obtained by the FSM scheme is in excellent agreement with reference data, the resolved turbulence kinetic energy in the central part of the gap region is significantly over-predicted. The more dissipative schemes, BCD20 and BCD, show lower levels of turbulence intensity in the gap between the cylinders, which is in better agreement with the reference data. Concerning the velocity distribution downstream of the rear cylinder, it can be noted, that the experimental data strongly depend on whether, or not, the boundary layer is trip on the rear cylinder. Without tripping the boundary layer on the rear cylinder, a much smaller recirculation zone behind the rear cylinder is observed, whereas in the tripped case, a significantly enlarged recirculation zone is observed. The size of the recirculation zone is directly linked to the separation point on the rear cylinder and the resulting trajectory of the free-shear layer. This clearly demonstrates, that the boundary-layer development on the rear cylinder is important, even though the rear cylinder is located in the highly turbulent wake of the upstream cylinder. Further, it is not too surprising, that the fully turbulent simulation approach, which does not account for laminar-turbulent transition, reproduce the experimental data for which the flow was tripped on the rear cylinder. The velocity distribution downstream of the rear cylinder is predicted by all schemes in good agreement with the reference data. The turbulence kinetic energy distribution downstream of the rear cylinder shows exactly the opposite trend observed for the gap region. The FSM scheme, with the lowest amount of additional numerical dissipation, exhibits the lowest intensity of turbulence fluctuations. The more dissipative schemes predict higher levels of turbulence intensity throughout. This seems counterintuitive, since increased levels of numerical dissipation enhances the damping of turbulence fluctuations, which should result in reduced levels of turbulence intensity. More insight into this issue can be gained from the power spectral density of streamwise velocity discussed next.

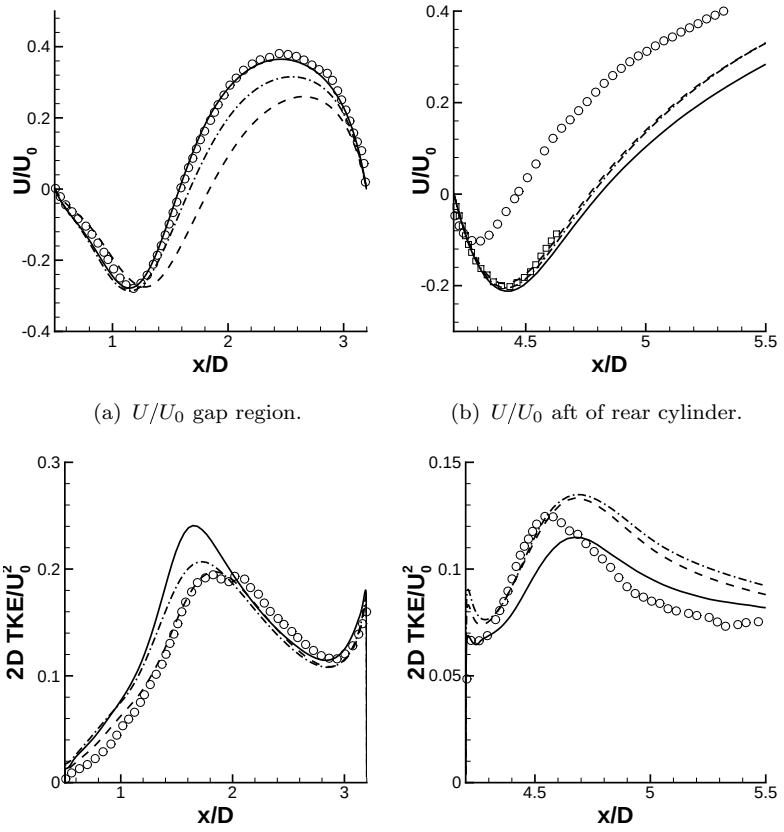

(a) U/U_0 gap region.

(b) U/U_0 aft of rear cylinder.

(c) TKE gap region.

(d) TKE aft of rear cylinder.

FIGURE 10.31: Streamwise velocity profiles U/U_0 and 2D TKE on the centreline ($y/D = 0$). (○) BART, (▫) BART (rear cylinder tripped). (—) new FSM convection scheme, (- - -) BCD20, ($- \cdot -$) BCD.

Predictions of the power spectral density (PSD) of surface pressure at the locations $\theta = 135°$, on the front cylinder and $\theta = 45°$ on the rear cylinder, are shown in figure 10.32. In addition, the PSD of streamwise velocity on the centreline, at $x/D = 2.5$ and $x/D = 4.5$, are also shown. The PSD of surface pressure on the upstream cylinder shows clear differences between each discretisation scheme. The new hybrid FSM scheme provides predictions clearly superior to BCD20 and BCD. The FSM scheme predicts the secondary peak at $St \approx 0.5$, where the Strouhal number is defined as $St = fD/U_0$. This peak is absent from the results obtained by BCD20 and BCD. In addition, FSM gives overall a more realistic picture of the PSD for Strouhal numbers $St > 1$. The predictions on the downstream cylinder show significantly less scatter, and all discretisation schemes provide good agreement with the reference data. Clear differences between each numerical scheme are also evident in the PSD of streamwise velocity. At both locations the hybrid FSM scheme shows the largest extent of $St^{-5/3}$ behaviour. The more dissipative schemes, BCD20 and BCD, are not able to reproduce a $-5/3$ region due to an overly large damping

of turbulence fluctuations for $St > 1$. The BCD scheme shows, as expected, the most pronounced damping at higher Strouhal numbers. It also seems that at the second location, downstream of the rear cylinder, the energy contained in the low Strouhal numbers is smaller for the FSM scheme, and more pronounced for the BCD20 and BCD schemes. This may explain why the FSM scheme predicts overall lower turbulence intensities downstream of the rear cylinder.

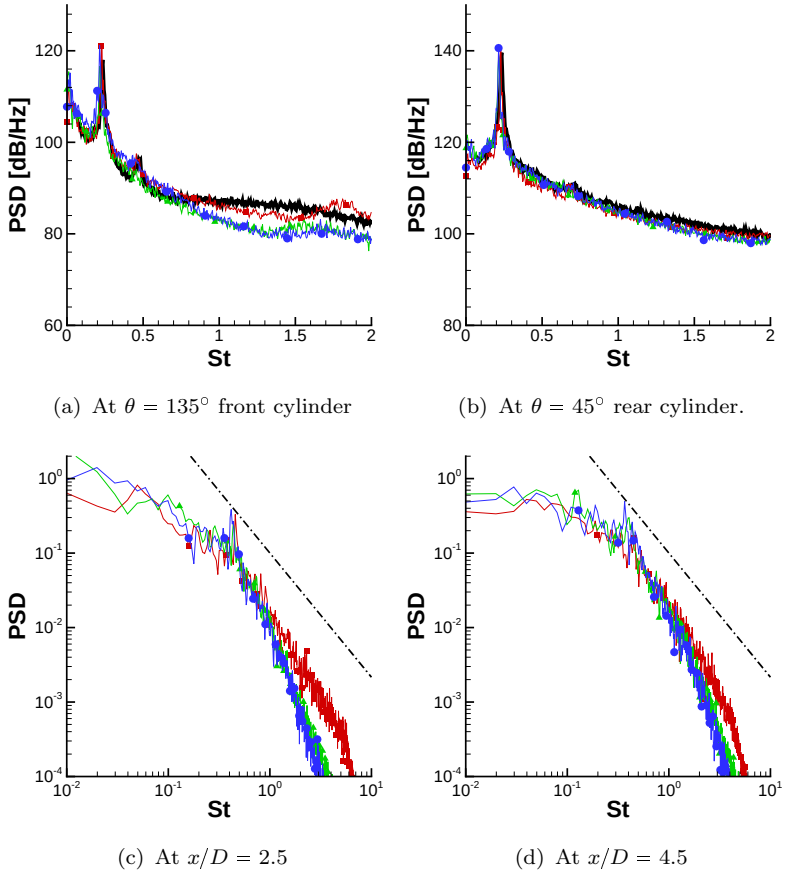

(a) At $\theta = 135^\circ$ front cylinder

(b) At $\theta = 45^\circ$ rear cylinder.

(c) At $x/D = 2.5$

(d) At $x/D = 4.5$

FIGURE 10.32: Surface pressure spectra and velocity spectra. (—) BART measurements. (■—■) new FSM convection scheme, (▲—▲) BCD20, (●—●) BCD.

10.3.4 Effect of Spanwise Domain Width

The baseline computational grid has a spanwise domain width of $L_z = 3D$. However, the experiments were performed using cylinders with a span of between $12D$ and $16D$, and show that the spanwise surface-pressure correlation does not go to zero until approximately $7D$. This indicates that three-dimensional effects are present in the flow. The question then arises, whether the spanwise domain width ($3D$) is sufficient to resolve the dominant three-dimensional effects in the flow, or whether a larger domain is required in order to improve the correlation with experiment. Therefore, the effect of the spanwise width of the computational domain is investigated in this section. For this purpose, simulations are performed on three different computational grids with different spanwise extents. The first grid has a spanwise width of $3D$ and 40 cells in the spanwise direction (FSM-3-40), the second grid has a spanwise width of $6D$ and 80 cells in the spanwise direction (FSM-6-80) and the largest grid has a spanwise width of $12D$ and 160 cells in the spanwise direction (FSM-12-160).

The distributions of mean-surface-pressure coefficient C_p and fluctuating-surface-pressure coefficient $C_{p'_{rms}}$ are shown in figure 10.33, for the upstream and downstream cylinder. The mean-surface-pressure distributions on both cylinders are virtually indistinguishable and are therefore not sensitive to the spanwise domain width. Small differences can be observed for the fluctuating-surface-pressure coefficient on the front cylinder. With increasing spanwise domain width, the intensity of surface-pressure fluctuations reduces, and hence provides better agreement with the reference data. However, the difference is very small and probably does not justify the considerably increased computational effort required for larger domains. The fluctuating-surface-pressure on the downstream cylinder is again predicted very similar by all domain widths.

The predictions of mean streamwise velocity and resolved two-dimensional turbulence kinetic energy k_{res}^{2D} on the centerline, $y/D = 0$, is shown in figure 10.34. The streamwise velocity distributions show only a very small sensitivity to the width of the computational domain. The FSM-12-160 predicts a slightly larger recirculation region and a slightly reduced maximum streamwise velocity magnitude, at around $x/D = 2.5$, in the gap between the cylinders. Similarly, the differences in resolved two-dimensional turbulence kinetic energy are also very small. The FSM-12-160 predicts a slightly lower magnitude of k_{res}^{2D} in the gap region, which is in better agreement with the reference data.

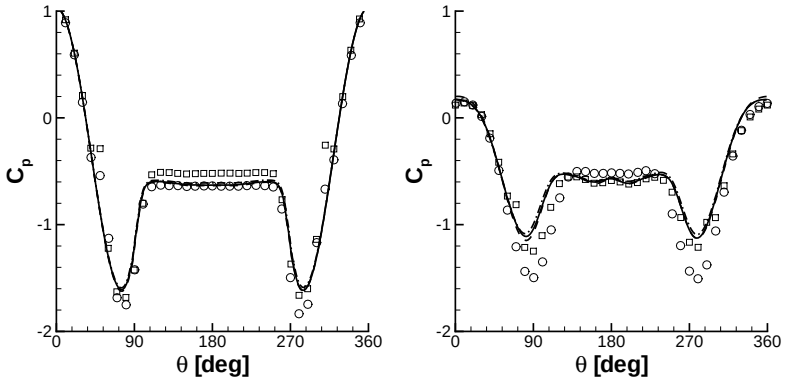

(a) C_p front cylinder. (b) C_p rear cylinder.

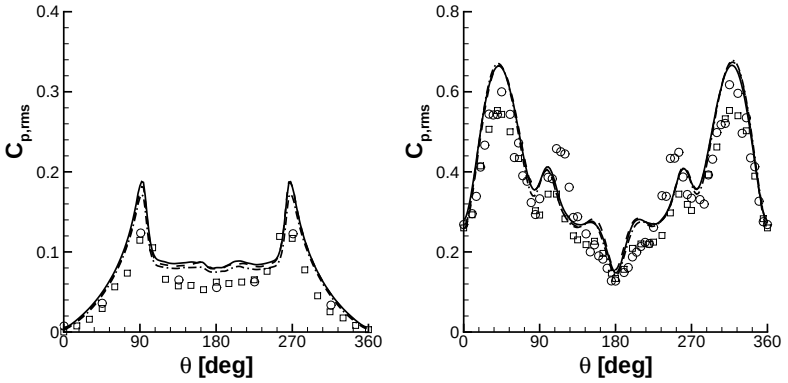

(c) $C_{p'_{rms}}$ front cylinder. (d) $C_{p'_{rms}}$ rear cylinder.

FIGURE 10.33: Mean-surface-pressure C_p and fluctuating-surface-pressure coefficient $C_{p'_{rms}}$. Front cylinder: (○) BART, (▫) QFF. Rear Cylinder: (○) BART, (▫) BART (rear cylinder tripped). (—) FSM-3-40, (- - -) FSM-6-80, (– · –) FSM-12-160.

Predictions of the spanwise surface-pressure correlation R_{pp} and PSD of surface-pressure at $\theta = 135°$, on the front and rear cylinder, are shown in figure 10.35. The spanwise correlation is an indicator of whether the resolution (cell count and domain extent) in the spanwise direction is adequate to reproduce the characteristic three-dimensional variation of the flow field.

Recall that the experiments were performed using cylinders with a span of between $12D$ and $16D$. The experiments show that the spanwise surface-pressure correlation does not go to zero until approximately $7D$. This indicates that three-dimensional effects are present in the flow. The spanwise surface-pressure correlation is well reproduced on both cylinder up to the spanwise distance of $z/D \approx 1.0$ for all domain widths. The spanwise domain width $3D$ of the FSM-3-40 case is clearly too small, since the spanwise correlation does not drop below $R_{pp} \approx 0.7$, and the flow is constrained by the periodic boundary conditions to maintain an artificially high correlation in the spanwise direction. The larger domains allows the spanwise

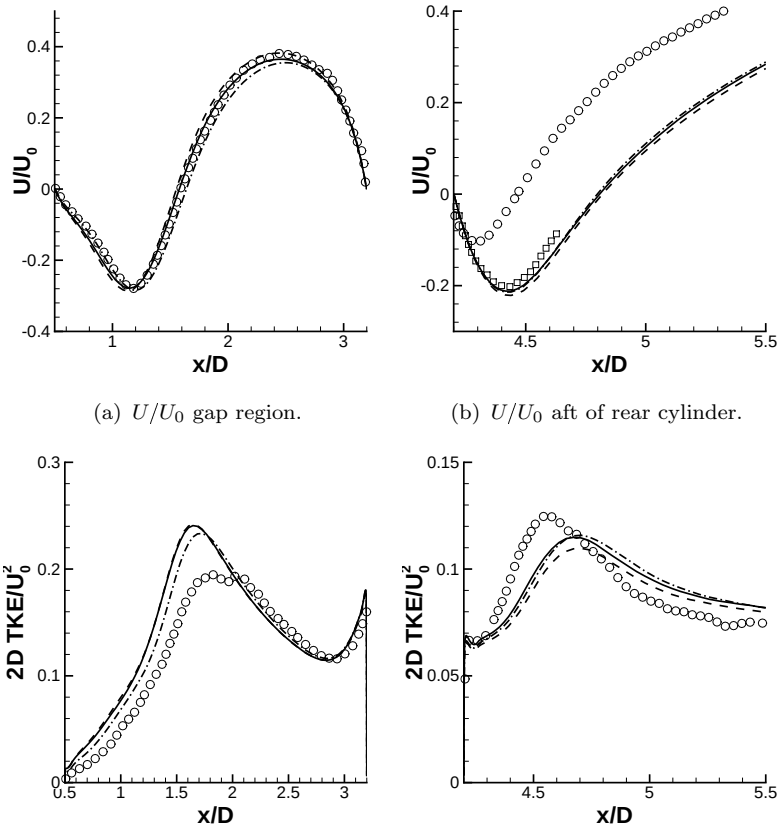

(a) U/U_0 gap region.

(b) U/U_0 aft of rear cylinder.

(c) TKE gap region.

(d) TKE aft of rear cylinder.

FIGURE 10.34: Streamwise velocity profiles U/U_0 and 2D TKE on the centreline ($y/D = 0$). (○) BART, (▫) BART (rear cylinder tripped). (—) FSM-3-40, (- - -) FSM-6-80, ($- \cdot -$) FSM-12-160.

correlation to reduce further. However, the spanwise correlation never drops below $R_{pp} \approx 0.5$ on both cylinders, even for the largest domain width of $12D$. This suggests that periodic boundary conditions are not fully justified, even for the largest domain width of $12D$. The same trend for the surface-pressure correlation is also observed in most of the simulations of the BANC I workshop participants, even on domain widths of $16D$ and with periodic boundary conditions in the spanwise direction. Only one simulation, with a domain width of $16D$, and where initially random suction and blowing on the cylinder walls is used to promote the development of vortex shedding, gave a surface-pressure correlation that goes to zero at $z/D \approx 7$ (see Lockard, 2011). It is not clear why the surface pressure remains highly correlated in the spanwise direction. Further insight could be gained by eliminating the uncertainty introduced by the periodic boundary conditions and by using a computational domain, which more closely resembles the experimental setup, i.e. a spanwise domain width of $12.4D$ or $16D$ with vertical side plates.

The PSD of surface pressure confirms the trend above for the fluctuating-surface-pressure distribution. On the upstream cylinder, the overall magnitude of surface-pressure fluctuations is reduced for increasing domain widths. The reduced intensity predicted on the FSM-12-160 grids is in better agreement with the reference data for the Strouhal number range $St \approx 0.3 - 0.7$. For Strouhal numbers $St > 0.7$, the intensity is too low and the FSM-3-40 grid provides better agreement with the reference data. On the downstream cylinder, the predictions are again similar for all domain widths. The results presented above clearly show that no systematic improvements are obtained for increasing domain widths. For this reason, the additional computational effort, required for larger spanwise domain widths, does not seem justified.

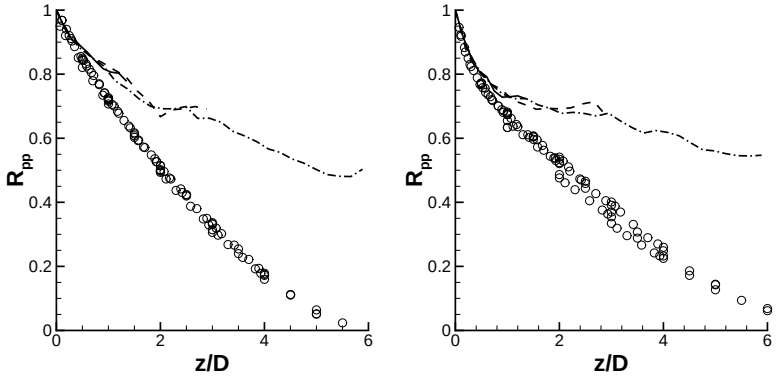

(a) R_{pp} at $\theta = 135^\circ$ on front cylinder (b) R_{pp} at $\theta = 135^\circ$ on rear cylinder

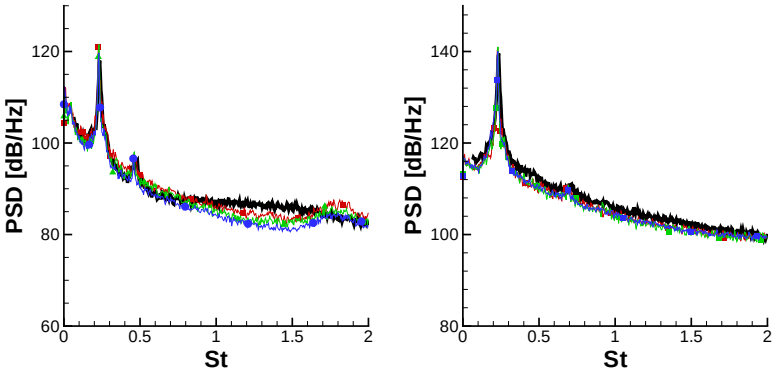

(c) At $\theta = 135^\circ$ front cylinder. (d) At $\theta = 45^\circ$ rear cylinder.

FIGURE 10.35: Spanwise surface-pressure correlation R_{pp} and PSD of surface pressure at the locations $\theta = 135^\circ$. (○) and (—) BART measurements. (—) and (■—■) FSM-3-40, (– – –) and (▲—▲) FSM-6-80, (– · –) and (●—●) FSM-12-160.

10.3.5 Effect of Grid Resolution

It is very tempting, particularly for two-dimensional configurations, to reduce the computational cost of a turbulence resolving simulation by using a small number of cells in the spanwise direction. The first objective of this section is to investigate the sensitivity of results with respect to the spanwise grid resolution. For this purpose simulations are performed on three different computational grids with different spanwise resolutions. All grids have a spanwise width of $6D$ and approximately 52000 cells in each xy-plane. The first grid has a spanwise resolution of 40 cells (FSM-6-40), the second grid has a spanwise resolution of 80 cells (FSM-6-80) and the finest grid has a spanwise resolution of 160 cells (FSM-6-160). The total cell counts are approximately 2×10^6, 4×10^6 and 8×10^6 cells, respectively. Note that the FSM-6-80 case results in almost isotropic cells in the gap region between both cylinder. In addition to this study, the effect of a finer resolution in the xy-plane is investigated by performing a simulation on a grid with 82000 cells in the xy-plane and 150 cells in the spanwise direction, which makes a total of approximately 12×10^6 cells. The spanwise domain width had to be reduced to $3D$ for this case in order to keep the computational cost affordable. The grid design of the finer grid is overall very similar to other grids used. The main difference is the increased grid density in the gap region and in the wake of the rear cylinder, and the use of a rectangular domain shape. The first wall-normal grid point is located at approximately $y^+ = 1$. This grid was kindly provided by M. Strelets from New Technologies and Services, St. Petersburg and will be referred to as the FSM-Strelets case. The Strelets grid is depicted in figure 10.36.

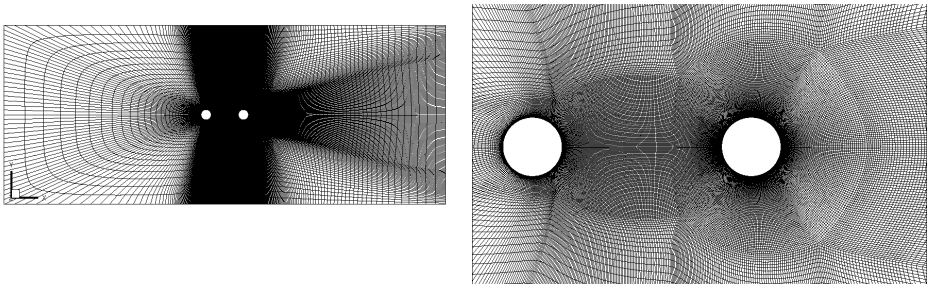

(a) xy-plane (b) xy-plane

FIGURE 10.36: Computational grid of Strelets.

The distributions of mean-surface-pressure coefficient C_p and fluctuating-surface-pressure coefficient $C_{p'_{rms}}$ are shown in figure 10.37 for both cylinders. The predictions of C_p obtained on the grid with the coarsest spanwise resolution (FSM-6-40)

clearly differ from the results obtained with a finer spanwise resolution. The coarse resolution case consistently predicts too high values of C_p on both cylinders, and hence shows the greatest departure from the reference data. The FSM-6-80 and FSM-6-160 cases show similar results in good agreement with the reference data. The FSM-Strelets case provides a slightly too low base pressure, and predicts the lowest values of C_p at the suction peaks at the locations $\theta = 90°$ and $\theta = 270°$. The fluctuating-surface-pressure coefficient shows a much more pronounced sensitivity to the grid resolution. The predictions of the fluctuating surface pressure on the upstream cylinder are improved when the resolution is doubled from the coarse (FSM-6-40) to the medium (FSM-6-80) spanwise resolution. It would be natural to expect, that a further grid refinement would again result in improved predictions, but surprisingly, a further increase in resolution shows the exact opposite trend. The two finest grids, FSM-6-160 and FSM-Strelets, predict the highest intensity of surface-pressure fluctuations and hence show the largest departure from the reference data. The same observation also holds for the downstream cylinder. It should be noted that the present results are only valid for the sepcific spanwise domain width used in the simulations. It may well be, that the trends observed here do not hold for simulations using a different spanwise domain width.

The predictions of mean streamwise velocity and resolved two-dimensional turbulence kinetic energy k_{res}^{2D} on the centerline, $y/D = 0$, are shown in figure 10.38. The coarse spanwise resolution case, FSM-6-40, shows a significantly too large recirculation zone behind the first cylinder, and a too low magnitude of maximum streamwise velocity in the gap region. Both fine resolution cases, FSM-6-160 and FSM-Strelets, show the exact opposite trend. The extent of the recirculation zone is predicted to be too small, and the maximum streamwise velocity in the gap region is too high compared to the corresponding measurement. Although, it is not clear why, the FSM-6-80 case is able to provide good agreement with reference data for the velocity distribution in the gap region between both cylinders. Note that the results presented in Garbaruk *et al.* (2010) using IDDES on the same grid as the FSM-Strelets case are qualitatively very similar to the results obtained here using the FSM-SST model. In order to shed some light on the possible cause of the large differences in the results, the instantaneous spanwise vorticity contours $\omega_z D/U_0$ are presented in figure 10.39. It is obvious that the too-large recirculation zone predicted on the FSM-6-40 grid is related to an overly large damping of the natural instability mechanisms in the free-shear layer, which results in a significantly delayed roll-up or breakdown of the free-shear layer. It seems likely that the overly large damping is a result of the increased turbulence model contribution

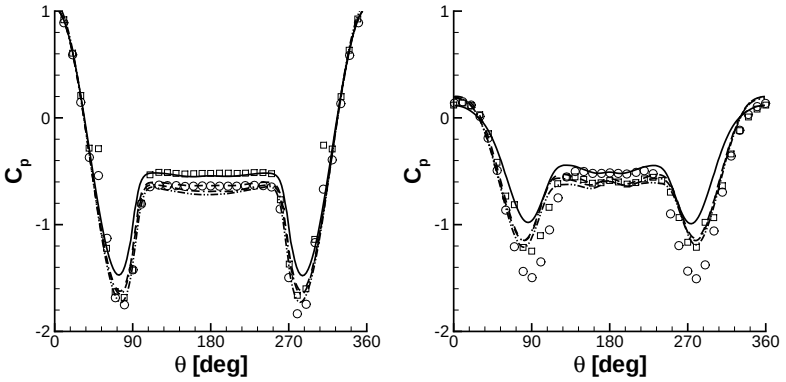

(a) C_p front cylinder. (b) C_p rear cylinder.

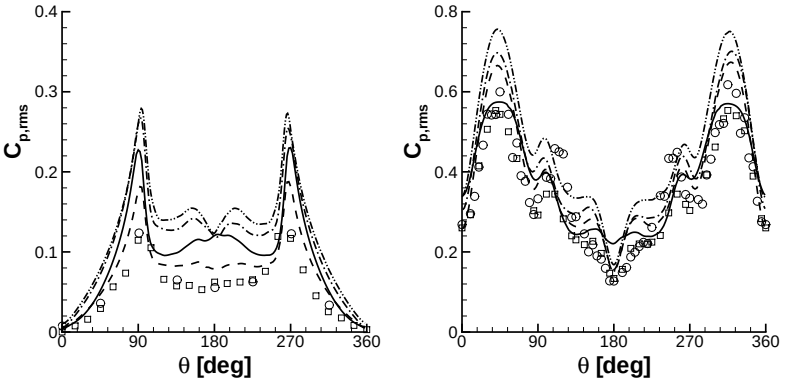

(c) $C_{p'_{rms}}$ front cylinder. (d) $C_{p'_{rms}}$ rear cylinder.

FIGURE 10.37: Mean-surface-pressure C_p and fluctuating-surface-pressure coefficient $C_{p'_{rms}}$. Front cylinder: (○) BART, (▫) QFF. Rear Cylinder: (○) BART, (▫) BART (rear cylinder tripped). (—) FSM-6-40, (- - -) FSM-6-80, (– · –) FSM-6-160, (– · ·–) FSM-Strelets.

through the turbulence model length scale $\Delta = (\Delta_x \Delta_y \Delta_z)^{1/3}$, which is increased by the factor $2^{1/3}$ compared to the FSM-6-80 case, which results in much better predictions. It should be noted at this stage that the O-grid topology of the computational grid makes it virtually impossible to provide a good numerical resolution of the free shear-layer in the direction perpendicular to the free-stream. The coarse resolution of the free-shear layer makes it difficult to accurately resolve the natural instability mechanisms of the shear layer and hence puts significant pressure on the turbulence model to provide the appropriate amount of damping in order to compensate the coarse numerical resolution. The FSM-6-80 case with the reduced turbulence model contribution through the length scale Δ seems to provide the correct amount of damping, such that the free-shear layer breaks down more quickly, and consequently results in the correct velocity distribution in the gap region. On the other hand, when the resolution in the spanwise direction is further refined, such as for the FSM-6-160 case, the damping of the turbulence model may actually

become insufficient to compensate the coarse resolution of the free-shear layer, and consequently results in a too quick breakdown of the shear layer and in a too short recirculation zone.

The distribution of turbulence kinetic energy in the gap region reflects the predictions of streamwise velocity. The FSM-6-40 case under-predicts the turbulence intensity in the gap region. The lower turbulence activity is less efficient in entraining high-speed free-stream fluid into the gap between the cylinders, which may shorten the recirculation zone and increase the maximum streamwise velocity in the gap. The FSM-6-160 and FSM-Strelets case predict excessive levels of turbulence intensity in the gap region, which results in enhanced entrainment of free-stream fluid and in a too short recirculation zone and too high magnitude of streamwise velocity in the gap region. The FSM-6-80 resolved intermediate levels of turbulence intensity, which are too high compared to the reference data, but seem to result in the correct amount of entrainment of free-stream fluid into the gap region, and good predictions of the velocity distribution.

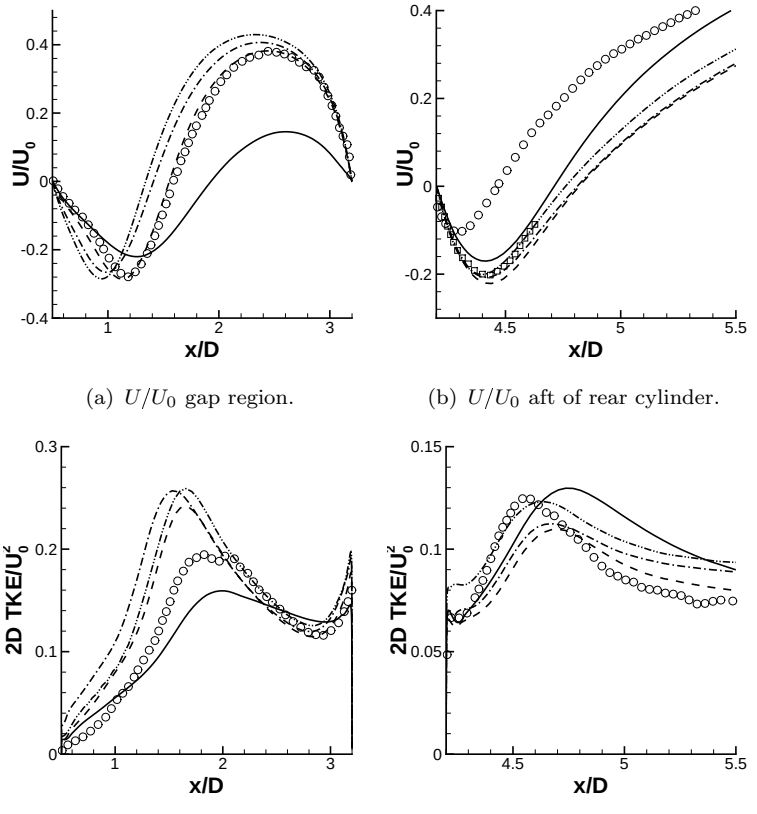

(a) U/U_0 gap region.

(b) U/U_0 aft of rear cylinder.

(c) TKE gap region.

(d) TKE aft of rear cylinder.

FIGURE 10.38: Streamwise velocity profiles U/U_0 and 2D TKE on the centreline ($y/D = 0$). (○) BART, (▫) BART (rear cylinder tripped). (—) FSM-6-40, (- - -) FSM-6-80, (— · —) FSM-6-160, (— · ·—) FSM-Strelets.

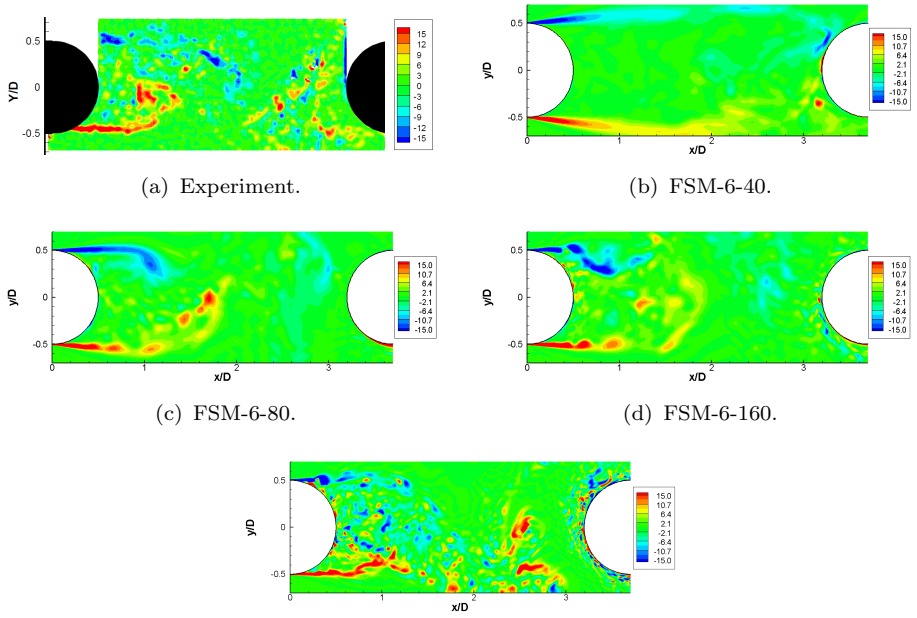

(a) Experiment.

(b) FSM-6-40.

(c) FSM-6-80.

(d) FSM-6-160.

(e) FSM-Strelets.

FIGURE 10.39: Normalised instantaneous spanwise vorticity $\omega_z D/U_0$.

Predictions of spanwise surface-pressure correlation R_{pp} and PSD of surface pressure at the locations $\theta = 135°$, on both cylinders, are shown in figure 10.40. All cases predict similar spanwise correlations, in good agreement with the corresponding measurements up to the location $z/D \approx 1$ on both cylinders. For $z/D > 1$, the departure in the predictions becomes more pronounced. The spanwise correlation on the upstream cylinder reaches an approximately constant value for $z/D > 2$ and does not drop below $R_{pp} \approx 0.7$ for all cases investigated here. The same behaviour is observed for the downstream cylinder, where FSM-6-80 and FSM-6-160 drop to an almost constant value of $R_{pp} \approx 0.7$. The correlation R_{pp} predicted by the FSM-6-40 case reduces to a slightly lower value of $R_{pp} \approx 0.6$. The plots of PSD of surface pressure confirms the predictions of $C_{p'_{rms}}$ discussed before. The two cases with the finest resolution, FSM-6-160 and FSM-Strelets, consistently show too high levels of surface-pressure fluctuations over almost the entire Strouhal number range. The FSM-6-40 case slightly under-predicts the magnitude of the peaks and primary vortex shedding frequency. In addition, the broadband content in the Strouhal number range $St \approx 0.4 - 1$ is over-predicted and the secondary peak in the spectra, which is present in all other cases, is absent in FSM-6-40. The FSM-6-80 case is able to predict the magnitude and frequency of the primary and secondary peaks, as well as the broadband content up to $St \approx 1$, in good agreement with the reference data, and hence provides the best overall performance. On the downstream cylinder, there is significantly less scatter in the results and the broadband content, as well

as the magnitude of the primary peak is well reproduced by all models. Only the FSM-6-40 case predicts a too low magnitude and frequency of the primary peak in the spectra. In addition, the secondary peak is absent in the results, and the broadband content is under-predicted compared to the other cases.

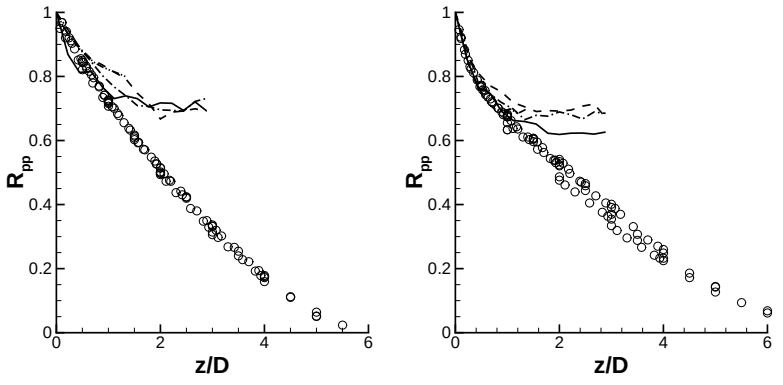

(a) R_{pp} at $\theta = 135^{\circ}$ on front cylinder (b) R_{pp} at $\theta = 135^{\circ}$ on rear cylinder

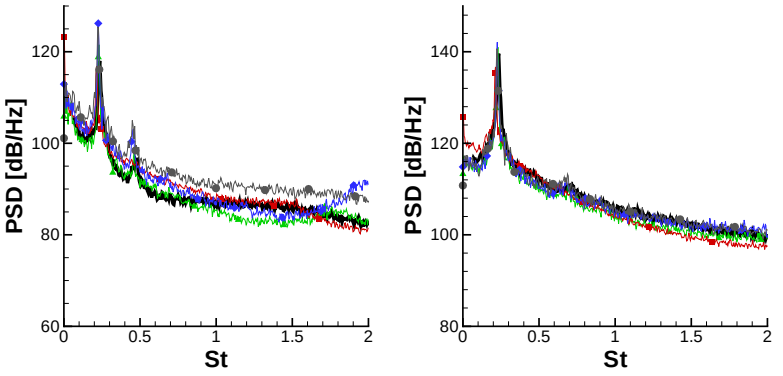

(c) At $\theta = 135^{\circ}$ front cylinder. (d) At $\theta = 45^{\circ}$ rear cylinder.

FIGURE 10.40: Spanwise surface-pressure correlation R_{pp} and PSD of surface pressure at the locations $\theta = 135^{\circ}$. (○) and (– – –) BART measurements. (■—■) FSM-6-40, (▲—▲) FSM-6-80, (◆—◆) FSM-6-160, (●—●) FSM-Strelets.

10.3.6 Sensitivity to the Turbulence Model

The sensitivity of results with respect to the underlying RANS model is investigated. For this purpose, simulations are performed using the FSM-SST, FSM-EASM and FSM-φ-α-EASM formulations. In addition, results obtained by IDDES and SAS, based on the k-ω-SST model, are also included in the comparison with the reference data. Note that the SAS model completely failed to resolve turbulence fluctuations in the three-dimensional diffuser case, since the instability mechanisms were insufficient to trigger flow unsteadiness. Nevertheless, the SAS model contains some interesting and unique features, and since SAS is expected to perform much better in the present case, due to the presence of strong instability mechanisms, it is included in the comparison. The FSM models are used in conjunction with the new hybrid FSM convection scheme; IDDES and SAS use the hybrid convection scheme of Travin *et al.* (2004*b*). All simulations are performed on the baseline computational grid with a spanwise width of $3D$ and 40 cells in the spanwise direction.

Instantaneous Flow Field

Instantaneous snapshots of the flow fields are visualised in figure 10.41 using iso-contours of the second invariant of the velocity gradient tensor $Q = \frac{1}{2}\left(\Omega^*_{ij}\Omega^*_{ij} - S^*_{ij}S^*_{ij}\right)$. This quantity can be used to identify coherent or vorticity-dominated structures in the flow field. It is evident, that all hybrid RANS/LES methodologies show the presence of resolved turbulence structures in the flow field. Nevertheless, there are some visible differences in the results obtained from the different simulations. The FSM-SST model shows the most rapid growth of shear layer instability. All other turbulence models predict a somewhat delayed onset of shear layer instability and the shear layer predicted by the FSM-EASM model does not show much resemblance to the typical Kelvin-Helmholtz instability mechanisms. Most of the flow fields show the presence of streamwise vortices in the gap region, with a characteristic spanwise extent of 2-3 cell widths Δ_z. These structures seem to be less pronounced in the predictions of the FSM-EASM and FSM-φ-α-EASM models, which are both based on a non-linear stress-strain relationship, and which exhibit more chaotic, irregular vortical structures in the flow field. The IDDES and SAS turbulence models show in general, somewhat larger vortical structures compared to the FSM approaches. This indicates a slightly higher contribution of the turbulence model, which effectively eliminates the smaller-scale turbulence structures observed in the predictions of the FSM models. The predictions of the flow field in the wake of the downstream cylinder is similarly resolved by all turbulence models. Only the FSM-EASM is able to maintain turbulence structures much farther downstream of the rear cylinder. This

is associated with the variable constant C_μ^{eff} in the eddy-viscosity relation, which reduces to $C_\mu^{eff} \approx 0.04 - 0.05$ for the EASM model.

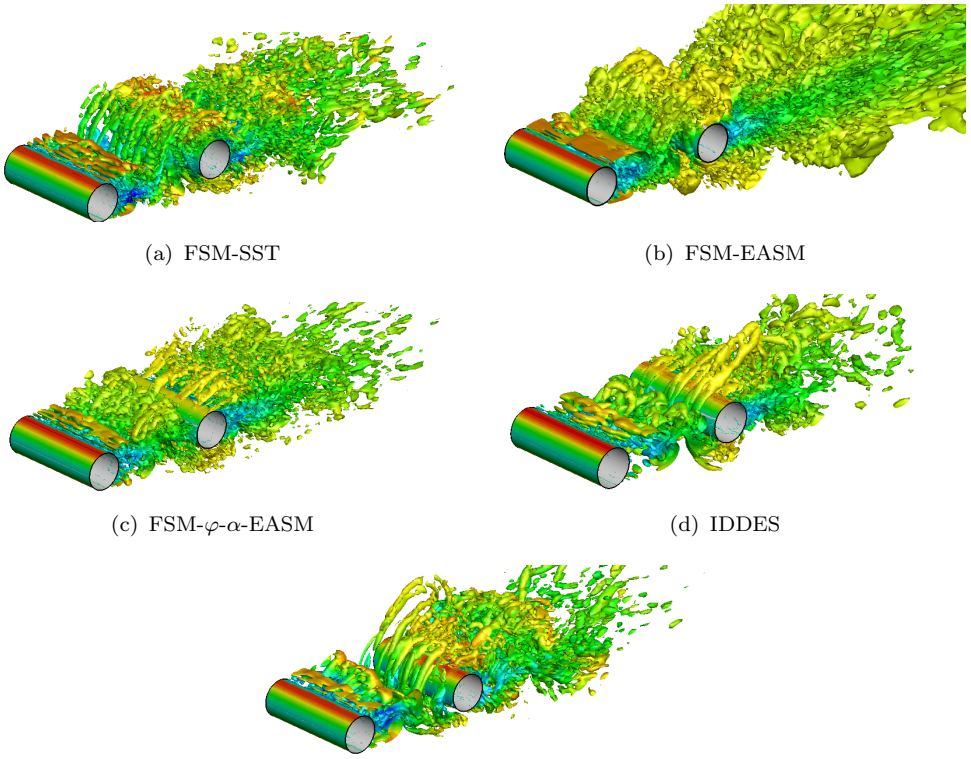

(a) FSM-SST (b) FSM-EASM

(c) FSM-φ-α-EASM (d) IDDES

(e) SAS

FIGURE 10.41: Iso-contours of $Q = 1.5U_0^2/D^2$, coloured by the instantaneous streamwise velocity.

These observations are confirmed in figure 10.42, which shows contour plots of instantaneous spanwise vorticity $\omega_z D/U_0$, obtained from the simulations and PIV data from the experiment. It is again clearly visible, that the FSM models are able to resolve finer-scale turbulence structures in the gap region and give better overall agreement with the PIV reference data, compared to the IDDES and SAS models. Despite the fairly coarse resolution of the free-shear layer, the development of Kelvin-Helmholtz type instabilities can be observed in the results from IDDES, FSM-SST and FSM-φ-α-EASM.

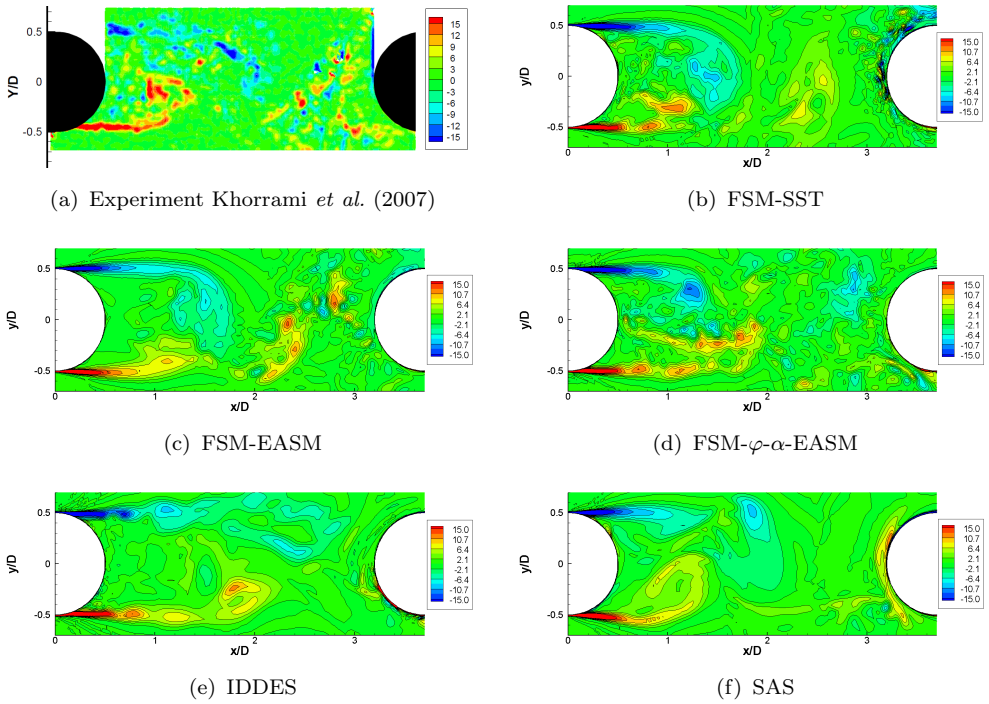

(a) Experiment Khorrami *et al.* (2007)

(b) FSM-SST

(c) FSM-EASM

(d) FSM-φ-α-EASM

(e) IDDES

(f) SAS

FIGURE 10.42: Normalised instantaneous spanwise vorticity $\omega_z D/U_0$.

Alternative Mean Flow Field

In has already been mentioned in the introduction to this test case, that the distance between the cylinders sets the type of interaction. Most of the computational grids and turbulence models used in this work converge to a state where vortices are being shed from the upstream cylinder. However, the simulation using IDDES converges to an alternative state where the vortex shedding from the upstream cylinder is suppressed, and the shear layer re-attaches to the downstream cylinder. Interestingly, the IDDES simulation converges to the first state with vortex shedding from the upstream cylinder for the first 120000 iterations, or $380D/U_0$ time units. After a transition phase and a simulation time larger than $500D/U_0$ time units, IDDES converges to a second state, with suppressed vortex shedding from the upstream cylinder. The resulting mean-flow fields of both states and instantaneous spanwise vorticity contours are presented in figure 10.43. The second state has also been observed in a simulation using the FSM-SST model on a grid with finer spanwise resolution, and has also been reported by some participants of the BANC I workshop (see Lockard, 2011). The suppression of vortex shedding from the upstream cylinder is usually observed for smaller gap spacings than used here. Nevertheless, according to Lockard (2011), some experiments conducted with the same gap spacing of $3.7D$ at different Reynolds number and spanwise lengths of the cylinders have also shown the alternative state predicted by the IDDES model. It is

not clear what causes the transition to the alternative state but, it is expected, that a range of parameters such as boundary conditions, computational grid, turbulence model and numerical discretisation contribute.

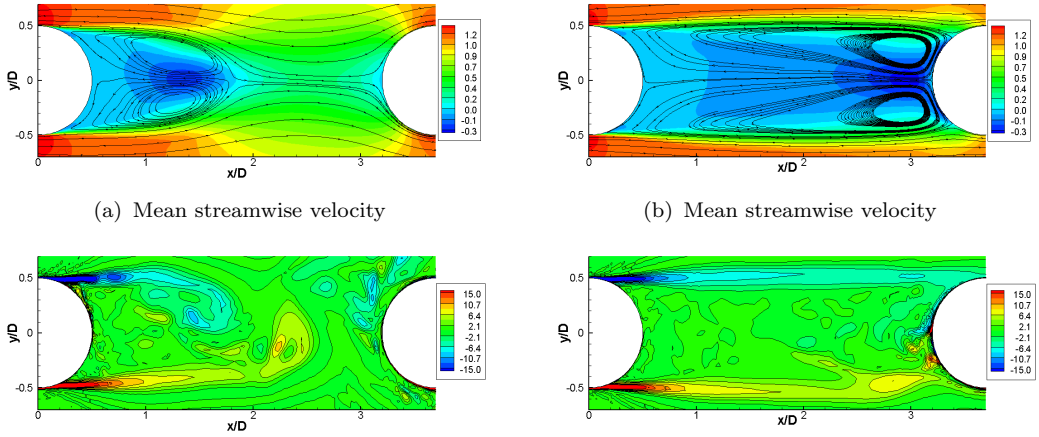

(a) Mean streamwise velocity

(b) Mean streamwise velocity

(c) Instantaneous spanwise vorticity $\omega_z D/U_0$

(d) Instantaneous spanwise vorticity $\omega_z D/U_0$

FIGURE 10.43: Alternative mean flow states.

Lift and Drag

The predicted drag coefficient $C_D = F_x/(0.5\rho U_0 A)$ is summarised in table 10.1, together with the primary vortex-shedding frequency and rms-values of fluctuating lift and drag coefficients. The primary vortex-shedding frequency measured in the experiment is $178[Hz]$, which corresponds to a Strouhal number of $St = 0.231$. Unfortunately, force measurements are not available as a reference. It is surprising that only the FSM-SST, FSM-EASM and SAS models are able to accurately predict the primary-vortex shedding frequency observed in the experiment. The FSM-φ-α-EASM predicts a Strouhal number approximately half of the measured value and IDDES predicts a Strouhal number that is too high, $St = 0.279$. In addition, the drag coefficient C_D, on the upstream cylinder as well as the $C_{L'_{rms}}$, are too small on both cylinders. Note that the IDDES results are evaluated for the first $380D/U_0$ time units only where the vortex-shedding from the upstream cylinder is still present in the simulation. The differences observed for the IDDES model can possibly be explained by the location of the separation point on the first cylinder. The IDDES model predicts the separation point of the mean flow at $\theta \approx 102°, 258°$, whereas, for example, the FSM-EASM predicts earlier separation at $\theta \approx 96°, 264°$. Due to the delayed separation predicted by the IDDES model, the development of the wake exhibits the behaviour of a wake at an effectively higher Reynolds number, which, according to Schewe (1983), shows a similar trend to what is observed here, namely an increase in vortex-shedding frequency and a reduction in drag coefficient. The

		upstream cylinder			downstream cylinder		
Model	St	C_D	$C_{L'_{rms}}$	$C_{D'_{rms}}$	C_D	$C_{L'_{rms}}$	$C_{D'_{rms}}$
FSM-SST	0.228	0.616	0.139	0.029	0.419	0.695	0.098
FSM-EASM	0.234	0.626	0.148	0.022	0.383	0.695	0.098
FSM-φ-α-EASM	0.101	0.559	0.128	0.023	0.353	0.523	0.070
IDDES	0.279	0.397	0.036	0.017	0.409	0.425	0.059
SAS	0.228	0.614	0.171	0.040	0.415	0.665	0.101

TABLE 10.1: Lift and drag coefficients.

cause for the delayed separation of the IDDES model is not quite clear, since the FSM-SST and SAS models, which are based on the same underlying RANS model, do not show this behaviour. There might also be a connection between the delayed separation and the occurrence of the alternative mean flow state in the predictions of the IDDES model. An investigation of this issue is left for future investigations. The separation point predicted by the FSM-φ-α-EASM model is the same as for the FSM-EASM model, and can therefore not be used to explain the failure to predict the correct vortex-shedding frequency. Unfortunately, a close inspection of the flow field and turbulence quantities did not reveal any possible sources which would explain the failure of the FSM-φ-α-EASM model.

Mean Flow Field

The distributions of the mean-surface-pressure coefficient C_p and fluctuating-surface-pressure coefficient $C_{p'_{rms}}$ are shown in figure 10.44. All turbulence models are able to predict the surface-pressure coefficient in good agreement with the reference data. The IDDES model shows the most pronounced suction peaks at $\theta \approx 90°$ and $\theta \approx 270°$ and also predicts a somewhat too high base pressure magnitude in the recirculation region on both cylinders. On the upstream cylinder, all other turbulence models reproduce the base pressure level observed in the BART facility, and predict a magnitude of the suction peaks, which matches the data from the QFF facility. On the downstream cylinder, the simulations are in good agreement with the reference data, and reproduce the measurement of the BART facility, which included a boundary-layer trip on the downstream cylinder. This is not surprising, since the fully turbulent simulation approach is not able to correctly predict the transitional flow occurring in the experiment without tripping of the boundary layer.

The predictions of fluctuating-surface-pressure coefficient on the upstream cylinder reflects the predictions of the rms-values of lift and drag coefficient discussed above. The IDDES model, which showed the lowest values of $C_{L'_{rms}}$ and $C_{D'_{rms}}$, also consistently predict a too low magnitude of surface-pressure fluctuations $C_{p'_{rms}}$. In addition, the location of the peak values, which approximately correspond to the separation location, are too far downstream and confirm the delayed separation. Similarly, the SAS model show the highest levels of $C_{L'_{rms}}$ and $C_{D'_{rms}}$ and hence significantly over-predicts the intensity of surface-pressure fluctuations. All FSM models predict the same results of $C_{p'_{rms}}$ in the separated flow region and show a slightly too high magnitude compared to the reference data. An interesting trend can be observed for the intensity of the peak values predicted by the FSM models. The arguably simplest underlying RANS model, FSM-SST, shows the most pronounced over-prediction of the peak values compared to the other FSM models. The FSM-EASM model shows reduced magnitude and the FSM-φ-α-EASM an even lower magnitude, which is in excellent agreement with the reference data. Concerning the predictions of fluctuating-surface-pressure coefficient on the downstream cylinder, all models are able to predict the correct location of the first and dominant peak, at $\theta \approx 45°, 315°$. These peaks correspond to the impingement points of the unsteady wake from the upstream cylinder. Nevertheless, the magnitude of fluctuating-surface-pressure shows significant differences among the models. The boundary-layer tripping on the downstream cylinder not only reduces the magnitude of the secondary peaks but also shifts the location of the peaks, which are associated with the separation location, further upstream compared to the untripped case. All simulations more closely reproduce the BART data with boundary-layer tripping on the downstream cylinder. The IDDES model predicts the lowest intensity of surface-pressure fluctuations around the impingement points but predicts the second and smaller peak, at $\theta \approx 135°, 225°$, in excellent agreement with the reference data. The FSM-φ-α-EASM model predicts the magnitude of surface-pressure fluctuations at the impingement point in best agreement with the reference data, but shows too low levels of $C_{p'_{rms}}$ and the largest departure around the separation points, and in the recirculation region. In addition, the secondary peaks, and with that the locations of the separation points, is predicted farther upstream compared to reference data, and predictions of the other turbulence models. The FSM-EASM shows the most pronounced peaks at the impingement locations but predicts realistic values of $C_{p'_{rms}}$ at the separation points and in the recirculation region. The FSM-SST and SAS models predict almost identical results with too intense pressure fluctuations around the impingement points and the highest magnitude of $C_{p'_{rms}}$ at the separation points and in the recirculation region.

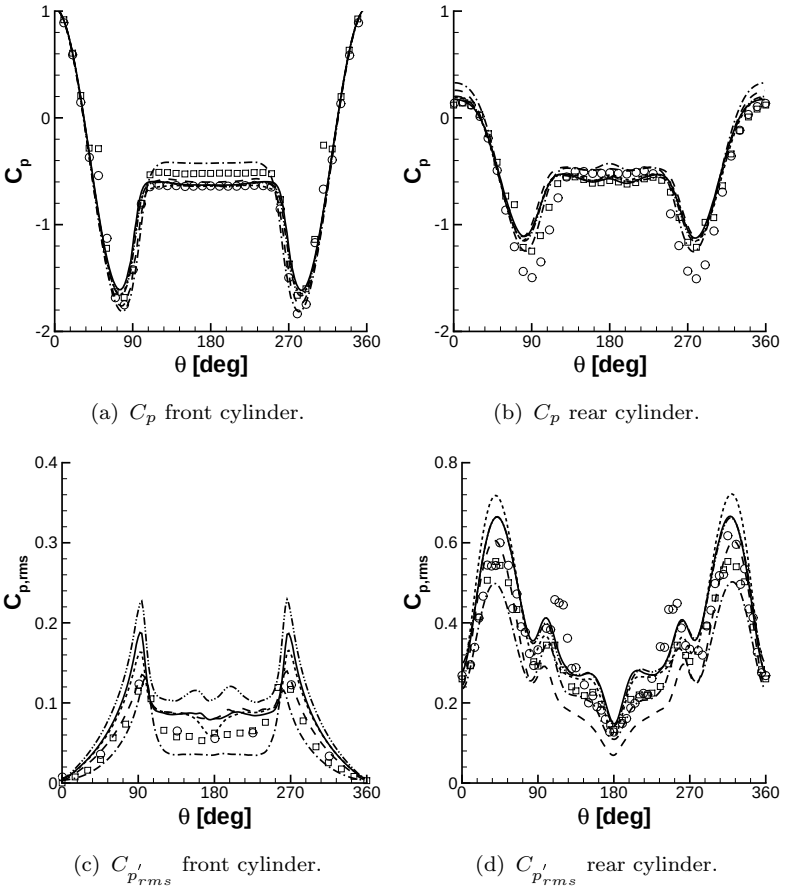

(a) C_p front cylinder. (b) C_p rear cylinder.

(c) $C_{p'_{rms}}$ front cylinder. (d) $C_{p'_{rms}}$ rear cylinder.

FIGURE 10.44: Mean-surface-pressure C_p and fluctuating-surface-pressure coefficient $C_{p'_{rms}}$. Front cylinder: (○) BART, (▫) QFF. Rear Cylinder: (○) BART, (▫) BART (rear cylinder tripped). (—) FSM-SST, (- - -) FSM-EASM, (– – –) FSM-φ-α-EASM, (– · –) IDDES, (– · ·–) SAS.

The predictions of mean streamwise velocity and resolved two-dimensional turbulence kinetic energy k_{res}^{2D} on the centerline, $y/D = 0$, are shown in figure 10.45. In addition, contour plots of turbulence intensity $I_x = \overline{u'}_{rms}/U_0$ and $I_y = \overline{v'}_{rms}/U_0$ are shown in figures 10.46 and 10.47. The velocity in the gap region clearly show a large sensitivity to the turbulence model. The FSM-SST model predicts the velocity distribution in excellent agreement with reference data. The FSM models based on more sophisticated RANS models, i.e. FSM-EASM and FSM-φ-α-EASM, show a somewhat too small recirculation zone, but show good agreement for the maximum reverse flow intensity occurring at $x/D \approx 1.2$ in the recirculation region. In addition, the maximum streamwise velocity in the gap region is over-predicted. The same observation holds for the SAS model with the difference, that the maximum streamwise velocity at approximately $x/D \approx 2.5$ is lower and hence in better agreement with the reference data. The IDDES model shows exactly the opposite trend;

the extent of the recirculation zone behind the upstream cylinder is too large and the maximum streamwise velocity in the gap region is under-predicted. Concerning the velocity distribution downstream of the rear cylinder, FSM-SST, IDDES and SAS provide similar predictions in excellent agreement with the reference data. Note that the simulations match the BART data with the boundary-layer tripped on the downstream cylinder. The FSM-EASM and FSM-φ-α-EASM models both over-predict the extent of the recirculation region behind the rear cylinder. This is associated with the mean separation point being slightly too far upstream, which consequently changes the trajectory of the free-shear layer and hence results in the too large recirculation zone.

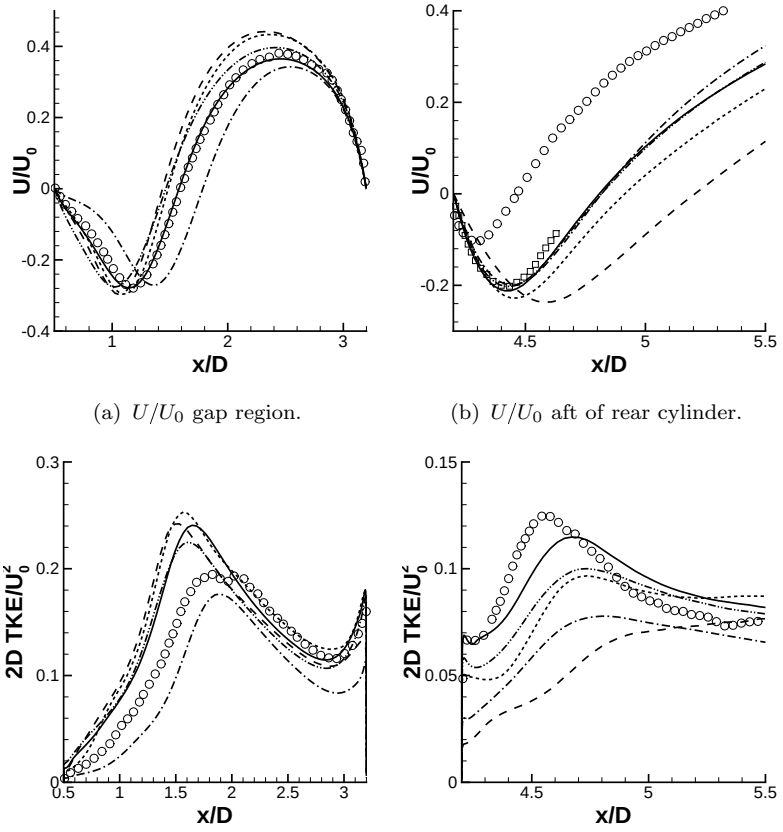

(a) U/U_0 gap region.

(b) U/U_0 aft of rear cylinder.

(c) TKE gap region.

(d) TKE aft of rear cylinder.

FIGURE 10.45: Streamwise velocity profiles U/U_0 and 2D TKE on the centreline ($y/D = 0$). (○) BART, (▫) BART (rear cylinder tripped). (—) FSM-SST, (- - -) FSM-EASM, (– – –) FSM-φ-α-EASM, (– · –) IDDES, (– · · –) SAS.

The resolved turbulence kinetic energy in the gap region is predicted very similar by most hybrid RANS/LES turbulence models. Only the IDDES model predicts much lower levels of resolved turbulence kinetic energy throughout the gap region. The low intensity of velocity fluctuations results in less efficient entrainment of

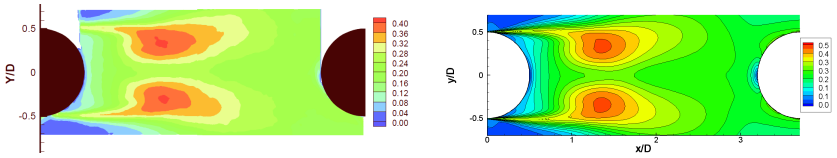

(a) Experiment. (b) FSM-SST.

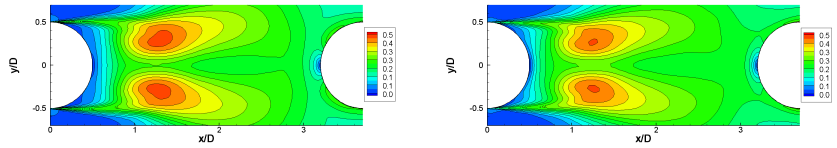

(c) FSM-EASM. (d) FSM-φ-α-EASM.

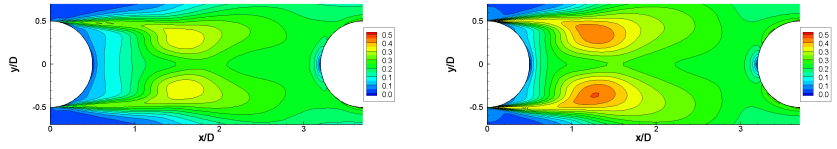

(e) IDDES. (f) SAS.

FIGURE 10.46: Turbulence intensity $I_x = \overline{u'}_{rms}/U_0$.

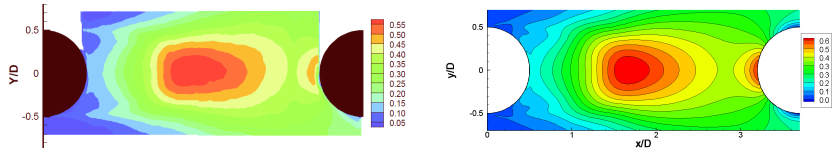

(a) Experiment. (b) FSM-SST.

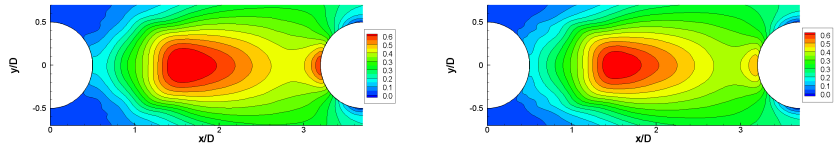

(c) FSM-EASM. (d) FSM-φ-α-EASM.

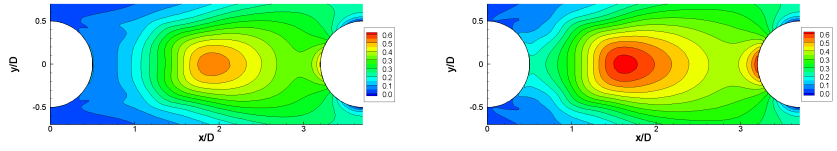

(e) IDDES. (f) SAS.

FIGURE 10.47: Turbulence intensity $I_y = \overline{v'}_{rms}/U_0$.

high-speed fluid from the free-stream, which contributes to the over-prediction of the size of the recirculation zone behind the upstream cylinder. Nevertheless, the IDDES model predicts the correct location of maximum turbulence intensity in the gap region. All other turbulence models predict the location of maximum turbulence kinetic energy too far upstream and over-predict the magnitude of maximum

turbulence kinetic energy, compared to the reference data. The higher intensity of velocity fluctuations is more efficient in entraining fluid from the free-stream, which may add to the shortening of the recirculation zone behind the upstream cylinder. Even though FSM-SST follows the same trend, the resulting velocity distribution in the gap region agrees very well with the reference data. The predictions of resolved turbulence kinetic energy behind the downstream cylinder shows significantly more scatter. All turbulence models show the same tendency of too low levels of turbulence intensity up to $x/D \approx 4.8$, and the location of maximum turbulence intensity is predicted too far downstream compared to the reference data. It should be noted that the measurements correspond to the BART data without tripping the boundary layer on the downstream cylinder. It can be expected that measurements including a boundary-layer trip on the downstream cylinder will be different in terms of the overall magnitude and location of maximum turbulence kinetic energy. Nevertheless, FSM-SST predicts overall the highest levels of turbulence kinetic energy and hence shows the best agreement with the reference data. The FSM-EASM and FSM-φ-α-EASM models predict much lower magnitudes of turbulence kinetic energy, and the FSM-φ-α-EASM shows the greatest departure from the reference data. Downstream of the rear cylinder, the departure observed in the predictions of turbulence kinetic energy by the FSM-EASM and FSM-φ-α-EASM model seem to correlate with the departure of the mean-velocity distribution from the reference data. The IDDES and SAS models both significantly under-predict the turbulence kinetic energy, but predict the mean-velocity distribution downstream of the rear cylinder in good agreement with the reference data.

The total (resolved plus modelled) shear stress is discussed next. Figure 10.48 shows two profiles of total shear stress, at the locations $x/D = 1$ and $x/D = 2.7$, in the gap between the cylinders. The region of interest at the first location, $x/D = 1$, is the free-shear layer at approximately $y/D \approx 0.5$. The highest levels of shear stress are predicted by the SAS and FSM-φ-α-EASM models. The high levels of shear stress are also reflected in the predictions of streamwise velocity in the gap region. Both model show the smallest extent of the recirculation behind the upstream cylinder. The FSM-EASM shows reduced levels of shear-stress in the free-shear layer, which are in good agreement with the experimental data. Nevertheless, the extent of the recirculation zone is still somewhat too small. The FSM-SST predicts levels of shear stress, which are slightly smaller compared to the corresponding measurement. However, the velocity distribution in the gap region shows the best agreement with the reference data of all models. The IDDES model shows the most pronounced

under-prediction of shear stress, which consequently results in the largest recirculation zone. Further downstream, at the location $x/D = 2.7$, the scatter in the results is significantly reduced. All models under-predict the peak-value of shear stress at the location $y/D \approx 4.0$. The FSM-SST predicts overall the highest level of shear stress, and hence shows the best agreement with the reference data. The peak-values of shear stress predicted by the FSM-EASM, IDDES and SAS models are almost identical. However, the peak-value predicted by the IDDES model is located much closer to the centreline. The FSM-φ-α-EASM now predicted the lowest level of shear stress. It is not clear why the shear stress of the FSM-φ-α-EASM has significantly reduced from the locations $x/D = 1$, where it was too high, to the location $x/D = 2.7$.

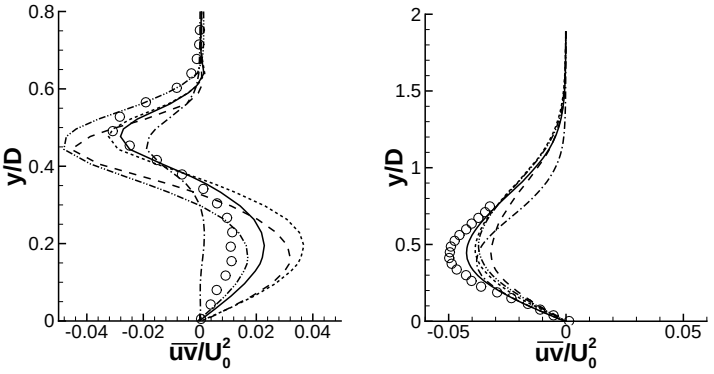

FIGURE 10.48: Profiles of total (resolved plus modelled) shear-stress. Left: at $x/D = 1$ and right: at $x/D = 2.7$. (—) FSM-SST, (- - -) FSM-EASM, (– – –) FSM-φ-α-EASM, (– · –) IDDES, (– · ·–) SAS.

Predictions of spanwise surface-pressure correlation R_{pp} and PSD of surface pressure are shown in figure 10.49. The IDDES model allows the spanwise surface-pressure correlation to drop to approximately $R_{pp} \approx 0.7$ on the first cylinder, and hence provides good agreement with the reference. In the predictions of all other cases, the spanwise correlation only drops to $R_{pp} \approx 0.8$ and remains too high, compared to the corresponding measurements. The correlation of the FSM-SST and SAS models are almost indistinguishable. The FSM-EASM and FSM-φ-α-EASM show overall the highest level of correlation R_{pp}. The high levels of correlation is also reflected in the iso-contour plots of Q in figure 10.41, where the free-shear layer shows a strong two dimensionality with almost no variation in the spanwise direction. On the downstream cylinder, the IDDES model again shows a rapid drop of R_{pp} and reaching levels much below the corresponding measurements. The best agreement is achieved by the SAS model, which nicely follows the trend observed in the experiment. The results of the FSM-SST model is of a similar quality, however, the correlation R_{pp} remains somewhat too high. The more advanced FSM-EASM and FSM-φ-α-EASM

models show least agreement with the reference data, and the spanwise correlation remains significantly too high over the cylinder span.

The PSD of surface pressure is discussed next. The results of the IDDES and FSM-φ-α-EASM models are not included in the comparison, since both models did not reproduce the correct primary vortex shedding and the results are largely in error. On the upstream cylinder, all three turbulence models, FSM-SST, FSM-EASM and SAS, show good agreement around the primary vortex shedding frequency, with a small over-prediction of the peak magnitude. The simulations are also able to predict the secondary peak at $St \approx 0.5$. The secondary peak is best predicted by the FSM-SST model, with both other models showing a significantly too high peak magnitude. The broadband contribution for $St > 1$ is also best resolved by FSM-SST. Both FSM-EASM and SAS under-predict the broadband levels by quite some margin. The predictions on the downstream cylinder show significantly less scatter compared to the upstream cylinder. All three turbulence models show good agreement around the primary vortex shedding frequency. In addition, all models are able to resolve the secondary peak, but under-predict the broadband levels. The FSM-SST model gives the highest broadband levels, and hence is in best overall agreement with the reference data.

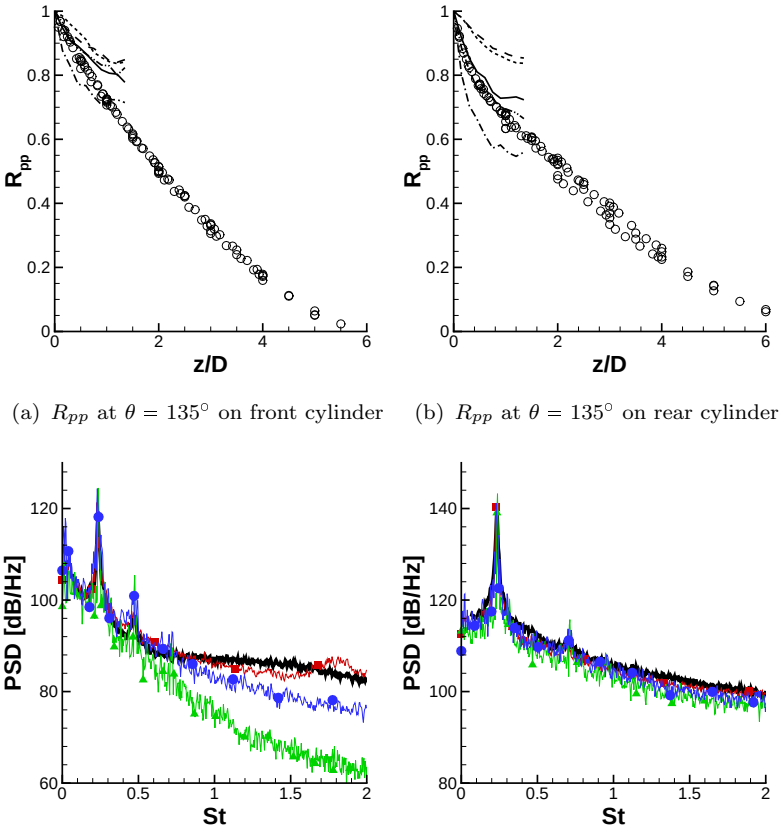

(a) R_{pp} at $\theta = 135^\circ$ on front cylinder

(b) R_{pp} at $\theta = 135^\circ$ on rear cylinder

(c) At $\theta = 135^\circ$ front cylinder.

(d) At $\theta = 45^\circ$ front cylinder.

FIGURE 10.49: Spanwise surface-pressure correlation R_{pp} and PSD of surface pressure. (○) and (—) BART measurements. (—) and (▪—▪) FSM-SST, (- - -) and (▲—▲) FSM-EASM, (– – –) FSM-φ-α-EASM, (– · –) IDDES, (– · ·–) and (●—●) SAS.

10.3.7 Summary

The simulations clearly demonstrate the advantages of a hybrid convection discretisation scheme. No results could be obtained with the unbounded CDS scheme, and the bounded TVD schemes significantly over-predicts the size of the recirculation zone behind the upstream cylinder. The hybrid FSM scheme, with a flow-dependent flux blending function, is able to deliver results in good agreement with the reference data. The tandem cylinder case is a difficult case to predict accurately, due to a high sensitivity of the flow to the resolution of the computational grid and turbulence model. A particularly high sensitivity of results is observed with respect to the resolution of the computational grid in the spanwise direction, as well as to the resolution in the xy-plane. Too-coarse spanwise resolution completely fails to provide reasonable predictions for the mean-flow field. Spanwise resolution, which yields approximately isotropic cells in the gap region between the cylinders, is found to provide the best results. The grids with finer resolution in the spanwise direction and with finer resolution in the xy-plane are found to deteriorate the results, compared to the coarser baseline grid. This seems not-intuitive, but may point towards a favourable cancellation of errors induced by the coarse grid and turbulence modelling. However, further testing is required to confirm this hypothesis. It was also argued that the definition of the turbulence length scale Δ may contribute to this behaviour and that the turbulence model might benefit from redefinition of this length scale. On the other hand, most results are insensitive to the spanwise domain width. This is linked to a spurious strong correlation of the flow in the spanwise direction, which does not completely vanish on the largest spanwise domain of $12D$. With increasing spanwise domain width, the intensity of surface-pressure fluctuations on the upstream cylinder reduces somewhat, and hence provides improved agreement with the reference data. Nevertheless, the difference is not pronounced enough to justify the increased computational cost associated with large spanwise domain widths. The flow is also very sensitive to the turbulence model used. The IDDES model transitioned after long simulation times to an alternative mean-flow state, where the vortex shedding is suppressed from the upstream cylinder. The FSM approach based on the most sophisticated RANS model predicts the fundamental vortex-shedding frequency of half the experimental value. The FSM-SST model provides the best agreement with reference data on the baseline computational grid followed by the SAS and FSM-EASM models.

Chapter 11

Summary and Outlook

11.1 Summary

A summary of the most important achievements and findings of this study is given in the following.

- The performance of two- and three-dimensional EASM closures is assessed on a range of different test cases, ranging from simple channel flow to massively separated flows and to complex three-dimensional flows. Based on these test cases, a fairly clear picture of the performance of the baseline EASM closure emerges. It is shown, that two- and three-dimensional EASM closures are capable of providing improved predictions for the three-dimensional flow in a three-dimensional diffuser, compared to turbulence models based on a linear stress-strain relationship. The more realistic predictions of the mean-velocity field are a consequence of improved predictions of the Reynolds-stress and anisotropy tensors. Nevertheless, the EASM closure shows deficiencies in predicting the correct near-wall behaviour of turbulence kinetic energy and the Reynolds-stress and anisotropy tensors when compared to the experimental reference data. For the massively separated flow over the NASA hump configuration, the mean-velocity field predicted by the EASM is not improved over more simple liner two-equation models, despite improved predictions of normal-Reynolds-stress components One of the shortcomings of the EASM is attributed to the behaviour of the variable C_{μ}^{eff}, which depends on the stain- and rotation-rate, and which reduces the contribution of the linear term in the stress-strain relationship to the shear stress in the free-shear layer, and

consequently over-predicts the extent of the recirculation zone. An important conclusion drawn from the test cases considered in this work is that the two- and three-dimensional formulations of the EASM closure predict equivalent or very similar results in three-dimensional flows. The three-dimensional EASM closure is not found to give improved, or significantly different, predictions, which suggests that the considerable additional numerical expense compared to the two-dimensional formulation is not justified in those cases.

- Several strategies and modifications are introduced to the baseline EASM, which aim at improving the predictions of the Reynolds-stress and anisotropy tensor close to the wall. The free parameters appearing in the near-wall-anisotropy modifications and in the damping function for the turbulence kinetic energy dissipation rate are optimised to provide the correct behaviour for planar channel flows. The modifications achieve improved predictions for both the Reynolds-stress and anisotropy tensors in the near-wall region, and predict the physically correct two-components state of turbulence near the wall. In addition, the near-wall budget of turbulence kinetic energy shows significant improvements over the baseline EASM. However, none of the modifications capture the reduction of the anisotropy components a_{11} and a_{22} very close to the wall, and fail to improve the anisotropy predictions at low strain rates, that occur towards the centre of the channel.

- A new RANS model is presented, which combines the advantages of the elliptic-blending approach for modelling near-wall flows, with the advantages of a non-linear stress-strain relationship to provide more accurate predictions of the Reynolds-stress and anisotropy fields in complex flows. The new non-linear elliptic-blending RANS model completely abandons viscosity-dependent blending or damping functions and their effect is more naturally included. The elliptic-blending approach is used in this work in conjunction with a k-ω model and not as usual, within the k-ϵ modeling framework. The proposed non-linear stress-strain relationship recovers the normal-Reynolds-stress and anisotropy predictions of the baseline EASM model away from the wall, where the quasi-homogeneous pressure-strain model of Speziale *et al.* (1991) provides good predictions for the Reynolds-stress and anisotropy tensor. Close to the wall, a near-wall-consistency constraint and additional near-wall-anisotropy modification are introduced, in order to improve the predictions of the quasi-homogeneous pressure-strain model. As a consequence, the highly anisotropic state of turbulence and the limiting two-component state are correctly reproduced as the wall is approached. The new φ-α-EASM further improves the

predictions of the normal-anisotropy components a_{11} and a_{33} very close to the wall and in situations, where the strain rate becomes small. It is also capable of fully reproducing the appropriate anisotropy-invariant map.

The new turbulence model predicts a higher overall magnitude of shear stress in the free-shear layer of the NASA hump configuration, which effectively shortens the recirculation zone and hence provides improved agreement with the reference data over the baseline EASM and φ-α-UMIST model. In addition, predictions of the anisotropy component a_{11} show an enlarged peak close to the wall, which is not predicted by the baseline EASM model; the near-wall-consistency constraint ensures that the a_{22} component approaches the correct limiting value of $a_{22} \rightarrow -2/3$ at the wall. For the flow in the three-dimensional diffuser, the new φ-α-EASM model shows the best predictions of the surface-pressure distribution. However, no systematic improvement of the mean-velocity field in the asymmetric diffuser was obtained by the new model.

- A hybrid RANS/LES/DNS framework is presented, which is able to provide the required amount of turbulence modeling for any mesh resolution, and seamlessly operates between RANS and DNS mode. This is achieved by a revised Flow Simulation Methodology, where the turbulence modelling contribution of a RANS model is rescaled using a damping function. The Flow Simulation Methodology is proposed in conjunction with a newly developed damping function and a tailored convection discretisation scheme, which further enhances the reliability and predictive accuracy of FSM. The hybrid convection scheme is based on a linear combination of the second-order central-difference and the linear-upwind scheme, with a flow-dependent flux-blending function. Such blended schemes are available in many CFD codes, which makes the implementation straightforward. It is conjectured that a sophisticated RANS model will improve the overall quality of the predictions of any hybrid RANS/LES model, not only in the RANS region, but also in the LES region. For this reason, the FSM approach is presented and calibrated for three different underlying RANS closures of different levels of sophistication. The turbulence models include the k-ω-SST, EASM-2D and φ-α-EASM schemes. The free parameters are calibrated for stationary homogeneous isotropic turbulence, in order to provide proper LES behaviour and a physically consistent energy cascade. It is demonstrated that the calibration constants exhibit an undesirable grid or resolution dependency, and

that any attempt to achieve boundedness of the convection discretisation inevitably deteriorates the results, unless the calibration constants are adjusted accordingly.

- The basic wall-modelled LES mode of FSM has been investigated for planar channel flow. It is demonstrated that the results for the mean-velocity profile and shear stress exhibit a gross sensitivity with respect to the convection discretisation scheme. The second-order upwind scheme and the TVD scheme are not recommended to be employed within a turbulence-resolving simulation, because the reduction of resolved shear stress is not compensated by an sufficient increase in modelled shear stress. This results in an under-prediction of total shear stress and in a mean-velocity profile, which is beyond the level of accuracy required in engineering applications. The hybrid FSM convection scheme, on the other hand, delivers results almost as accurate as the Central-Difference Scheme. It is further shown that the mean-velocity predictions are insensitive to the choice of calibration constants C_α and β, but are sensitive to the underlying RANS model. Even though the shape of the damping function F is influenced by the specific choice of the calibration constants, the total shear stress and hence the mean-velocity profile is predicted very consistently, almost independently of the specific value of C_α and β. The sensitivity with respect to the RANS model is mainly caused by different distributions of the damping function F. In order to eliminate the strong sensitivity of the damping function on the underlying RANS model, an extension to FSM is introduced, which modifies the damping function close to the wall, such that it takes a more consistent distribution for all underlying turbulence models. In addition, the modification provides improved predictions of the mean-velocity profile. With the modification included, the most sophisticated underlying RANS model, φ-α-EASM, provides the best predictions for the mean-velocity profile and asymptotic near-wall behaviour of all normal-Reynolds-stress components, for the $Re_\tau = 395$ case. It is shown that the small log-layer mismatch visible in the results is caused by an under-prediction of total (resolved plus modelled) shear stress at the switching location. It is, consequently, suggested that the mismatch could potentially be eliminated by enhancing either the resolved or modelled contribution to the shear stress at the switching location. For the high-Reynolds-number channel flow ($Re_\tau = 18000$), the FSM-EASM and FSM-φ-α-EASM models provide clearly improved predictions over FSM based on the k-ω-SST model. The FSM-EASM shows the best predictions,

with the log-layer mismatch almost eliminated and similar to the predictions of IDDES.

- The performance of the wall-modelled LES mode of FSM is assessed for the complex flow in a three-dimensional diffuser, which inlcudes three-dimensional boundary-layer separation. The sensitivity study of the convection discrectisation scheme confirms that a bounded scheme is not recommended in turbulence-resolving simulations, since it will inevitably deteriorate the results. The bounded-difference scheme almost completely suppresses flow separation on the centre plane, whereas the CDS and hybrid FSM schemes give results in much better agreement with the reference data. The hybrid FSM schemes retains the accuracy of the CDS, and does not contaminate the resolved flow field with elevated levels of numerical dissipation. This also ensures a more realistic $-5/3$ behaviour of the velocity fluctuation spectra.

  All hybrid RANS/LES models investigated in this work predict the correct flow topology in the diffuser and therefore provide significantly improved predictions compared to pure RANS simulations. Only the SAS method is generally not able to sustain any turbulence fluctuations in the diffuser and effectively operates in RANS mode. The FSM and IDDES models show a slight departure from the reference data, for the simulations on the coarse baseline grid, in terms of predicting the correct extent of the separated flow region in the diffuser. In the predictions of the IDDES model, separation from the top wall occurs too late and results in too small a recirculation zone. All FSM models, on the other hand, exhibit premature separation just downstream of the sharp corner. It is found that different levels of resolved turbulence fluctuations provided from the inflow duct simulation, particularly close to the wall, influence the downstream development of the flow in the diffuser and are responsible for the observed differences between each model. A grid refinement improves the predictions of the separated flow region downstream of the sharp corner and hence provides results in good agreement with reference data. The results of FSM are also sensitive to the underlying RANS model. The FSM-SST and FSM-EASM give slightly better overall predictions, compared to the more sophisticated FSM-φ-α-EASM, which shows the most pronounced over-prediction of streamwise velocity close to the bottom wall.

- The simulations of the flow around the tandem cylinder configuration clearly highlight the advantages of an accurate hybrid convection discretisation scheme, with a flow-dependent flux blending function. In the present case, no results

could be obtained with the unbounded central-difference scheme and all TVD schemes result in over-prediction of the size of the recirculation zone behind the upstream cylinder. An extensive grid sensitivity study is conducted and reveals a high sensitivity of results to the resolution of the computational grid in the spanwise direction, as well as to the resolution in the xy-plane. The baseline computational grid, which has a spanwise resolution such that approximately isotropic cells are obtained in the gap region between the cylinders, is found to provide the best results and good agreement with the reference data. On the other hand, the computational grid with too coarse a spanwise resolution is found not suitable for a turbulence-resolving simulation and fails to provide sufficiently accurate predictions of the mean-flow field. The computational grids with a finer resolution in spanwise direction and with a finer resolution in the xy-plane are found to deteriorate the results, compared to the coarser baseline grid. It is speculated that this is might be caused by a favourable cancellation of errors induced by the coarse grid and the turbulence model. Further testing is required to confirm this hypothesis. It is also argued that the definition of the turbulence length scale Δ may contribute to this behaviour and that the turbulence model might benefit from redefinition of this length scale. The sensitivity study has also revealed that most results are insensitive to different spanwise domain widths. Only the intensity of surface-pressure fluctuations on the upstream cylinder reduces somewhat with increasing domain width, and hence provides improved agreement with the reference data. Nevertheless, the difference is not pronounced enough to justify the large computational cost associated with large spanwise domain widths. The very small sensitivity of the results with respect to the spanwise domain width is associated with a spurious, too strong spanwise correlation of the flow. The spanwise surface-pressure correlation does not go to zero on the largest computational grid, with a span of $12D$. It is argued that lateral periodic boundary conditions contribute to this effect. The flow around the tandem cylinder configuration is also very sensitive to the turbulence modelling approach. The IDDES model transitioned after long simulation times to an alternative mean-flow state where the vortex shedding from the upstream cylinder is suppressed. The FSM approach, based on the most sophisticated underlying RANS model, predicts a fundamental vortex shedding frequency of half the experimental value. The FSM-SST model provides overall the best agreement with reference data on the baseline computational grid, followed by the SAS and FSM-EASM models.

11.2 Outlook

In the following, a few points are discussed that have not been covered in the present work, but are suggested as being worthwhile topics for future exploration.

- The near-wall anisotropy modifications presented in chapter 7 have only been applied and tested for the flow in a planar channel. Since they are computationally less expensive, compared to the new φ-α-EASM model, it may be worthwhile to investigate how these rather simple modifications perform in more complex flows.

- The new φ-α-EASM model presented in chapter 8 exhibited convergence difficulties for some cases. During the course of this work no satisfying solution could be found to improve this situation. In addition, the near-wall anisotropy and consistency modifications are targeted to improve the predictions in shear flows, and are inactive in cases of, for example, flow impingement. Even though reattaching flows have been part of the test cases presented in this work, it seems worthwhile to also investigate and potentially optimise the performance of the new model for the isolated flow impingement normal to a wall.

- The modified Flow Simulation Methodology presented in chapter 9 is able to operate in a RANS/LES and DNS mode. From an industrial perspective, it seems very appealing to introduce the capability to operate in VLES mode, where most of the turbulence kinetic energy is statistically represented by the turbulence model, and only a fraction is resolved by the simulation. No satisfying solution could be found here to introduce VLES capabilities. However, it is believed that this issue may be worthwhile to explore in the future.

Bibliography

Abdol-Hamid, K. S. & Girimaji, S. S. 2004 A Two-Stage Procedure Towards the Efficient Implementation of PANS and other Hybrid Turbulence Models. *Tech. Rep.*. NASA TM-2004-213260.

Abe, K. 2005 A hybrid LES/RANS approach using an anisotropy-resolving algebraic turbulence model. *International Journal of Heat and Fluid Flow* **26**, 204–222.

Abe, K., Jang, Y. J. & Leschziner, M. A. 2003 An investigation of wall-anisotropy expressions and length-scale equations for non-linear eddy-viscosity models. *International Jounral of Heat and Fluid Flow* **24**, 181–198.

Abe, K., Kondoh, T. & Nagano, Y. 1997 On Reynolds-stress experssions and near-wall scaling parameters for predicting wall and homogeneous turbulent shear flows. *International Journal of Heat and Fluid Flow* **18**, 266–282.

Abid, R., Morrison, J. H., Gatski, T. B. & Speziale, C. G. 1997 Prediction of Complex Aerodynamic Flows with Explicit Algebraic Stress Models. *AIAA 96-0565* .

Aider, J. & Danet, A. 2006 Large-eddy simulation study of upstream boundary conditions influence upon a backward-facing step. *COMPTES RENDUS MECANIQUE* **334**, 447–453.

Apsley, D. D. & Leschziner, M. A. 1998 A new low-Reynolds-number nonlinear two-equation turbulence model for complex flows. *International Jounral of Heat and Fluid Flow* **19**, 209–222.

Baggett, J. S. 1998 On the feasibility of merging LES with RANS for the near-wall region of attached turbulent flows. *Center of Turbulence Research, Annual Research Briefs* .

Balaras, E. & Benocci, C. 1994 Subgrid-scale models in finite-difference simulations of complex wall bounded flows. *In AGARD, Application of Direct and Large Eddy Simulation to Transition and Turbulence 6* .

Batten, P., Goldberg, U. & Chakravarthy, S. 2000 Sub-Grid Turbulence Modelling for Unsteady Flow with Acoustic Resonances. *AIAA Paper No. 00-0473* .

Batten, P., Goldberg, U. & Chakravarthy, S. 2002 LNS - An Approach Towards Embedded LES. *AIAA Paper No. 2002-0427, 40th Aerospace Sciences Meeting and Exhibit, Reno/NV* .

Batten, P., Goldberg, U. & Chakravarthy, S. 2003 Using Synthetic Turbulence to Interface RANS and LES. *AIAA 2003-81, 41st Aerospace Sciences Meeting and Exhibit, Reno, Nevada* .

Batten, P., Goldberg, U. & Chakravarthy, S. 2004 Interfacing Statistical Turbulence Closures with Large-eddy Simulation. *AIAA Journal* **42, 3**.

Batten, P., Goldberg, U., Peroomian, O. & Chakravarthy, S. 2009 Recommendations and best practice for the current state of the art in turbulence modelling. *International Journal of Computational Fluid Dynamics* **23,4**, 363–374.

Baurle, R. A., Tam, C. J., Edwards, J. R. & Hassan, H. A. 2003 Hybrid Simulation Approach for Cavity Flows: Blending, Algorithm, and Boundary Treatment Issues. *AIAA Journal* **41, 8**, 1463–1480.

Benarafa, Y., Cioni, O., Ducros, F. & Sagaut, P. 2006 RANS/LES coupling for unsteady turbulent flow simulation at high Reynolds number on coarse meshes. *Computer Methods in Applied Mechanics and Engineering* **195, 23-24**, 2939–2960.

Boussinesq, J. 1877 Théorie de l'Écoulement Tourbillant. *Mem. Présentés par Divers Savants Acad. Sci. Inst. Fr.* **23**, 46–50.

Breuer, M., Jaffrezic, B. & Arora, K. 2007*a* Hybrid LES-RANS technique based on a one-equation near-wall model. *Theoretical and Computational Fluid Dynamics* .

Breuer, M., Jaffrezic, B. & Delgado, A. 2007*b* Hybrid LES-RANS Method Based on an Explicit Algebraic Stress Model. *Advancesin Hybrid RANS-LES*

Modelling, Papers Contributed to the 2007 Symposium of Hybrid RANS-LES Methods, Corfu, Greece .

Bunge, U., Mockett, C. & Thiele, F. 2007 Guidelines for implementing Detached-Eddy Simulation using different models. *Aerospace Science and Technology* **11, 5**, 376–385.

Cabot, W. & Moin, P. 1999 Approximate Wall Boundary Conditions in the Large-Eddy Simulation of High Reynolds Number Flow. *Flow, Turbulence and Combustion* **63**, 269–291.

Celic, A. 2004 Performance of Modern Eddy-Viscosity Turbulence Models. PhD thesis, Institut für Aerodynamik und Gasdynamik, Universität Stuttgart.

Chaouat, B. & Schiestel, R. 2005 A new partiall integrated transport model for subgrid-scale stresses and dissipation rate for turbulent developing flows. *Physics of Fluids* **17**.

Chaouat, B. & Schiestel, R. 2009 Progress in subgrid-scale transport modelling for continuous hybrid non-zonal RANS/LES simulations. *International Journal of Heat and Fluid Flow* **30**, 602–616.

Cherry, E. M., Elkins, C. J. & Eaton, J. K. 2008 Geometric sensitivity of three-dimensional separated flows. *International Jounral of Heat and Fluid Flow* **29**, 903–811.

Cherry, E. M., Elkins, C. J. & Eaton, J. K. 2009 Pressure measurements in a three-dimensional separated diffuser. *International Jounral of Heat and Fluid Flow* **30**, 1–2.

Coleman, G.N., Kim, J. & Spalart, P.R. 2003 Direct numerical simulation of a decelerated wall-bounded turbulent shear flow. *Journal of Fluid Mechanics* **495**.

Craft, T. J. & Launder, B. E. 1995 Reynolds stress closure designed for complex geometries. *International Journal of Heat and Fluid Flow* **17**, 245–254.

Craft, T. J., Launder, B. E. & Suga, K. 1995 Development and application of a cubic eddy-viscosity model of turbulence. *International Journal of Heat and Fluid Flow* **17, 108-115**.

Dahlstrom, S. & Davidson, L. 2003 Hybrid RANS/LES employing Interface Condition with Turbulent Structure. *Turbulence, Heat and Mass Transfer* **4**, 689–696.

Daley, B. J. & Harlow, F. H. 1970 Transport Equations in Turbulence. *The Physics of Fluids* **13, 11**, 2634–2649.

Davidson, L. 2006 Evaluation of the SST-SAS Model: Channel Flow, Asymmetric Diffusor and Axisymmetric Hill. *European Conference on Computational Fluid Dynamics, ECCOMAS CFD, TU Delft, The Netherlands* .

Davidson, L. & Billson, M. 2006 Hybrid LES-RANS using synthesized turbulent fluctuations for forcing in the interface region. *International Journal of Heat and Fluid Flow* **27**, 1028–1042.

Davidson, L. & Peng, S. H. 2003 Hybrid LES-RANS modelling: a one-equation SGS model combined with a k-ω model for predicting recirculating flows. *International Journal for Numerical Methods in Fluids* **43**, 1003–1018.

Deardorff, J. W. 1973 The use of subgrid transport equations in a three-dimensional model of atmospheric turbulence. *ASME Journal of Fluid Engineering* pp. 429–438.

Deck, S. 2005 Zonal-Detached-Eddy-Simulation of the Flow Around a High-Lift Configuration. *AIAA Journal* **43, 11**.

Deng, G. B., Queutey, P. & Visonneau, M. 2005 Three-Dimensional Flow Computation with Reynolds Stress and Algebraic Stress Models. *Engineering Turbulence Modelling and Experiment 6, Editior: W. Rodi* pp. 389–398.

Durbin, P. A. 1991 Near-Wall Turbulence Closure Modeling Without Damping Functions. *Theoretical and Computational Fluid Dynamics* **3**, 1–13.

Durbin, P. A. 1993 A Reynolds stress model for near-wall turbulence. *Journal of Fluid Mechanics* **249**, 465–498.

Durbin, P. A. 1995*a* Separated Flow Computations with the k- ϵ- v^2 Model. *AIAA Journal* **33, 4**, 659–664.

Durbin, P. A. 1995*b* Turbulence modeling for non-equilibrium flow. *Center of Turbulence Research, Annual Research Briefs* .

Durbin, P. A. 1996 On the k-ϵ stagnation point anomaly. *International Jounral of Heat and Fluid Flow* **17**, 89–90.

Durbin, P. A. & Petterson-Reif, B. A. 2001 *Statistical Theory and Modeling for Turbulent Flows*. John Wiley & Sons Ltd.

Egorov, Y. & Menter, F. R. 2007 Development and Application of the SST-SAS Turbulence Model in the DESIDER Project. In *Second Symposium on hybrid RANS/LES Methods, Corfu, Greece*.

Egorov, Y., Menter, F. R., Lechner, R. & Cokljat, D. 2010 The Scale-Adaptive Simulation Methodology for Unsteady Turbulent Flow Predictions. Part 2: Application to Complex Flows. *Flow Turbulence and Combustion* **85**, 139–165.

Elmiligui, A., Abdol-Hamid, K. S., Massey, S. J. & Pao, S. P. 2004 Numerical Study of Flow Past a Cricular Cylinder Using RANS, Hybrid RANS/LES and PANS Formulations. In *22nd Applied Aerodynamics Conference and Exhibit, Providence, Rhode Island*.

Eswaran, V. & Pope, S. B. 1988 An examination of forcing in direct numerical simulation of turbulence. *Computers & Fluids* **16,3**, 257–278.

Fadai-Ghotbi, A., Freiss, C., Manceau, R., Gatski, T. B. & Boree, J. 2009 Toward a consistent formalism for seamless hybrid RANS-LES modelling in inhomogeneous turbulence based on temporal filtering. In *Proceedings of the Sixth International Symposium on Turbulence and Shear Flow Phenomena, Seaoul, Korea*.

Fasel, H. F., Seidel, J. & Wernz, S. 2002 A Methodology for Simulations of Complex Turbulent Flows. *Journal of Fluids Engineering* **124, 4**, 933–942.

Fasel, H. F., von Terzi, D. A. & Sandberg, R. D. 2006 A Methodology for Simulating Compressible Turbulent Flows. *Journal of Applied Mechanics* **73, 3**, 405–412.

Ferziger, J. H. & Peric, M. 2002 *Computational Methods for Fluid Dynamics, third, rev. edition*. Springer-Verlag.

Franke, M., Wallin, S. & Thiele, F. 2005 Assessment of explicit algebraic Reynolds-stress turbulence models in aerodynamic computations. *Aerosapce Science and Technology* **9**, 573–581.

Froehlich, J. & von Terzi, D. 2008 Hybrid LES/RANS Methods for the Simulation of Turbulent Flows. *Progress in Aerospace Sciences* **44, 5**, 349–377.

Fureby, C., Gosman, A. D., Tabor, G. & Weller, H. G. 1997*a* Large Eddy Simulation of Turbulent Channel Flows. In *Turbulent Shear Flows 11*.

Fureby, C., Tabor, G., Weller, H. G. & Gosman, A. D. 1997*b* A comparative study of subgrid scale models in homogeneous isotropic turbulence. *Physics of Fluids* **9, 5**, 1416–1429.

Fureby, C., Tabor, G., Weller, H. G. & Gosman, A. D. 1997*c* Differential subgrid stress models in large eddy simulation. *Physics of Fluids* **9, 11**, 3578–3580.

Garbaruk, A., Shur, M., Strelets, M., Spalart, P. R. & Balakrishnan, R. 2010 DDES and IDDES of Tandem Cylinders. In *Proceedings of the Benchmark problems for Airframe Noise Computations BANC*.

Gatski, T. B., Hussaini, M. Y. & Lumley, J. L., ed. 1996 *Simulation and Modeling fo Turbulent Flows*. Oxford University Press Inc.

Gatski, T. B. & Jongen, T. 2000 Nonlinear eddy viscosity and algebraic stress models for solving complex turbulent flows. *Progress in Aerospace Science* **36**, 655–682.

Gatski, T. B. & Rumsey, C. L. 2002 Linear and Nonlinear Eddy Viscosity Models. *in Closure Strategies for Turbulent and Transitional Flows. Edited by N.D. Sandham and B.E. Launder. Cambridge University Press* .

Gatski, T. B. & Speziale, C. G. 1993 On explicit algebraic stress models for complex turbulent flows. *Journal of Fluid Mechanics* **254**, 59–78.

Germano, M. 1998 Comment on "Turbulence Modeling for Time-Dependent RANS and VLES: A Review. *AIAA Journal* **36, 9**.

Gibson, M. M. & Launder, B. E. 1978 Ground effects pn pressure fluctuations in the atmospheric boundary layer. *Journal of Fluid Mechanics* **86, 3**, 491–511.

Girimaji, S. S. 1996 Fully-Explicit and Self-Consistent Algebraic Reynolds Stress Model. *Theoretical and Computational Fluid Dynamics* **8, 6**, 387–402.

Girimaji, S. S. 1997 A Galilean invariant explicit algebraic Reynolds stress model for turbulent curved flows. *Physics of Fluids* **9, 4**, 1067–1077.

Girimaji, S. S. 2006 Partially-Averaged Navier Stokes Model for Turbulence: A Reynolds-Averaged Navier-Stokes to Direct Numerical Simulation Bridging Method. *Journal of Applied Mechanics* **73, 3**, 143–421.

Girimaji, S. S., Jeong, E. & Srinivasan, R. 2006 Partially Averaged Navier-Stokes Method for Turbulence: Fixed Point Analysis and Comparison With Unsteady Partially Averaged Navier-Stokes. *Journal of Applied Mechanics* **73**, 422–429.

Greenblatt, D., Paschal, K. B., Yao, C. S., Harris, J., Schaeffler, N. W. & Washburn, A. E. 2004 A Separation Control CFD Validation Test Case Part 1: Baseline and steady Suction. In *2nd AIAA Flow Control Conference, June 28 – July 1, 2004, Portland, OR*.

Greenblatt, D., Paschal, K. B., Yao, S. C., Harris, J., Schaeffler, N. W. & Washburn, A. E. 2006 Experimental Investigation of Separation Control Part 1: Baseline and Steady Suction. *AIAA Journal* **44, 12**, 2820–2830.

Grundestam, O., Wallin, S. & Johansen, A. V. 2005 An explicit algebraic Reynolds stress model based on a nonlinear pressure strain rate model. *International Journal of Heat and Fluid Flow* **26**, 732–745.

Gullman-Strand, J., Toernblom, O., Lindgren, B., Amberg, G. & Johansen, A. V. 2004 Numerical and experimental study of separated flow in a plane asymmetric diffuser. *International Jounral of Heat and Fluid Flow* **25**, 451–460.

Hamba, F. 2003 A Hybrid RANS/LES Simulation for Turbulent Channel Flow. *Theoretical and Computational Fluid Dynamics* **16**, 387–403.

Hamba, F. 2006 A hybrid RANS/LES simulation of high-Reynolds-number channel flow using additional filtering at the interface. *Theoretical and Computational Fluid Dynamics* **20, 2**, 89–101.

Hanifi, A., Alfredsson, P. H., Johansson, A. V. & Henningson, D. S., ed. 1999 *Transition, Turbulence and Combustion Modelling, Lecture Notes from 2nd ERCOFTAC Summerschool held in Stockholm, 10-16 June, 1998*. Kluwer Academic Publishers.

Hanjalic, K. 1994 Advanced turbulence closure models: a view of current status and future prospects. *International Journal of Heat and Fluid Flow* **15, 3**, 178–203.

Hanjalic, K. & Launder, B. E. 1972 A Reynolds stress model of turbulence and its application to thin shear flows. *Journal of Fluid Mechanics* **51**.

Hanjalic, K., Popovac, M. & Hadziabdic, M. 2004 A robust near-wall elliptic-relaxation eddy-viscosity turbulence model for CFD. *International Journal of Heat and Fluid Flow* **25**, 1047–1051.

Hellsten, A. 2002 Curvature Corrections for Albebraic Reynolds Stress Modeling: A Discussion. *AIAA Journal* **40,9**, 1909–1911.

Hellsten, A. 2004 New Two-Equation Turbulence Model for Aerodynamic Applications. PhD thesis, Helsinki University of Technology, Laboratory of Aerodynamics.

Hellsten, A. 2005 New Advanced k-ω Turbulence Model for High-Lift Aerodynamics. *AIAA Journal* **43, 9**, 1857–1869.

Hinze, J. O. 1975 *Turbulence, 2nd ed.*. New York: McGraw-Hill.

Hirsch, C. 1994 *Numerical Computation of Internal and External Flows. Volume 1: Fundamentals of Numerical Discretisation*. John Wiley & Sons Ltd.

Hussain, A. K. M. F. & Reynolds, W. C. 1970 The mechanics of an organized wave in turbulent shear flow. *Journal of Fluid Dynamics* **41**, 241–258.

Hussaini, M. Y., Thangam, S., Woodruff, S. L. & Zhou, Y. 2006 Development of a Continuous Model for Simulation of Turbulent Flows. *Journal of Applied Mechanics* **73, 3**, 441–448.

Hutchins, N. & Marusic, I. 2007 Evidence of very long meandering features in the logarithmic region of turbulent boundary layers. *Journal of Fluid Mechanics* **579**, 1–28.

Inuzuka, M. & Abe, K. 2007 A Hybrid LES/RANS Approach Using Anisotropic-Resolving Algebraic Turbulence Models for Predicting Turbulent Heat Transfer. *Heat Transfer - Asian Reseach* **35, 5**.

Israel, D. M. 2005 A New Approach for Turbulent Simulation in Complex Geometries. PhD thesis, Department of Aerospace & Mechanical Engineering, University of Arizona.

Issa, R. I. 1986 Solution of the implicitly discretized fluid flow equation by operator-splitting. *Journal of Computational Physics* **62**, 40–65.

Jakirlic, S. & Hanjalic, K. 2002 A new approach to modelling near-wall turbulence energy and stress dissipation. *Journal of Fluid Mechanics* **459**, 139–166.

Jang, Y. J., Leschziner, M. A., Abe, K. & Temmerman, L. 2002 Investigation of Anisotropy-Resolving Turbulence Models by Reference to Highly-Resolved LES Data for Separated Flow. *Flow, Turbulence and Combustion* **69**, 161–2003.

Jang, Y. J., Temmerman, L. & Leschziner, M. A. 2001 Investigation of anisotropy resolving turbulence models by reference to highly-resolved LES data for separated flow. *ECCOMAS Computational Fluid Dynamics Conference,Swansea, Wales, Uk.* .

Jasak, H. 1996 Error Analysis and Estimation for the Finite Volume Method with Applications to Fluid Flow. PhD thesis, Department of Mechanical Engineering, Imperial College of Science, Tehcnology and Medicine.

Jenkins, L, Neuhart, D, McGinley, C & Choudhari, M 2006 Measurements of Unsteady Wake Interference Between Tandem Cylinders. In *Paper No. AIAA-2006-3202*. 36th AIAA Fluid Dynamics Conference and Exhibit.

Jimenez, J., Wray, A. A., Saffman, P. G. & Rogallo, R. S. 1993 The structure of intense vorticity in isotropic turbulence. *Journal of Fluid Mechanics* **255**, 65–90.

Johansen, A. V. & Hallback, M. 1994 Modelling of rapdid pressure-strain in Reynolds-stress closures. *Journal of Fluid Mechanics* **269**, 143–168.

Jones, W. P. & Launder, B. E. 1972 The Prediction of Laminarization with a Two-Equation Model of Turbulence. *International Journal of Heat and Mass Transfer* **15**, 301–314.

Jouvray, A. & Tucker, P. G. Liu, Y. 2007 Nonlinear RANS models when predicting more complex geometry room air flows. *International Journal of Heat and Fluid Flow* **28**, 275–288.

Kaneda, Y., Ishihara, T., Yokokawa, M., Itakura, K. & Uno, A. 2003 Energy dissipation rate and energy spectrum in high resolution direct numerical simulation of turbulence in a periodic box. *Physics of Fluids* **12,1**, L21–L24.

Karlatiras, G. & Papadakis, G. 2006 Near-Wall Modifications of an Explicit Algebraic Reynolds Stress Model Using Elliptic Blending. *Flow, Turbulence and Combustion* **77**, 257–275.

Keating, Anthony & Piomelli, U. 2006 A dynamic stochastic forcing method as a wall-layer model for large-eddy simulation. *Journal of Turbulence* **7, 12**.

Keshmiri, A., Cotton, M. A., Addad, Y., Rolfo, S. & Billard, F. 2008 RANS AND LES INVESTIGATIONS OF VERTICAL FLOWS IN THE FUEL PASSAGES OF GAS-COOLED NUCLEAR REACTORS. In *Proceedings of the 16th International Conference on Nuclear Engineering ICONE16-48372, May 11-15 2008, Orlando, Florida, USA*.

Khorrami, M. R., Choudhari, M. M., Lockard, D. P., Jenkins, L. N. & McGinley, C. 2007 Unsteady Flow Field Around Tandem Cylinders as Prototype Component Interaction in Airframe Noise. *AIAA Journal* **45, 8**, 1930–1941.

Kok, J. C. 1999 Resolving the dependence on free-stream values for the k-ω turbulence model. *National Aerosapace Laboratory, NLR-TP-99295* .

Kolmogorov, A. N. 1941 The local structure of turbulence in incompressible viscous fluids for very large Reynolds number. *Dokl. Akad. Nauk.* **30**, 301–305.

Kolmogorov, A. N. 1942 Equations of Turbulent Motion of an Incompressible Fluid. *Izvestia Academy of Sciences* **6 ,1-2**, 56–58.

Lai, Y. G. & So, R. M. C. 1991 On Near-Wall Turbulent Flows Modelling. *Journal of Fluid Mechanics* **221**, 641–673.

Lakshmipathy, S. & Girimaji, S. S. 2006 Partially-averaged Navier-Stokes method for turbulent flows: K-ω model implementation. In *44th Aerospace Science Meeting and Exhibit, Reno, Nevada*.

Larsson, J., Lien, F. S. & Yee, E. 2006 Feedback-controlled forcing in hybrid LES/RANS. *International Journal of Computational Fluid Dynamics* **20, 10**, 687–699.

Larsson, J., Lien, F. S. & Yee, E. 2007 The artificial buffer layer and the effects of forcing in hybrid LES/RANS. *International Journal of Heat and Fluid Flow* **28**, 1443–1459.

Launder, B. E. 1989 Second-moment closure: present and future? *International Journal of Heat and Fluid Flow* **10, 4**, 282–300.

Launder, B. E., Reece, G. J. & Rodi, W. 1975 Progress in the development of a Reynolds-stress turbulence closure. *Journal of Fluid Mechanics* **68, 3**, 537–566.

Launder, B. E. & Sandham, N. D., ed. 2002 *Closure Strategies for Turbulent and Transitional Flows*. Cambridge University Press.

Launder, B. E. & Sharma, B. I. 1974 Application of the Energy Dissipation Model of Turbulence to the Calculation of Flow Near a Spinning Disc. *Letters in Heat and Mass Transfer* **1, 2**, 131–138.

Laurence, D. R., Uribe, J. C. & Utyuzhnikov, S. V. 2004 A robust Formulation of the $v^2 - f$ Model. *Flow, Turbulence and Combustion* **73**, 169–185.

Lien, F. S. & Durbin, P. A. 1996 Non linear k-ϵ-v^2 modelling with the application to high lift. *In: Procedings of the Summer Program, Stanford University* pp. 5–22.

Lien, F. S. & Kalitzin, G. 2001 Computations of transonic flow with the v^2-f turbulence model. *International Jounral of Heat and Fluid Flow* **22**, 53–61.

Liu, Nan-Suey & Shih, Tsan-Hsing 2006 Turbulence modeling for Very Large-Eddy Simulation. *AIAA Journal* **44, 4**.

Lockard, D. P. 2011 Summary of the Tandem Cylinder Solutions from the Benchmark problems for Airframe Noise Computations-I Workshop. In *Proceedings of the 49th Aerospace Sciences Meeting Including the New Horizons Forum and Aerospace Exposition, AIAA-2011-0353*.

Lockard, D. P., Khorrami, M. R., Choudhari, M. M., Hutcheson, F. V., Brooks, T. F. & Stead, D. J. 2007 Tandem Cylinder Noise Predictions. In *13th AIAA/CEAS Aeroacoustics Conference*.

Luebke, H., Schmidt, St., Rung, T. & Thiele, F. 2001 Comparison of LES and RANS in bluff-body flows. *Journal of Wind Engineering* **89**, 1471–1485.

Lumley, J. L. & Newman, G. R. 1977 The return to isotropy of homogeneous turbulence. *Journal of Fluid Mechanics* **82, 1**, 161–178.

Lund, T. S. & Novikov, E. A. 1992 Parameterization of subgrid-scale stress by the velocity gradient tensor. *Tech. Rep.*. Center for Turbulence Research, Annual Research Brief.

Manceau, R. 2003 Accounting for Wall-Induced Reynolds Stress Anisotropy in Explicit Algebraic Stress Models. *Procedings of the 3rd Symposium on Turb. Shear Flow Phenomena, Sendai, Japan* .

Manceau, R. & Hanjalic, K. 2002 Elliptic blending model: A new near-wall Reynolds-stress turbulence closure. *Physics of Fluids* **14, 2**, 744–754.

Manceau, R., Wang, M. & Laurence, D. R. 2001 Inhomogeneity and anisotropy effects on the redistribution term in Reynolds-averaged Navier-Stokes modelling. *Journal of Fluid Mechanics* **438**, 307–338.

Mansour, N. N., Kim, J. & Moin, P. 1988 Reynolds-stress and dissipation-rate budgets in a turbulent channel flow. *Journal of Fluid Mechanics* **194**, 15–44.

Marstropp, L., Brethouwer, G., Grundestam, O. & Johanson, A. V. 2009 Explicit algebraic subgrid stress models with application to rotating channel flow. *Journal of Fluid Mechanics* **639**, 403–432.

Menon, S., Yeung, P. K. & Kim, W. W. 1996 Effect of subgrid scale models on the computed interscale energy transfer in isotropic turbulence. *Computers & Fluids* **25, 2**, 165–180.

Menter, F. R. 1992 Improved Two-Equation K-ω Turbulence Models for Aerodynamic Flows. *NASA Technical Memorandum 103975* .

Menter, F. R. 1994 Two-Equation Eddy-Viscosity Turbulence Models for Engineering applications. *AIAA Journal* **32, 8**, 1598–1604.

Menter, F. R. 2009 Review of the shear-stress transport turbulence model experience from an industrial perspective. *International Journal of Computational Fluid Mechanics* **23, 4**, 305–316.

Menter, F. R. & Egorov, Y. 2005 A Scale Adaptive Simulation Model Using Two-Equation Models. *43rd AIAA Aerospace Sciences Meeting and Exhibit, Reno, Nevada* .

Menter, F. R. & Egorov, Y. 2010 The Scale-Adaptive Simulation Methodology for Unsteady Turbulent Flow Predictions. Part 1: Theory and Model Description. *Flow Turbulence and Combustion* **85**, 113–138.

Menter, F. R., Kuntz, M. & Bender, R. 2003 A Scale-Adaptive Simulation Model for Turbulent Flow Predictions. *AIAA 2003-0767, 41st Aerospace Sciences Meeting and Exhibit, Reno, Nevada* .

Mockett, C. 2009 A comprehensive study of detached-eddy simulation. PhD thesis, Technischen Universität Berlin, Fakultät Verkehrs- und Maschinensysteme.

Moser, R. D., Kim, J. & N., Mansour. N. 1999 Direct numerical simulation of aturbulent channel flow up to $Re_\tau = 590$. *Physics of Fluids* **11, 4**.

Naji, H., Mompean, G. & Yahyaoi, O. E. 2004 Evaluation of explicit algebraic stress models using direct numerical simulations. *Journal of Turbulence* **5, 38**.

Nikitin, N. V., Nicoud, F., Wasistho, B., Squires, K. D. & Spalart, P. R. 2000 An approach to wall modeling in large-eddy simulations. *Physics of Fluids* **12, 7**, 1629–1632.

Ohlsson, J., Schlatter, P., Fischer, P. F. & Henningson, D. S. 2010 Direct numerical simulation of separated flow in a three-dimensional diffuser. *Journal of Fluid Mechanics* **650**, 307–318.

Parneix, S., Durbin, P. A. & Behnia, M. 1998 Computation of 3D Turbulent Boundary Layers Using the V2F Model. *Flow, Turbulence and Combustion* **60**, 19–46.

Patankar, S. V. 1981 *Numerical Heat Transfer and Fluid FLow*. Hemisphere Bublishing Corporation.

Patel, V. C., Rodi, W. & Scheuerer, G. 1985 Turbulence Models for Near-Wall and Low-Reynolds Number Flows: A Review. *AIAA Journal* **23, 9**, 1308–1319.

Peric, M. 1985 A Finite Volume method for the prediction of three-dimensional fluid flow in complex ducts. PhD thesis, Imperial College, University of London.

Piomelli, U. & Balaras, E. 2002 Wall-Layer Model for Large-Eddy-Simulation. *Annual Review of Fluid Mechanics* **34**, 349–374.

Piomelli, U., Balaras, E., Pasinato, H., Squires, K. D. & Spalart, P. R. 2003 The inner-outer layer interface in large-eddy simulations with wall-layer models. *International Journal of Heat and Fluid Flow* **24**, 538–550.

Poole, David 2006 *Linear Algebra: A Modern Introduction*. Thomson Brooks/-Cole.

Pope, S. B. 1975 A more general effective-viscosity hypothesis. *Journal of Fluid Mechanics* **72, 2**, 331–340.

Pope, S. B. 2000 *Turbulent Flows*. Cambridge University Press.

Quemere, P. & Sagaut, P. 2002 Zonal multi-domain RANS/LES simulations of turbulent flows. *International Journal of Numerical Methods in Fluids* **40**, 903–925.

Rahman, M. M., Rautaheimo, P. & Siikonen, T. 2001 Modifications for an explicit algebraic stress model. *International Journal for Numerical Methods in Fluids* **35**, 221–245.

Rasam, A., Brethouwer, G., Schlatter, P. & Johansen, A. V. 2011 Effect of modelling, resolution and anisotropy of subgrid-scales on large eddy simulations of channel flow. *Journal of Turbulence* **12, 10**, 1–20.

Reichardt, H. 1951 Vollstaendige Darstellung der turbulenten Geschwindigkeiteverteilung in glatten Leitungen. *Zeitschrift fuer Angewandte Mathematik und Mechanik* **31**, 209–219.

Reynolds, W. C. & Hussain, A. K. M. F. 1972 The mechanics of an organized wave in turbulent shear flow. part 3. theoretical models and comparisons with experiment. *Journal of Fluid Mechanics* **54, 2**, 263–288.

Rodi, W. 1972 The prediction of free turbulent boundary layers by use of a two-equation model of turbulence. PhD thesis, Ph.D. Thesis, University of London.

Rodi, W. 1976 A new algebraic relation for calculating the Reynolds stresses. *Zeitschrift fuer angewandte Mathematik und Mechanik* **56**.

Rodi, W. & Mansour, N. N. 1993 Low Reynolds number k-ϵ modelling with the aid of direct simulation data. *Journal of Fluid Mechanics* **250**, 509–529.

Rodi, W. & Scheuerer, G. 1983 Calculation of Curved Shear Layers with Two-Equation Turbulence Models. *Physics of Fluids* **26**, 1422–1436.

Rotta, J. C. 1951 Statistische Theory nichthomogener Turbulenz. *Zeitschrift fuer Physik* **129**, 547–572.

Rotta, J. C. 1968 Uber eine Methode zur Berechnung turbulent Scherstroemungen. *Aerodynamische Versuchsanstalt Goettingen, Report 69A14* .

Rumsey, C. L. & Gatski, T. B. 2001 Recent Turbulence Model Advances Applied to Multielement Airfoil Calculation. *Journal of Aircraft* **38, 5**, 904–910.

Rumsey, C. L., Gatski, T. B. & Morrison, J. H. 1999 Turbulence Model Predictions of Extra-Strain Rate Effects in Strongly-curved Flows. *37th Aerosapce Sciences Meeting & Exhibit, Reno, NV, AIAA 99-0157* .

Rumsey, C. L., Gatski, T. B. & Morrison, J. H. 2000 Turbulence Model Predictions of Strongly Curved Flow in a U-Duct. *AIAA Journal* **38, 8**, 1394–1402.

Rumsey, C. L. & Greenblatt, D. 2009 Flow Control Predictions Using Unsteady Reynolds-Averaged Navier-Stokes Modeling: A Parametric Study. *AIAA Journal* **47, 9**, 2259–2262.

Sagaut, P. 2001 *Large-Eddy Simulation for Incompressible Flows - An Introduction*. Third Edition, Springer Berling Heidelber New York.

Sagaut, P, Deck, Sebastien & Terracol, Marc 2006 *Multiscale and Multiresolution Approaches in Turbulence*. Imperial College Press.

Sandberg, R. D. & Fasel, H. F. 2006 Investigation of Supersonic Wakes Using Conventional and Hybrid Turbulence Models. *AIAA Journal* **44, 9**.

Sarkar, A. & So, R. M. C. 1997 A critical evaluation of near-wall two-equation models against direct numerical simulation data. *International Journal of Heat and Fluid Flow* **18**, 197–208.

Schewe, G. 1983 On the force fluctuations acting on a circular cylinder in crossflow from subcritical up to transcritical Reynolds numbers. *Journal of Fluid Mechanics* **133**, 265–285.

Schiestel, R. & Dejoan, A. 2005 Towards a new partially integrated transport model for coarse grid and unsteady turbulent flow simulations. *Theoretical and Computational Fluid Dynamics* **18**, 443–468.

Schluter, J. U. & Pitsch, H. 2001 Consistent boundary conditions for integrated LES/RANS simulations: LES outflow conditions. *Center of Turbulence Research, Annual Research Briefs* .

Schneider, H., von Terzi, D., Bauer, H. J. & Rodi, W. 2010*a* Impact of Secondary Vortices on Separation Dynamics in 3D Asymmetric Diffusers. In *8th ERCOFTAC Workshop on Direct and Large-Eddy Simulation*.

Schneider, H., von Terzi, D., Bauer, H. J. & Rodi, W. 2010*b* Reliable and Accurate Prediction of Three-Dimensional Separation in Asymmetric Diffusers Using Large-Eddy Simulation. *JOURNAL OF FLUIDS ENGINEERING* **132, 3**.

Schumann, U. 1977 Realizability of Reynolds-stress turbulence models. *The Physics of Fluids* **20, 5**, 721–725.

Shih, T. H., Zhu, J. & Lumley, J. L. 1995 A new Reynolds stress algebraic equation model. *Computational Methods in Applied Mechanical Engineering* **125**, 287–302.

Shima, N. 1988 A Reynolds Stress Model for Near-Wall and Low-Reynolds-Number Regions. *Journal of Fluids Engineering* **110**, 38–44.

Shur, M., Spalart, P. R., Squires, K. D., Strelets, M. & Travin, A. 2005 Three Dimensionality in Reynolds-Averaged Navier-Stokes Solutions Around Two-Dimensional Geometries. *AIAA Journal* **43, 6**, 1230–1242.

Shur, M. L., Spalart, P. R., Strelets, M. Kh. & Travin, A. K. 2008 A hybrid RANS/LES approach with delayed-DES and wall-modelled LES capabilities. *International Jounral of Heat and Fluid Flow* **29**, 1638–1649.

Smagorinsky, J. 1963 General Circulation Experiment With the Primitive Equations. 1. The Basic Experiment. *Monthly Weather Review* **91, 3**, 99–164.

So, R. M. C., Lai, Y. G. & Zhang, H. S. 1991 Second-Order Near-Wall Turbulence Closures: A Review. *AIAA Journal* **29, 11**, 1819–1835.

Song, C. S. & Park, S. O. 2009 Numerical simulation of low past a square cylinder using Part-Averaged Navier-Stokes model. *Journal of Wind Engineering and Industrial Aerodynamics* **97**, 37–47.

Spalart, P. R. 2001 Young-Person's Guide to Detached-Eddy Simulation Grids. *NASA / CR-2001-211032* .

Spalart, P. R. 2009 Detached Eddy Simulation. *Annual Review of Fluid Mechanics* **41**, 181–202.

Spalart, P. R. & Allmaras, S. R. 1992 A One-Equation Turbulence Model for Aerodynamic Flows. *AIAA Paper 92-0439* .

Spalart, P. R., Deck, S., Shur, M. L., Squires, K. D., Strelets, M. Kh. & Travin, A. 2006 A new version of detached-eddy simulation, resistant to ambiguous grid densities. *Theoretical and Computational Fluid Dynamics* **20**, 181–195.

Spalart, P. R., Jou, W. H., Strelets, M. & Allmaras, S. R. 1997 Comments on the Feasibility of LES for Wings, and on a Hybrid RANS/LES Approach. *First AFOSR International Conference on DNS/LES, Ruston, Louisiana, USA* .

Spalart, P. R. & Rumsey, C. L. 2007 Effective inflow conditions for turbulence models in aerodynamic calculations. *AIAA Journal* **45, 10**, 2544–2553.

Spencer, A. J. & Rivlin, R. S 1959 The theory of matrix polynomials and its application to the mechanics of isotropic continua. *Archive for Rational Mechanics and Analysis* **2**, 309–336.

Speziale, C. G. 1997 Comparison of Explicit and Traditional Algebraic Stress Models of Turbulence. *AIAA Journal* **35, 9**, 1506–1509.

Speziale, C. G. 1998*a* A Combined Large-Eddy Simulation and Time-Dependent RANS Capability for High-Speed Compressible Flows. *Journal of Scientific Computing* **13, 3**.

Speziale, C. G. 1998*b* Turbulence Modeling for Time-Dependent RANS and VLES: A Review. *AIAA Journal* **14, 3**.

Speziale, C. G., Abid, R. & Anderson, E. C. 1992 A criticial evaluation of two-equation models for near wall turbulence. *AIAA Journal* **30, 2**, 324–331.

Speziale, C. G., Sarkar, S. & Gatski, T. B. 1991 Modelling the pressure-strain correlation of turbulence: an invariant dynamical systems approach. *Journal of Fluid Mechanics* **227**, 245–272.

Squires, Kayle D. 2004 Detached-Eddy Simulation: Current Status and Perspectives. *Proceedings of Direct and Large-Eddy Simulation* **5**.

Squires, K. D., Forsythe, J. R., Morton, S. A. andStranf, W. Z., Wurtzler, K. E., Tomaro, F., Grismer, M. J. & Spalart, P. R. 2002 Progress on Detached-Eddy Simulation of Massively Separated Flows. *AIAA-2002-1021, AIAA Aerospace Sciences Meeting and Exhibit, 40th, Reno, NV* .

Suga, K. & Abe, K. 2000 Nonlinear eddy viscosity modelling for turbulence and heat transfer near wall and shear-free boundaries. *International Journal of Heat and Fluid Flow* **21**, 37–48.

Taulbee, S. B. 1992 An improved algebraic Reynolds stress model and corresponding nonlinear stress model. *Physics of Fluids* **4, 11**, 2555–2561.

Taulbee, S. B. 1994 Stress relation for three-dimensional turbulent flows. *Physics of Fluids* **6, 3**, 1399–4101.

Temmerman, T., Haziabdic, M., Leschziner, M. A. & Hanjalic, K. 2005 A Hybrid two layer URANS-LES appraoch for the large-eddy simulation at high Reynolds numbers. *International Journal of Heat and Fluid Flow* **26**, 173–190.

Tennekes, H. & Lumley, J. L. 1972 *A first course in turbulence*. The MIT Press.

Tessicini, F., Temmerman, T. & Leschziner, M. A. 2006 Approximate near-wall treatments based on zonal and hybrid RANS-LES methods for LES at high Reynolds numbers. *International Journal of Heat and Fluid Flow* **27**, 789–799.

Travin, A., Shur, M., Spalart, P. & Strelets, M. 2004*a* On URANS Solutions with LES-like Behaviour. *Congress on Computational Methods in Applied Sciences and Engineering, ECCOMAS* .

Travin, A., Shur, M., Strelets, M. & Spalart, P. R. 2004*b* Physical and Numerical Upgrades in the Detached-Eddy Simulation of Complex Turbulent Flows. In *Advances in LES of Complex Flows* (ed. R. Moreau, R. Friedrich & W. Rodi), *Fluid Mechanics and Its Applications*, vol. 65, pp. 239–254. Springer Netherlands.

Uribe, J. C., Jarrin, N., Prosser, R. & Laurence, D. R. 2010 Development of a Two-velocities Hybrid RANS-LES Model and its Application to a Trailing Edge Flow. *Flow Turbulence and Combustion* **85, 2**, 181–197.

Versteeg, H. K. & Malalasekera, W. 2007 *An Introduction to Computational Fluid Dynamics. The Finite Volume Method, second edition.*. Pearson Education Limited.

de Villiers, Eugene 2006 The Potential of Large-Eddy Simulation for the Modeling of Wall Bounded Flows. PhD thesis, Imperial College of Science, Technology and Medicine, Department of Mechanical Engineering, Thermofluids Section.

Wallin, S. & Johansen, A. V. 2000 An explicit algebraic Reynolds stress model for incompressible and compressible turbulent flows. *Journal of Fluid Mechanics* **403**, 89–132.

Wallin, S. & Johansen, A. V. 2002 Modelling streamline curvature effects in explicit algebraic Reynolds stress turbulence models. *International Journal of Heat and Fluid Flow* **23**, 721–730.

Wang, C., Dejoan, A. & Leschziner, M. A. 2005 Assessing the Role of Curvature Effects in the Representation of Anisotropy Transport in Albebraic Reynolds-Stress Modelling Applied to Separated Flows. *Flow, Turbulence and Combustion* **74**, 409–429.

Weinmann, M. & Sandberg, R. D. 2009 Suitability of Explicit Algebraic Stress Models for predicting complex three-dimensional flows. In *19th AIAA Computational Fluid Dynamics, San Antonio, Texas. AIAA-2009-3663*.

Weller, H. G., Tabor, G., Jasak, H. & Fureby, C. 1998 A tensorial approach to computational continuum mechanics using object-oriented techniques. *Computers in Physics* **12, 6**, 620–631.

Wilcox, D. C. 1988 Reassessment of the Scale-Determining Equation for Advanced Turbulence Models. *AIAA Journal of Aircraft* **26, 11**, 1299–1310.

Wilcox, D. C. 1993 Comparison of Two-Equation Turbulence Models for Boundary Layers with Pressure Gradient. *AIAA Journal* **31, 8**, 1414–1421.

Wilcox, D. C. 1998 *Turbulence Modeling for CFD, 2nd Edition*. DCW Industries Inc.

Wilcox, D. C. 2008 Formulation of the k-ω Turbulence Model Revisited. *AIAA Journal* **46, 11**, 2823–2837.

Wolfshtein, M. 1969 The velocity and Temperature Distribution of One-Dimensional Flow Turbulence Augmentation and Pressure Gradient. *International Journal of Heat and Mass Transfer* **12**, 301–318.

Xiao, X., Edwards, J. R. & Hassan, H. A. 2004 Blending Functions in Hybrid Large-Eddy/Reynolds-Averaged Navier-Stokes Simulations. *AIAA Journal* **42, 12**.

Yan, J., Eschricht, D., Thiele, F. & Li, X 2009 Modeling and simulation of coaxial jet flow. *New Trends in Fluid Mechanics Research, Part 3* pp. 138–141.

Ying, R. & Canuto, M. 1996 Turbulence Modelling Over Two-Dimensional Hills Using An Algebraic Reynolds Stress Expression. *Boundary-Layer Meteorology* **77**, 69–99.

Zdravkovich, M.M. 1987 Review of flow interference between two circular cylinders in various arrangements. *ASME Journal of Fluids Engineering* **99**, 618–631.

Zhang, H. L., Bachman, C. R. & Fasel, H. F. 2000 Application of a New Methodology for Simulations of Complex Turbulent Flows. *AIAA Paper 2000-2535* .